U.PORTO

FEUP FACULDADE DE ENGENHARIA
UNIVERSIDADE DO PORTO

A METHODOLOGY FOR THE ASSESSMENT OF THE
TRAIN RUNNING SAFETY ON BRIDGES

Pedro Aires Moreira Montenegro e Almeida
2015

A dissertation presented to the Faculty of Engineering of the University of Porto
for the degree of Doctor in Civil Engineering.

Supervisor: Professor Rui Calçada
Co-Supervisor : Professor Nelson Vila Pouca

"CONVITE

Defronte da cabana de bambu
respira a esmeralda de um lago.

Virás quando tiveres tempo,
beberemos chá,
na casa de barro coroada de colmo
não encontrarás conforto.

É fácil saber qual é:
frente à porta e antes da cabana de bambu
uma árvore pujante de eternas
afogueadas gemas
anuncia os futuros visitantes."

(in Oferenda Oriental, Aires Montenegro)

À Alice

THESIS EXAMINING COMMITTEE

The present thesis has been examined on March 12, 2015, at the Faculty of Engineering of the University of Porto by the following committee:

President:

- Dr. Rui Manuel Carvalho Marques de Faria (by delegation of the Dean of the Faculty of Engineering of the University of Porto), Full Professor of the Civil Engineering Department of the Faculty of Engineering of the University of Porto, Porto, Portugal.

Examiners:

- Dr. Makoto Tanabe, Professor of the Department of Mechanical Engineering of the Faculty of Engineering of the Kanagawa Institute of Technology, Atsugi, Japan.

- Dr. José Maria Goicolea Ruigómez, Full Professor of the Escuela de Ingenieros de Caminos, Canales y Puertos of the Polytechnic University of Madrid, Madrid, Spain.

- Dr. João Carlos Pombo, Associate Professor in Railway Engineering of the School of Energy, Geoscience, Infrastructures & Society of the Heriot-Watt University, Edinburgh, United Kingdom.

- Dr. Raimundo Moreno Delgado, Full Professor (Emeritus) of the Civil Engineering Department of the Faculty of Engineering of the University of Porto, Porto, Portugal.

- Dr. Rui Artur Bártolo Calçada, Full Professor of the Civil Engineering Department of the Faculty of Engineering of the University of Porto, Porto, Portugal (Supervisor).

GENERAL CONTENTS

ABSTRACT

This thesis focuses on the development of a methodology for the assessment of the train running safety on bridges. Particular attention is given to the running stability against moderate and frequent earthquakes which, although may not pose a significant threat to the structural integrity, can jeopardize the train running safety.

In light of this objective, an overview of recent studies carried out in the field of rail traffic stability over bridges is presented, along with a review of the different existing methods for analyzing the dynamic response of the vehicle-structure system.

After going through the most common modeling alternatives, the train-structure interaction method proposed in this work is presented. Special emphasis is given to the wheel-rail contact model used to calculate the contact forces that are generated in the contact interface between the wheel and rail. Most of the existing methods treat the contact forces in the normal and tangential directions as external forces, whereas the present formulation uses a finite element to model the behavior in the contact interface, based on the Hertz theory and Kalker's rolling friction laws. To couple the vehicle and structure, the governing equilibrium equations of both systems are complemented with additional constraint equations that relate the displacements of the contact nodes of the vehicle with the corresponding nodal displacements of the structure. These equations form a single system, with displacements and contact forces as unknowns, that is solved directly using an optimized block factorization algorithm. The proposed model is based on the finite element method, which allows the analysis of structures and vehicles with any degree of complexity. The present formulation is implemented in MATLAB, being the vehicles and structure modeled with ANSYS.

The implemented vehicle-structure interaction tool is validated with three numerical applications and with the results obtained in an experimental test. First, the results obtained with the creep force models implemented in the proposed method are compared with those obtained with the Kalker's exact theory of rolling contact implemented in the software CONTACT. In the second application, the tests performed in the Manchester Benchmark are revisited and replicated with the proposed numerical tool. The third numerical application consists in the hunting stability analysis of a suspended wheelset. The results obtained with the

proposed method for the lateral displacements and yaw rotations of the wheelset are compared with those obtained with a semi-analytical model described in the literature. In the last application, an experimental test conducted in the rolling stock test plant of the Railway Technical Research Institute in Japan, in which a full scale railway vehicle runs over a track with vertical and lateral deviations is reproduced numerically. The results obtained with the proposed method are compared with the experimental results and also with the results obtained using the software DIASTARS.

Finally, a study regarding the running safety of a high-speed train moving over a viaduct under seismic conditions is conducted using the developed train-structure interaction method. The studied viaduct is based on an existing flyover type structure of the Portuguese railway network, while the vehicle consists of a Japanese Shinkansen high-speed train. The seismic action is represented in terms of artificial accelerograms generated from the elastic spectra described in EN 1998-1, while the irregularity profiles are generated based on analytical power spectral density functions. Since no significant nonlinear behavior is likely to be exhibited in the columns for the levels of seismicity considered in this work, all the analysis are performed in the elastic domain with a reduction in the stiffness of the columns to account for the concrete cracking. The running safety analysis of the railway vehicle running over the viaduct is assessed based on four derailment criteria, being the influence of the seismic intensity level, the vehicle running speed and the track quality on the running safety evaluated separately. At the end, all the information obtained in the dynamic analyses is condensed in the so-called running safety charts, which consist in the global envelope of each analyzed safety criteria as function of the running speed of the vehicle and the seismic intensity level.

RESUMO

A presente dissertação centra-se no desenvolvimento de uma metodologia para avaliação da segurança de circulação de comboios sobre pontes. É dada particular atenção à estabilidade de circulação na presença de sismos de intensidade moderada que, embora possam não constituir uma ameaça à integridade estrutural da ponte, podem pôr em causa a segurança de circulação.

À luz deste objetivo, começa-se por apresentar um resumo dos estudos levados a cabo recentemente no âmbito da segurança de tráfego ferroviário em pontes, conjuntamente com uma revisão dos diferentes métodos apresentados na bibliografia com vista à análise da resposta do sistema veículo-estrutura.

Após avaliar-se o atual estado do conhecimento na área, apresenta-se a formulação do método de interação veículo-estrutura desenvolvido no presente trabalho. É dada uma ênfase especial ao modelo de contacto roda-carril usado para o cálculo das forças de contacto geradas na interface de contacto. Na maioria dos métodos existentes, as forças de contacto nas direções normal e tangencial são tratadas como sendo forças externas, enquanto a presente formulação utiliza um elemento finito para modelar a interface de contacto, baseado na teoria de Hertz e nas leis de atrito de rolamento propostas por Kalker. Com vista ao acoplamento do veículo com a estrutura, as equações de equilíbrio dinâmico são complementadas com equações de compatibilidade que relacionam os deslocamentos dos nós de contacto do veículo com os correspondentes deslocamentos nodais da estrutura. Estas equações constituem um sistema único, cujas incógnitas são deslocamentos e forças de contacto, que pode ser resolvido diretamente através de um algoritmo de fatorização em blocos. A ferramenta proposta é baseada no método dos elementos finitos, permitindo assim a análise de veículos e estruturas com qualquer nível de complexidade. A presente formulação encontra-se implementada em MATLAB, sendo os veículos e a estrutura modelados com recurso a ANSYS.

A ferramenta de interação veículo-estrutura implementada é validada através de três aplicações numéricas e de um ensaio experimental. Assim, a primeira aplicação consiste na comparação dos resultados obtidos pelos modelos de atrito de rolamento implementados no presente método com os resultados obtidos através da teoria exata de Kalker implementada no software CONTACT. Na segunda aplicação, os testes realizados no Benchmark de Manchester

são revisitados e replicados com a ferramenta numérica proposta. A terceira aplicação consiste na análise de estabilidade de um eixo isolado face ao movimento de lacete por ele experimentado. Os deslocamentos laterais e rotações de lacete obtidos com a ferramenta desenvolvida são comparados com os resultados obtidos através de um modelo semi-analítico descrito na bibliografia. Na última aplicação, é reproduzido numericamente um ensaio experimental realizado na instalação de testes de material circulante do Railway Technical Research Institute no Japão. Neste teste foi ensaiado um veículo ferroviário à escala real a circular sobre uma via sujeita a desvios verticais e laterais impostos por atuadores. As respostas do veículo obtidas com a ferramenta proposta são confrontadas com as respostas experimentais, bem como com os resultados obtidos no software DIASTARS.

Por último, é realizado um estudo da segurança de circulação de um comboio de alta-velocidade a circular sobre um viaduto sujeito a ações sísmicas. O viaduto estudado é baseado numa estrutura do tipo *flyover* existente na rede ferroviária Portuguesa, enquanto o veículo consiste num comboio de alta velocidade Japonês. A ação sísmica é representada sob a forma de acelerogramas artificiais gerados a partir dos espetros elásticos descritos na EN 1998-1. Já as irregularidades são geradas com base em funções analíticas de densidade espetral de potência. Uma vez que não é espectável que o comportamento dos pilares atinja um nível significativo de não-linearidade, todas as análises são realizadas no domínio elástico, tendo-se tido em conta a redução de rigidez dos pilares devido à fendilhação. A estabilidade de circulação é analisada com base em quatro critérios de descarrilamento, sendo a influência da intensidade sísmica, da velocidade do veículo e da qualidade da via na segurança avaliada separadamente. No final, toda a informação obtida nas análises dinâmicas é condensada em mapas de segurança de circulação. Estes mapas consistem na envolvente global de cada critério analisado em função da velocidade de circulação do veículo e da intensidade sísmica.

概要

　　本論文は，橋梁上を走行する列車の走行安全性の評価手法の高度化を目的としたものである．特に，構造物自体の安定性には重大な脅威とはならないものの，上部工に大きな振動が発生した場合に列車の走行安全性に脅威を及ぼす可能性がある，比較的小規模かつ頻発する地震に対する走行安全性を対象とした．

　　この目的のもと，橋梁上の鉄道交通の安定性の分野に関する近年の研究について概要をまとめ，鉄道車両/構造物システムの動的応答の数値解析に関する既往の手法をレビューした．

　　最も一般的なモデル化手法の選択肢を経て、本研究で提案された鉄道車両/構造物の構造連成手法を提示した．車輪/レール間の接触界面に発生する接触力を評価するための，車輪/レール間の接触モデルに特に着目した．既往のほとんどの手法は，接触面方向，法線方向の接触力を外力として取り扱っているが，提案した定式化の中では，接触界面を表現するために，Hertz の接触理論と Kalker の転がり摩擦の法則に基づいた有限要素を用いた．鉄道車両と構造物の連成を考慮するため，両システムの支配平衡方程式は，車両側の接触節点の変位と，対応する構造物側の節点変位とを関連付ける制約式を追加することで補完されている．これらの各システムの方程式は独立しており，最適化ブロック分解アルゴリズムを使用して直接得られる未知数である，変位と接触力を含んでいる．提案手法は有限要素法に基づいていることから，高度に複雑な構造物，鉄道車両の解析も可能である．提案手法では，ANSYS で鉄道車両や構造物をモデル化し，MATLAB で実装している．

　　実装された鉄道車両/構造物の連成解析ツールの妥当性を，三つの数値計算アプリケーションの結果と，一つの実験結果を用いて検証した．第一に，提案手法で実装されているクリープ力モデルにより得られた結果と，ソフトウェア CONTACT に実装されている Kalker の転がり接触理論を用いて得られたものと比較する．第二に，マンチェスター・ベンチマークで行われたテストを対象に，提案数値解析手法で再現した．第

三に，取り出した輪軸の蛇行安定解析を対象とした．提案方法を用いて得られた車輪の横方向変位およびヨー回転角の結果と，文献に記載された半解析モデルを用いて得られた結果とを比較した．最後に，日本の鉄道総合技術研究所で行われた高速車両走行試験台の実験試験を数値解析により再現した．車両走行試験は，実物大の鉄道車両が水平方向および鉛直方向に不整のある軌道上を走行する条件で行われた．提案手法による結果は，車両走行試験装置の実験結果，およびソフトウェア DIASTARS を用いて得られた結果と比較した．

　最後に，開発した鉄道車両/構造物の解析手法を用いて，高架橋上を高速走行する鉄道車両の地震時走行安全性に関して検討を行った．対象構造物は，ポルトガルの鉄道ネットワークに実在する高架道路型高架橋とし，車両は日本の新幹線高速鉄道で使用されている車両とした．地震作用は，EN-19981 に記載されている弾性スペクトルから人工に生成された加速度を用いた．軌道不整形状は，分析パワースペクトル密度関数に基づいて生成した．本検討で対象とした地震動レベルにおいては，柱に有意な非線形挙動が現れる可能性が想定されないことから，すべての解析は，コンクリートのひび割れを考慮するために柱剛性を低下させた弾性領域で行った．高架橋上を走行する鉄道車両の走行安全性に関する四つの脱線基準を，走行安全性に影響を与える地震動の大きさ，車両の走行速度，軌道の品質に基づいて評価した．最終的に，動的解析で得られた全結果を基に，列車走行速度と地震動の大きさの関数として，数値解析から得られた安全基準を全て安全側に包絡する，いわゆる走行安全性チャートを作成した．

LIST OF PUBLICATIONS

The following publications have been derived from the development of the present thesis.

International scientific journals

- Neves, S.G.M., Montenegro, P.A., Azevedo, A.F.M., Calçada, R. *A direct method for analyzing the nonlinear vehicle–structure interaction*, Engineering Structures, 2014, **69**, pp. 83-89. DOI:10.1016/j.engstruct.2014.02.027.

- Montenegro, P.A., Calçada, R., Vila Pouca, N., Tanabe, M. *Running safety assessment of trains moving over bridges subjected to earthquakes*, Earthquake Engineering and Structural Dynamics, 2015a, (submitted).

- Montenegro, P.A., Neves, S.G.M., Calçada, R., Tanabe, M., Sogabe, M. *Wheel-rail contact formulation* for analyzing the lateral train-structure dynamic interaction, Computers & Structures, 2015, **152**, pp. 200-214. DOI:10.1016/j.compstruc.2015.01.004.

International conference proceedings

- Montenegro, P.A., Calçada, R., Vila Pouca, N. *A wheel-rail contact model pre-processor for train-structure dynamic interaction analysis*, In J. Pombo (Ed), Railways 2012 - 1st International Conference on Railway Technology: Research, Development and Maintenance, Las Palmas de Gran Canaria, Spain, 2012.

- Montenegro, P.A., Neves, S.G.M., Azevedo, A.F.M., Calçada, R. "*A nonlinear vehicle-structure interaction methodology with wheel-rail detachment and reattachment*", In M. Papadrakakis, N.D.Lagaros, V. Plevris (Ed), COMPDYN 2013 - 4th ECCOMAS Thematic Conference on Computational Methods in Structural Dynamics and Earthquake Engineering, Kos, Greece, 2013.

- Montenegro, P.A., Neves, S.G.M., Calçada, R., Tanabe, M., Sogabe, M. "*A three dimensional train-structure interaction methodology: Experimental validation*", In J. Pombo (Ed), Railways 2014 - 2nd International Conference on Railway Technology: Research, Development and Maintenance, Ajaccio, Corsica, France, 2014.

- Neves, S.G.M., Montenegro, P.A., Azevedo, A.F.M., Calçada, R. "*A direct method for analysing the nonlinear vehicle-structure interaction in high-speed railway lines*", In J. Pombo (Ed), Railways 2014 - 2nd International Conference on Railway Technology: Research, Development and Maintenance, Ajaccio, Corsica, France, 2014.

- Montenegro, P.A., Neves, S.G.M., Calçada, R., Tanabe, M., Sogabe, M. "*A nonlinear vehicle-structure interaction methodology for the assessment of the train running safety*", In A. Cunha, E. Caetano, P. Ribeiro, G. Müller (Ed), EURODYN 2014 - 9th International Conference on Structural Dynamics, Porto, Portugal, 2014.

- Montenegro, P.A., Calçada, R., Vila Pouca, N. "*Dynamic stability of trains moving over bridges subjected to seismic excitations*", In P. Iványi and B.H.V. Topping (Ed), ECT 2014 - 9th International Conference on Engineering Computational Technology, Naples, Italy, 2014.

National conference proceedings

- Montenegro, P.A., Calçada, R., Vila Pouca, N. "*A vehicle-structure interaction method for analyzing the train running safety*", In A. Filho, J. Sousa and R. Pinto (Ed), IBRACON 2014 - 56th Brazilian Conference on Concrete - 4th Symposium on Railway and Road Infrastructure, Natal, Brazil, 2014

- Montenegro, P.A., Calçada, R., Vila Pouca, N. "*Avaliação da segurança de circulação de um comboio de alta-velocidade sobre um viaduto em condições sísmicas*", In J.M. Catarino, J. Almeida Fernandes, M. Pipa and J. Azevedo (Ed), JPEE 2014 - 5as Jornadas Portuguesas de Engenharia de Estruturas, Lisbon, Portugal, 2014.

ACKNOWLEDGMENTS / AGRADECIMENTOS

It has been a long journey, longer than expected, filled with both exciting moments and frustrating days. However, in the end, the feeling of accomplishment, the personal and professional experience earned and the new friendships established, compensate most of the drawbacks experienced during this last five years. Therefore, I want to express my sincere gratitude to all who have accompanied me during my PhD that, through their friendship and understanding, contributed to the achievement of this thesis. In particular, I would like to thank:

- My supervisor, Prof. Rui Calçada, for his unconditional support and encouragement throughout my research work. The encouraging words given in the most difficult times were, in most cases, as important as the useful scientific discussions that took place during these last five years. Therefore, I want to thank him not only for the knowledge acquired during this journey, but also for the friendship established between us.

- My co-supervisor, Prof. Nelson Vila Pouca, for the pleasant and informal stance that he showed during our discussions. His contribution for a better understanding of topics regarding earthquake engineering was of the utmost importance for the development of this work. Our friendship that started almost ten years ago, still during my graduation, will always be kept in the future.

- Prof. Makoto Tanabe for granting me the opportunity of doing an internship in Japan in the Kanagawa Institute of Technology and in the Railway Technical Research Institute (RTRI). I wish to thank him for the warm welcome in his institution and for his unconditional scientific and personal support during my stay in Japan. I'll always remember the help he provided during my time in Tokyo in terms of scientific advice, bureaucratic issues, language barriers and cultural adaptation. Finally, I also wish to thank him for all the paperwork provided to apply for the Japanese student visa.

- Dr. Masamichi Sogabe for being my supervisor during my internship in the RTRI. I wish to express my gratitude for the valuable scientific advices given during my stay, as well as the experimental data provided for the validation of the models developed in this

work. I also want to thank him for his friendship demonstrated both during work and during more relaxed times.

- Fundação para a Ciência e Tecnologia for the financial support provided under the PhD grant SFRH/BD/48320/2008.

- REFER for the data provided regarding the Alverca railway viaduct.

- My friend and engineer Sérgio Neves for all his friendship and scientific support given during the implementation of the train-structure interaction method developed in this work. Moreover, I wish to thank him for the knowledge he provided me in terms of programming, especially in MATLAB.

- Prof. Rui Faria, from the Faculdade de Engenharia da Universidade do Porto, for the helpful discussions regarding the nonlinear formulation of the contact model.

- Prof. Jose Maria Goicolea, from the Universidad Politécnica de Madrid (UPM), for his valuable scientific advices, especially regarding the lateral dynamics of the train-structure system. I wish to express my gratitude for his availability to exchange some impressions that introduce me to the topic of this work.

- Dr. Pablo Antolín, from the UPM, for his helpful advices regarding the train-structure dynamics and for all the literature provided in the beginning of this work.

- Dr. Edwin Vollebregt, from the Technische Universiteit Delft and VORtech Computing, for helping me on validating the creep models implemented in this work.

- Prof. Simon Iwnicki and Dr. Philip Shackleton, from the Institute of Railway Research in Huddersfield, for the data provided from the Manchester Benchmark to validate the wheel-rail contact model implemented in this work.

- Prof. João Pombo, from the Heriot Watt University, for our valuable discussions regarding the wheel-rail contact models and for the literature provided during this work.

- All the members of the Structural Mechanics Lab of the RTRI where I spent two months during my internship, namely Dr. Humiaki Uehan, Munemasa Tokunaga, Tsutomu Watanabe, Shintaro Minoura, Matsuoka Kodai, Hidenori Takagi and Ms. Sawako Murai. I wish to thank them for the warm welcome and for the nice welcome and farewell dinners presented to me. Moreover, I will always remember the wonderful coffee given by Ms. Murai everyday at 10:30 and 15:30 sharp.

- My friend and engineer Munemasa Tokunaga, for being my *mentor* of the Japanese culture, for helping me during my stay in Japan and, more recently, for translating the abstract of this thesis to Japanese language.

- Dr. Hajime Wakui and Dr. Nobuyuki Matsumoto, from the RTRI, for their valuable scientific advices during my stay in Tokyo.

- Ms. Yoko Taniguchi, from the International Affairs Division of the RTRI, for helping me in the bureaucratic issues regarding my internship.

- All colleagues from the railways research group of my faculty, namely, Alejandro de Miguel, Andreia Meixedo, Carlos Albuquerque, Cristiana Bonifácio, Cristina Ribeiro, Diogo Ribeiro, Joana Delgado, João Barbosa, João Francisco, João Rocha, Joel Malveiro, Nuno Santos, Nuno Ribeiro, Pedro Jorge and Sérgio Neves.

- All other friends from my faculty, in particular, André Monteiro, Despoina Skoulidou, Diogo Oliveira, Jiang Yadong, Luís Macedo, Luís Martins, Mário Marques, Miguel Araújo, Miriam López, Nuno Pereira and Rui Barros.

- My closest friends, Artur Santos, Francisco Cruz, João Rosas, Jorge Veludo, Nuno Guerra, Pedro Baltazar and Rui Conceição.

- À minha família mais chegada, em particular à Avó Fininha, Babá, Chico, Golias, Madrinha Elisa, Madrinha São, Manel Zé, Manuel João, Milu, Tia Graça, Tio Miguel e Sebastião, por todo o apoio dado ao longo desta jornada.

- Aos meus pais, Papá e Mamã, irmãos, Joana e João, cunhado, Fábio, e sobrinhos, Alice e Henrique, por me terem ouvido e compreendido nos momentos mais difíceis deste trabalho. Peço desculpas por alguns momentos de menor paciência da minha parte que foram ocorrendo ao longo destes últimos cinco anos, em especial no primeiro ano, quando tudo parecia impossível.

- À Erica, por ter sido um dos grandes pilares ao longo destes últimos anos nos quais desenvolvi este trabalho. A ela devo grande parte desta *conquista* porque, apesar de não ter colaborado de uma forma direta no desenvolvimento dos trabalhos, soube-me sempre apoiar nos momentos em que pensei desistir, nos momentos em que estive fora e em todos os outros momentos em que, por causa do trabalho, não pude estar presente. Agradeço ainda o facto de me ter ajudado a treinar as apresentações que fui fazendo ao

longo deste período, ao ponto de decorar termos como *"contact point"*, *"wheel-rail contact"* e *"train running safety"*.

- Por fim, mas nem por isso menos importante, gostaria de agradecer à minha sobrinha Alice que, no último ano e meio, percorreu um caminho que nunca ninguém quis imaginar que uma menina como ela tivesse que percorrer. Eu precisei de 29 anos para arranjar coragem para percorrer recentemente os 21 km de uma meia-maratona...e precisarei ainda de pelo menos mais um ano para conseguir atingir os 42 km. No entanto, a Alice, com apenas 4 anos, já percorreu dezenas de maratonas e em todas elas não só chegou ao fim, como também as venceu, sem se queixar uma única vez de todo o esforço despendido. Por tudo isto e mais alguma coisa, a ela dedico esta tese.

January 6, 2015

TABLE OF CONTENTS

LIST OF SYMBOLS

For clarity purposes, all the abbreviations, notations and symbols presented in this list are defined in the text when first used. Generally, the use of the same symbol for different entities is avoided. However, in situations in which such procedure proved to be inadequate, the risk of misunderstanding is minimized by preventing the simultaneous use of the same symbol for different entities in the same context. The list is ordered alphabetically.

ABBREVIATIONS

2D / 3D	Two-dimensional / Three-dimensional
AAR	Association of American Railroads
BS	Bending Shape deflection
CWC	Characteristic Wind Curve
DOF	Degree of Freedom
EN	European Norm
GPU	Graphic Processing Unit
HSLM	High Speed Load Model
JIS	Japanese Industrial Standards
NA	National Annex
PGA	Peak Ground Acceleration
PSD	Power Spectral Density
RTRI	Railway Technical Research Institute
SI	Spectral Index
TS	Translation Shape deflection
TSI	Technical Specifications for Interoperability
UIC	International Union of Railways

NOTATIONS

$d(\cdot)$	Elemental variation of $(\cdot)$
$\Delta(\cdot)$	Increment or variation of $(\cdot)$
$\dot{(\cdot)}$	First time derivative of $(\cdot)$
$\ddot{(\cdot)}$	Second time derivative of $(\cdot)$
$\lvert(\cdot)\rvert$	Modulus of $(\cdot)$
$\lVert(\cdot)\rVert$	Norm of $(\cdot)$
$(\cdot)\cdot(\circ)$	Scalar product between $(\cdot)$ and $(\circ)$.
$(\cdot)\times(\circ)$	Cross product between $(\cdot)$ and $(\circ)$.
$(\cdot)_0$	Referred to the initial value
$(\cdot)_A$	Referred to the alignment irregularity
$(\cdot)_b$	Referred to the base shear
$(\cdot)_{bg}$	Referred to the bogie
$(\cdot)_C$	Referred to the cross level irregularity
$(\cdot)^{ce}$	Referred to the contact element
$(\cdot)_c$	Referred to the contact point coordinate system
$(\cdot)_{cb}$	Referred to the carbody
$(\cdot)_{cr}$	Referred to cracking
$(\cdot)_{dyn}$	Referred to dynamic
$(\cdot)_{eff}$	Referred to effective
$(\cdot)_{ela}$	Referred to elastic
$(\cdot)_{ext}$	Referred to the external loads
$(\cdot)_F$	Referred to the free nodal degrees of freedom
$(\cdot)_G$	Referred to the gauge irregularity
$(\cdot)_g$	Referred to the global coordinate system
$(\cdot)^{IV}$	Referred to the intersection volume

$(\cdot)_I$	Referred to the free nodal degrees of freedom belonging to linear elements
$(\cdot)^i$	Referred to the iteration i
$(\cdot)^{lft}/(\cdot)_{lft}$	Referred to the left side
$(\cdot)_{lim}$	Referred to the limit value of $(\cdot)$
$(\cdot)_{max}$	Referred to the maximum
$(\cdot)_n$	Referred to the nth quantity / Referred to the normal contact force
$(\cdot)_O$	Referred to the origin of a coordinate system
$(\cdot)_P$	Referred to the prescribed degrees of freedom
$(\cdot)_R$	Referred to the free nodal degrees of freedom belonging to nonlinear elements
$(\cdot)^{rht}/(\cdot)_{rht}$	Referred to the right side
$(\cdot)_r$	Referred to the rail / Referred to the rail profile coordinate system
$(\cdot)_S$	Referred to the structure
$(\cdot)_{sta}$	Referred to static
$(\cdot)^T$	Referred to the transpose of $(\cdot)$
$(\cdot)^t$	Referred to the time step t
$(\cdot)^{te}$	Referred to the target element
$(\cdot)_t$	Referred to the target element coordinate system
$(\cdot)_{tc}$	Referred to the track centerline coordinate system
$(\cdot)_V$	Referred to the vehicle / Referred to the elevation irregularity
$(\cdot)_w$	Referred to the wheel / Referred to the wheel profile coordinate system
$(\cdot)_{ws}$	Referred to the wheelset / Referred to the wheelset coordinate system
$(\cdot)_{w,t}$	Referred to the wheel tread
$(\cdot)_{w,f}$	Referred to the wheel flange
$(\cdot)_{x,y,z}$	Referred to the x, y or z axis
$(\cdot)_Y$	Referred to the degrees of freedom belonging of the internal nodes added by the contact element
$(\cdot)_\eta$	Referred to the lateral creepage / creep force

$(\cdot)_\xi$	Referred to the longitudinal creepage / creep force
$(\cdot)_\phi$	Referred to the spin creepage / spin creep moment

SCALARS

Latin symbols

A	Amplitude / Irregularity scale factor / Hertz geometric parameter
$a, \dot{a}, \ddot{a}$	Displacement, velocity and acceleration
$\ddot{a}_g$	Ground motion acceleration
a, b	Semi-axes of the contact ellipse
B	Hertz geometric parameter
C_h	Hertz constant
d	Penetration between the two contacting bodies
E	Young modulus
F	Force
f	Frequency
$f(s)$	Surface defining function
G	Shear modulus
h	Vertical distance
I	Intensity function
i, j	Indices
K_h	Hertz generalized stiffness coefficient
L	Span length
l	Half of the gauge
M	Moment
m, n	Hertz coefficients
Q	Vertical contact force

R	Radius of curvature
R_0	Initial rolling radius of the wheel
R_r	Correlation function
r	Irregularity
$\dot{r}$	Rigid body slip at the contact area
S	Power spectral density function
s	Surface parameter
$\dot{s}$	Actual slip at the contac area
T	Structural period / Return period of the seismic action
t	Time / Deck twist
V	Vehicle speed
v	Relative tangential elastic displacement at the contact area
x, y, z	Cartesian coordinate in a 3D coordinate system
Y	Lateral contact force

Greek symbols

α	Parameter of the α method
β	Newmark integration parameter
Γ	Contact area
γ	Contact angle / Newmark integration parameter
δ	Deflection / Displacement
ε	Tolerance / Gradient of tangential stress
$\zeta_{N,W,P,R,U}$	Safety criteria factors (Nadal, Weinstock, Prud'homme, rail rollover and wheel unloading)
θ	Hertz angular parameter
θ_t	Angular rotation between decks
κ	Surface curvature

λ	Wavelength
μ	Friction coefficient
ν	Poisson's ratio
σ	Normal stress
τ	Tangential stress
υ	Creepage
ϕ	Roll angle or rotation / Phase angle
ψ	Yaw angle or rotation
Ω	Spatial frequency
ω	Angular frequency

VECTORS AND MATRICES

Latin symbols

$\mathbf{a}, \dot{\mathbf{a}}, \ddot{\mathbf{a}}$	Displacement, velocity and acceleration vectors
$\mathbf{C}$	Damping matrix
$\mathbf{D}$	Force transformation matrix
$\mathbf{d}_{wr}$	Vector defining the relative position between wheel and rail
$\mathbf{e}$	Unit base vector
$\mathbf{F}$	Load vector
$\mathbf{H}$	Displacements transformation matrix
$\mathbf{K}$	Stiffness matrix
$\overline{\mathbf{K}}$	Effective stiffness matrix
$\mathbf{M}$	Mass matrix
$\mathbf{n}$	Normal vector
$\mathbf{P}$	Vector of external applied loads
$\mathbf{R}$	Vector of nodal forces corresponding to the internal element stresses

r	Irregularity vector
S	Vector of support reactions
T	General transformation matrix
t	Tangential vector
u	Position vector
v	Displacements of the contact point
X	Contact force vector

Greek symbols

Ψ	Residual force vector

Chapter 1

INTRODUCTION

1.1   SCOPE OF THE THESIS

In the 21st century, with the globalization playing an increasingly important and influential role in societies and markets, the development of new transport infrastructures that allow an efficient movement of passengers and goods is of the utmost importance. Railway transport, in particular the high-speed railways, have been playing a key role in this context, contributing for the sustainable development of countries, both in terms of economic growth and social development. This type of transport has several advantages over others, namely road and air, mostly related with the lower transportation costs, the lower environmental impact and safety. Additionally, the reduction in travel time due to the increase of speed, along with an improvement in passenger comfort, also contributes for the greater competitiveness of rail transport.

The experience acquired in the countries which already implemented high-speed railways provides insight into the impact of this mean of transport in the development of those countries. Sánchez Doblado (2007), for example, refers that in Spain, the new high-speed railway network has strengthened the social and territorial cohesion and made an undeniable contribution for the economy of the country. Barron de Angoiti (2008) also provides important information regarding the market share of high-speed trains. The author refers that since the high-speed line between Paris and Brussels opened, the carried passengers by train grew from 24 % to 50 % of

total traffic (see Figure 1.1a). Another example in the evolution of the modal split is the Spanish high-speed line between Madrid and Seville. In this case, considering only the passengers carried by train and air transport, the high-speed train obtains more than 80 % of the share, against the 33 % before the high-speed line was opened (see Figure 1.1b). According to the statistics presented by the author, even considering the effect of the low cost air companies, the high-speed services continue to have advantage in terms of market share. As an example, the Eurostar that links London to Paris carries 81 % of the total passengers that travel by train or plane. The high-speed train is therefore a new concept of rail transport characterized by a high standard of reliability and safety, which may assume a very attractive alternative for the movement of people and goods.
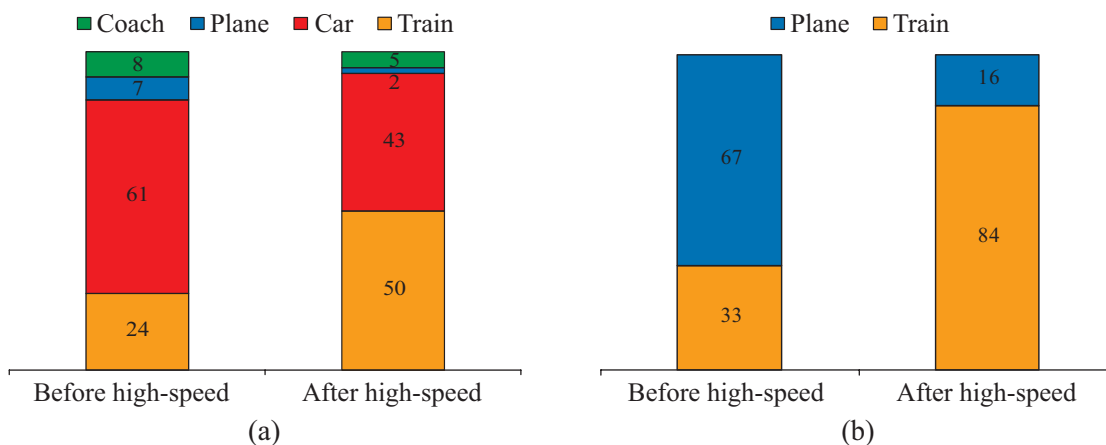
Figure 1.1 - Evolution of the transport modal split (adapted from Barron de Angoiti (2008)): (a) Paris-Brussels line and (b) Madrid-Seville line.

The fast development in the last decades of several high-speed rail networks around the globe made it necessary to build new railway lines that would meet the strict design requirements of this type of transport. Thus, the necessity to ensure smoother tracks with larger curve radius resulted in new railway lines with a high percentage of viaducts and bridges. Some countries in Asia, for example, such as China, Japan and Taiwan, have a highly developed high-speed railway network in which some of the lines have more than 75 % of viaducts (Ishibashi, 2004; Kao and Lin, 2007; Dai et al., 2010), as shown in Figure 1.2.
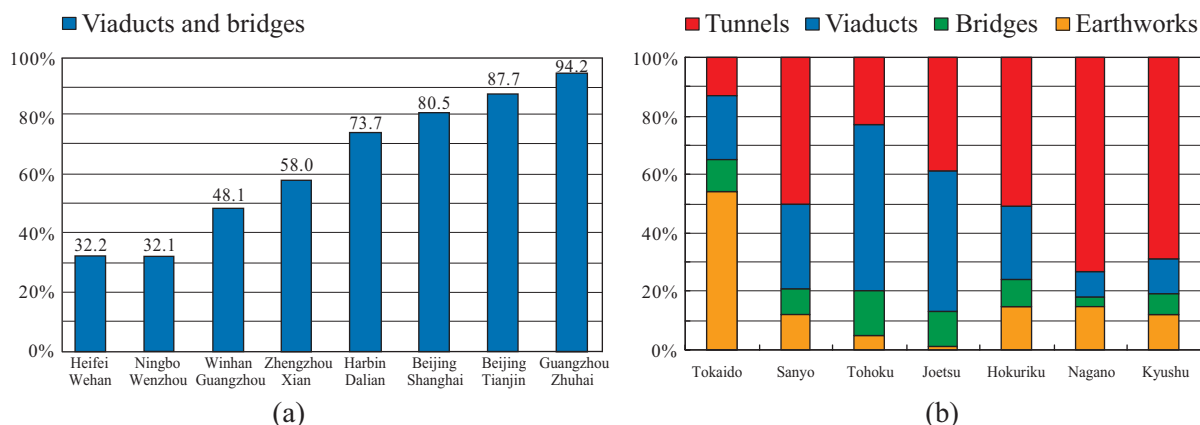
Figure 1.2 - Infrastructures in high-speed railways: (a) railway viaducts in China (adapted from Dai et al., 2010) and (b) railway infrastructures in Japan (adapted from Ishibashi, 2004).

This reality led to an increase in the probability of a train being over a bridge during the occurrence of hazards that might compromise its running safety. Some of these bridges are situated in regions prone to earthquakes, which led to new concerns among the railway engineering community. Countries such as Japan, China, Taiwan, Spain and Italy, which have an extensive high-speed railway network, are good examples of this reality. In the Portuguese case, the new high-speed line that is projected to connect Lisbon to Madrid is also situated in a region prone to earthquakes. Therefore, events such as the derailments that occurred during the Kobe Earthquake in January 1995 (see Figure 1.3a), the Shinkansen high-speed train derailment at 200 km/h during the Mid-Niigata Earthquake in October 2004 (see Figure 1.3b) or the train derailments caused by strong crosswinds reported by Baker et al. (2009), gave the railway engineers the impetus for analyzing the running safety of trains on bridges.

Figure 1.3 - Train derailments on bridges: (a) derailment during the Kobe Earthquake (CorbisImages, 2014) and (b) derailment during the Mid-Niigata Earthquake (Ashford and Kawamata, 2006)

Few studies, however, were carried out so far concerning this topic, resulting in a lack of regulation in the existing standards, especially regarding the running safety under seismic conditions. Only the Japanese Seismic Design Standard for Railway Structures (RTRI, 1999) and, more recently, the Displacement Limit Standard for Railway Structures (RTRI, 2006), have addressed this topic. In the European standards, however, the stability of railway vehicles during earthquake is not addressed, being the EN 1991‑2 (2003) and the EN 1990-Annex A2 (2001) limited to design criteria for railway bridges in ordinary conditions, and the EN 1998-2 (2005) restricted to design criteria related to the structural safety. This is an important drawback, since the running safety of trains might be jeopardized not only by intense seismic actions, such as those used to design the bridge, but also by moderate earthquakes, which may not cause significant damage to the structure.

Hence, taking into consideration the existing gap regarding this topic, both in terms of regulation and available studies, a methodology for assessing the train running safety on bridges is proposed in this thesis.

1.2 MOTIVATION AND OBJECTIVES

The motivation for developing the present thesis arises from the fact that few studies were carried out so far concerning the safety assessment of railway vehicles when travelling on bridges during the occurrence of hazards. This gap resulted in a lack of regulation in the current European standards, especially with regard to the risk of derailment under seismic conditions, since the standards related to earthquake design are restricted to criteria regarding structural integrity. Hence, given the current state of knowledge, it is the opinion of the author that the development of a numerical tool able to realistically predict the dynamic behavior of the train-structure system and the risk of derailment under adverse conditions is of the utmost importance in railway engineering.

Under this context, the main objective of the present thesis consists of developing a methodology for the assessment of the train running safety on bridges. To fulfill this goal, the topics that are described bellow have to be addressed.

The first topic to be addressed consists of developing a computational tool to simulate the dynamic interaction between railway structures and vehicles subjected to any kind of excitation. Special attention is given to the wheel-rail contact, since it is the key point for the

analysis of the contact forces that support and guide the vehicle through the railway line. An understanding of the nature of these forces is therefore essential to the study of the running safety of railway vehicles. Hence, the definition of the mathematical formulation of the wheel-rail contact model is essential. In the present work, the numerical modeling of the vehicle and structure is performed with the commercial software ANSYS (2010), being the structural matrices imported by MATLAB (2011), in which the aforementioned formulation is implemented.

The validation of the proposed vehicle-structure interaction formulation is also a crucial issue to be addressed. Some studies in the past present several numerical applications that serve as validation instruments for this type of tools. However, the majority of these applications only concern the vertical dynamics, neglecting the effects that arise from the contact between the wheel and the rail in the other directions. Therefore, in the present work, the proposed formation is validated using numerical results obtained with other softwares, as well as experimental data obtained in a test performed in the Railway Technical Research Institute (RTRI) in Japan.

Furthermore, the development of realistic models of both the railway structure and the vehicle is also an important objective of this work. In a large number of studies related with running safety, the flexibility of the track is sometimes neglected, being the problem restricted to the dynamic behavior of the vehicle. In the present work, the finite element method is used to overcome some of these limitations, since it allows a detailed modeling not only of the structure, but also of the track, which may have an important influence in the dynamic response of the vehicle.

As mentioned before, the present work aims to assess the running safety of trains, not only during ordinary operation, but also during the occurrence of hazards which may significantly increase the risk of derailment. In this thesis, special attention is given to moderate earthquakes with high probability of occurrence. It is known, however, that even the ground motions that do not represent a major threat to the structure may jeopardize the running safety of the vehicle due to excessive vibrations. Therefore, a methodology for modeling the seismic behavior of railway structures subjected to moderate earthquakes should be another topic to be addressed in the present thesis.

Finally, the present work aims to present a complete and realistic study regarding the running safety of high-speed trains on bridges under seismic conditions. To achieve this, a real

train and viaduct are considered in the case study, in which several scenarios are analyzed, with different train speeds, seismic intensities and track irregularity levels. The running safety assessment is performed using criteria based on contact forces between the wheel and rail, being the risk of derailment extensively analyzed for each of the aforementioned scenarios.

1.3   STRUCTURE OF THE THESIS

As a consequence of the objectives described in the previous section, the structure of the present thesis is divided in seven chapters, being this first one devoted to present the scope and the main objectives of the thesis.

In Chapter 2, a state of the art regarding the aspects related to the assessment of the train running safety on bridges is presented. Here, an overview of the recent studies carried out in the field of rail traffic stability over bridges, with special focus on the running safety against earthquakes, is exposed. Attention is also given to the different methods proposed by several authors to study the train-structure interaction, being their advantages and disadvantages discussed in this chapter. Since the majority of the running safety criteria are related with the control of the contact forces between wheel and rail, special attention is given to the wheel-rail contact models incorporated on the train-structure interaction tools. At the end of the chapter, a summary of the recommendations and norms regarding the stability and safety of trains, defined in standards from Europe, Japan and U.S.A. is presented.

After presenting the current state of knowledge, the methodology proposed in this work for the assessment of the train running safety on bridges is described in Chapter 3. An overview of the methodology is presented, along with a brief description of each part that composes it. Then, each part, with the exception of the train-structure interaction method that is presented separately in Chapter 4 due to its importance in the whole methodology, is described in more detail in the following sections. First, the main sources of excitations of the vehicle considered in the present work, namely the track irregularities and earthquake, are described. Additionally, although no significant damage is expected to occur on the structure for the levels of seismicity considered in this work, a methodology to account for the reduction in the stiffness of the bridge piers due to concrete cracking is proposed and described in this chapter. Lastly, the derailment mechanisms that may occur during the passage of a train over a bridge, together with the safety criteria used to analyze the possible occurrence of such phenomena, are discussed.

As mentioned above, Chapter 4 is exclusively devoted to the formulation of the train-structure interaction method developed in the present work. The first part of the chapter comprehends the description of the implemented finite contact element used to model the behavior of the contact interface between the wheel and rail. Then, special attention is given to the mathematical formulation of the wheel-rail contact model proposed in this work. The contact model is divided into three main steps, which are described in detail in this chapter. They are: 1) the geometric problem, consisting of the detection of the contact points between wheel and rail; 2) the normal contact problem, in which the normal contact forces are computed; 3) the tangential contact problem, where the creep forces that appear due to the rolling friction contact are calculated. Moreover, the method used to couple the vehicle and the structure, referred to as the direct method, is described. In this method, the governing equations of motion of the vehicle and structure are complemented with additional constraint equations that relate the displacements of the contact nodes of the vehicle with the corresponding nodal displacements of the structure. These equations form a single system, with displacements and contact forces as unknowns, that is solved directly using an optimized block factorization algorithm. The present formulation is implemented in MATLAB, being the models of the structure and vehicles developed in the finite element method software ANSYS.

In Chapter 5, the train-structure interaction method developed in the present thesis and described in Chapter 4 is validated with three numerical applications and one experimental test. The first numerical application consists of validating the creep force models implemented in the proposed method by comparing the results given by them with those obtained with the commercial software CONTACT (2011). This software is a useful instrument for validation, since, although it cannot be used in the dynamic simulation analysis of railway vehicles due to its excessive computational cost, it provides exact solutions for the wheel-rail tangential problem. In the second application, the tests performed in the Manchester Benchmark, which consisted of prescribing lateral displacements and yaw rotations to a single wheelset to analyze its behavior, are revisited and reproduced with the proposed method. The results are compared with those obtained with the several railway simulation softwares tested in the benchmark. Then, in the third numerical application, a hunting stability analysis of a suspended wheelset is performed. In this application, the lateral displacements and yaw rotations of the wheelset obtained with the proposed method are compared with those obtained with semi-analytical equations presented in the literature. Finally, an experimental test conducted in the rolling stock test plant of the RTRI, in which a full scale railway vehicle runs over a track with vertical and

lateral deviations, is reproduced numerically. The numerical results are validated with the experimental data from the test and with results obtained with the software DIASTARS developed by Tanabe et al. (2008).

In Chapter 6, the computational tool developed in this work is used to evaluate the running safety of a high-speed train moving on a viaduct under seismic conditions. The studied viaduct is based on an existing flyover type structure of the Portuguese railway network situated in the city of Alverca, while the vehicle consists of a Japanese Shinkansen high-speed train. The seismic action is represented in terms of artificial accelerograms generated from the elastic spectra described in EN 1998-1 (2004), while the irregularity profiles are generated based on analytical power spectral density functions. Moreover, the calculation of the effective stiffness of the piers of the viaduct, using the methodology proposed in Chapter 3 to account for concrete cracking caused by the earthquakes, is presented. The running safety analysis of the railway vehicle running on the viaduct is assessed based on the derailment criteria described in Chapter 3. The influence in the running safety of the seismic intensity level, vehicle running speed and track quality is evaluated separately. At the end of the chapter, all the information obtained in the dynamic analyses is condensed in the so-called running safety charts, which consist of the global envelope of each analyzed safety criteria as function of the running speed of the vehicle and of the seismic intensity level.

Finally, in Chapter 7, overall conclusions are drawn and the perspectives for future research in the field of railway dynamics as a consequence of this work are suggested.

Chapter 2

STATE OF THE ART

2.1 INTRODUCTION

In the present chapter, a state of the art regarding the running safety of railway vehicles on bridges is presented, along with the existing numerical tools and standards used to address this problem. First, an overview of the recent studies carried out in the field of rail traffic stability on bridges, with special focus on the running safety against earthquakes, is presented. Then, a review of the different existing methods for analyzing the dynamic response of the vehicle-structure system is performed, emphasizing the main advantages and disadvantages of each one in terms of accuracy and computational cost. Since the majority of the running safety criteria are related with the control of the contact forces between the wheel and rail, the wheel-rail contact model used in the vehicle-structure interaction tool is of the utmost importance to obtain accurate results. Therefore, the third part of the chapter aims to describe some of the most common wheel-rail contact models existing in the literature. The whole wheel-rail contact model can be divided in three main parts, namely the geometric, the normal and the tangential contact problems, which are discussed separately in this part of the chapter. Finally, a summary of the recommendations and norms defined in the standards from Europe, Japan and U.S.A. regarding the stability and safety of trains is presented.

2.2 PAST STUDIES CONCERNING THE ASSESSMENT OF THE TRAIN RUNNING SAFETY ON BRIDGES

In the last decades, especially due to the development of the high-speed railway networks around the world, the necessity to ensure smoother tracks with larger curve radius resulted in new railway lines with a high percentage of viaducts and bridges. Some of these bridges are situated in regions prone to earthquakes or in deep valleys, in which strong crosswinds are frequent. This reality led to new concerns among the railway engineering community, since it may represent an additional risk factor for the trains. Therefore, events such as the derailments that occurred during the Kobe Earthquake, in January 1995, the Shinkansen high-speed train derailment at 200 km/h during the Mid-Niigata Earthquake, in October 2004, or the train derailments caused by strong crosswinds reported by Baker et al. (2009), provided the impetus for analyzing the running safety of trains moving on bridges.

Few studies, however, were carried out so far concerning this topic, resulting in a lack of regulation in the existing standards, especially regarding the running safety under seismic conditions. Only the Japanese Seismic Design Standard for Railway Structures (RTRI, 1999) and, more recently, the Displacement Limit Standard for Railway Structures (RTRI, 2006), have addressed this topic (see Section 2.5.3). In the European standards, however, the stability of railway vehicles during earthquake is not addressed, being EN 1991‑2 (2003) and EN 1990‑Annex A2 (2001) limited to design criteria for railway bridges in ordinary conditions (see Section 2.5.2), and EN 1998-2 (2005) restricted to design criteria related to the structural safety. This is an important drawback, since the running safety of trains might be jeopardize not only by intense earthquakes, such as those used to address the no-collapse requirement referred in EN 1998-1 (2004), but also by moderate events, which may not cause significant damage to the structure. Regarding the crosswind assessment, the European standards are broader in scope, being the wind loads on railway viaducts defined in EN 1991‑1‑4 (2005) and the running safety of railway vehicles against crosswinds addressed in EN 14067‑6 (2010). However, few criteria, based solely on the vertical contact forces, namely the wheel unloading and vehicle overturning criteria, are defined in these standards to assess the running safety.

Most of the studies about the running safety of railway vehicles during earthquakes have been carried out in the 90s after the Kobe Earthquake. Nevertheless, even before this event, Tanabe et al. (1987; 1993) developed the first version of DIASTARS, a software intended to

simulate the dynamic interaction between the train and the railway structure during earthquake. The algorithm takes advantage of the modal transformations performed to the displacements of both the train and structure in order to effectively solve large-scale railway systems. The equations of motion of the train-structure system are then solved with modal coordinates using the Newmark method. More recent versions of DIASTARS (Tanabe et al., 2003; Tanabe et al., 2008) also include the nonlinear behavior of the bridge piers during earthquakes and the actual geometry of the wheel and rail profiles in the contact model. The later versions of the software were validated using results obtained in experimental tests performed in a shaking table (Miyamoto et al., 2004; Tanabe et al., 2008) and in a rolling stock test plant (Sogabe et al., 2005; 2006), as shown in Figure 2.1.
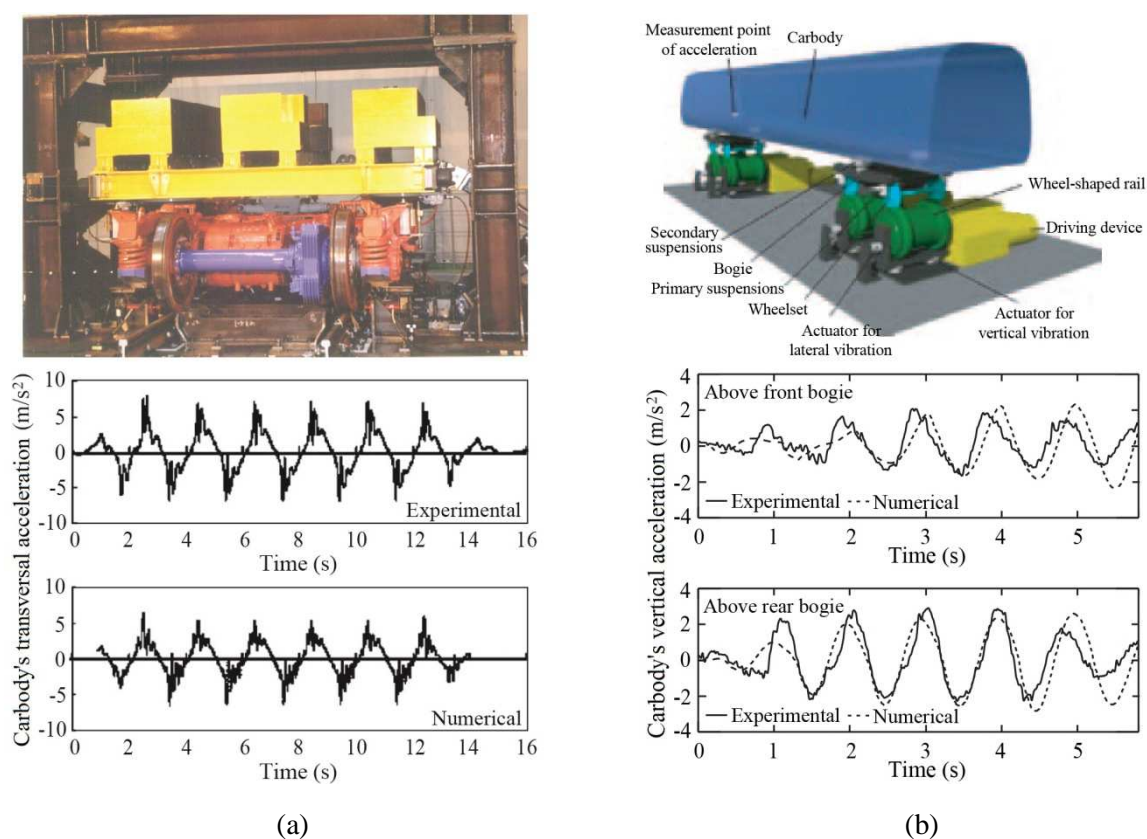
Figure 2.1 - Validation of DIASTARS: (a) shaking table test (adapted from Tanabe et al. (2008)) and (b) rolling stock test (adapted from Sogabe et al. (2005)).

As mentioned above, after the Kobe Earthquake in 1995, several studies about the risk of derailment during earthquakes have been carried out. Miura (1996) studied the effects of earthquake-induced displacements of tracks in the train running safety, while Miyamoto et al. (1997) studied the influence of the lateral and vertical ground motions in the vehicle safety using sine waves of different frequencies as the input excitation. The authors concluded that the

vehicle running safety against earthquakes has a stronger relation to the lateral ground motions than to the vertical excitations. The results, however, were obtained under several simplifying assumptions, such as the consideration of sine wave vibrations without phase shift between the wheelsets and neglecting the asynchronous vibrations and track irregularities. Therefore, according to the authors, the comparison between these results and results obtained with real earthquakes should be performed with special care.

Yang and Wu (2002) analyzed the stability of trains resting and travelling on bridges subjected to scaled natural records (see Figure 2.2). In this work, a train-structure interaction method based on condensation techniques (Yang and Wu, 2001) was used to perform the analysis, being the running safety of the train evaluated by a derailment index. The ground motions were scaled to have moderate peak ground accelerations of 0.8 m/s^2 in order to guarantee that the bridge remain elastic during the earthquake. The authors concluded that, when the train was resting on the bridge, the vertical excitation had a small influence in the train stability. However, in the scenarios where the train was moving, the presence of nearfault vertical excitations drastically affected the stability of the train, resulting in a decrease of the maximum allowable speed that guarantees the safety of the vehicle.
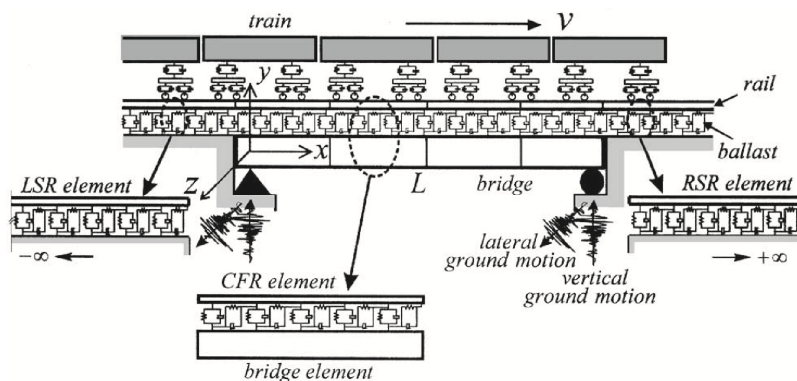
Figure 2.2 - Model proposed by Yang and Wu (2002) of a train running on a railway bridge subjected to seismic ground motions.

As mentioned earlier, strong crosswinds may also jeopardize the running safety of the vehicle, especially when it is crossing a viaduct. Xu et al. (2004) carried out a study regarding the dynamic response of a train-bridge coupling system subjected to crosswinds. The case study was performed with a train of two locomotives and ten passenger coaches running at 160 km/h on an existing cable-stayed bridge submitted to crosswinds with an average speed of 30 m/s. The wind forces acting on the bridge were generated using a spectral representation method and measured aerodynamic coefficients, while the wind load acting on the train was simulated

taking into account the effects of the vehicle speed and the spatial correlation with the wind forces acting on the bridge. The authors evaluated the running safety of the train with the derailment factor and with the wheel unloading criterion, concluding that the train remained safe for the specified wind action. In fact, the differences between the derailment factor with and without wind load were not significant for this particular case. However, according to the authors, a parametric study would be necessary to draw more general conclusions.

Li et al. (2005) developed an analytical model for study the dynamics of the wind-vehicle-bridge system. The model took into account several aspects regarding the wind action, such as the fluid-solid interaction between the wind and the bridge, the stochastic definition of the wind load and the time dependence of the system due to the movement of the vehicle. The authors discussed the influence of the wind load in the response of the bridge and the vehicle by comparing the results obtained in two distinct scenarios: one without crosswinds and another with a wind load with an average speed of 25 m/s. In both scenarios, the vehicle speed was 250 km/h. The results showed a significant increase in the lateral and vertical accelerations of the vehicle's carbody, resulting in a variation of the vertical wheel loads due to the rolling moments induced by the lateral wind. According to the authors, these variations in the vertical contact forces may represent a significant threat to the vehicle's running safety.

Luo (2005) and Luo and Miyamoto (2007) made important contributions to the development of a code-type procedure for evaluating the running safety of trains under seismic conditions. The authors evaluated the dynamic behavior of several railway vehicles using simplified analytical models and observed that the response of the vehicles were strongly dependent on the frequency components of the ground motions. As a result, the authors developed a code-type provision based on a concept of energy balance, in which the spectral intensity is used as an assessment index for the running safety. This index, which is presented in the Displacement Limit Standard for Railway Structures (RTRI, 2006), reflects the amount of energy of the seismic wave that influences the vehicle vibration.

Several studies were conducted on long-span bridges subjected to earthquakes, in which the spatial variability of the ground motion resulted in important differences in the responses when compared with those obtained with synchronous motions at all supports (Nazmy and Abdel-Ghaffar, 1992; Alexander, 2008). Xia et al. (2006) presented a model of the coupled train-bridge system subjected to non-uniform excitations. In this study, the authors evaluated the influence of the spatial variation of the ground motion in the running safety of a train

moving on a multi-span continuous bridge. They found that neglecting the moving wave effect may lead to unsafe conclusions regarding the stability of the vehicle. Later, Yau and Frýba (2007), Frýba and Yau (2009) and Yau (2009) carried out research on the dynamic response of suspended bridges subjected to non-uniform excitations (see Figure 2.3) and similar conclusions were drawn. However, in their studies, the vehicle was modeled as a set of moving loads or moving oscillators, which is usually insufficient to assess the train's running safety.
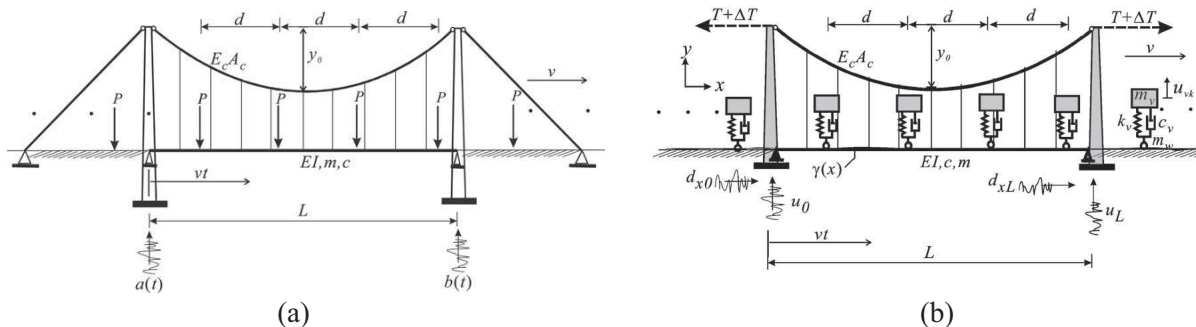
Figure 2.3 - Suspended bridges subjected to non-uniform excitations: (a) vehicle modeled as a set of moving loads (Yau and Frýba, 2007) and (b) as a set of moving oscillators (Yau, 2009).

Kim and Kawatani (2006) evaluated the seismic response of steel monorail bridges using a three-dimensional dynamic model, with particular focus to moderate ground motions with high probability of occurrence. However, the study was mainly directed towards the response of the bridge, with small emphasis given to the train's running safety and passenger's comfort.

Sogabe et al. (2007) investigated the train running quality during earthquakes in long-span bridges with tall piers. The authors studied the influence of the structural damping and the train speed in the running safety, concluding that the structural damping has a stronger influence on both the structure and the vehicle response. The research also included a study regarding possible improvement methods, such as sliding bearing systems or an increase in the stiffness of the piers, in order to enhance the train running quality.

Nishimura et al. (2008) analyzed the derailment risk of railway vehicles running on a track subjected to sinusoidal excitations with different frequencies, using a criterion based on the wheel lift displacement instead of the traditional coefficients based on the wheel-rail contact forces. The authors concluded that the running safety was compromised when the vehicle suffered rocking motions, with significant wheel lift at low frequency excitations, and when the wheel flange impacts onto the rail at high frequency excitations.

Baker et al. (2009) presented a state of the art of the research that has been carried out on the crosswind effects on road and railway vehicles. Regarding the running safety of railway vehicles, the authors stated that the main interest has been focused on the definition of the Characteristic Wind Curves (CWC), which define the limit wind speed that leads to the overturning of the vehicle caused by a wheel unloading of 90 %. These limits can be evaluated through a simplified conservative approach based on a quasi-static analysis or through a dynamic approach performed in the time domain. According to the authors, only the latter is able to account for the effects of the contact phenomena between wheel and rail. Moreover, only through a dynamic analysis of the vehicle, subjected to the unsteady aerodynamic forces and moments caused by crosswinds, it is possible to make an evaluation of the effects associated with the crosswinds other than the vehicle's rollover. In fact, turbulent crosswinds can result in a decrease in the running safety of the vehicles if specific vibration modes are excited. However, dynamic approaches in the time domain can be computationally expensive and, in the majority of the cases, more complex than the quasi-static approaches.

Guo et al. (2010) studied the running safety of a train running on the Tsing Ma suspension bridge in China, subjected to turbulent crosswinds of different speeds. The authors evaluated the running safety of the train with two criteria from the Chinese railway design standard, namely the derailment factor and the wheel unloading criterion, and presented the results in the form of CWCs (see Figure 2.4). As mentioned earlier, these curves illustrate the relationships between the mean wind velocity and the critical train speed that leads to derailment. The results showed that the running safety was controlled by the derailment factor for wind velocities up to 15 m/s (see Figure 2.4a) and by the wheel unloading criterion for velocities above that value (see Figure 2.4b). Furthermore, when the mean wind velocity reached 30 m/s, the critical train speed dropped to nearly zero, indicating that the rail traffic on the bridge should be closed.
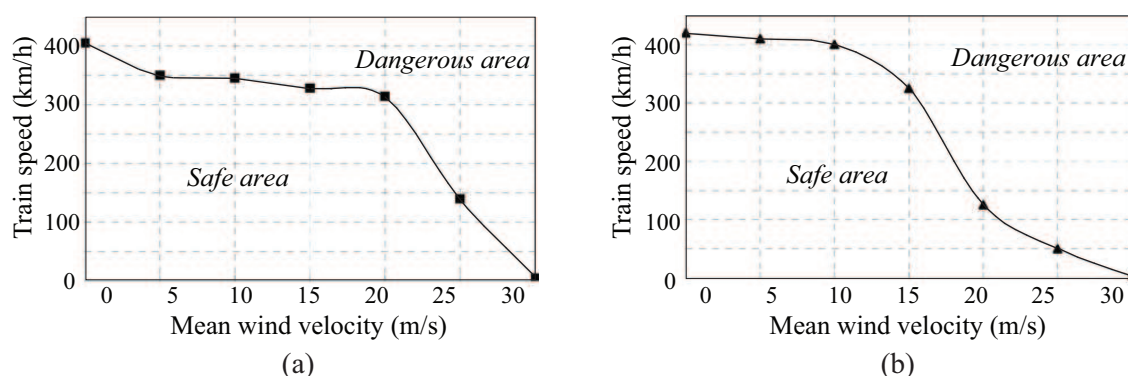
Figure 2.4 - Characteristic Wind Curves: (a) derailment factor and (b) wheel unloading criterion (adapted from Guo et al., 2010)

More recently, Tanabe at al. (2011; 2012) studied the post-derailment behavior of high-speed trains running on railway structures. Once the derailment occurs, the wheel loses contact with the rail and touches down on the track structure. According to the authors, the wheel-track contact model is divided into two parts: the vertical contact between the wheel and the track structure (see Figure 2.5a) and the lateral contact between the wheel and the safe guard (see Figure 2.5b). This was an important improvement, especially during earthquake, since the vehicle has to remain safe within the railway structure even after derailment.
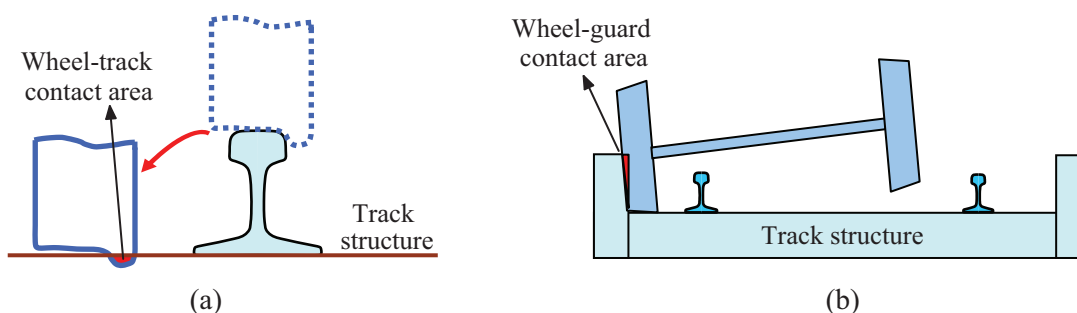
Figure 2.5 - Post-derailment behavior: (a) wheel-track vertical contact and (b) wheel-guard lateral contact (adapted from Tanabe et al. (2011)).

Antolín (2013) presented a train-structure interaction model developed in the software ABAQUS (2010), taking advantage of its capabilities for solving multibody and finite element systems for the vehicle and the structure, respectively. The vehicle-structure interaction was established through a wheel-rail contact model based on kinematic relations between the wheelset and the track. The work focused on the study of a high-speed train crossing an existing railway viaduct belonging to the Spanish railway network, the Ulla river viaduct, subjected to strong lateral winds. Several dynamic analyses were performed in this study, comprising a vast range of train speeds and wind velocities, in which the running safety of the train was evaluated based on the Prud'homme and wheel unloading criteria. By taking into account all the combinations of train and wind speeds, and considering the different wind time-histories for each speed and the track irregularities, Antolín (2013) built the CWCs to evaluate the critical train speeds for each wind velocity (see Figure 2.6). The influence of the structure flexibility was also studied, as can be seen in Figure 2.6. However, the author concluded that it does not play an important role in the running safety of the vehicle for this particular case, since the CWCs were very similar.
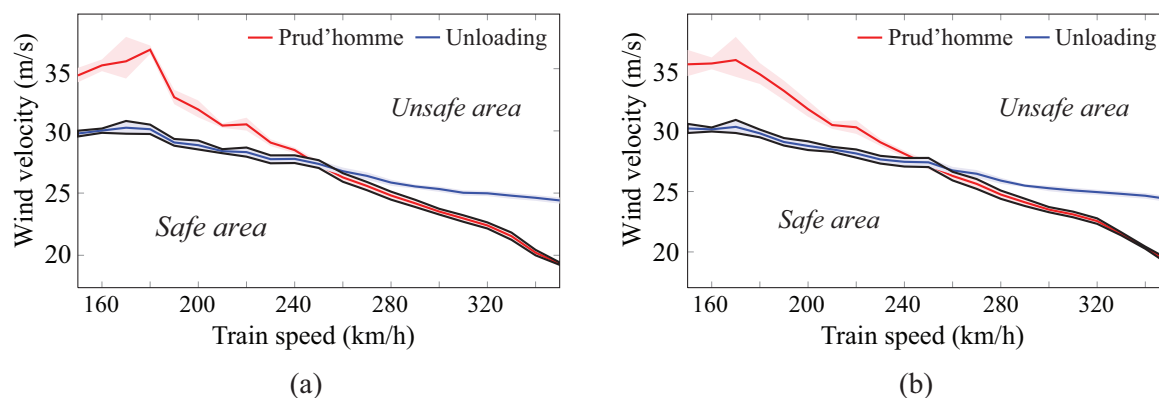
Figure 2.6 - Characteristic Wind Curves: (a) flexible structure and (b) rigid structure (adapted from Antolín (2013))

2.3 METHODS FOR ANALYZING THE DYNAMIC BEHAVIOR OF THE STRUCTURE AND VEHICLE

In the present section, a review of the different existing methods for analyzing the dynamic response of the structure and railway vehicles is presented. Three main methods for studying the dynamic behavior of a railway viaduct and/or vehicle can be distinguished: 1) moving loads model (Section 2.3.1), in which the vehicle is modeled as a set of moving loads of fixed magnitude; 2) virtual path method (Section 2.3.2), in which the deformation of the viaduct due to the action of the vehicle, computed with moving loads, is prescribed to the vehicle in order to obtain its response and 3) vehicle-structure interaction methods (Section 2.3.3), in which the viaduct and the vehicle interact with each other as a coupled dynamic system. These methods vary in complexity, computational cost and accuracy, as will be discussed in the following sections.

2.3.1 Moving loads model

The moving loads model is based on the assumption that the vehicle's action over the structure may be defined by means of moving loads of fixed magnitude that represent the static load of each wheelset (Frýba, 1996; Goicolea and Gabaldón, 2012). The train is therefore characterized by a set of constant loads F_i, separated from each other according to the train geometry, as shown in Figure 2.7. Hence, the interaction between the vehicle and structure is neglected, being the method limited to the study of the dynamic response of the structure.
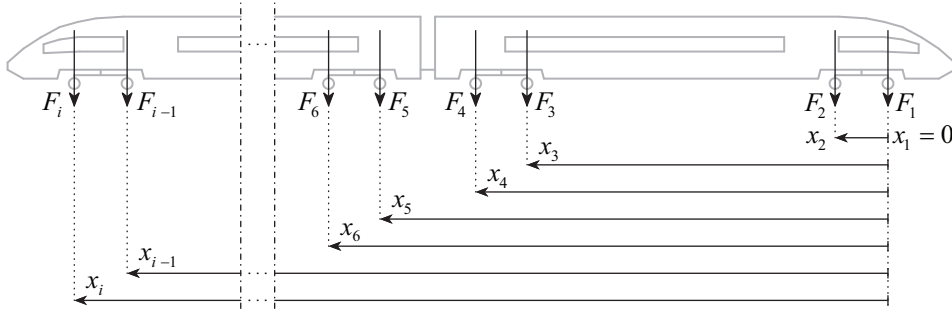
Figure 2.7 - Moving loads model.

The dynamic response of the structure can be calculated by solving the following dynamic equation of motion:

$$\mathbf{M}\ \ddot{\mathbf{a}} + \mathbf{C}\ \dot{\mathbf{a}} + \mathbf{K}\ \mathbf{a} = \mathbf{F}_{ext} + \mathbf{F}_i \qquad (2.1)$$

where $\mathbf{M}$, $\mathbf{C}$ and $\mathbf{K}$ are the mass, damping and stiffness matrices of the structure, respectively, $\mathbf{a}$ are the nodal displacements, $\mathbf{F}_{ext}$ are the externally applied nodal loads and $\mathbf{F}_i$ are the time-dependent moving loads that represent the action of the vehicle over the structure (see Figure 2.7). Equation (2.1) can be solved using direct integration techniques, such as the Newmark method (Clough and Penzien, 2003), α method (Hughes, 2000), among others, or using the modal superposition method (Chopra, 1995; Clough and Penzien, 2003). The direct integration methods allow the solution of both linear and nonlinear systems, while the modal superposition method is usually applied to linear models. However, since the latter method allow the representation of the behavior of the structure with N degrees of freedom using n chosen modes of vibration, in which $n << N$, the integration of the n modal equations of motion implies a significant reduction in the computational cost.

2.3.2 Virtual path method

The virtual path method consists of an uncoupled approach to the vehicle-structure dynamics that do not consider the interaction between these two systems, but allows the calculation of an approximate response of both the vehicle and structure.

The method is divided into two phases, in which the first consists of the calculation of the so-called virtual path for the vehicle wheels. The virtual path results from the calculation of the dynamic response of the structure subjected to the action of the vehicle described by a moving load model. The second phase consists of prescribing the time-history of displacements of the structure to the wheels of the vehicle in order to obtain its uncoupled response. Track

irregularities may be added to the virtual path in order to account for their effect in the response of the vehicle. Figure 2.8 illustrates the two aforementioned phases that compose the virtual path method.
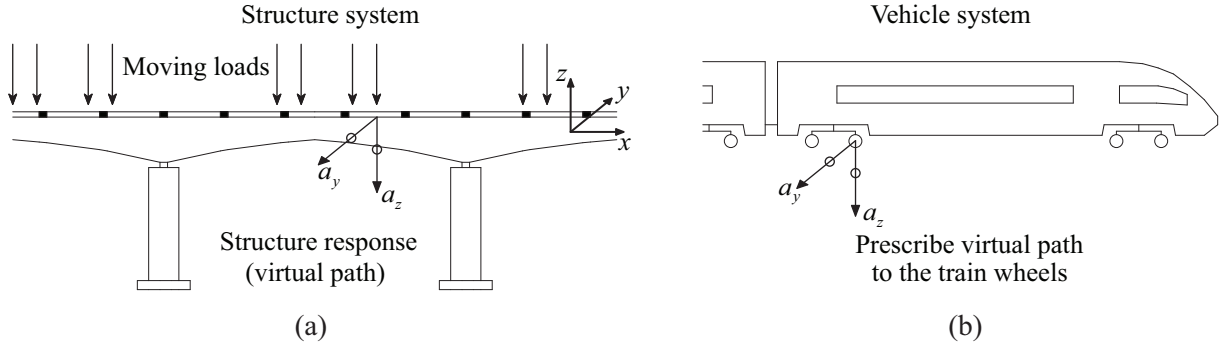
Figure 2.8 - Virtual path method: (a) phase 1 and (b) phase 2.

Unlike the moving load model, this method allows the calculation, though simplified, of the response of the vehicle. However, the interaction between the structure and the vehicle may be significant in some cases. Furthermore, the study of the riding comfort of passengers or running safety of trains requires more complex models, which usually includes the effects of the wheel-rail contact. Such effects cannot be captured by this method, limiting it to simplified analysis for obtaining a first estimate of the response of the vehicle. A study involving the virtual path method may be found in Goicolea and Antolín (2011).

2.3.3 Vehicle-structure interaction methods

2.3.3.1 Iterative method

The iterative method is a widely used technique to solve the vehicle-structure interaction problem (Hwang and Nowak, 1991; Yang and Fonder, 1996; Delgado and Santos, 1997; Lei and Noda, 2002; Xia et al., 2008; Nguyen et al., 2009a; Lee and Kimb, 2010). This method establishes the equilibrium of forces acting on the contact interface and uses an iterative procedure to impose the constraint equations that relate the displacements of the contact nodes of the vehicle with the corresponding displacements of the structure.

The two subsystems, the vehicle and structure, are modeled as two separate substructures, whose decoupled governing equilibrium equations may be expressed as

$$\begin{bmatrix} \mathbf{M}_S & \mathbf{0} \\ \mathbf{0} & \mathbf{M}_V \end{bmatrix} \begin{bmatrix} \ddot{\mathbf{a}}_S \\ \ddot{\mathbf{a}}_V \end{bmatrix} + \begin{bmatrix} \mathbf{C}_S & \mathbf{0} \\ \mathbf{0} & \mathbf{C}_V \end{bmatrix} \begin{bmatrix} \dot{\mathbf{a}}_S \\ \dot{\mathbf{a}}_V \end{bmatrix} + \begin{bmatrix} \mathbf{K}_S & \mathbf{0} \\ \mathbf{0} & \mathbf{K}_V \end{bmatrix} \begin{bmatrix} \mathbf{a}_S \\ \mathbf{a}_V \end{bmatrix} = \begin{bmatrix} \mathbf{F}_S \\ \mathbf{F}_V \end{bmatrix} \qquad (2.2)$$

where **M**, **C** and **K** are the mass, damping and stiffness matrices, respectively, **a** are the nodal displacements, **F** is the load vector and the subscripts *S* and *V* indicate structure and vehicle, respectively.

According to the iterative method developed by Delgado and Santos (1997), each time step involves the following operations at each iteration *i*+1:

a) The structure is subjected to the action of the moving loads corresponding to the wheelsets of the train. Each moving load F_S^{i+1} is given by

$$F_S^{i+1} = F_{sta} + F_{dyn}^i \tag{2.3}$$

where F_{sta} is the static load of the wheelset and F_{dyn}^i is the dynamic component of the interaction force calculated in the previous iteration *i*. In the first iteration, at each time step, the forces $\mathbf{F}_{dyn}^i$ are equal to those calculated in the previous time step. By solving the system of equations corresponding to the structure (see equation (2.2)), the nodal displacements $\mathbf{a}_S^{i+1}$ are computed, and, from the shape functions of the finite elements, it is possible to compute the displacements of the structure under the contact nodes $\mathbf{a}_Y^{i+1}$;
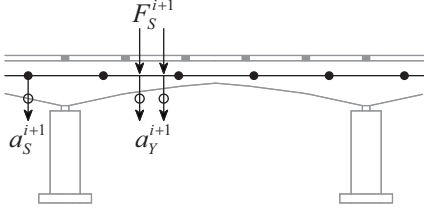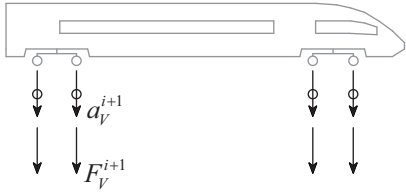
b) At the same time, the displacements $\mathbf{a}_V^{i+1}$, which correspond to the displacements of the structure under the contact nodes $\mathbf{a}_Y^{i+1}$ added to a given irregularity **r** that may exist between the wheel and the rail, are imposed to the contact nodes of the vehicle. By solving the system of equations corresponding to the vehicle (see equation (2.2)), the reaction forces at the contact nodes are computed. These reactions correspond to the dynamic component of the interaction force $\mathbf{F}_{dyn}^{i+1}$ to be applied to the structure in the next iteration;

c) At the end of each iteration, the following convergence criterion is verified:

$$\frac{\left\| \mathbf{F}_{dyn}^{i+1} - \mathbf{F}_{dyn}^i \right\|}{\left\| \mathbf{F}_{dyn}^i \right\|} \le \varepsilon \tag{2.4}$$

where ε is a specified tolerance. If the desired degree of convergence is achieved, the procedure may advance to the next time step, otherwise, the iterative process continues.

The iterative procedure described above is schematized in Table 2.1.

Table 2.1 - Iterative method for solving the vehicle-structure interaction problem.

	Structure	Vehicle
Scheme		
Load	$\mathbf{F}_S^{i+1} = \mathbf{F}_{sta} + \mathbf{F}_{dyn}^i$	$\mathbf{a}_V^{i+1} = \mathbf{a}_Y^{i+1} + \mathbf{r}$
Result	$\mathbf{a}_S^{i+1} \rightarrow \mathbf{a}_Y^{i+1}$	$\mathbf{F}_{dyn}^{i+1} = \mathbf{F}_V^{i+1}$
Convergence criterion	$\dfrac{\left\| \mathbf{F}_{dyn}^{i+1} - \mathbf{F}_{dyn}^i \right\|}{\left\| \mathbf{F}_{dyn}^i \right\|}$ $\begin{cases} \text{if} \leq \varepsilon \rightarrow \text{next step} \\ \text{if} > \varepsilon \rightarrow \text{next iteration} \end{cases}$	

A similar approach is proposed by Yang and Fonder (1996), which uses an acceleration scheme, namely the relaxation and Aitken techniques, to improve the convergence rate. Lei and Noda (2002) also used a similar scheme, in which the contact forces are computed using the Hertz formula, being penetrations and separations between wheel and rail allowed.

The iterative methods described above are limited to the vertical interaction between vehicle and structure. However, other authors have developed alternative iterative methods to deal also with the lateral interaction. Nguyen et al. (2009a; 2009b) developed a three-dimensional dynamic interaction model, in which the loss of contact between wheel and rail is allowed, using tensionless stiffness springs in the vertical direction. In the lateral direction, the contact is idealized by a spring-dashpot in order to model both the normal contact, caused by the impact between wheel and rail, and the tangential contact due to the creep forces. However, the model proposed by Nguyen et al. (2009a; 2009b) does not consider the wheel-rail geometry, being the contact point between wheel and rail fixed throughout the analysis. Hence, although this approach accounts for the lateral dynamics of the vehicle, it is limited to the analysis of ordinary operation scenarios in which the movement of the vehicle does not suffer significant lateral disturbances caused by external sources, such as earthquakes or crosswinds.

Xia et al. (2008) and Zhang et al. (2008) also proposed a three-dimensional vehicle-structure interaction method based on an iterative method, called displacement corresponding relationship method, in which the relative movement between wheel and rail follows a given assumption. In this method, the wheelset hunting motion is assumed to be known and is

regarded as a lateral excitation to the vehicle. This excitation is imposed at the wheels as a prescribed displacement a_h, which can be expressed approximately as (Dukkipati, 2000; Yang et al., 2004)

$$a_h(x) = A_h \cos\left(\frac{2\pi x}{\lambda_h} + \phi_h\right) \tag{2.5}$$

where A_h, λ_h and ϕ_h are the hunting amplitude, wavelength and random phase angle, respectively. The system of equations (2.2) is solved using a direct integration technique, in which the displacement corresponding relationship between the vehicle and structure systems is determined iteratively. As in the aforementioned approach proposed by Nguyen et al. (2009a; 2009b), this model is restricted to the analysis of scenarios in ordinary operating conditions, since it cannot predict the response of the vehicle due to other actions besides the hunting motion.

2.3.3.2 Condensation method

Yang and Yau (1997) developed a finite element called *vehicle-bridge interaction element* (see Figure 2.9a) that, according to the authors, is both accurate and efficient for modeling the vehicle-bridge interaction. Yang and Yau (1997) modeled the vehicle as a sequence of lumped sprung masses, the bridge with beam elements and the track with lumped masses, springs and dashpot elements to simulate the ballast behavior. The method consists firstly of formulating the two equations of motion of the system, one for the bridge and another for the lumped sprung masses forming the vehicle. The vehicle equation is then discretized using Newmark's finite difference formulas, being its degrees of freedom condensed into the bridge elements that are in contact. Since the vehicle is modeled as a series of sprung masses, the resulting interaction element ignores the pitching effect of the vehicle, which may significantly affect the response of the whole system. Therefore, Yang et al. (1999) presented an improved interaction element, in which the vehicle is modeled with a rigid beam supported by two spring-dampers (see Figure 2.9b), and later, Yang and Wu (2001) and Wu et al. (2001) developed a procedure capable of simulating vehicles of varying complexity, as shown in Figure 2.9c. The detailed formulation of the different versions of the interaction element, as well as a series of applications on high-speed railways may be found in Yang et al. (2004).

(a)

(b)

(c)
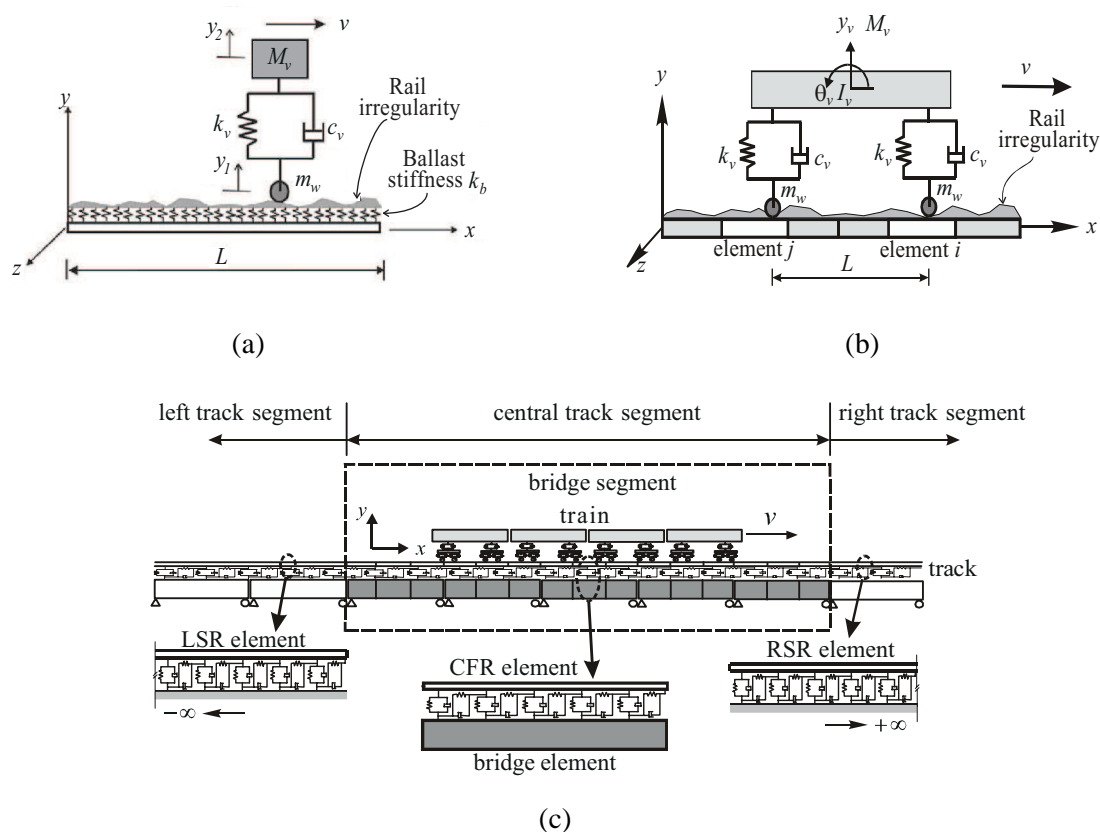
Figure 2.9 - Vehicle-bridge interaction elements: (a) original element, (b) element considering the pitching effect and (c) vehicle with an higher degree of complexity (Yang et al., 2004).

The so-called vehicle-bridge interaction element, which results from this procedure based on condensation techniques, preserve the properties of symmetry and bandwidth. However, since the position of each contact point changes over time, the system matrix used in this method is usually time-dependent and must be updated and factorized at each time step, which may demand a considerable computational effort.

2.3.3.3 Direct method

Neves et al. (2012) proposed a new algorithm, referred to as the *direct method*, in which the governing equilibrium equations of the vehicle and structure are complemented with additional constraint equations that relate the displacements of the contact nodes of the vehicle with the corresponding nodal displacements of the structure, with no separation being allowed. The irregularities at the contact interface can be considered in the constraint equations and the vehicle and structure subsystems may be modeled with various types of finite elements with any degree of complexity, such as beams, springs, shells, and solids, as shown in Figure 2.10.
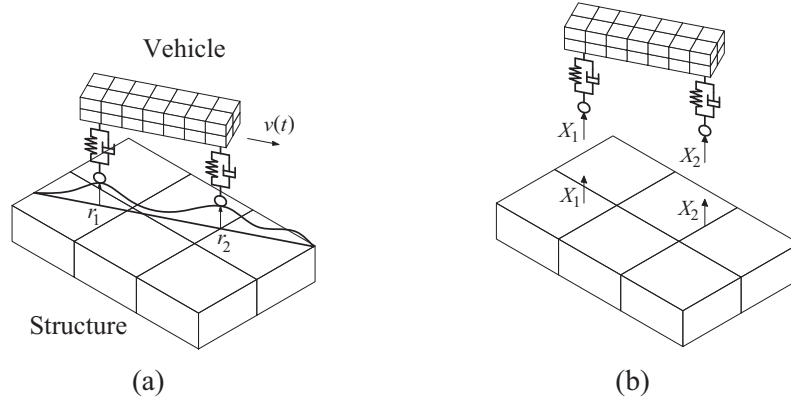
Figure 2.10 - Vehicle-structure interaction system: (a) schematic illustration and (b) free body diagram (Neves et al., 2012).

The equations of motion and the constraint equations form a single system, with displacements and contact forces as unknowns, that is solved directly using an optimized block factorization algorithm, thus avoiding the iterative procedure describe in Section 2.3.3.1 to satisfy the constraint equations. The single system of linear equations is expressed in matrix form as

$$\begin{bmatrix} \overline{\mathbf{K}}_{FF} & \overline{\mathbf{D}}_{FX} \\ \overline{\mathbf{H}}_{XF} & \mathbf{0} \end{bmatrix} \begin{bmatrix} \mathbf{a}_F^{t+\Delta t} \\ \mathbf{X}^{t+\Delta t} \end{bmatrix} = \begin{bmatrix} \overline{\mathbf{F}}_F \\ \overline{\mathbf{r}} \end{bmatrix} \tag{2.6}$$

where $\overline{\mathbf{K}}_{FF}$ is the effective stiffness matrix of the vehicle-structure system, $\overline{\mathbf{D}}_{FX}$ and $\overline{\mathbf{H}}_{XF}$ are transformation matrices that relate, respectively, the contact forces in the local coordinate system with the nodal forces in the global coordinate system and the nodal displacements of the structure in the global coordinate system with the displacements of the auxiliary points defined in the local coordinate system, $\mathbf{a}_F^{t+\Delta t}$ and $\mathbf{X}^{t+\Delta t}$ are the nodal displacements and contact forces, respectively, at the current time step, $\overline{\mathbf{F}}_F$ is the load vector and $\overline{\mathbf{r}}$ are the irregularities at the contact interface.

Later, Neves et al. (2014) extended the formulation to allow the separation between wheel and rail, by developing a contact search algorithm that detects which elements are in contact, being the constraints imposed only when contact occurs. Since in this formulation only frictionless contact is considered, the constraint equations are purely geometric and relate the displacements of the contact node with the displacements of the corresponding target element. Due to the nonlinear nature of the contact problem, an iterative scheme based on the Newton method (Owen and Hinton, 1980; Bathe, 1996) is used to solve the equation of motion of the

vehicle-structure system. Thus, the system of equations (2.6) is rewritten in an incremental form as

$$
\begin{bmatrix} \overline{\mathbf{K}}_{FF} & \overline{\mathbf{D}}_{FX} \\ \overline{\mathbf{H}}_{XF} & \mathbf{0} \end{bmatrix} \begin{bmatrix} \Delta \mathbf{a}_F^{i+1} \\ \Delta \mathbf{X}^{i+1} \end{bmatrix} = \begin{bmatrix} \boldsymbol{\psi} \left(\mathbf{a}_F^{t+\Delta t,i}, \mathbf{X}^{t+\Delta t,i} \right) \\ \overline{\mathbf{r}} \end{bmatrix}
\tag{2.7}
$$

where $\Delta \mathbf{a}_F^{i+1}$ and $\Delta \mathbf{X}^{i+1}$ are the incremental nodal displacements and contact forces, respectively, at the current iteration and $\boldsymbol{\psi}$ is the residual force vector, which depends on the nodal displacements and contact forces calculated in the previous Newton iteration. The iterative scheme continues until the condition

$$
\frac{\left\| \boldsymbol{\psi} \left(\mathbf{a}_F^{t+\Delta t,i+1}, \mathbf{X}^{t+\Delta t,i+1} \right) \right\|}{\left\| \mathbf{P}_F^{t+\Delta t} \right\|} \leq \varepsilon
\tag{2.2.8}
$$

is fulfilled, where $\mathbf{P}_F^{t+\Delta t}$ is the vector of the external applied loads at the current time step and ε is a specified tolerance. Note that the iterative procedure used in this method is not related with the compatibility of displacements between vehicle and structure, as shown in the methods described in Section 2.3.3.1, but with the nonlinear nature of the contact due to the consideration of contact loss.

2.3.3.4 *Methods considering the wheel and rail geometries*

The methods mentioned in the previous sections are restricted to railway dynamic analysis under ordinary operating conditions, since they cannot deal with extreme scenarios, such as strong lateral winds or earthquakes, in which the lateral impacts between wheel flange and rail may strongly influence the dynamic behavior of the system. To overcome this limitation, the geometries of the wheel and rail profiles have to be taken into account and a fully nonlinear formulation has to be used. In wheel-rail contact problems, since the normal and tangential forces significantly depend on the geometric characteristics of the surfaces near the contact point, the accuracy used for defining these surfaces is crucial.

According to Shabana et al. (2008), the formulation of the wheel-rail contact problem may be classified in two different approaches in terms of the way the normal contact forces are computed. In the first approach, named *constraint contact formulation* (Shabana et al., 2001), nonlinear kinematic constraints are used to impose the contact conditions, where the penetration between the wheel and the rail is not allowed. By imposing these constraints using, for example, the Lagrange multipliers method or the penalty method (Wriggers, 2002), one

degree of relative motion between wheel and rail is eliminated and the normal contact force is calculated as a constraint force. In the second approach, however, no degrees of freedom are eliminated, being the normal contact force defined as function of the penetration between wheel and rail, using any of the normal contact theories described later in Section 2.4.2. This approach is called *elastic contact formulation* and it is adopted by many authors, such as Shabana et al. (2004), Pombo et al. (2007), Tanabe et al. (2008), Sugiyama and Suda (2009), Zhai et al. (2009), Du et al. (2012) or Antolín (2013).

Another distinction that is usually made between formulations that take into account the profile geometries is related with the algorithm used to locate the contact point position. According to Sugiyama et al. (2009), there are two different approaches for determining the contact points between wheel and rail. They are the *offline contact search*, in which the location of the contact points is precalculated through a contact geometry analysis and stored in a contact lookup table to be later interpolated during the dynamic analysis, and the *online contact search*, where the position of the contact points is computed during the dynamic analysis using iterative procedures at every time step. A more detailed discussion about these two approaches is presented in Section 2.4.1.

Despite the method used to deal with the coupling between wheel and rail, the formulations which take into account the geometry of the wheel and rail profiles are the most suitable and accurate to deal with railway dynamics.

2.4   WHEEL-RAIL CONTACT MODELS

In the present section, an overview of the existing wheel-rail contact models is presented. The location of contact points between wheel and rail and the consequent calculation of the contact forces that are generated in the contact interface is one of the most important issues in railway dynamics. Therefore, several approaches varying in complexity can be found in the literature to solve the wheel-rail contact problem. The wheel-rail contact models are generally divided into three main steps: 1) the geometric problem (Section 2.4.1), consisting of the detection of the contact points; 2) the normal contact problem (Section 2.4.2), in which the normal contact forces are computed, and 3) the tangential contact problem (Section 2.4.3), where the creep forces that appear due to the rolling friction contact are calculated. The different approaches that can be found in the literature for solving each of these problems are described in the following sections.

2.4.1   Geometric contact problem

2.4.1.1 Offline contact search

In the offline contact search, an analysis of the geometry of the surfaces is previously performed, being the location of the contact points precalculated and stored in a lookup table. To perform the contact geometry analysis, the following assumptions are assumed:

a)   The wheelsets are considered as rigid bodies;

b)   The contact between wheel and rail occurs at only one point in each wheel;

c)   No separation between wheel and rail is allowed.

Under this assumptions, the relative vertical displacement and roll rotation, due only to geometric considerations, can be computed as a function of the relative lateral displacement (and yaw rotation in the case of a three dimensional contact analysis) between the wheelset and rails and stored in a lookup table to be later interpolated during the dynamic analysis. Moreover, the location of the contact points, as well as the remaining contact characteristics needed for the solution of the normal and tangential contact problem, such as the contact angle, rolling radius and curvatures, may also be calculated and stored.

As an example, Figure 2.11 illustrates, in graphic form, the results obtained in a 2D and 3D contact geometry analysis. In Figure 2.11a (Antolín et al., 2012), the yaw rotations are not taken into account in the contact analysis, being the results exclusively dependent on the relative lateral displacement Δy_w between the wheelset and rail, whereas in Figure 2.11b (Bozzone et al., 2011), the contact point position also depends on the relative yaw rotation $\Delta \psi_w$.

(a)   (b)
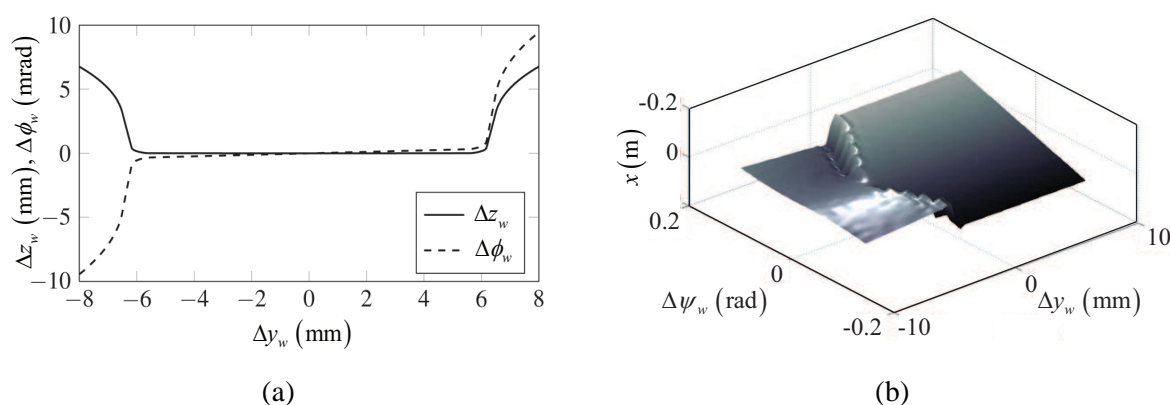
Figure 2.11 - Contact lookup tables in graphic form: (a) vertical displacement Δz_w and roll rotation $\Delta \phi_w$ in a 2D analysis (adapted from Antolín et al., 2012) and (b) longitudinal contact point position x in a 3D analysis (adapted from Bozzone et al., 2011).

This approach is computationally attractive, since it does not require any additional calculation during the dynamic analysis other than the table interpolation. However, it does not account for the penetration between the wheel and the rail, which may have a significant influence in the computation of the contact forces. This limitation is overcome in the online contact approach described in the next section. Several studies using the offline contact search may be found in Santamaria et al. (2006), Tanabe et al. (2008), Bozzone et al. (2011) and Antolín et al. (2012).

2.4.1.2 Online contact search

In the online contact search, the location of contact points is determined during the dynamic simulation using iterative procedures at every time step. Since the location of the contact points is predicted directly with the information of the current time step, a more accurate solution is usually achieved in comparison with that obtained using the offline search. Furthermore, the online contact search does not require the wheelset to be rigid, allowing the detection of contact points in vehicles with independent wheels or flexible wheelsets. Two other important advantages of this approach consists in the possibility of considering small penetrations between the wheel and rail, essential for the accuracy of the normal contact forces calculation, and of detecting multiple contact points in the same wheel-rail pair.

Figure 2.12 illustrates two approaches for predicting the location of the contact points using an online contact search. In Figure 2.12a, the contact point is determined based on a nodal search algorithm, in which the geometric surfaces are discretized in several points, being the contact point formed by the nodal pair that leads to the maximum indentation (Chen and Zhai, 2004; Shabana et al., 2005; Antolín, 2013). In Figure 2.12b however, the profile surfaces are described by mathematical functions and the contact point position is determined by solving a set of nonlinear algebraic equations that define the geometric contact conditions based on the normal and tangential vectors to the surfaces (Pombo et al., 2007; Shabana et al., 2008; Sugiyama and Suda, 2009; Falomi et al., 2010). The latter method is computationally more efficient than the nodal search algorithm and its accuracy does not depend on the degree of discretization of the profile geometry. However, multiple solutions can be obtained for the system of nonlinear equations if one of the contact surfaces is not convex (Pombo, 2004). This can be an important limitation if the potential contact point lies on the concave region that exist in the transition between the wheel tread and flange.
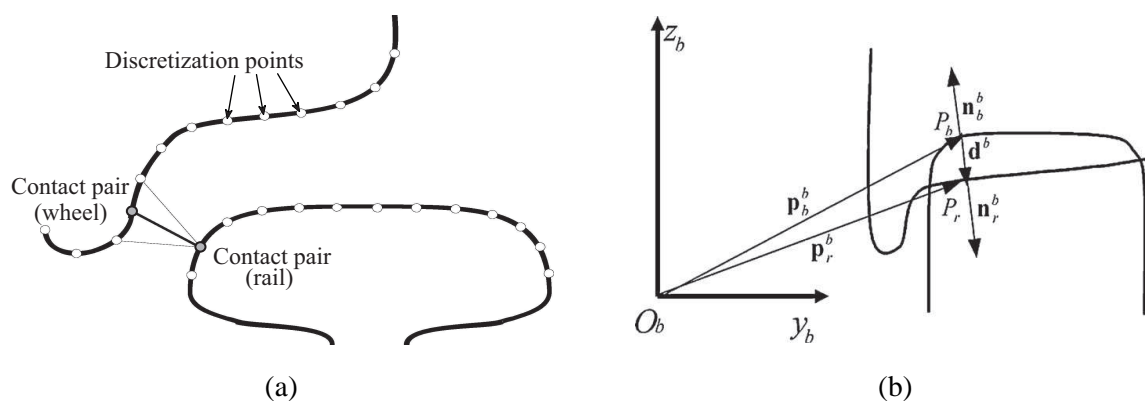
Figure 2.12 - Online contact search: (a) nodal search algorithm (adapted from Shabana et al., 2005) and (b) algorithm based on the solution of a set of geometric contact conditions (Falomi et al., 2010).

2.4.2 Normal contact problem

The main objective of the normal contact problem consists of determining the contact area between wheel and rail, as well as the distribution of normal contact pressure that appears when the two bodies are compressed against each other. In railway engineering, the methods used to solve the normal contact problem can be divided into two types: the methods based on elliptical contact areas and non-elliptical contact areas.

The first methods are based on the Hertz theory (Hertz, 1882), in which the contact area between two contacting bodies is elliptical and the pressure distribution assumes a semi-ellipsoidal shape, being the normal stresses null at the edges of the contact area and maximum at its center. This is the most used method in railway dynamic simulation codes. However, the Hertz theory has some limitations, since it is based on certain assumptions which are not always satisfied in wheel-rail contact, such as non-conformal and frictionless surfaces, constant curvatures along the contact area or the nonexistence of plastic deformations in the contact zone. Nevertheless, in most of railway applications, the Hertz contact theory seems to be sufficiently adequate for the computation of the normal contact forces during a dynamic analysis (Andersson et al., 1999), providing a reasonable compromise between computational efficiency and accuracy.

More complex and realistic contact shapes may be necessary (see Figure 2.13), however, for analyzing local problems such as wear, in which a detailed analysis of the local stresses in the contact area is essential. In this analysis, the influence of the non-constant curvatures in the calculation of the contact area may be significant and, in some situations, the contact between the two bodies may be conforming due to worn profiles. Furthermore, multiple contact zones,

which cannot be solved using a single ellipse, may appear when the geometry of the contacting bodies does not satisfy the Hertz assumptions. Therefore, several authors have developed new theories to deal with these limitations, which, according to Piotrowski and Chollet (2005), can be divided into the following two categories:

a) Multi-Hertzian methods: the Hertz theory is applied to each contact zone, forming a contact area with multiple ellipses;

b) Non-Hertzian methods: assume a semi-elliptical distribution of stresses only along the direction of rolling.

The multi-Hertzian methods (Pascal, 1993; Ayasse et al., 2000) are based on the fact that, in each contact zone, the conditions for using the Hertz theory are met. Under this assumption, the contact problem may be solved using multiple ellipses whose dimensions and pressure distribution are obtained independently.

In the non-Hertzian methods proposed, for example, by Ayasse and Chollet (2005), Quost et al. (2006) or Piotrowski and Kik (2008), a semi-elliptical normal stress distribution is assumed only in the rolling direction. The similarity of the stress distribution to that resulting from the Hertz theory allows the use of the Hertz solution to solve, in an approximate way, the normal contact problem for conditions in which the geometry of the contacting bodies does not rigorously satisfy the Hertz assumptions. Generally, the contact area is discretized into independent longitudinal strips with constant curvature, allowing the consideration of both elliptical and non-elliptical contact shapes.
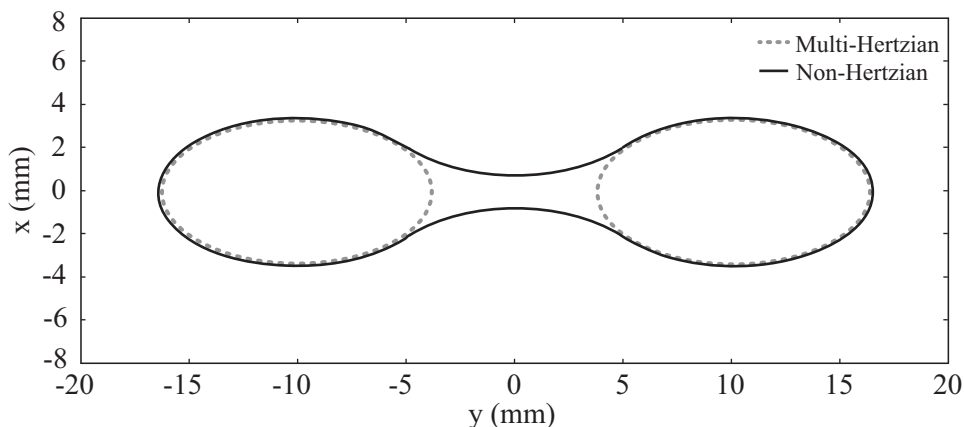
Figure 2.13 - Contact area based on a multi-Hertzian and on a non-Hertzian method
(adapted from Quost et al. (2006)).

2.4.3 Tangential contact problem

If two bodies that are compressed against each other are allowed to roll over each other, some points on the contact area may slip while others may adhere. The difference between the tangential strains of the bodies in the adhesion area leads to a small apparent slip, called creep. The creep, which depends on the relative velocities of the two bodies at the contact point, is crucial for the determination of the tangential forces that are developed in the contact area, called creep forces. Hence, the creep may be defined as a combined elastic and frictional behavior in which two elastic bodies that roll over each other share a contact area where both slip and adhesion occur simultaneously.

Several creep force theories were developed and implemented in many simulation softwares for dynamic analysis of railway vehicles. The first theory was developed by Carter (1926) to deal with two-dimensional problems. After that, Johnson (1958) extended Carter's theory to the three-dimensional case of two spheres without spin and, later, Vermeulen and Johnson (1964) developed a new extension to deal with smooth half-spaces, also without spin. This drawback was overcome by Kalker (1967) with the development of the linear theory of rolling contact. However, this theory is limited to small creepages, since it is assumed that the slip region is very small and its effect can be neglected.

Since the wheel-rail contact problem is highly nonlinear, the aforementioned linear theories have strong limitations when dealing with real problems. The Johnson and Vermeulen's theory ignores the effect of the spin creepage, which may be important, especially when flange contact occurs (Piotrowski, 1982), while Kalker's linear theory is limited to small creepages. Therefore, new nonlinear rolling contact theories have been developed to allow more realistic studies.

In 1979, Kalker (1979) developed the exact theory of rolling contact, also called variational theory, in which the constitutive law is obtained by deriving the tangential displacement-stress relationship using the general elasticity theory. This formulation was first implemented in the computer code DUVOROL (Kalker, 1979) for dealing with contact problems limited to elliptical contact areas and later, in 1982, in the program CONTACT (Kalker, 1982b) to solve any type of contact problem between bodies that could be described by half-spaces. However, despite the solution for the wheel-rail contact problem given by this formulation is exact, its excessive computational cost makes it impracticable to be used in dynamic analysis of railway vehicles. Therefore, Kalker (1982a) developed the simplified theory to overcome the excessive computational effort required by the exact theory and implemented it in the FASTSIM code.

The main difference of the Kalker's simplified theory in relation to the exact theory consists in the adoption of a much simpler tangential displacement-stress relationship. Nevertheless, the calculation time required by the simplified theory may still be too high in certain complex systems.

Shen et al. (1983) developed the heuristic nonlinear creep force model, in which the creep forces calculated by the Kalker's linear theory are corrected by a reduction coefficient based on the nonlinear creep force saturation law of Johnson and Vermeulen. However, although the effect of spin creepage on the creep forces is considered and the computational cost is low, Kalker (1991) stated that the heuristic theory leads to unsatisfactory results in the case of high values of spin.

Some of the aforementioned drawbacks were overcome by the Polach method (Polach, 1999) and the Kalker's book of tables (Kalker, 1996), implemented in the USETAB code. In spite of the simplifications used in Polach's formulation, the spin effect is considered and, in comparison to other approximate methods, the differences observed between the calculated values and the exact theory are relatively small. Regarding the Kalker's book of tables, it consists in a precalculated table that is generated based on the exact theory, and which may be interpolated during the dynamic analysis. The estimate error resulting from USETAB is approximately 1.5 % compared with the exact theory (Shabana et al., 2008). An overview of the wheel-rail rolling contact theories developed by Kalker may be found in the publication of Zaazaa and Schwab (2009).

2.5   NORMS AND RECOMMENDATIONS CONCERNING THE SAFETY OF RAILWAY TRAFFIC

2.5.1   Introduction

The majority of the existing standards regarding the design of railway bridges are mainly focused on the structural safety, both in terms of ultimate limit states and service limit states. However, few recommendations regarding the running safety of the railway vehicles during ordinary operating conditions or during the occurrence of less probable events, such as earthquakes or strong crosswinds, have been proposed so far. The present section summarizes some of the main criteria regarding the stability and running safety of trains on railway viaducts, defined in the standards from Europe, Japan and U.S.A.

2.5.2 European standards

In Europe, the main criteria regarding the stability of the track and, consequently, the stability of railway vehicles, are presented in the EN 1990‑Annex A2 (2001) and in the EN 1991‑2 (2003). The verifications defined by these standards are primary related with the control of deformations (see Section 2.5.2.1) and vibrations on bridges (see Section 2.5.2.2), since, according to EN 1990‑Annex A2 (2001), "*Excessive bridge deformations can endanger traffic by creating unacceptable changes in vertical and horizontal track geometry, excessive rail stresses and vibrations in bridge structures*". Moreover, "*Excessive vibrations can lead to ballast instability and unacceptable reduction in wheel rail contact forces*".

The Technical Specifications for Interoperability in Europe (TSI, 2002) and the EN 14067-6 (2010) also define criteria to guarantee the running safety of trains in the European railway network. These criteria are mostly related with the control of the wheel-rail contact forces, as described in Section 2.5.2.3.

2.5.2.1 Criteria regarding the bridge deformation control

2.5.2.1.1 Vertical deflection of the deck

The limitation of the vertical deflection of the deck in each span is designed to ensure an acceptable vertical track radii and generally robust structures. Thus, according to EN 1990‑Annex A2 (2001), the maximum total vertical deflection δ_v (see Figure 2.14) measured along the track due to the characteristic values of the vertical traffic load models LM71 and SW/0, as appropriate[1], defined in EN 1991‑2 (2003), cannot exceed $L/600$, where L is the span length.
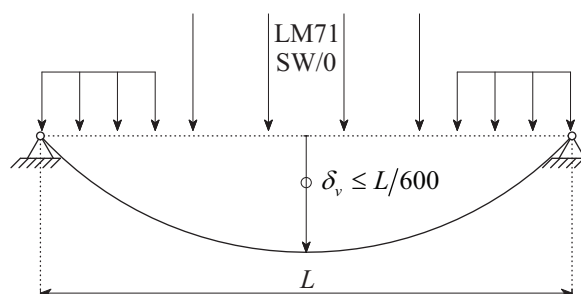
Figure 2.14 - Vertical deflection of the deck δ_v.

---

[1] For continuous bridges, both the load model LM71 and SW/0 have to be considered in the design.

2.5.2.1.2   Transverse deflection of the deck

According to EN 1990‑Annex A2 (2001), the transversal deflection of the deck δ_h has to be limited to ensure that the angular variation and horizontal radius of curvature satisfy the limits specified in Table 2.2. The angular variations refer to the transversal rotations at the end of the deck θ_h or to the relative transversal rotations between two adjacent spans $\theta_{h1} + \theta_{h2}$, as depicted in Figure 2.15. This condition has to be checked for characteristic combinations of: load model LM71 and SW/0, as appropriate, multiplied by the dynamic factor, wind loads, nosing force, centrifugal forces in accordance with EN 1991‑2 (2003) and the effect of transverse differential temperature across the bridge.
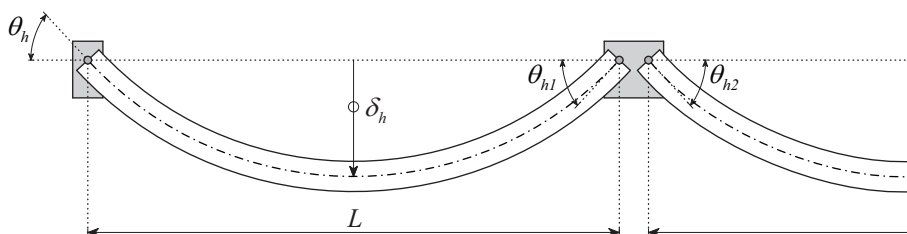
Figure 2.15 - Transverse deflection of the deck δ_h and angular variations at the deck ends θ_h (plan view).

Table 2.2 - Design limit values of angular variation and radius of curvature (EN 1990-Annex A2, 2001).

Speed V (km/h)	Maximum angular variation (rad)	Maximum radius of curvature (m)	
		Single span	Multi-span
$V \leq 120$	0.0035	1700	3500
$120 < V \leq 200$	0.0020	6000	9500
$V > 200$	0.0015	14000	17500

2.5.2.1.3   Deck twist

The deck twist criterion defined in EN 1990‑Annex A2 (2001) aims to minimize the risk of train derailment. The maximum twist t (see Figure 2.16) of a track gauge of 1435 mm measured over a length of 3 m should not exceed the values given in Table 2.3. The twist of the bridge deck is calculated taking into account the characteristic values of the load model LM71, as well as the load models SW/0 or SW/2, as appropriate, and the High-Speed Load Models (HSLM) including centrifugal effects, as defined in EN 1991‑2 (2003).
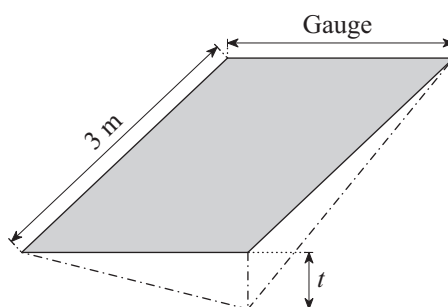
Figure 2.16 - Definition of deck twist *t* (adapted from EN 1990‑Annex A2 (2001)).

Table 2.3 - Design limit values of deck twist (EN 1990-Annex A2, 2001).

Speed *V* (km/h)	Maximum twist (mm/3m)
$V \leq 120$	$t \leq 4.5$
$120 < V \leq 200$	$t \leq 3.0$
$V > 200$	$t \leq 1.5$

Additionally, the total twist given by the combined twist of the track when the bridge is unloaded (for example in a transition curve) with the twist of the bridge due to the traffic load defined above is limited to 7.5 mm/3 m.

2.5.2.1.4   Vertical displacement of the upper surface at the end of the deck

This requirement is intended to avoid destabilizing the track, to limit uplift forces on the rail fastening systems and to limit additional rail stresses. According to EN 1991‑2 (2003), the vertical displacement of the upper surface of the deck δ_v (see Figure 2.17) relative to the adjacent construction (abutment or another deck) due to the load model LM71 and SW/0, as appropriate, and due to the vertical temperature differential, cannot exceed 3 mm or 2 mm in lines whose maximum allowed speed is up to 160 km/h or over 160 km/h, respectively.
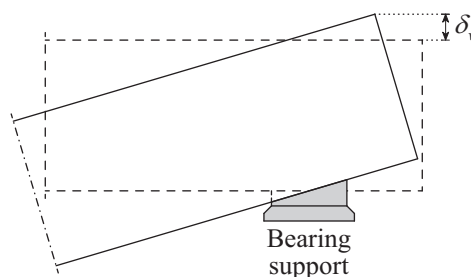
Figure 2.17 - Vertical displacement of the upper surface of the deck δ_v.

2.5.2.1.5   Longitudinal displacement of the upper surface at the end of the deck

The longitudinal displacement of the upper surface at the end of the deck has to be limited to minimize disturbance to track ballast and adjacent track formation. EN 1991‑2 (2003) limits the longitudinal displacement of the deck δ_b relative to the adjacent construction (abutment or another deck) due to traction or braking to 5 mm for continuous welded rails without expansion devices or to 30 mm for rails with expansion devices. For vertical traffic loading defined by the load model LM71 and SW/0, as appropriate, the longitudinal displacement δ_h (see Figure 2.18) of the upper surface at the end of the deck cannot exceed 8 mm if the combined behavior of structure and track is considered in the numerical model or 10 mm if not.
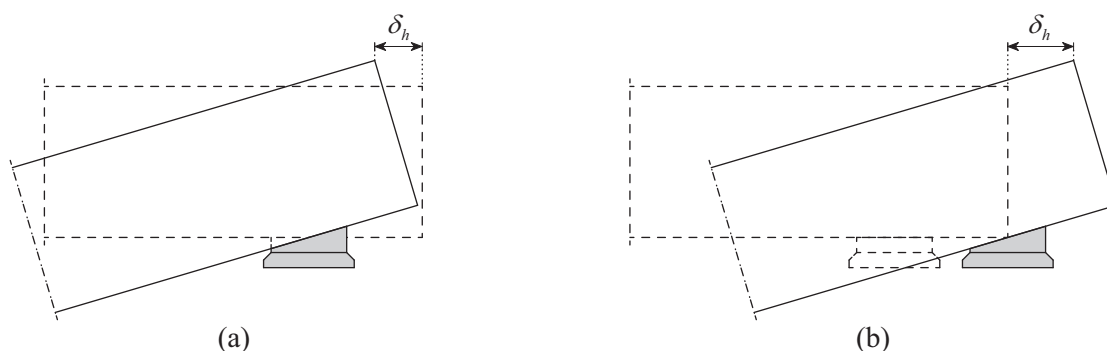
Figure 2.18 - Longitudinal displacement of the upper surface of the deck δ_h: (a) fixed support and (b) guided support.

2.5.2.2   Criteria regarding the bridge vibration control

2.5.2.2.1   Vertical acceleration of the deck

To ensure traffic safety, the verification of maximum vertical peak deck acceleration due to the rail traffic loads should be regarded as a traffic safety requirement at the serviceability limit state for the prevention of track instability. Therefore, according to EN 1990‑Annex A2 (2001), the maximum allowed vertical acceleration of the bridge deck should not exceed 3.5 m/s^2 on ballasted tracks and 5 m/s^2 on slab tracks.

The acceleration is calculated by a dynamic analysis with real high-speed train models and with the load models HSLM, defined in EN 1991‑2 (2003), considering only one loaded track. In the calculations, only the contributions of the mode shapes with frequencies up to 30 Hz or to 1.5 times the frequency of the first mode of vibration of the element being analyzed, including at least the first three modes, should be taken into account.

2.5.2.2.2   Lateral vibration of the deck

This requirement is intended to avoid the occurrence of resonance between the lateral motion of the vehicle and the bridge. According to EN 1990‑Annex A2 (2001), the first natural frequency of lateral vibration of a span should not be less than 1.2 Hz.

2.5.2.3 Criteria regarding the control of the wheel-rail contact forces

2.5.2.3.1   Maximum dynamic vertical wheel load

According to TSI (2002), the maximum dynamic vertical wheel load applied by interoperable high-speed trains should not exceed the values given in Table 2.4.

Table 2.4 - Limit values for the dynamic vertical wheel load (adapted from TSI (2002)).

Maximum Speed V (km/h)	Maximum dynamic wheel load (kN)
$200 < V \leq 250$	180
$250 < V \leq 300$	170
$V > 300$	160

2.5.2.3.2   Maximum total dynamic lateral contact force applied by a wheelset

The maximum total dynamic lateral contact force applied by a wheelset should be limited to avoid track damage and consequent instability of the vehicle. Therefore, the maximum allowed dynamic lateral force Y_{max} applied by a wheelset is given by (TSI, 2002)

$$\sum_{ws} Y_{\max} = 10 + \frac{2Q_0}{3} \left[\text{kN} \right]$$

(2.9)

where Q_0 is the static load per wheel in kilonewtons and *ws* indicates wheelset. This criterion was firstly introduced by Prud'homme (1967) and is widely adopted in railway engineering (see Section 3.5 of Chapter 3 for a detailed description of the Prud'homme criterion).

2.5.2.3.3   Ratio of the lateral to the vertical contact forces of a wheel

The TSI (2002) also specifies a limit for the ratio of the lateral to the vertical contact forces of a wheel. This ratio was firstly introduced by Nadal (1908) and aims to control the risk of a wheel climbing the rail, which can lead to derailment (see Section 3.5 of Chapter 3 for a detailed description of the Nadal criterion). The maximum allowed *Y/Q* ratio in each wheel is 0.8, where *Y* and *Q* are the lateral and vertical contact forces in a wheel.

2.5.2.3.4   Wheel unloading

EN 14067-6 (2010) defines the wheel unloading as a safety criterion against crosswinds. According to this norm, the risk of derailment may be significant if the wheel unloading exceeds 90 % of the average static wheel load in the most critical running gear (see Section 3.5 of Chapter 3 for a detailed description of the wheel unloading criterion).

2.5.3   Japanese standards

The main specifications regarding the stability of railway vehicles in Japan are presented in the Displacement Limit Standard for Railway Structures (RTRI, 2006). Since Japan is a country prone to earthquakes, the Displacement Limit Standard provides recommendations not only for the running safety of trains during ordinary operating conditions, but also in seismic conditions. This is a very important issue, since this type of events strongly contributes to higher levels of lateral vibrations on the viaducts that may significantly increase the risk of derailment.

According to the Displacement Limit Standard (RTRI, 2006), the required performance of railway structures in terms of displacement limits is categorized into two types of verifications regarding the stability of the vehicle, namely *safety* and *restorability*, which in turn incorporate the following items:

a)   Verification of safety: *running safety in ordinary conditions* and *displacements associated with the running safety in seismic conditions* (see Section 2.5.3.1);

b)   Verification of restorability: *restorability of track damage in ordinary conditions* and *displacement of track damage in seismic conditions* (see Section 2.5.3.2).

The two types of specifications described above are verified according to the girder deflection δ due to the passage of the vehicle, irregularity of the track at the ends of the girder r and angular rotation on track surfaces θ_t, as shown in Figure 2.19. The irregularity index, which can be defined in the lateral or vertical directions according to the type of verification (Figure 2.19b depicts only the vertical direction for exemplification purposes), comprehends scenarios such as the deformation of the supports, deformations at the girders ends or deformations in the transition zones. The angular rotations on track surfaces, which are also defined for both the lateral and vertical directions, may be caused by lateral deflections of the bridge piers during an earthquake or by relative deflections between adjacent spans (see Figure 2.19c).
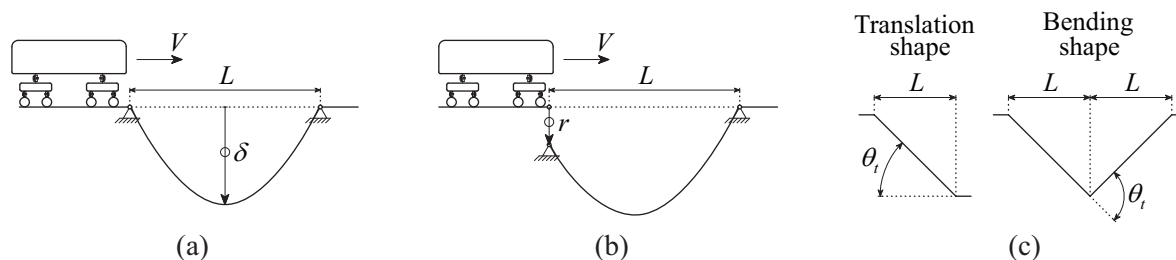
Figure 2.19 - Structural displacements: (a) girder deflection δ, (b) irregularity r and (c) angular rotation θ_t (adapted from RTRI (2006)).

2.5.3.1 Verification of safety

The verification of safety may be performed using indexes based on the wheel-rail contact forces or based on structural displacements. The first option requires a complex train-structure interaction model capable of simulating the behavior of the whole system, while the verification made with the second option may be performed by computing the design structural displacements due to the train and seismic loads by static and spectral analyses, respectively.

In practice, for the design of railway bridges, the verifications regarding the running safety of vehicles are usually performed using the structural displacement indexes for simplicity. These indexes are presented in the form of tables for the several types of existing trains in Japan, and consist of design limit values of precalculated structural displacements using a train-structure interaction tool. The limit values were calculated based on the wheel-rail contact indexes, namely the Nadal criterion (referred to as derailment quotient in the standard), which consists of the quotient between the lateral and vertical contact force in a wheel, and the wheel unloading criterion, which consists of the reduction of the wheel vertical load relative to the static value (the running safety criteria are described in more detail in Section 3.5 of Chapter 3). The design limit value for both the derailment quotient and wheel unloading ratio proposed by the Displacement Limit Standard (RTRI, 2006) is 0.8.

2.5.3.1.1 Running safety in ordinary conditions

The verification of the running safety in ordinary condition aims to guarantee the adequate performance of the structure in order to ensure that the railway vehicle runs smoothly under all actions expected to occur during the design life of the structure in ordinary conditions. The design limit values for the structural displacement indexes, namely the girder deflection, the irregularity of the track at the ends of the girder in the vertical direction and the angular rotation on track surfaces (see Figure 2.19) are presented in Tables 2.5, 2.6 and 2.7, respectively.

Table 2.5 - Design limit values of girder deflection δ for the running safety in ordinary conditions (RTRI, 2006).

Train type	Number of spans	Maximum speed (km/h)	Span Length L (m)		
			10 - 40	40 - 60	60 - 100 (>)
Shinkansen	Single span	260	L/700		
		300	L/900		
		360	L/1100		
	Multi-span	260	L/1200		L/1400
		300	L/1500		L/1700
		360	L/1900		L/2000
Conventional (electric/diesel)	Single span	160	L/500		
	Multi-span	130	L/500		
		160	L/600		
Locomotive	Single span	130	L/400		
	Multi-span	130	L/600	L/700	

Table 2.6 - Design limit values of vertical irregularity of the track r for the running safety in ordinary conditions (RTRI, 2006).

Train type	Maximum speed (km/h)	Single span (mm)	Multi-span (mm)
Shinkansen	260	2.0	3.0
	300	1.5	2.5
	360	1.0	2.0
Conventional, Locomotive	160	3.0	4.0

Table 2.7 - Design limit values of angular rotation on track θ_t for the running safety in ordinary conditions (RTRI, 2006).

Train type	Maximum speed (km/h)	Vertical direction θ_t ($\times 1/1000$)		Lateral direction θ_t ($\times 1/1000$)	
		Translation shape	Bending shape	Translation shape	Bending shape
Shinkansen	210	4.0	4.0	2.0	2.0
	260	3.0	3.0	1.5	2.0
	300	2.5	2.5	1.0	1.0
	360	2.0	2.0	1.0	1.0
Conventional, Locomotive	130	6.0	9.0	2.0	3.0
	160	6.0	6.0	2.0	2.5

2.5.3.1.2 Displacements associated with the running safety in seismic conditions

The verification of the running safety in seismic condition aims to guarantee the adequate performance of the structure in order to reduce the probability of derailment of a railway vehicle during an earthquake. The running safety in seismic conditions is verified in terms of the lateral vibration of the structure and in terms of the structural displacement indexes, namely the lateral irregularity and the lateral angular rotations (see Figure 2.19).

Regarding the lateral vibration of the structure, the Displacement Limit Standard (RTRI, 2006) specifies design limit values for the vibration displacements caused by Level-1 earthquake motion[2] (RTRI, 1999). The vibration displacements are evaluated based on a concept of energy balance, called Spectral Intensity (SI) index, which reflects the amount of energy of the seismic wave that influences the vehicle vibration (see Luo (2005) and Luo and Miyamoto (2007) for more details about the SI index). The verification is performed by computing the equivalent natural period of the structure T_{eq} and checking if it falls in the safety area given by the chart depicted in Figure 2.20 (the chart provides SI values for various types of soils according to the Seismic Design Standard (RTRI, 1999)).
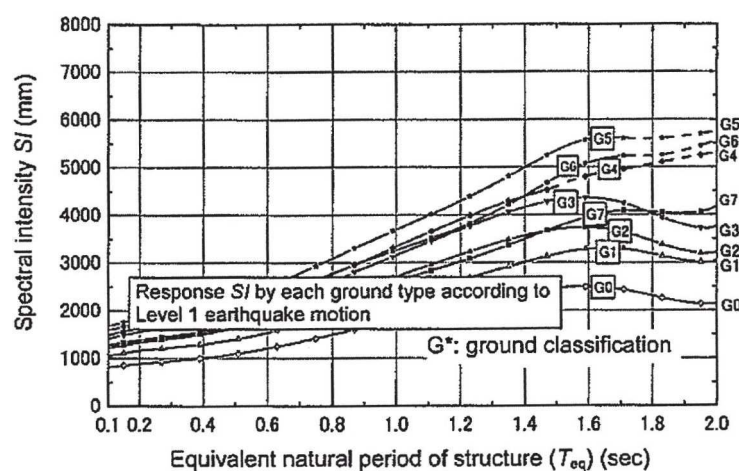
Figure 2.20 - Limit values of the SI index associated with the running safety in seismic conditions (RTRI, 2006).

The design limit values for the structural displacement indexes, namely the lateral irregularity and the lateral angular rotations, are given in Table 2.8. These limits cannot be exceeded by the response of the structure when subjected to the Level-1 earthquake motion.

---

[2] According to Seismic Design Standard (RTRI, 1999), Level-1 earthquake motion is prescribed based on the acceleration response spectrum determined for firm ground (bedrock), associated with a reference return period of 50 years and with a maximum spectral acceleration of 2.5 m/s[2] (5% viscous damping).

Table 2.8 - Design limit values of lateral angular rotations and irregularities for the running safety in seismic conditions (RTRI, 2006).

| Direction | Maximum speed (km/h) | Angular rotation θ_t ($\times 1/1000$) | | | Irregularity r (mm) |
| | | Translation shape | | Bending shape | |
		$L = 10$ m	$L = 30$ m		
Lateral	130	7.0	7.0	8.0	14.0
	160	6.0	6.0	6.0	12.0
	210	5.5	3.5	4.0	10.0
	260	5.0	3.0	3.5	8.0
	300	4.5	2.5	3.0	7.0
	360	4.0	2.0	2.0	6.0

2.5.3.2 *Verification of restorability*

The verification of restorability specifies two performance levels based on the amount of damage of the track. They are the *performance level 1*, in which the track meets the necessary requirements for a safe runnability and can be used without repairs, and *performance level 2*, in which the normal functions of the track can be recovered in a short time but repair is necessary. The verifications in both ordinary and seismic conditions aim to guarantee the performance level 1 in order to ensure the safe stability of the track and, consequently, of the railway vehicle.

Like in the safety verification reported in Section 2.5.3.1, the verification of restorability may also be performed by developing a complex model of the entire structure, including the track, using the stresses of each component of the track as the verification index, or by using structural displacement indexes (see Figure 2.19). In practice, the second option is usually adopted for simplicity, being the design limit values of the structural displacement indexes defined in the Displacement Limit Standard (RTRI, 2006).

2.5.3.2.1 Restorability of track damage in ordinary conditions

The design limit values for the structural displacement indexes in ordinary conditions, namely the irregularity of the track at the ends of the girder and the angular rotation on track surfaces (see Figure 2.19) in both vertical and lateral directions are presented in Table 2.9. The limits depend on the track type (slab track or ballast track) and on the type of rails used in Japan (50kgN rail and 60kg rail).

Table 2.9 - Design limit values of angular rotations and irregularities for the running safety in ordinary conditions (RTRI, 2006).

Direction	Track type	Angular rotation θ_t ($\times$1/1000) (Translation/bending shape)			Irregularity r (mm)	
		50kgN Rail	60kg Rail		50kgN Rail	60kg Rail
			Conventional	Shinkansen		
Vertical	Slab	3.5	3.0	3.0	3.0	2.0
	Ballast	6.0	5.5	7.0		
Lateral	Slab	4.0	4.0	4.0	2.0	2.0
	Ballast	5.5	5.0	5.5		

2.5.3.2.2 Restorability of track damage in seismic conditions

The design limit values for the structural displacement indexes in seismic conditions, namely the irregularity of the track at the ends of the girder and the angular rotation on track surfaces (see Figure 2.19) in both vertical and lateral directions are presented in Table 2.10. This limits aim to guarantee the performance level 1 of restorability when the structure is subjected to the Level 1 earthquake motion defined in the Seismic Design Standard (RTRI, 1999).

Table 2.10 - Design limit values of angular rotations and irregularities for the running safety in seismic conditions (RTRI, 2006).

Direction	Track type	Angular rotation θ_t ($\times$1/1000) (Translation/bending shape)		Irregularity r (mm)	
		50kgN Rail	60kg Rail	50kgN Rail	60kg Rail
Vertical	Slab	5.0	3.5	4.5	3.5
	Ballast	7.5	6.5	3.5	4.0
Lateral	Slab	6.0	6.0	2.0	2.0
	Ballast	8.0	8.0	2.0	2.0

2.5.4 North American standards

The running safety requirements adopted in the U.S.A., defined by the Manual of Standards of the Association of American Railroads (AAR, 2011), are currently used only for freight vehicles. However, a short description of the main requirements is presented, since most of those requirements and criteria may also be used in the assessment of the running safety of passenger trains.

Chapter XI of the Manual of Standards of the AAR (AAR, 2011) defines a series of criteria for the safety assessment of railway vehicles that may be divided into the following categories:

a) Verification of derailment (see Section 2.5.4.1);

b) Verification of dynamic stability (see Section 2.5.4.2);

The criteria defined in the Manual of Standards of the AAR (AAR, 2011) to perform the verifications described above are related with the control of the ratios between the lateral Y and vertical Q contact forces, such as the Nadal criterion, referred to as single wheel Y/Q ratio in the standard, the Weinstock criterion, referred to as axle sum Y/Q ratio, and the rail roll criterion, termed bogie-side Y/Q ratio (the running safety criteria are described in more detail in Section 3.5 of Chapter 3). Only levels that are exceeded for more than 0.05 s are considered. The standard recommends that the verifications should be made using an extensive series of tests performed on especially developed test tracks backed up by numerical analysis.

2.5.4.1 Verification of derailment

The verification of derailment defined in the Manual of Standards of the AAR (AAR, 2011) requires the vehicle to be tested over a number of track sections with a specified geometry. Moreover, the rail surface friction coefficient is required to be measured and cannot be less than 0.4. During the tests, the vehicle is equipped with load measuring wheelsets to quantify the contact forces between wheel and rail, being the test data filtered to remove contents above 15 Hz. The verification comprehends specifications related to curving and to the response to several types of track irregularities, as described below.

2.5.4.1.1 Requirements to steady state curving

The requirements for steady state curving aim to ensure that the resulting contact forces between wheel and rail are safe from any tendency to derail. The curving tests have to be performed on a curve with a radius of 250 m belonging to a track whose cant angle provides a balance speed between 32 km/h and 48 km/h. Acceptable performance in both the numerical analysis and tests requires that the single wheel Y/Q ratio and the axle sum Y/Q ratio do not exceed 1.0 and 1.5, respectively.

2.5.4.1.2   Requirements for transition curves

The requirements for transition curves are designed to ensure the satisfactory negotiation of curves leading into and away from a constant radius curve. The numerical analysis and tests are required to demonstrate a reasonable margin of safety from derailment, especially under conditions of reduced vertical wheel loading. The transition curve has a rate of change of 1 degree in the cant angle in every 6 m, leading to a curve with a constant radius of 250 m. The vehicle is loaded asymmetrically according to the AAR loading rules in order to obtain the maximum wheel unloading. Acceptable performance in both the numerical analysis and tests demands that the single wheel Y/Q ratio and the axle sum Y/Q ratio does not exceed 1.0 and 1.5, respectively, and that the minimum vertical wheel load is never less than 10 % of the static wheel load.

2.5.4.1.3   Requirements for dynamic curving

This requirement aims to guarantee the satisfactory negotiation of the vehicle over a curved track with a combination of gauge and cross level irregularities (see Section 3.3.2 of Chapter 3 for a detailed description of the track irregularities types). The tests have to be performed on a test track with a 25.4 mm alignment irregularity in the outer rail of the curve, resulting in a 25.4 mm variation in gauge, as shown in Figure 2.21. Additionally, a cross level variation with a maximum amplitude of 25.4 mm is also considered. An acceptable performance in the tests requires the fulfillment of the same limits specified for the transition curves.
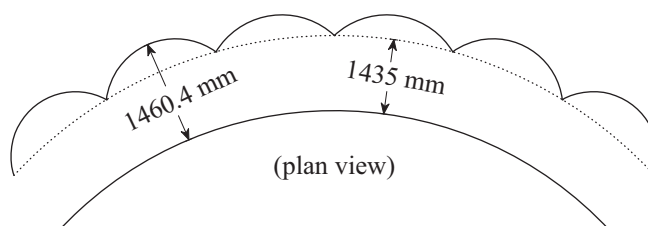
Figure 2.21 - Dynamic curving track section (adapted from Elkins and Carter (1993)).

2.5.4.1.4   Response to elevation irregularity

The requirement regarding the response to elevation irregularities (geometrical error in the longitudinal-vertical plane, see Section 3.3.2 of Chapter 3) aims to ensure the satisfactory runnability over a track that provides pitching and bouncing excitations to the vehicle. The test track contains ten parallel perturbations with a wavelength of 11.9 m and a maximum vertical

amplitude of 19 mm, as depicted in Figure 2.22. During the test, acceptable performance requires that the minimum vertical wheel load is never less than 10 % of the static wheel load.

Figure 2.22 - Elevation irregularity track section (adapted from Elkins and Carter (1993)).

2.5.4.1.5 Response to cross level irregularity

This requirement is intended to ensure the satisfactory runnability over a track that provides roll and twist oscillatory excitations to the vehicle. The tests have to be performed on a track stretch of 122 m with vertical perturbations with a wavelength of 11.9 m that provides a maximum cross level irregularity (difference in the elevation of the rails along the longitudinal direction, see Section 3.3.2 of Chapter 3) of 19 mm, as illustrated in Figure 2.23. Acceptable performance in the tests demands that the axle sum Y/Q ratio does not exceed 1.5 and that the minimum vertical wheel load is never less than 10 % of the static wheel load.

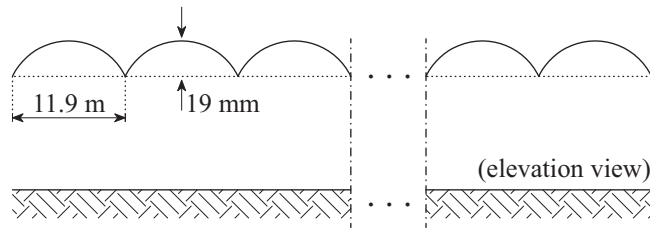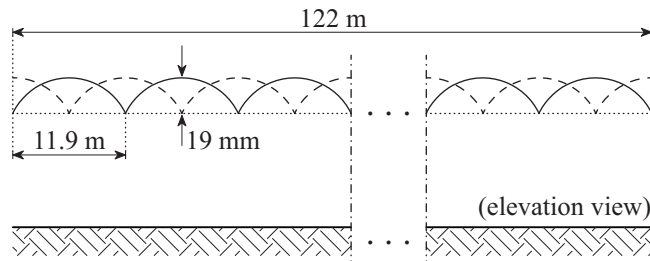Figure 2.23 - Cross level irregularity track section (adapted from Elkins and Carter (1993)).

2.5.4.1.6 Response to alignment irregularity

The last requirement is designed to guarantee the satisfactory negotiation of track containing misalignments that provide yaw and roll excitations to the vehicle. The alignment irregularities (geometrical error in the lateral direction of the horizontal plane, see Section 3.3.2 of Chapter 3) in the 61 m test track stretch, depicted in Figure 2.24, are sinusoidal, with a wavelength of 11.9 m, an amplitude of 31.8 mm and a constant gauge of 1460 mm. Acceptable performance during the tests requires that the bogie-side Y/Q ratio and the axle sum Y/Q ratio does not exceed 0.6 and 1.5, respectively.
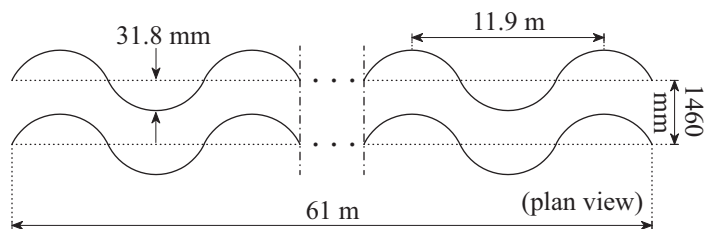
Figure 2.24 - Alignment irregularity track section (adapted from Elkins and Carter (1993)).

2.5.4.2 *Verification of dynamic stability*

According to the Manual of Standards of the AAR (AAR, 2011), the tests regarding the verification of dynamic stability are performed to ensure the absence of lateral instability or hunting within the operating speed of the vehicle. Numerical analyses are also performed to predict the speed at which the lateral oscillations of the wheelset may lead to a continuous flange-rail contact and to demonstrate that the magnitude of the wheel-rail contact forces and the carbody lateral acceleration remain below the limit values. The limit values to guarantee an acceptable performance regarding the dynamic stability of the vehicle consist of an unweighted standard deviation of the carbody lateral acceleration of 2.6 m/s^2 and an axle sum *Y/Q* ratio of 1.5.

Chapter 3

FRAMEWORK OF THE METHODOLOGY FOR THE ASSESSMENT OF THE TRAIN RUNNING SAFETY ON BRIDGES

3.1 INTRODUCTION

In the present chapter, a methodology for assessing the train running safety on bridges is presented (Montenegro et al., 2015a). Although the methodology may be applied to assess the safety of trains subjected to several kinds of actions, such as, among others, earthquakes, crosswinds or accident loads, the present work mainly focuses on the first. First, the proposed methodology is introduced, along with a brief description of the background history of past derailments caused by earthquakes. Then, the main source of excitations to the vehicle considered in the present work, namely the earthquake and the track irregularities, are described. Regarding the seismic action, since the running safety of the trains might be jeopardized not only by intense shakings, but also by moderate earthquakes that do not cause significant damage to the structure, only seismic events with relatively low return periods and high probability of occurrence are considered in the present work. Therefore, no significant nonlinearity is likely to be exhibited in the bridge piers for these levels of seismicity. Nevertheless, the reduction in the stiffness of the piers due to concrete cracking is accounted for, using a methodology developed by Montenegro et al. (2015a) and exposed in the third part

of the present chapter. Finally, the derailment mechanisms that may occur during the passage of a train over a bridge, together with the safety criteria used to analyze the possible occurrence of such phenomena, are presented.

3.2   OVERVIEW OF THE METHODOLOGY FOR THE ASSESSMENT OF THE TRAIN RUNNING SAFETY ON BRIDGES

3.2.1   Background

The strict design requirements for high-speed railways is leading to an increase in the number of viaducts in the railway networks around the world in order to ensure smoother tracks with larger curve radius. This reality leads to an increase in the probability of a train being over a bridge during the occurrence of hazards that might compromise its running safety. As an example, countries such as China, Japan and Taiwan, which are prone to earthquakes, have a highly developed high-speed railway network in which some of the lines have more than 75 % of viaducts (Ishibashi, 2004; Kao and Lin, 2007; Dai et al., 2010). Therefore, events such as the derailment that occurred during the Kobe Earthquake in January 1995, the Shinkansen high-speed train derailment at 200 km/h during the Mid-Niigata Earthquake in October 2004 or the train derailments caused by strong crosswinds reported by Baker et al. (2009), gave railway engineers the incentive for studying the running safety of trains on bridges.

Few studies, however, were carried out so far concerning this topic, resulting in a lack of regulation in the existing codes, especially regarding the running safety of vehicles under seismic conditions. In the European standards, the stability of railway vehicles during earthquake is not addressed, being both EN 1991‑2 (2003) and EN 1990-Annex A2 (2001) limited to design criteria for railway bridges in ordinary conditions and EN 1998-2 (2005) restricted to design criteria related to the structural safety. However, the running safety of trains might also be jeopardized by moderate earthquakes that do not represent a significant threat to the structural integrity. Yang and Wu (2002) state that "*for railway bridges, it is possible that the bridge itself may remain safe during the earthquake, but may not be safe enough for the trains to move over it due to excessive vibrations*", and concluded saying that "*the safety of moving trains over the bridge under earthquake excitations is a subject of great concern in railway engineering*". Hence, taking into consideration the existing gap regarding this topic, both in terms of regulation and available studies, a methodology for assessing the running safety of trains on bridges is presented.

3.2.2   Description of the methodology

Figure 3.1 illustrates the framework of the proposed methodology for the assessment of the train running safety on bridges. The methodology consists of calculating the wheel-rail contact forces during the passage of the train over the bridge in order to evaluate the risk of derailment through existing running safety criteria. The dynamic analyses are performed with the train-structure interaction method developed by Montenegro et al. (2015b) and described later in Chapter 4.
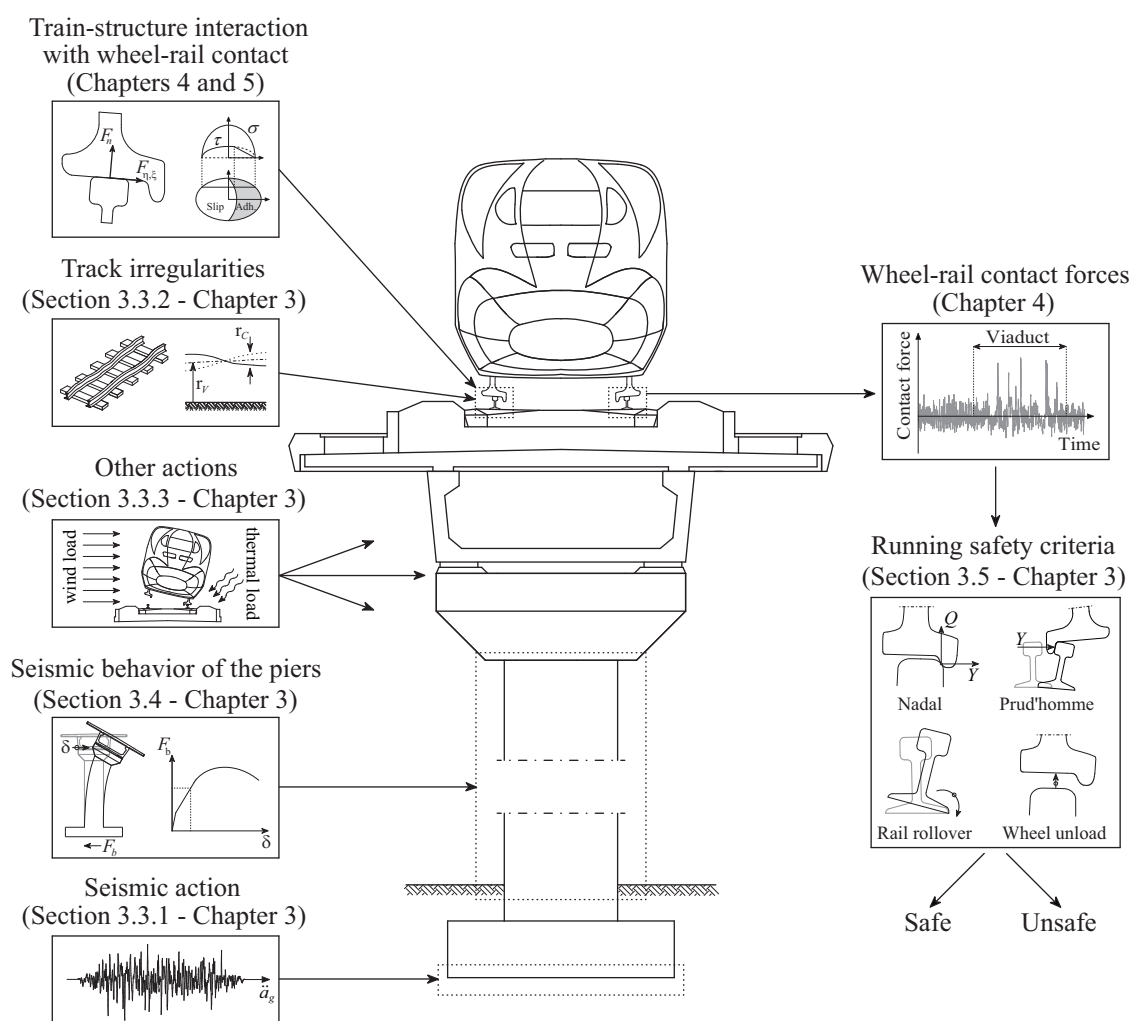
Figure 3.1 - Framework of the methodology for the assessment of the train running safety on bridges.

Although the methodology is generalized to allow the safety assessment of trains under any kind of conditions, as shown in Figure 3.1, the present work focuses mainly on the running safety against earthquakes. Thus, the seismic motion is represented in terms of ground acceleration time-histories using artificial accelerograms (Section 3.3.1) that are generated from the elastic spectra described in EN 1998-1 (2004), with peak ground accelerations (PGA)

corresponding to moderate events with relatively high probability of occurrence and low return periods. Since no significant nonlinearity is likely to be exhibited in the bridge piers for these levels of seismicity, all the analysis are performed in the elastic domain with a reduction in the stiffness of the piers to account for concrete cracking. The reduced stiffness, referred to as effective stiffness, is calculated based on the methodology developed by Montenegro et al. (2015a) and described in Section 3.4. This methodology is divided into three main steps, which consist of:

a)   Nonlinear static analysis to assess the horizontal monotonic behavior of the piers;

b)   Nonlinear dynamic analysis to evaluate the maximum response at the top of the pier;

c)   Calibration of the effective stiffness based on the two aforementioned analyses.

Track irregularities, which consist of deviations of the rail from its ideal geometry, are also an important source of excitation for the vehicle. In the present work, the irregularity profiles are generated based on analytical power spectral density (PSD) functions (Section 3.3.2).

Finally, the running safety of the train is evaluated using safety criteria based on the wheel-rail contact forces that are recommended by the several codes reported in Section 2.5 of Chapter 2, such as Nadal (1908), Prud'homme (1967), rail rollover (AAR, 2011) and wheel unloading (EN 14067-6, 2010) criteria (Section 3.5). Therefore, for each scenario, the circulation is considered to be safe as long as none of the safety criteria is violated during the whole time the vehicle is crossing the bridge.

3.3   SOURCES OF EXCITATION OF THE TRAIN-STRUCTURE SYSTEM

3.3.1   Seismic action

3.3.1.1 *Representation of the seismic action*

The seismic excitations adopted in the present work consist of artificial accelerograms generated from the elastic spectra described in EN 1998-1 (2004), with PGA corresponding to moderate events with return periods less than 475 years, which is the reference return period of the design seismic action associated with the no-collapse requirement. This type of seismic actions is of the utmost importance, since the running safety of trains might be jeopardized not only by intense earthquakes, but also by moderate seismic events, which may not cause significant damage to the structure. Figure 3.2 illustrates an example of one of the generated

accelerograms (return period equal to 310 years), as well as the respective response spectrum adjustment to the target spectrum given by EN 1998-1 (2004).
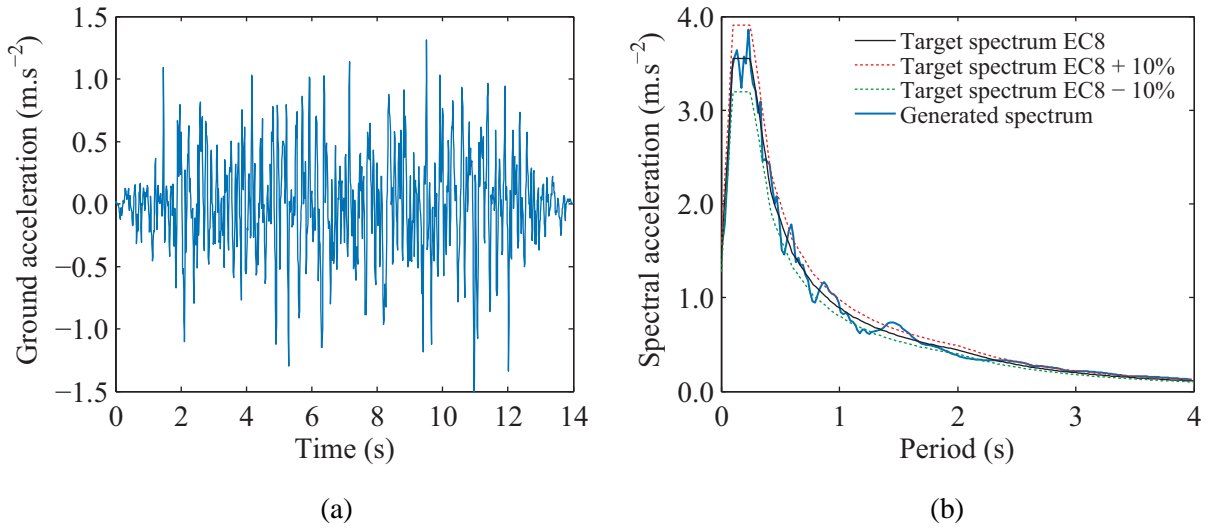

Figure 3.2 - Example of a generated ground motion: (a) accelerogram and (b) spectrum adjustment.

3.3.1.2 *Generation of artificial accelerograms*

The artificial accelerograms are generated with the software SeismoArtif (2013), which uses a method based on a random process of adjustment by correction in the frequency domain. This method defines the artificial ground motion considering a target spectrum and adapting the frequency content through an iterative process using the Fourier Transformation Method.

The ground motion $\ddot{a}_g(t)$ is generated based on the fact that each periodic function can be expressed as a series of sinusoidal waves, and is defined as (Gasparini and Vanmarcke, 1976)

$$\ddot{a}_g(t) = I(t)\sum_n A_n \sin(\omega_n t + \phi_n) \tag{3.1}$$

where A_n, ω_n and ϕ_n are the amplitude, frequency and phase angle, respectively, of the *n*th sinusoidal wave considered, and $I(t)$ an intensity function to simulate the transient nature of the earthquake. By defining a vector of amplitudes and simulating different arrays with a random set of phase angles, it is possible to obtain different processes with the same general aspect but with different characteristics. These random processes are stationary and their characteristics do not change with time. In the present method, the random phase angles ϕ_n are uniformly distributed in the range $[0, 2\pi]$.

The method used by SeismoArtif to generate the artificial accelerograms comprehends an iterative process. Therefore, for each cycle, the response spectrum generated for the simulated ground motion is compared with the target spectrum at a set of control frequencies, being the correction of the random process performed in the frequency domain. Figure 3.3 outlines the main steps of the artificial accelerogram generation process.
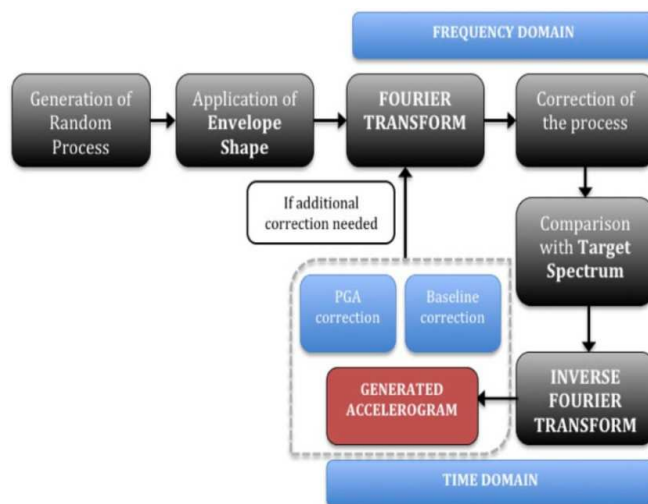
Figure 3.3 - Schematization of the generation process of artificial accelerograms (SeismoArtif, 2013).

3.3.2 Track irregularities

3.3.2.1 Types of track irregularities

Track irregularities are an important source of excitation for both the structure and the vehicle. The irregularities are deviations of the track from the design geometry (see Figure 3.4) that can be divided into the following four types (Frýba, 1996; Andersson et al., 1999):

a) Elevation level: geometrical error in the longitudinal-vertical plane;

b) Alignment: geometrical error in the lateral direction of the horizontal plane;

c) Cross level: difference in the elevation of the rails along the longitudinal direction;

d) Gauge: variation in the track gauge.
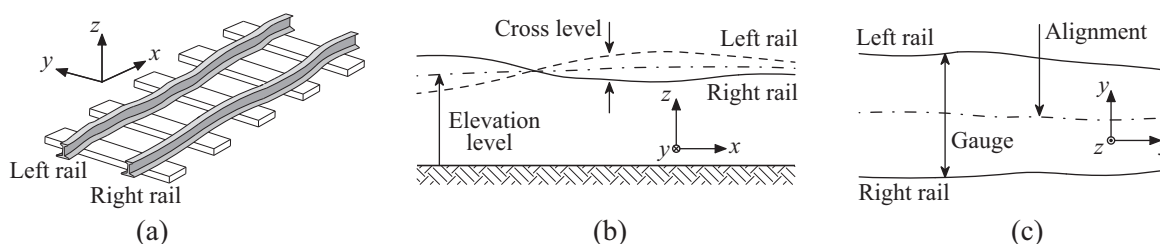
Figure 3.4 - Types of track irregularities: (a) perspective view; (b) elevation view and (c) plan view.

Therefore, considering r_y and r_z as the lateral and vertical deviations, respectively, the elevation r_V, alignment r_A, cross level r_C and gauge r_G irregularities can be defined as function of the longitudinal coordinate x as following:

$$r_V(x) = \frac{1}{2}\left(r_z^{rht} + r_z^{lft}\right) \tag{3.2a}$$

$$r_A(x) = \frac{1}{2}\left(r_y^{rht} + r_y^{lft}\right) \tag{3.2b}$$

$$r_C(x) = r_z^{rht} - r_z^{lft} \tag{3.2c}$$

$$r_G(x) = r_y^{rht} - r_y^{lft} \tag{3.2d}$$

where the superscripts *lft* and *rht* indicate left and right rails, respectively.

3.3.2.2 Power spectral density functions

In order to account for the track irregularities in the train-structure interaction analysis, it is necessary to analytically describe the track geometry. However, since it is usually difficult to have access to a detailed description of the track, the irregularities are commonly defined as a stationary stochastic process that may be described by PSD functions.

Each of the aforementioned irregularity profiles r can be understood as a stochastic Gaussian ergodic process that is characterized by the mean value $\bar{r}$ given by (Claus and Schiehlen, 1998)

$$\bar{r} = \lim_{L \to \infty} \frac{1}{L} \int_0^L r(x)\,dx \tag{3.3}$$

and by the correlation function R_r that can be written as

$$R_r(\zeta) = \lim_{L \to \infty} \frac{1}{L} \int_0^L r(x)\,r(x-\zeta)\,dx \tag{3.4}$$

The Fourier transform of the correlation function results in the PSD function S, which can be defined as

$$S(\Omega) = \int_{-\infty}^{+\infty} R_r(\zeta)e^{-j\Omega\zeta}\,d\zeta \tag{3.5}$$

where Ω is the spatial frequency.

According to Claus and Schiehlen (1998), various measurements of track irregularities have shown that the PSD can be standardized and expressed as

$$S_{A,V}(\Omega) = \frac{1}{2} A_{A,V} \frac{\Omega_c^2}{\left(\Omega_r^2 + \Omega^2\right)\left(\Omega_c^2 + \Omega^2\right)} \tag{3.6a}$$

$$S_{G,C}(\Omega) = \frac{1}{l^2} A_{G,C} \frac{\Omega_c^2 \Omega^2}{\left(\Omega_r^2 + \Omega^2\right)\left(\Omega_c^2 + \Omega^2\right)\left(\Omega_s^2 + \Omega^2\right)} \tag{3.6b}$$

where the subscripts A, V, G and C indicate the alignment, elevation level, gauge and cross level irregularities, l is half of the gauge, A is the irregularity scale factor, and Ω_c, Ω_r and Ω_s are constant factors. According to Claus and Schiehlen (1998), the values of these constant factors, which are representative of the European railway network, are

$$\Omega_c = 0.8246 \, \text{rad/m} \tag{3.7a}$$

$$\Omega_r = 0.0206 \, \text{rad/m} \tag{3.7b}$$

$$\Omega_s = 0.4380 \, \text{rad/m} \tag{3.7c}$$

The PSD functions of the elevation irregularity for three distinct levels of track quality are represented, for exemplification purposes, in Figure 3.5. The three PSD functions refer to the low, medium and high levels of irregularities described by Claus and Schiehlen (1998), represented by scale factors of $A_{low} = 0.59233 \times 10^{-6} \, \text{rad.m}$, $A_{medium} = 1.08922 \times 10^{-6} \, \text{rad.m}$ and $A_{high} = 1.58610 \times 10^{-6} \, \text{rad.m}$, respectively.
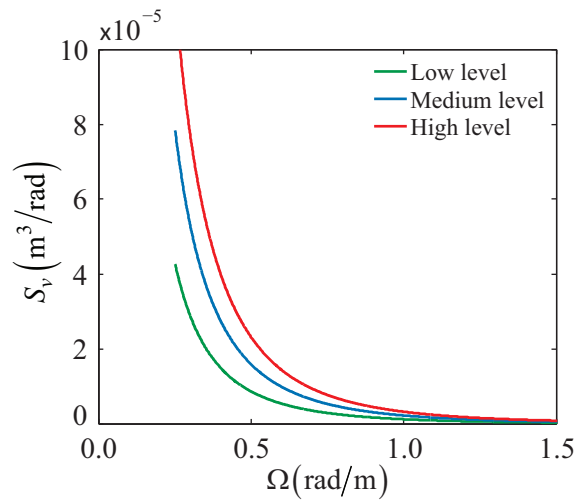

Figure 3.5 - PSD functions of the alignment irregularity for three distinct levels of track quality.

3.3.2.3 Generation of irregularity profiles

The irregularity profiles can be generated using the modified spectral representation method described in Hu and Schiehlen (1997). According to the authors, the irregularity profile function *r(x)* is given by

$$r(x) = \sqrt{2} \sum_{n=0}^{N-1} A_n \cos(\Omega_n x + \phi_n)$$
(3.8)

where ϕ_n are random phase angles uniformly distributed in the range $[0, 2\pi]$ and Ω_n are a series of N spatial discrete frequencies defined in the interval $[\Omega_0, \Omega_f]$ with increments $\Delta\Omega$, in which Ω_0 and Ω_f are the minimum and maximum frequencies considered. The coefficients A_n are defined as

$$A_0 = 0$$
(3.9a)

$$A_1 = \sqrt{\left(\frac{1}{\pi} S(\Omega_1) + \frac{4}{6\pi} S(\Omega_0)\right) \Delta\Omega}$$
(3.9b)

$$A_2 = \sqrt{\left(\frac{1}{\pi} S(\Omega_2) + \frac{1}{6\pi} S(\Omega_0)\right) \Delta\Omega}$$
(3.9c)

$$A_n = \sqrt{\left(\frac{1}{\pi} S(\Omega_n)\right) \Delta\Omega} \quad ; \quad n = 3, 4, \ldots, N-1$$
(3.9d)

Finally, the rail deviations to be imposed during the train-structure interaction dynamic analyses are given by

$$r_y^{lft}(x) = r_A(x) + \frac{1}{2} r_G(x)$$
(3.10a)

$$r_y^{rht}(x) = r_A(x) - \frac{1}{2} r_G(x)$$
(3.10b)

$$r_z^{lft}(x) = r_V(x) + \frac{1}{2} r_C(x)$$
(3.10b)

$$r_z^{rht}(x) = r_V(x) - \frac{1}{2} r_C(x)$$
(3.10b)

3.3.3   Other sources of excitation

Although the present work is only focused on the running safety of trains under seismic conditions, the methodology proposed in the present chapter is capable of dealing with any other type of external loads that may influence the running stability of the railway vehicle. Therefore, static or dynamic wind loads (Section 8 of EN 1991-1-4 (2005) and EN 14067-6 (2010)), applied both to the structure and vehicle, accident loads due to impact on supporting members of the structure caused by derailed trains passing under or adjacent to structures (Section 4.5 of EN 1991-1-7 (2006)) or thermal loads that may cause the rails to buckle (UIC 774-3-R, 2001), are all actions that can put the stability of the vehicle at risk as well and that may also be considered in the model.

3.4   MODELING OF THE SEISMIC BEHAVIOR OF THE BRIDGE PIERS

3.4.1   Introduction

According to EN 1998-2 (2005), when an equivalent linear analysis is used, the effective flexural stiffness of a reinforced concrete member should correspond to the secant stiffness at the theoretical yield point. However, the present study focus on the train running safety on bridges during moderate earthquakes in which, in general, the piers do not experience significant damage and the yield point is not reached. Thus, an alternative methodology to estimate the effective stiffness of the bridge piers to be used in the train-structure interaction analyses performed in the elastic domain is presented. The methodology is divided in the following steps: 1) a nonlinear static analysis to evaluate the horizontal monotonic behavior of the piers; 2) a nonlinear dynamic analysis to determine the maximum displacement at the top of the pier when subjected to the seismic excitations and 3) calibration of the effective stiffness in order to obtain, with a linear dynamic analysis, levels of displacement similar to those obtained with the nonlinear dynamic analysis. These three steps are described in detail in Sections 3.4.2 through 3.4.4.

3.4.2   Monotonic response of the bridge piers

The first step of the methodology consists of performing a nonlinear monotonic static analysis to evaluate the horizontal response of the piers, as depicted in Figure 3.6. In this type of analysis, the idealized representation of the structure is subjected to a constant gravity load F_w and to a monotonically increasing force or displacement δ at the pier top that represent the

inertial effects from the earthquake (Elnashai and Sarno, 2008). Since the forcing function is increased until the ultimate capacity of the pier is reached, the structure model has to account for the effects of both the material inelasticity and the geometric nonlinearity. Thus, to perform this type of analysis, the piers are commonly modeled using frame elements with distributed inelasticity based on the displacement-based formulation, in which the sectional stress-strain state is obtained through the integration of the nonlinear uniaxial material response of the individual fibers used to discretize the cross-section.

The results obtained with the monotonic analysis are expressed in terms of a capacity curve (see Figure 3.6), which consists in the relation between the global base shear force F_b and the displacement δ at the top of the pier. In the present work, the nonlinear monotonic static analysis is performed using the software SeismoStruct (2013) .
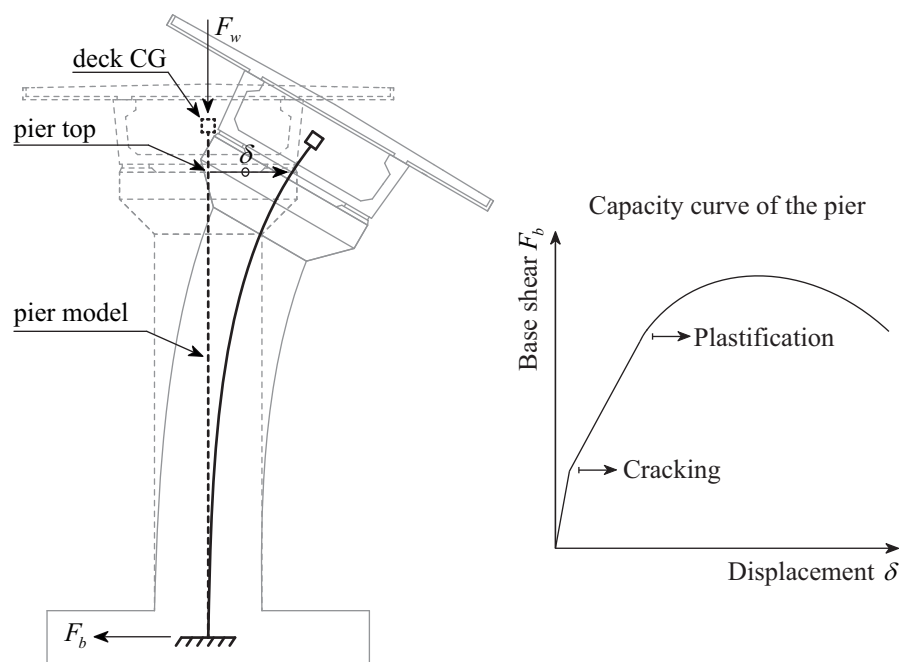
Figure 3.6 - Nonlinear monotonic static analysis.

3.4.3 Nonlinear dynamic analysis

The second step of the methodology consists of performing a nonlinear dynamic analysis to predict the inelastic response of the piers subjected to the seismic excitation. The structure, whose model also have to account for the effects of material and geometric nonlinearities, is subjected to the seismic ground motion $\ddot{a}_g$ applied at the base of the piers, as depicted in Figure 3.7. Then, the maximum displacement at the top of the pier δ_{max} is computed. This value, together with the horizontal capacity of the piers obtained in the monotonic analysis

presented in the previous section, is used to calibrate the effective stiffness of the piers, as shown in Section 3.4.4.

Due to the dynamic nature of the analysis, damping has to be accounted for in order to obtain a realistic result. The hysteretic component of damping, which is usually responsible for the dissipation of the majority of the energy introduced by the earthquake load, is already included within the elements with nonlinear behavior. However, since the proposed methodology focuses on the analysis of the seismic behavior of piers that do not experience significant levels of plasticity, the non-hysteretical damping that is mobilized during the dynamic response of the structure, through phenomena such as friction and energy radiation, also plays an important role. Therefore, this energy dissipation mechanism is accounted by means of Rayleigh damping (Clough and Penzien, 2003), with an equivalent viscous damping ratio fixed in the frequencies of the pier obtained using the elastic stiffness of an uncracked cross-section and using the effective stiffness estimated with the Annex C of EN 1998-2 (2005) for reinforced concrete ductile members. This criterion is based on the fact that the natural frequency of the piers after the calibration of the effective flexural stiffness is somewhere between the two aforementioned frequencies. The nonlinear dynamic analysis is also performed using the software SeismoStruct.

Figure 3.7 - Nonlinear dynamic analysis.
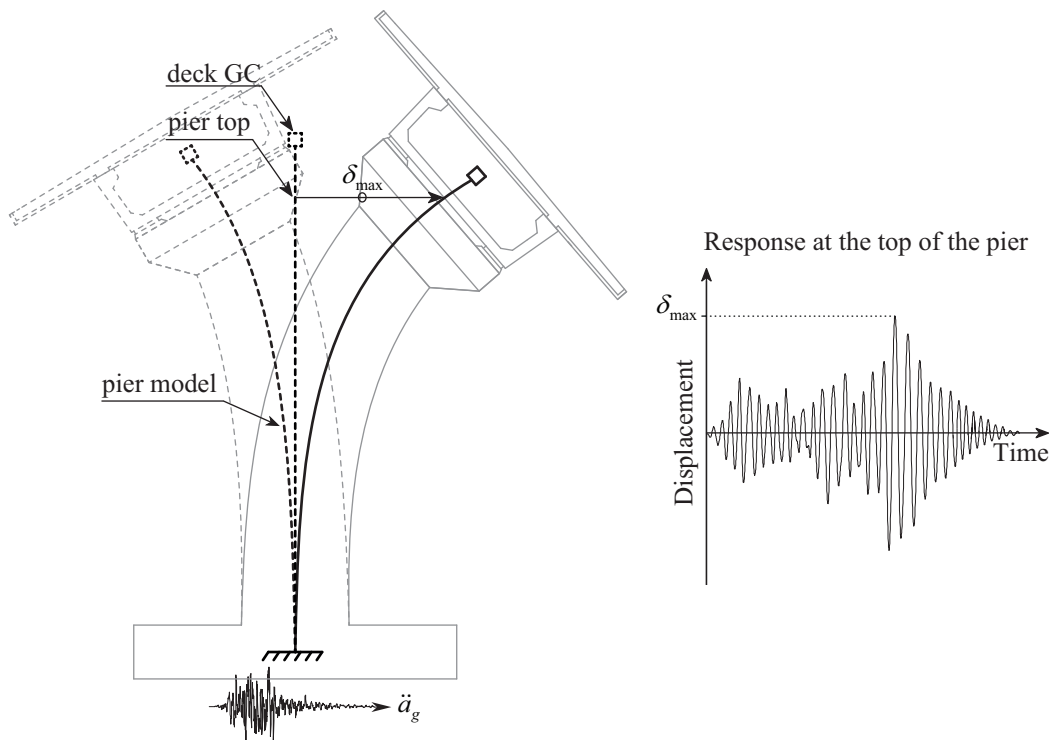
3.4.4   Calibration of the effective stiffness of the bridge piers

The final step of the present methodology consists of calibrating the effective stiffness of the piers in order to obtain, with a linear dynamic analysis, levels of displacement similar to those obtained with the nonlinear dynamic analysis presented in the previous section. Thus, the base shear force F_b, obtained in the capacity curve (see Section 3.4.2), corresponding to the maximum displacement at the top of the pier δ_{max} computed in the nonlinear dynamic analysis (see Section 3.4.3) is evaluated, as depicted in Figure 3.8. The effective flexural stiffness of the pier will correspond to the secant stiffness at the aforementioned point. The stiffness is calculated numerically or, in the case of simple structures whose flexural stiffness can be approximated by a closed-form expression, analytically.
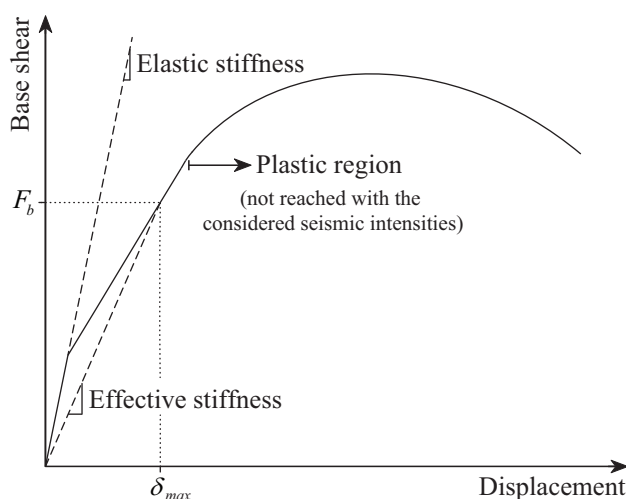
Figure 3.8 - Base shear force F_b corresponding to the maximum displacement δ_{max} at the top of the pier.

3.5   DERAILMENT MECHANISMS AND SAFETY CRITERIA

The assessment of the running safety of trains is a topic of the utmost importance in railway engineering. Therefore, it is important to ensure that the criteria used to evaluate the safety of vehicles are realistic enough to avoid the occurrence of derailments. Train derailments are the result of wheels running off the rails that provide the necessary guidance to the vehicle. The reasons for wheels running off the rail can be difficult to ascertain. However, the final scenario of derailment may result in wheels climbing off the rail, gauge widening or rail rollover, causing the wheels to fall between the rails (Wu and Wilson, 2006). Hence, any situation that may reduce the lateral guidance provided by the rails will surely increase the risk of derailment.

According to their causes, the derailment mechanisms can be classified into the following categories: 1) wheel flange climbing; 2) track panel shift; 3) gauge widening and 4) wheel unloading. Each of these derailment mechanisms have to be controlled and avoided using appropriate safety criteria during the design of the structure. In Section 2.5 of Chapter 2, the norms and recommendations defined in several standards for the assessment of rail traffic safety were introduced and summarized. Among these, the criteria based on the control of the wheel-rail contact forces, namely the Nadal, Prud'homme, rail roll and wheel unloading criteria, are adopted in the present methodology for the assessment of the train running safety.

3.5.1   Wheel flange climbing

3.5.1.1 Derailment mechanism

The derailments caused by wheel flange climbing are the result of excessive lateral and/or vertical vibrations of the track that may cause the wheel to climb over the rail, resulting in a reduction of lateral guidance provided by the rail. This kind of derailment generally occurs when the wheel experiences a high level of lateral force combined with a reduction in the vertical contact force on the flanging wheel. Phenomena such as earthquakes or strong winds combined with high levels of track irregularities can strongly contribute to this type of derailments.

According to Wu and Wilson (2006), the mechanism of derailment caused by the wheel flange climbing over the rail can be illustrated in three phases, as shown in Figure 3.9. In phase 1, the wheel moves towards the rail due to the action of the lateral load F_l imposed to the vehicle, causing the formation of a lateral friction force F_η, called creep force (see Section 4.5 of Chapter 4), which opposes the flange climbing. In phase 2, when the flange touches the rail, the lateral velocity of the wheel decreases due to the increasing contact angle. Consequently, the lateral creep force reverses direction and starts to assist the flange climbing. After reaching the maximum contact angle, the lateral velocity of the wheel increases again, resulting in another inversion of the lateral creep force direction (phase 3). As a result, the creep force opposes once again the climbing motion of the wheel.
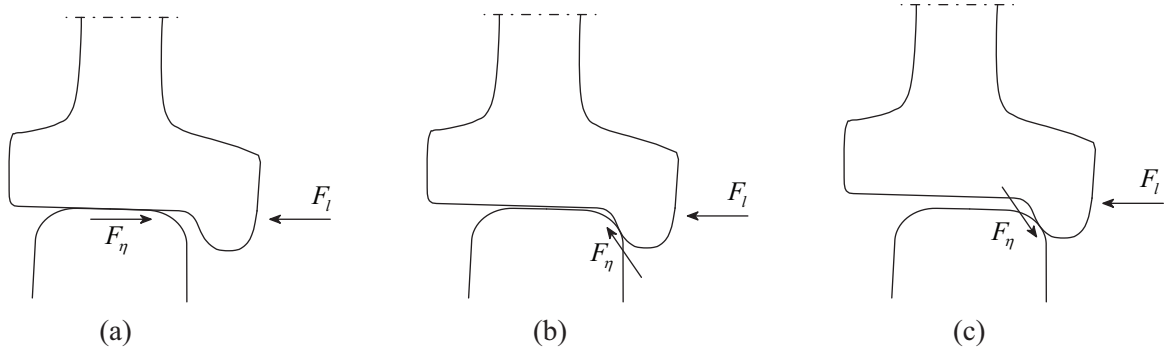
Figure 3.9 - Mechanism of derailment caused by wheel flange climbing: (a) phase 1, (b) phase 2 and (c) phase 3.

3.5.1.2 Nadal criterion

One of the most common criterion used to assess the derailment caused by wheel flange climbing was proposed by Nadal (1908) in the beginning of the 20th century. This criterion limits the ratio between the lateral Y and vertical Q contact force in each wheel, commonly known as derailment index or derailment coefficient, in order to minimize the risk of derailment. Based on a simple equilibrium of forces between the wheel and rail at a single contact point in the flange, as depicted in Figure 3.10, the Y/Q ratio, referred to in this work as the Nadal factor ζ_N, can be expressed as

$$\zeta_N = \frac{Y}{Q} = \frac{\tan \gamma - \dfrac{F_\eta}{F_n}}{1 + \dfrac{F_\eta}{F_n} \tan \gamma} \tag{3.11}$$

where γ is the contact angle between the wheel and rail, F_n the normal contact force and F_η the lateral creep force. Nadal proposed the criterion for the saturation condition, leading to

$$\zeta_N = \frac{Y}{Q} = \frac{\tan \gamma - \mu}{1 + \mu \tan \gamma} \tag{3.12}$$

where μ is the friction coefficient. The limit value for the Y/Q ratio varies from country to country, depending on the friction coefficient considered and on the wheel flange inclinations. According to TSI (2002), the Y/Q ratio in any wheel of the train should not exceed 0.8. The same limit is imposed in Japan (RTRI, 2006), while in the U.S.A. and China the Y/Q ratio is allowed to reach 1.0 (AAR, 2011 and Jun and Qingyuan (2005)).
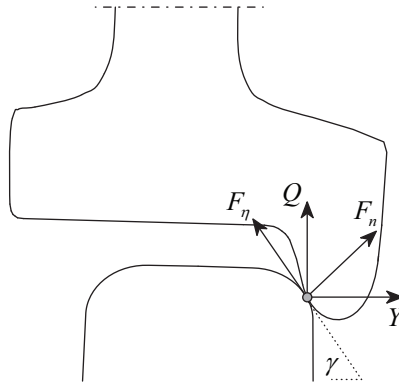
Figure 3.10 - Forces acting at the flange contact point.

According to Wu and Wilson (2006), the Nadal criterion agrees with scenarios when a large angle of attack is experienced, such as curve negotiations. However, for small angles of attack, the criterion proved to be very conservative, since it does not consider the effects of friction in the non-flanging wheel (see Section 3.5.1.3) and assumes that the flange climbing derailment occurs instantaneously once the *Y/Q* ratio limit is exceeded. In fact, both field tests and simulations have proven that the derailments caused by wheel flange climbing occur only when the *Y/Q* ratio limit is exceeded for a certain period of time (see Section 3.5.1.4).

3.5.1.3 Weinstock criterion

Weinstock (1984) proposed a less conservative criterion, named Weinstock criterion or wheelset sum *Y/Q* ratio, which takes into account not only the effects of friction in the flanging wheel, but also in the non-flanging wheel of the same wheelset. This criterion evaluates the *Y/Q* ratio in the flanging wheel using the Nadal criterion, while the *Y/Q* ratio in the non-flanging wheel is considered to be equal to the friction coefficient since the contact angle is small in the tread region (see equation (3.12)). Thus, using the same force equilibrium scheme shown in the previous section, but considering the contribution of the two wheels of the same wheelset (see Figure 3.11), the wheelset sum *Y/Q* ratio, referred to in this work as the Weinstock factor ζ_W, is given by

$$\zeta_W = \sum_{ws} \frac{Y}{Q} = \frac{\tan \gamma_A - \mu_A}{1 + \mu_A \tan \gamma_A} + \mu_B \tag{3.13}$$

where *ws* indicates wheelset and the subscripts *A* and *B* indicate the flanging and non-flanging wheel, respectively, as illustrated in Figure 3.11. This criterion is mainly used in the U.S.A. and, according to the Chapter XI of the Manual of Standards of the AAR (AAR, 2011), the wheelset sum *Y/Q* ratio given by equation (3.13) should not exceed 1.5.
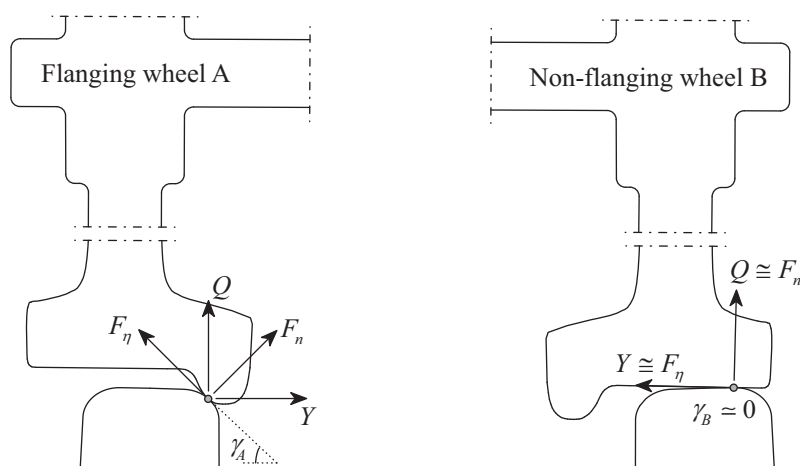
Figure 3.11 - Forces acting at the flanging and non-flanging wheel of the same axle.

3.5.1.4 Modified Nadal criterion based on the lateral impact duration

The Nadal criterion assumes that the flange climbing derailment occurs instantaneously once the Y/Q ratio limit is exceeded. However, numerical simulations performed by Ishida and Matsuo (1999) of a Shinkansen wheelset running at various speeds and considering different values of angles of attack and amplitudes of lateral force, showed that the derailments occurred only when the Y/Q ratio limit is exceeded for a certain period of time. In fact, the derailment of a railway vehicle due to flange climbing occurs only when the wheel rises more than 30 mm relative to the rail, which corresponds to the flange height (Nishimura et al., 2008). Thus, Ishida and Matsuo (1999) proposed a modified Nadal criterion based on the lateral impact duration.

The relation between the time duration in which the Y/Q ratio exceeds 1.0 and the height of wheel rise obtained in one of the numerical simulations performed by Ishida and Matsuo (1999) is presented in Figure 3.12. It can be observed that for the wheel to rise more than 30 mm in respect to the rail, the Y/Q ratio must exceed the limit value for nearly 0.1 s. Moreover, for impulsive loads in which the Y/Q ratio exceeds the limit value during a short period of time (around 0.01 s), the wheel lifts less than 0.5 mm, which is far below the derailment level. Thus, in order to obtain less conservative results with comparison to those obtained with the Nadal criterion, but at the same time, to guarantee the running safety of the vehicle against wheel flange climbing, Ishida and Matsuo (1999) set the Y/Q ratio limit at 0.8 and considered that the vehicle is in risk of derailment only when this limit is exceeded for more than 0.015 s. This period of time, in which the Y/Q ratio exceeds the limit, corresponds to a wheel lift of 1 mm, as shown in Figure 3.12. This modified Nadal criterion based on the lateral impact duration has been adopted by the Japanese standards to deal with the assessment of the train running safety.
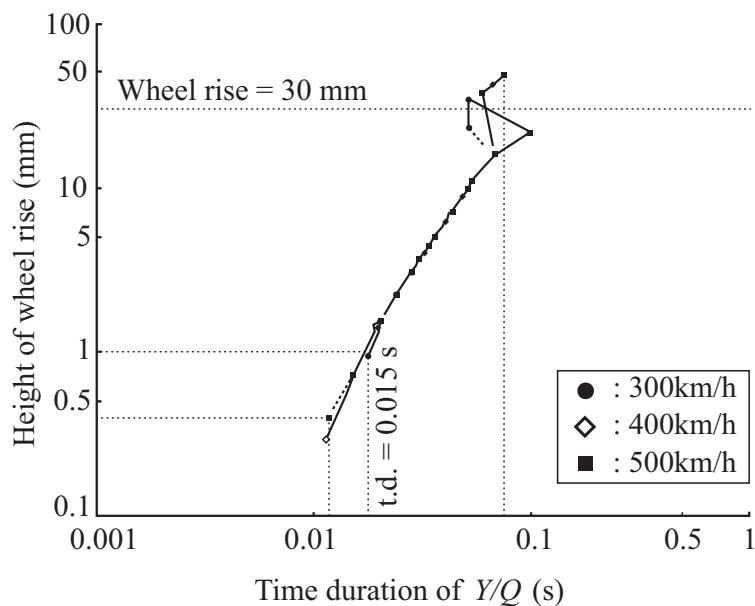
Figure 3.12 - Time duration of the *Y/Q* ratio versus the height of wheel rise obtained in the simulation of a Shinkansen wheelset running at different speeds (adapted from Ishida and Matsuo, 1999).

3.5.2 Track panel shift

3.5.2.1 Derailment mechanism

The track panel shift is the lateral displacement of the track panel, which includes the rails and the sleepers, over the ballast, as shown in Figure 3.13. As the cumulative lateral displacement of the track panel over the ballast increases, the wheels may lose guidance, resulting in one wheel falling between the rails and the other outside the track. This phenomenon is mainly caused by repeated lateral axle loads applied to the rails, and is associated with tracks that possess low lateral resistance, such as poorly laid tracks, newly laid tracks and newly maintained tracks, or with tracks laid over soft subgrades.

According to Elkins and Carter (1993) and Wu and Wilson (2006), the track panel shift phenomenon has become increasingly important with the increase of train speeds and loads. In fact, the increase in speed generally results in an increase in the unbalanced forces on curves or on poorly aligned tracks. These unbalanced forces act to force the rail outwards in a curve, resulting in panel shift and, consequently, leading to a higher risk of derailment. Moreover, the greater use of continuously welded rail also contributes for increasing the probability of panel shift due to the buckling phenomenon caused by temperature changes in the rails.
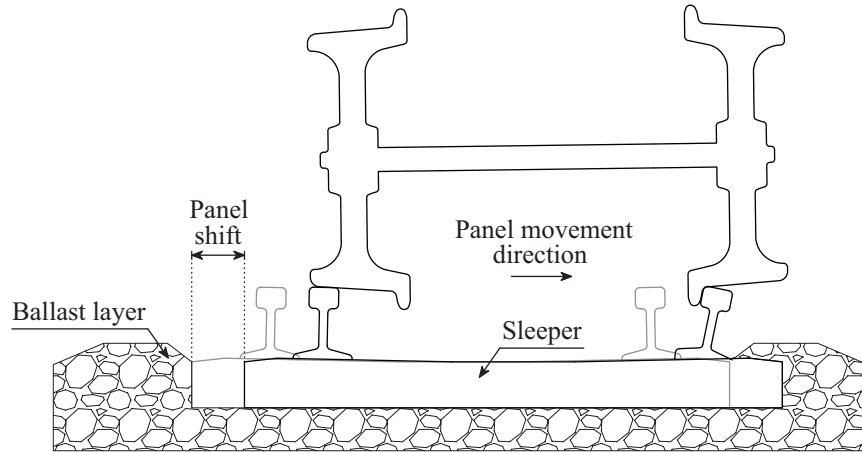
Figure 3.13 - Mechanism of derailment caused by track panel shift.

3.5.2.2 Prud'homme criterion

Research performed by the French National Railways Company (Sonneville and Bentot, 1955) suggested that the lateral load induced by a single wheelset should be limited to prevent excessive track panel shift. Subsequent research reported by Prud'homme (1967) specified the following criterion for limiting the total lateral force Y exerted by a wheelset on the track :

$$\sum_{ws} Y = 10 + \frac{2Q_0}{3} \, [\text{kN}]$$

(3.14)

where Q_0 is the static load per wheel in kilonewtons. The criterion is adopted in Europe by the TSI (2002). In this work, the Prud'homme factor ζ_P is expressed in a dimensionless form as

$$\zeta_P = \frac{\sum_{ws} Y \, [\text{kN}]}{10 + \frac{2Q_0}{3} \, [\text{kN}]}$$

(3.15)

3.5.3 Gauge widening caused by rail rollover

3.5.3.1 Derailment mechanism

A derailment caused by gauge widening usually involves the combination of wide gauges and large rail lateral deflections, mainly due to the rail rollover. The rail rollover is a result of important impacts between wheel and rail that occur when the wheelsets experience high angles of attack due to the poor steering of the bogie. These impacts lead to large lateral forces exerted on the rails that may deflect them further. This type of derailment may occur when the gauge faces of the two rails are spread enough to allow one of the wheels to drop between the rails, as illustrated in Figure 3.14.
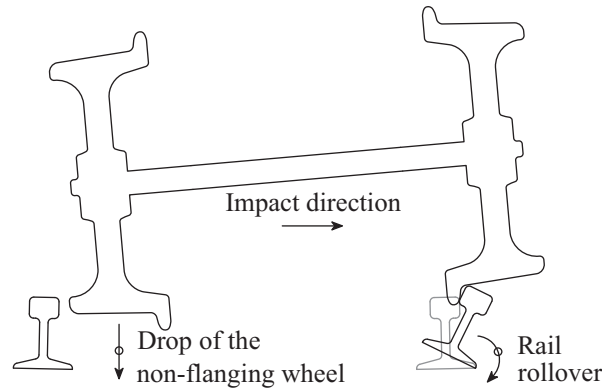
Figure 3.14 - Mechanism of derailment caused by rail rollover.

3.5.3.2 Rail roll criterion

The Manual of Standards of the AAR (AAR, 2011) reports a rail roll criterion based on the rotation mechanism of the rail about a pivot point *P* situated in the outward side corner of the foot of the rail, as shown in Figure 3.15. The overturning moment *M* about the pivot point *P* is given by

$$M = Y\,h - Q\,d \tag{3.16}$$

where *h* is the height of the rail and *d* the horizontal distance between the pivot point and the contact point (see Figure 3.15). Just before the rail starts to roll, the moment *M* tends to cancel, leading to the following *Y/Q* ratio limit to avoid the rail to roll:

$$\frac{Y}{Q} = \frac{d}{h} \tag{3.17}$$

Note that the *Y/Q* ratio presented in equation (3.17) does not account for the restraints provided by the rail fasteners and torsional stiffness of the rail section. However, according to Elkins and Carter (1993), during the development of the rail roll criterion, the torsional stiffness of the length of rail between wheels in close proximity proved to be significant. Therefore, the combined effects of all the wheels of the same side of the bogie are included in the criterion, thus giving

$$\zeta_R = \frac{\sum\limits_{bg\ side} Y}{\sum\limits_{bg\ side} Q} = \frac{d}{h} \tag{3.18}$$

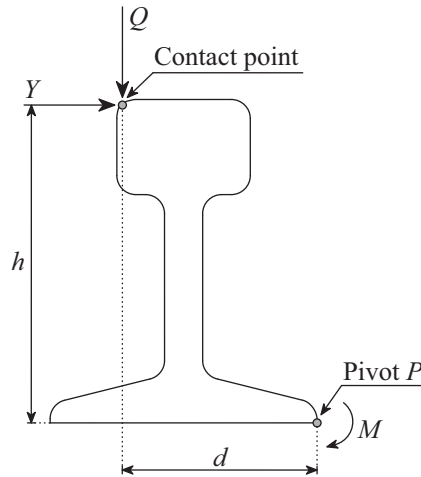where ζ_R is the rail roll factor and *bg* indicates bogie.

Figure 3.15 - Illustration of the rail roll criterion.

For typical rail sections used in the U.S.A., the *d/h* ration is about 0.6 when contact takes place in the gauge side of the rail. Thus, bogie side sum *Y/Q* ratio given by equation (3.18) should not exceed that value (AAR, 2011).

3.5.4 Wheel unloading

When the vibrations experienced by the vehicle are such that some wheels lose contact with the rail, a derailment by wheel unloading may occur. These severe vibrations, in both the vertical and the lateral directions, may be caused by several sources of excitation, such as track irregularities, earthquakes, crosswinds, among others.

The wheel unloading limit for the ratio between the reduction of the wheel vertical load ΔQ and the static load per wheel Q_0, referred to as the wheel unloading factor ζ_U, is given by

$$\zeta_U = \frac{\Delta Q}{Q_0} = \frac{Q_0 - Q}{Q_0} \tag{3.19}$$

where Q is the dynamic vertical load of the wheel. In a limit situation, in which a wheel loses the contact with the rail, the dynamic load is null, and the $\Delta Q/Q_0$ ratio becomes 1.0. However, to avoid such extreme situation, the limits to the wheel unloading ratio that can be found in the literature are less than 1.0 in the majority of the countries. In Europe, EN 14067-6 (2010), relative to aerodynamics in railway applications for crosswind assessment, specifies a limit value of 0.9 for the $\Delta Q/Q_0$ ratio. More conservative limits of 0.8 and 0.65 are adopted in Japan and China, respectively (Jun and Qingyuan, 2005; RTRI, 2006).

3.5.5 Summary of the running safety criteria

Table 3.1 presents a summary of the aforementioned running safety criteria, including the quantities calculated in each criterion, their theoretical and practical limits and the respective literature references.

Table 3.1 - Summary of the running safety criteria.

Derailment type	Criterion	Criterion factor	Physical meaning of the limit	Limit value	Reference
Flange climbing	Nadal	$\zeta_N = \dfrac{Y}{Q}$	$\dfrac{\tan\gamma - \mu}{1 + \mu\tan\gamma}$	0.8	Nadal (1908) TSI (2002)
	Weinstock	$\zeta_W = \sum_{ws}\dfrac{Y}{Q}$	$\dfrac{\tan\gamma_A - \mu_A}{1 + \mu_A \tan\gamma_A} + \mu_B$	1.5	Weinstock (1984) AAR (2011)
	Modified Nadal	$\zeta_N = \dfrac{Y}{Q}$ (0.015 s)	$\dfrac{\tan\gamma - \mu}{1 + \mu\tan\gamma}$	0.8	Ishida and Matsuo (1999)
Panel shift	Prud'homme	$\zeta_P = \dfrac{\sum_{ws} Y}{10 + \dfrac{2Q_0}{3}}$	$\dfrac{\sum_{ws} Y\,[\text{kN}]}{10 + \dfrac{2Q_0}{3}\,[\text{kN}]}$	1.0	Prud'homme (1967) TSI (2002)
Gauge widening	Rail roll	$\zeta_R = \dfrac{\sum_{bg\ side} Y}{\sum_{bg\ side} Q}$	$\dfrac{d}{h}$	0.6	AAR (2011)
Wheel unloading	Unloading	$\zeta_U = \dfrac{\Delta Q}{Q_0}$	$\dfrac{Q_0 - Q}{Q_0}$	0.9	EN 14067-6 (2010)

3.6 CONCLUDING REMARKS

A methodology for evaluating the running safety of trains on bridges is proposed (Montenegro et al., 2015a). The methodology consists of evaluating the risk of derailment using running safety criteria based on the wheel-rail contact forces, which are computed during the dynamic analysis of the train-structure system. Although the methodology is generalized to allow the safety assessment of trains under any kind of conditions, the present work focuses mainly on the running safety against earthquakes.

The procedure for generating the artificial accelerograms used to represent the seismic motion is introduced. Since the running safety of trains might be jeopardized not only by intense shakings, but also by moderate earthquakes, which may not cause significant damage to the structure, the artificial ground motions used in the present work correspond to moderate seismic events with relatively high probability of occurrence. Nevertheless, although the bridge piers are not expected to experience significant damage for these levels of seismicity, a methodology to account for the reduction in their stiffness due to concrete cracking is proposed. This methodology is divided in three main steps, culminating with the calibration of the effective stiffness of the cracked piers.

Track irregularities are also introduced as an important source of excitations to the vehicle in addition to the seismic action. The irregularity profiles are generated based on a stationary stochastic process described by PSD functions.

Finally, the main derailment mechanisms, namely the wheel flange climbing, track panel shift, rail rollover and wheel unloading, are presented together with the running safety criteria used to avoid each of these type of derailment.

Chapter 4

DEVELOPMENT OF A METHOD FOR ANALYZING THE DYNAMIC TRAIN-STRUCTURE INTERACTION

4.1 INTRODUCTION

This chapter presents the formulation of the train-structure interaction method developed in this work for evaluating the running safety of trains moving over bridges (Montenegro et al., 2015b). First, the contact element used to model the behavior of the contact interface between wheel and rail is presented. Then, a wheel-rail contact model is proposed to compute the internal forces of that element, which correspond to the contact forces that are generated in the contact interface. The algorithm associated with the contact model is divided into three main steps: 1) the geometric problem, consisting of the detection of the contact points; 2) the normal contact problem, in which the forces are determined based on the Hertz nonlinear theory and 3) the tangential contact problem, where the creep forces that appear due to the rolling friction contact are calculated using three distinct methods. Finally, the method used to couple the vehicle and the structure is presented. This method, referred to as the direct method (Neves et al., 2012; Neves et al., 2014), complements the governing equilibrium equations of the vehicle and structure with additional constraint equations that relate the displacements of the contact nodes of the vehicle to the corresponding nodal displacements of the structure. These equations form a single system, in which the unknowns are both displacements and contact forces. The proposed model is based on the finite element method, which allows the analysis of structures

and vehicles with any degree of complexity and the consideration of the deformations undergone by the two systems. The present formulation is implemented in MATLAB (2011). The vehicles and structure are modeled with ANSYS (2010), being their structural matrices imported by MATLAB.

4.2 WHEEL-RAIL CONTACT FINITE ELEMENT

4.2.1 Description of the element

In the majority of the currently available methods for analyzing the train-structure interaction, the normal and tangential contact forces are treated as external forces. However, it is generally more efficient to use a finite element formulation based on the contact laws for the normal and tangential directions. Therefore, a node-to-segment contact element that takes into account the behavior of the contact interface is proposed (see Figure 4.1).
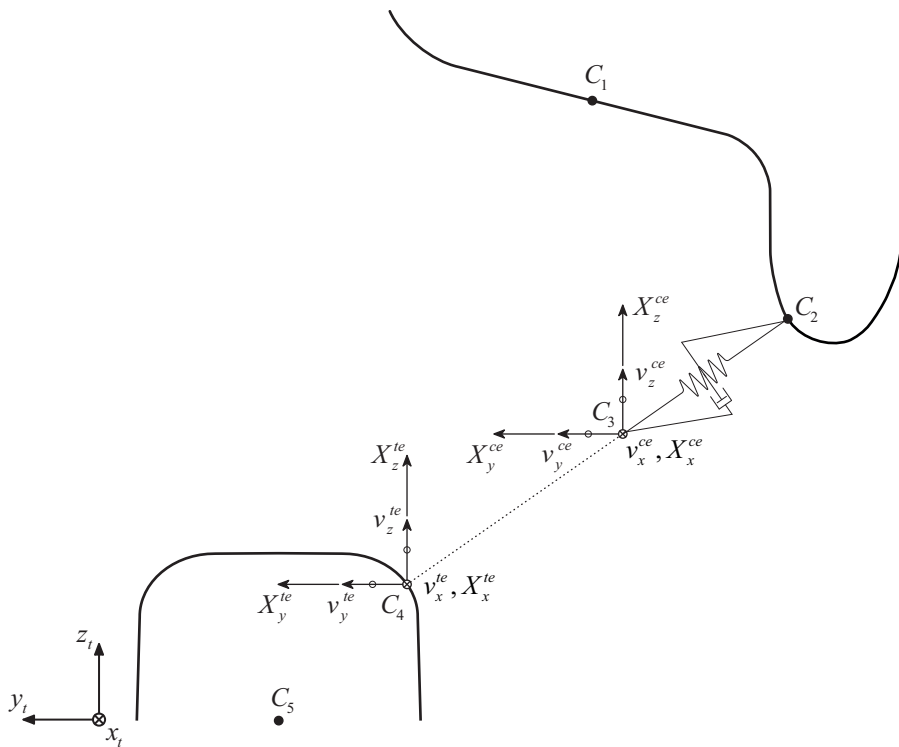
Figure 4.1 - Target and node-to-segment contact elements.

Figure 4.1 shows the forces **X** acting at the contact interface and the displacements **v** of the contact point, which are defined in the local coordinate system of the target element (x_t, y_t, z_t). The superscripts *ce* and *te* indicate contact and target elements, respectively. The x_t axis has the direction of the longitudinal axis of the target element, the y_t axis is parallel to the track plane

and the z_t axis completes the right-handed system. The node C_1 is a nodal point of the vehicle and the pilot point of the rigid surface of the wheel. The point C_5 is an auxiliary internal point of a target element of the structure and the pilot point of the rigid surface of the rail. The motions of the rigid surfaces of the wheel and rail are governed by the degrees of freedom of the corresponding pilot node. The auxiliary points C_2 and C_4 belong to the rigid surfaces of the wheel and rail, respectively. When contact occurs, the proposed enhanced node-to-segment contact element adds the internal node C_3 and the finite element connecting the point C_2 and the node C_3 in order to take into account the contact behavior in the normal and tangential directions, using the formulation described in Section 4.4.

When contact occurs, the node C_3 and the auxiliary point C_4 are coincident. The constraint equations that relate the displacements of these nodes are imposed using the direct method proposed by Neves et al. (2014), which is extended to deal with three-dimensional contact problems. Since in the proposed contact element there are no moments transmitted across the contact interface, the constraint equations only relate the translational displacements in the three directions. This approach is acceptable, since the creep spin moments as well as the moments caused by the lateral slip are small in comparison with other moments acting on the system (Polach, 1999). The relative motions between the wheel and rail are accounted by the finite element connecting the point C_2 and the node C_3. The irregularities present at the contact interface can be considered in the constraint equations for the vertical and lateral directions.

Since the auxiliary points C_4 and C_5 do not belong to the mesh of the structure, the constraint equations that relate the displacements of the auxiliary point C_4 and the node C_3, and the forces applied at the point C_4 have to be transformed in order to be associated with the degrees of freedom of the nodes of the target element. A similar transformation has to be applied to the finite element connecting the point C_2 and the node C_3 in order to be associated with the degrees of freedom of the node C_1.

4.2.2 Coordinate system of the element

The stiffness and damping matrices of the contact element depicted in Figure 4.1 are first calculated in the contact point coordinate system (x_c, y_c, z_c) illustrated in Figure 4.2 and then transformed to the global coordinate system. This local coordinate system follows the motion of the contact point, being its origin attached to the center of the contact area.
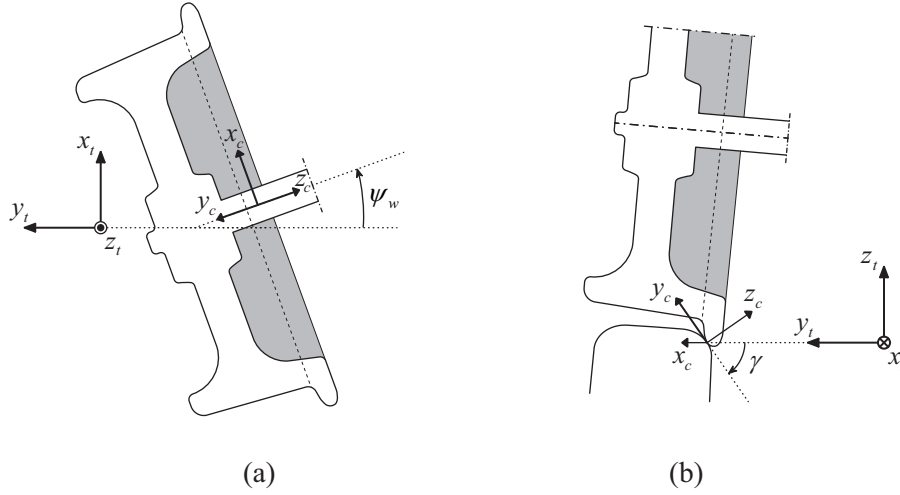
(a)   (b)

Figure 4.2 - Contact point coordinate system: (a) top view and (b) front view.

The z_c axis is oriented along the direction normal to the contact plane, the x_c axis points towards the longitudinal direction of motion and the y_c axis completes the right-handed system. The normal forces are defined along the z_c axis, and the longitudinal and lateral tangential forces are defined along the x_c and y_c axes, respectively. The yaw and contact angles are denoted by ψ_w and γ, respectively.

The transformation matrix $\mathbf{T}^{gc}$ from the global coordinate system to the contact point coordinate system is given by

$$\mathbf{T}^{gc} = \mathbf{T}_x^{tc}\, \mathbf{T}_z^{tc}\, \mathbf{T}^{gt} \tag{4.1}$$

where

$$\mathbf{T}_z^{tc} = \begin{bmatrix} \cos\psi_w & \sin\psi_w & 0 \\ -\sin\psi_w & \cos\psi_w & 0 \\ 0 & 0 & 1 \end{bmatrix} \tag{4.2}$$

$$\mathbf{T}_x^{tc} = \begin{bmatrix} 1 & 0 & 0 \\ 0 & \cos\gamma & \sin\gamma \\ 0 & -\sin\gamma & \cos\gamma \end{bmatrix} \tag{4.3}$$

The matrices $\mathbf{T}_z^{tc}$ and $\mathbf{T}_x^{tc}$ transform from the target element coordinate system to the contact point coordinate system, and correspond to a rotation of ψ_w about the z_t axis and a rotation of γ about the x_t, respectively. The matrix $\mathbf{T}^{gt}$ represents the standard transformation from the global coordinate system to the local coordinate system of the target element (Bathe, 1996).

The nodal forces $\mathbf{R}^c$ corresponding to the internal element stresses, the tangent stiffness matrix $\mathbf{K}^c$ and the tangent damping matrix $\mathbf{C}^c$ of the wheel-rail contact element are transformed from the local point coordinate system to the global coordinate system, according to

$$\mathbf{R}=\mathbf{T}^{gc^T}\mathbf{R}^c \tag{4.4}$$

$$\mathbf{K}=\mathbf{T}^{gc^T}\mathbf{K}^c\,\mathbf{T}^{gc} \tag{4.5}$$

$$\mathbf{C}=\mathbf{T}^{gc^T}\mathbf{C}^c\,\mathbf{T}^{gc} \tag{4.6}$$

where $\mathbf{T}^{gc}$ is the transformation matrix defined by equation (4.1). The superscript c indicates that the quantity is defined with respect to the contact point coordinate system.

4.3   GEOMETRIC CONTACT PROBLEM

4.3.1   Parameterization of the rail and wheel profiles

The calculation of the contact points depends on the correct representation of the wheel and rail surfaces and is a key point for obtaining an accurate solution of the contact problem. In the present formulation, the profile surfaces are parameterized as a function of surface parameters using piecewise cubic interpolation. The parameterization of each surface is performed using cubic splines, defined from a set of control points that are representative of the profile geometry.

In situations where the yaw rotation plays an important role, such as curve negotiations or railway turnouts, the wheel may contact the rail in two points located at different diametric sections, namely at the tread and the flange. In these circumstances, the flange contact point can be located ahead or behind the tread contact point, giving origin to lead or lag contact configurations, respectively (Pombo et al., 2007). Since only straight track scenarios are analyzed, this type of analysis is beyond the scope of the present thesis, restricting the contact point search to only one plane. Therefore, the geometric parameterization is formulated in terms of two surface parameters s_r and s_w that define the lateral location of the contact point in the rail and wheel, respectively, with respect to their local coordinate systems.

4.3.1.1 Coordinate systems of the rail and wheel profiles

The rail profile coordinate system (x_r, y_r, z_r) is fixed with the rail and has its origin at the point where the wheel contacts the rail when the wheelset is centered with the track. The y_r and z_r axes belong to the rail cross section plane, being the former oriented along the tangent to the surface at the contact point. The transformation from the target element coordinate system to the rail profile coordinate system is given by

$$\mathbf{T}^{tr} = \begin{bmatrix} 1 & 0 & 0 \\ 0 & \cos \phi_r & \sin \phi_r \\ 0 & -\sin \phi_r & \cos \phi_r \end{bmatrix} \tag{4.7}$$

where ϕ_r is the roll rotation of the rail about the target element longitudinal axis x_t.

The wheel profile coordinate system (x_w, y_w, z_w) has the same origin of the rail profile coordinate system, being the orientation defined by the roll rotation of the wheel about the x_t axis. Since the contact point search is restricted to only one plane, the yaw angle contribution is neglected in the geometric problem (Falomi et al., 2010; Tanabe et al., 2011; Antolín et al., 2012). Thus, the transformation from the target element coordinate system to the wheel profile coordinate system can be written as

$$\mathbf{T}^{tw} = \begin{bmatrix} 1 & 0 & 0 \\ 0 & \cos \phi_w & \sin \phi_w \\ 0 & -\sin \phi_w & \cos \phi_w \end{bmatrix} \tag{4.8}$$

where ϕ_w is the roll rotation of the wheel about the target element longitudinal axis x_t.

4.3.1.2 Parameterization of the rail profile

The two-dimensional surface geometry of the rail is described in terms of the surface parameter s_r, as depicted in Figure 4.3.
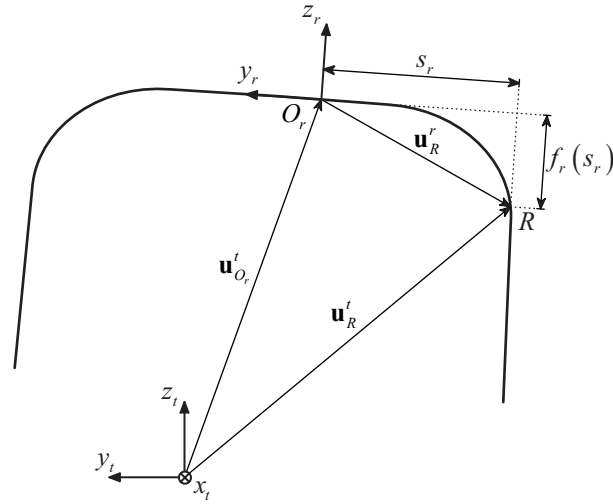
Figure 4.3 - Parameterization of the rail profile.

The position vector $\mathbf{u}_R^t$ of an arbitrary point R of the rail surface, defined with respect to the target element coordinate system, is given by

$$\mathbf{u}_R^t = \mathbf{u}_{O_r}^t + \mathbf{T}^{tr^T}\mathbf{u}_R^r \tag{4.9}$$

where $\mathbf{u}_{O_r}^t$ is the position vector of the origin of the rail profile coordinate system, defined with respect to the target element coordinate system, and $\mathbf{u}_R^r$ is the position vector of the arbitrary point of the rail surface defined in the rail profile coordinate system, written as

$$\mathbf{u}_R^r = \begin{bmatrix} 0 & s_r & f_r(s_r) \end{bmatrix}^T \tag{4.10}$$

in which $f_r(s_r)$ is the function defining the rail surface.

In the implemented wheel-rail contact method, the normal and tangent vectors to the rail surface at the contact point are necessary to calculate its location. The tangent vector to the rail surface at the contact point along the lateral direction $\mathbf{t}_{r,y}^t$ defined with respect to the target element coordinate system is given by

$$\mathbf{t}_{r,y}^t = \mathbf{T}^{tr^T}\mathbf{t}_{r,y}^r \tag{4.11}$$

where the tangent vector $\mathbf{t}_{r,y}^r$, defined with respect to the rail profile coordinate system, is obtained by differentiating the rail surface function with respect to the surface parameter, i.e.,

$$\mathbf{t}_{r,y}^r = \begin{bmatrix} 0 & 1 & \dfrac{df_r(s_r)}{ds_r} \end{bmatrix}^T \tag{4.12}$$

79

Since the location of the contact point is determined through a planar geometric analysis, the tangent vector along the longitudinal direction $\mathbf{t}_{r,x}^t$ has the same direction as the x_t axis. The normal vector to the rail surface $\mathbf{n}_r^t$ at the contact point defined with respect to the target element coordinate system is given by

$$\mathbf{n}_r^t = \mathbf{t}_{r,x}^t \times \mathbf{t}_{r,y}^t \tag{4.13}$$

with $\mathbf{n}_r^t$ pointing outwards from the surface.

Finally, the contact angle γ, defined between the lateral tangent vector and the track plane, is given by

$$\gamma = \tan^{-1}\left(\frac{df_r(s_r)}{ds_r}\right) + \phi_r \tag{4.14}$$

Notice that the roll rotation ϕ_r is the angle between the rail profile coordinate system and the target element coordinate system.

4.3.1.3 Parameterization of the wheel profile

The present method allows the detection of two contact points between the wheel and rail. To this end, the wheel is parameterized by two functions, one for the tread $f_{w,t}$ and another for the flange $f_{w,f}$, making the location of the contact points in each region of the wheel fully independent. The division between tread and flange is made in the point with maximum concave curvature, as shown in Figure 4.4. The contact point and the point with maximum concave curvature are denoted by *cp* and *mc*, respectively.
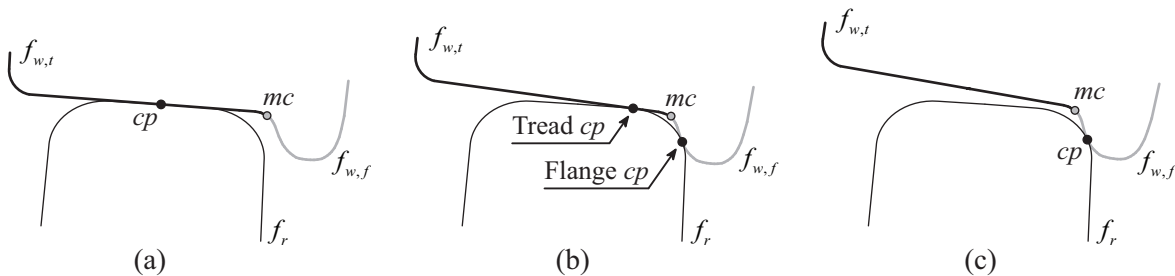

Figure 4.4 - Division into tread and flange: (a) tread contact, (b) double contact and (c) flange contact.

Figure 4.5 shows the parameterization of the wheel profile in terms of a single surface parameter s_w to clarify the illustration. However, each of the aforementioned functions that define the wheel surface is defined by an independent surface parameter.
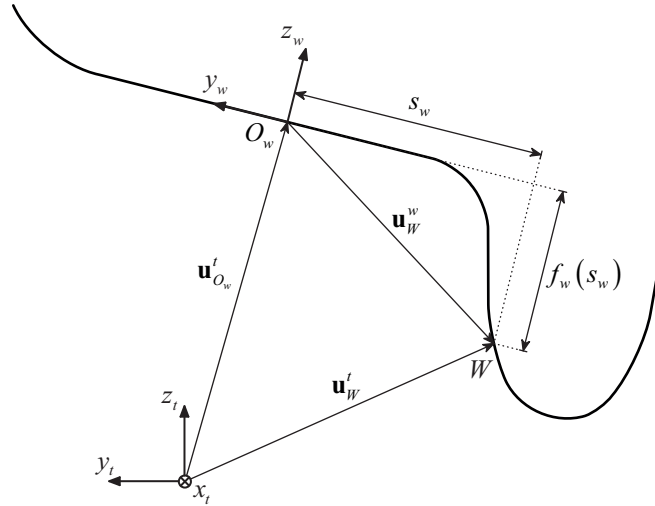
Figure 4.5 - Parameterization of the wheel profile.

The position vector $\mathbf{u}_W^t$ of an arbitrary point W of the wheel surface, defined with respect to the target element coordinate system, is given by

$$\mathbf{u}_W^t = \mathbf{u}_{O_w}^t + \mathbf{T}^{tw^T} \mathbf{u}_W^w \qquad (4.15)$$

in which $\mathbf{u}_{O_w}^t$ is the position vector of the origin of the wheel profile coordinate system, defined with respect to the target element coordinate system, and $\mathbf{u}_W^w$ is the position vector of the arbitrary point of the wheel surface defined in the wheel profile coordinate system, written as

$$\mathbf{u}_W^w = \begin{bmatrix} 0 & s_w & f_w(s_w) \end{bmatrix}^T \qquad (4.16)$$

where $f_w(s_w)$ is the function defining the wheel surfaces.

The tangent and normal vectors to the wheel surface at the contact point, $\mathbf{t}_{w,y}^t$ and $\mathbf{n}_w^t$, defined with respect to the target element coordinate system, are calculated in an analogous way as in Section 4.3.1.2.

4.3.2 Contact point search

After defining the surfaces of the contacting bodies, the next step of the geometric problem consists of determining the position of the contact points between the wheel and the rail. In the present work, two algorithms for the detection of contact points are implemented. The first algorithm is used to detect the position of contact points lying on convex regions of the surfaces (see Section 4.3.2.1), while the second one is applied when the contact point is located on concave regions (see Section 4.3.2.2), as illustrated in Figure 4.6. Although the latter approach

is not restricted to concave regions, its higher computational cost makes it less attractive to solve the geometric problem than the convex contact search algorithm. Therefore, the concave contact search is performed only if the convex contact algorithm fails to find a single solution on a convex region, as explained later in Section 4.3.2.2. In the particular case of wheel-rail contact, if no wear is present, the only concave region is located on the wheel profile, in the transition zone between the tread and the flange.
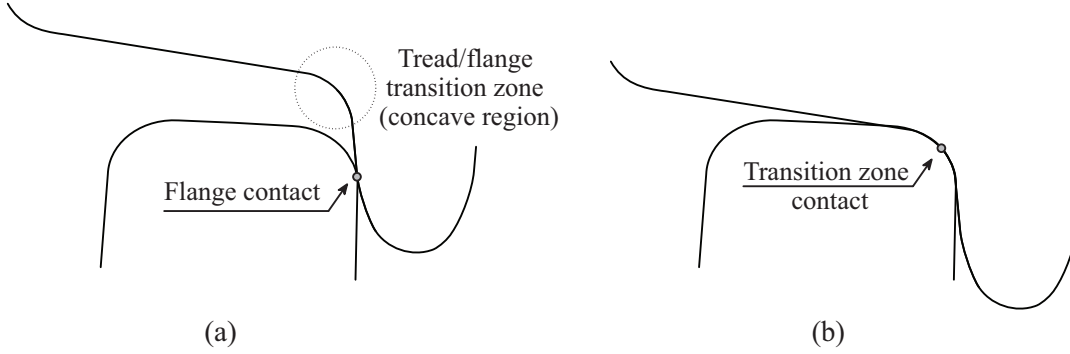

(a)   (b)

Figure 4.6 - Contact point between wheel and rail: (a) contact in a convex region and (b) contact in a concave region.

4.3.2.1 Convex contact search

To determine the location of the potential contact points between the wheel and rail in convex regions, the following set of nonlinear equations is used:

$$\begin{cases} \mathbf{t}_{r,y}^{t} \cdot \mathbf{d}_{wr}^{t} = 0 \\ \mathbf{t}_{w,y}^{t} \cdot \mathbf{n}_{r}^{t} = 0 \end{cases} \tag{4.17}$$

where $\mathbf{t}_{r,y}^{t}$, $\mathbf{t}_{w,y}^{t}$ and $\mathbf{n}_{r}^{t}$ are defined in Section 4.3.1 and $\mathbf{d}_{wr}^{t}$ is the vector that defines the relative position of the point of the wheel with respect to the point of the rail (see Figure 4.7), given by

$$\mathbf{d}_{wr}^{t} = \mathbf{u}_{W}^{t} - \mathbf{u}_{R}^{t} \tag{4.18}$$

where $\mathbf{u}_{W}^{t}$ and $\mathbf{u}_{R}^{t}$ are given by equations (4.15) and (4.9). The first condition described by equation (4.17) ensures that the tangent vector to the rail is perpendicular to the vector defining the relative position of the point of the wheel with respect to the point of the rail. The second condition ensures that the normal vector to the rail is perpendicular to the tangent vector to the wheel, as depicted in Figure 4.7.
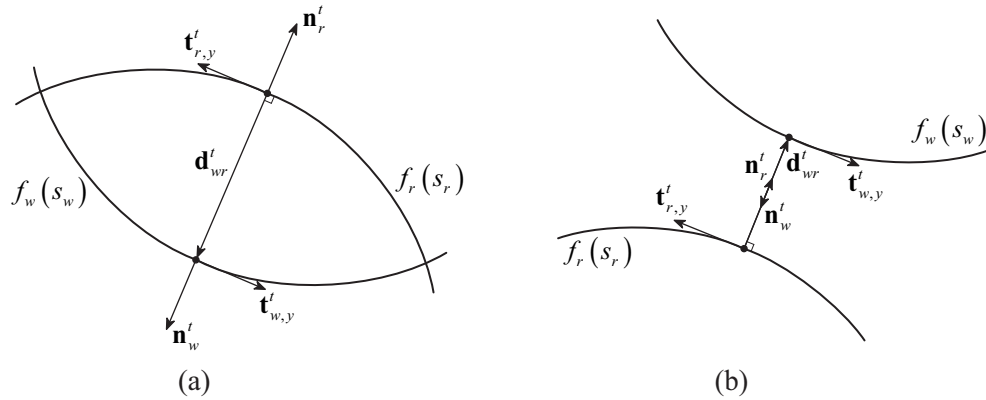
Figure 4.7 - Potential contact points between the two surfaces: (a) contact and (b) no contact.

In the present formulation, an internal function of MATLAB is used to solve the nonlinear algebraic equations (4.17). This function uses an iterative scheme based on the Newton method together with a trust-region technique to improve the robustness of the algorithm and handle situations where the Jacobian matrix of the algebraic equations is singular.

The system of equations (4.17) may have multiple solutions if one of the contact surfaces is not convex. This may occur if the potential contact point lies on the concave regions that exist in the transition between the wheel tread and flange (the rail surface is assumed to be always convex). Therefore, after solving the system of equations (4.17), the algorithm checks the convexity sign of the wheel surface at the calculated potential contact point by computing its curvature κ_{w,y_c} along the lateral direction y_c of the contact point coordinate system (see Figure 4.2). According to Garg and Dukkipati (1984), the radius of curvature of a surface is considered to be positive if the corresponding center of curvature is within the body, i.e., if the surface is convex. Thus, the potential contact point lies on a convex region if the following condition is fulfilled:

$$\kappa_{w,y_c} > 0 \tag{4.19}$$

otherwise, the potential contact point lies on a concave region and the solution obtained with the system of equations (4.17) is discarded. When this situation occurs, the concave contact search algorithm, presented in Section 4.3.2.2, is used to determine the actual position of the contact point. The calculation of the curvature of the contacting surfaces is described later in Section 4.4.2.

The final condition which the potential contact points lying in a convex region have to fulfill is that the parametric surfaces have to intersect each other. As shown in Figure 4.7b, the

conditions described in equation (4.17) are satisfied but there is no contact. This condition can be expressed mathematically as

$$\mathbf{d}_{wr}^{t} \cdot \mathbf{n}_{r}^{t} \leq 0 \tag{4.20}$$

which means that the intersection between two bodies is guaranteed only if the vectors $\mathbf{d}_{wr}^{t}$ and $\mathbf{n}_{r}^{t}$ point in opposite directions, as shown in Figure 4.7a. The penetration d between the two bodies in contact is given by

$$d = \left\| \mathbf{d}_{wr}^{t} \right\| \tag{4.21}$$

Since the contact point detection is a nonlinear problem, an initial estimate for the solution has to be given to start the iterative process. In most cases, in order to reduce the number of iterations, the solution obtained in the previous iteration/step is used as an initial guess to solve the current iteration. However, if flange contact occurs, the contact point position suffers an abrupt jump from the tread to the flange and the previous obtained solution may not be an appropriate estimation for the current iteration. This can cause the solution to converge very slowly or even diverge. Therefore, an accurate prediction of jumps in the contact point position leads to a faster solution and eliminates some of the causes responsible for convergence problems during the contact solver.

The contact point jump detection proposed in this paper consists of precalculating a lookup table, similar to those used in the multibody formulations (Santamaria et al., 2006; Tanabe et al., 2008; Bozzone et al., 2011; Antolín et al., 2012). These lookup tables follow the assumption of a rigid contact between wheel and rail, in which the surface parameters that define the contact point position can be computed as a function of the relative lateral displacement between the center of mass of the wheelset and the track centerline. Thereafter, the proposed table can predict if there is a contact point in the flange for a given relative lateral displacement. Since the proposed model is based on the finite element method instead of a multibody formulation, this table is only used to estimate if there is flange contact. If so, the surface parameters obtained by table interpolation are used as an initial guess to detect the potential new flange contact point. This procedure leads to a more accurate initial estimate of the solution and, consequently, to a higher convergence rate when solving the nonlinear algebraic equations (4.17). The procedure for implementing the contact lookup table is described in Appendix A.

4.3.2.2 Concave contact search

The concave contact approach consists of determining the location of the contact points in the regions where the convex contact approach cannot find a single solution, i.e., in concave surfaces (see condition (4.19)). Unlike the algorithm used in the convex contact approach, the accuracy of this algorithm depends on the degree of discretization of the profiles. Therefore, although this approach may also be used to locate the contact points in convex regions, the high computational cost that is required to achieve a good solution makes it computationally less attractive. As a result, the concave contact approach is used only if the convex approach finds a solution that lies in a concave region.

In the concave contact search approach, the rail and wheel surfaces are discretized in n_r and n_w points, respectively. This discretization is performed by interpolating the profile functions described in Section 4.3.1, being the position vectors of each point in the rail and wheel surfaces given by equations (4.9) and (4.15), respectively. Hence, the evaluation of the potential contact between the two surfaces consists of determining if any of these points lie inside the opposite surface, forming the so-called intersection volume, illustrated in Figure 4.8.

To determine which points belong to the intersection volume, the points belonging to the rail surface are projected into the wheel surface and vice-versa. Then, the vertical distances between the points of each surface and the respective projection on the other surface, $h_{r,i}$ and $h_{w,j}$, are computed as

$$h_{r,i} = \left(\mathbf{u}_{r,i}^t - \overline{\mathbf{u}}_{r,i}^t \right) \cdot \mathbf{e}_{z_t} , \quad i = 1, 2, \ldots, n_r \tag{4.22a}$$

$$h_{w,j} = \left(\overline{\mathbf{u}}_{w,j}^t - \mathbf{u}_{w,j}^t \right) \cdot \mathbf{e}_{z_t} , \quad j = 1, 2, \ldots, n_w \tag{4.22b}$$

where $\overline{\mathbf{u}}_{r,i}^t$ and $\overline{\mathbf{u}}_{w,j}^t$ are the position vectors of the projections along the vertical direction of the ith rail point into the wheel surface and of the jth wheel point into the rail surface (see Figure 4.8), respectively, defined with respect to the target element coordinate system, $\mathbf{u}_{r,i}^t$ and $\mathbf{u}_{w,j}^t$ are defined by equations (4.9) and (4.15), respectively, and $\mathbf{e}_{z_t}$ is a unit base vector of the target element coordinate system. The point i of the rail surface and the point j of the wheel surface belong to the intersection volume if the following conditions are fulfilled, respectively:

$$h_{r,i} > 0 \tag{4.23a}$$
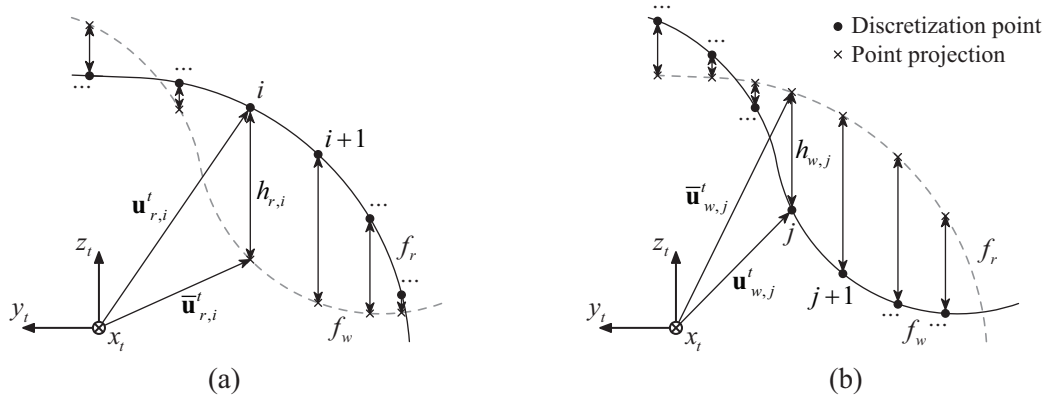
$$h_{w,j} > 0 \qquad\qquad (4.23b)$$

Figure 4.8 - Intersection volume: (a) projection of rail points and (b) projection of wheel points.

If there are no points belonging to the intersection volume, the bodies are not in contact and the potential contact point is discarded from further considerations. On the other hand, when contact is detected, each point of one of the surfaces belonging to the intersection volume has a potential contact pair in the other surface. Thus, the potential contact pair of a given point of the rail surface belonging to the intersection volume is the closest point of the wheel surface, which also belongs to the intersection volume, and vice-versa. The distance d_i between the ith rail point belonging to the intersection volume and the point of the wheel surface j that forms the potential contact pair is given by

$$d_i = \min_j \left\{ \sqrt{ \left[\left(\mathbf{u}_{r,i}^t - \mathbf{u}_{w,j}^t \right) \cdot \mathbf{e}_{y_t} \right]^2 + \left[\left(\mathbf{u}_{r,i}^t - \mathbf{u}_{w,j}^t \right) \cdot \mathbf{e}_{z_t} \right]^2 } \right\}, \quad i=1,\ldots,n_r^{IV} \ \text{and} \ j=1,\ldots,n_w^{IV} \quad (4.24)$$

where n_r^{IV} and n_w^{IV} are, respectively, the number of points of the rail and wheel surfaces which belong to the intersection volume.

Finally, out of all the pairs giving the maximum distance between the rail point and the correspondent wheel point, the pair where contact occurs is the one that leads to the maximum penetration d, given by

$$d = \max \{ d_i \}, \quad i = 1,\ldots, n_r^{IV} \qquad\qquad (4.25)$$

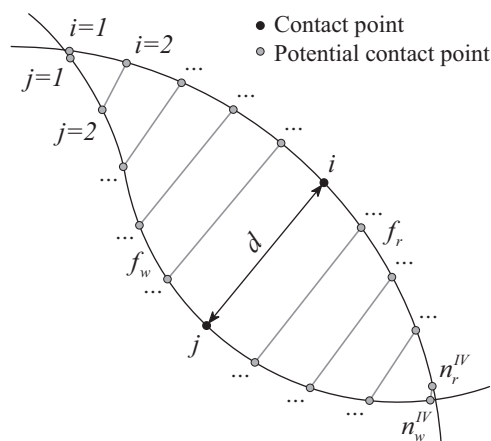A schematic representation of the selection of the contact pair ij is depicted in Figure 4.9.

Figure 4.9 - Contact pair selection.

4.4 NORMAL CONTACT PROBLEM

4.4.1 Hertz contact theory

When two non-conforming bodies are compressed against each other they will deform in the vicinity of the point of first contact, touching over an area that is small when compared with the dimensions of those bodies and with the relative radii of curvature of the surfaces. On the other hand, if the shape of the bodies fit exactly at the contact region, a conformal contact occurs, i.e., the contact between those bodies is not restricted to only one point. In the present method, the normal contact problem is analyzed based on the nonlinear Hertz theory (Hertz, 1882).

According to the Hertz theory, the contact area between two contacting bodies is elliptical and the pressure distribution assumes a semi-ellipsoidal shape, being the normal stresses null at the edges of the contact area and maximum at the center. The assumptions used in the Hertz theory can be summarized as follows:

a) The surfaces of the bodies are continuous and non-conformal;

b) The surfaces are frictionless;

c) The longitudinal and lateral curvatures of the bodies are constant along the contact area;

d) The contacting bodies are elastic, and no plastic deformations occur in the contact area;

e) The stresses caused by the contact force vanish at a distance far from the contact area;

f) The contacting bodies can be considered as elastic half-spaces.

Note that, in a wheel-rail contact problem, the assumptions of the Hertz theory are not met, since the surfaces of the contacting bodies are not totally frictionless and may be conforming.

Moreover, the wheel and rail profiles may have non-constant curvatures in the contact area and plastic deformations may occur in the contact zone. Nevertheless, in most railway applications, the Hertz theory seems to be sufficiently adequate for the computation of the normal contact forces during a dynamic analysis (Andersson et al., 1999). More complex and realistic contact shapes may be necessary for analyzing local problems, such as wear. However, this is out of the scope of the present thesis.

4.4.2 Geometry of the surfaces in contact

Following the aforementioned assumptions, Hertz assumed that the surfaces of the contacting bodies (see Figure 4.10) may be expressed as

$$z_1 = A_1\, x_1^2 + B_1\, y_1^2 \tag{4.26a}$$

$$z_2 = A_2\, x_2^2 + B_2\, y_2^2 \tag{4.26b}$$

where x_i and y_i are the directions of the principal curvatures of body i and A_i and B_i are constants that depend on the body i geometry ($i = 1, 2$). The gap between the two bodies is defined as

$$h = z_1 - z_2 \tag{4.27}$$

which can be rewritten as

$$h = A\,x^2 + B\,y^2 + C\,x\,y \tag{4.28}$$

where x and y are the directions which form an angle α and β with the principal directions of the bodies 1 and 2, respectively (see Figure 4.10).
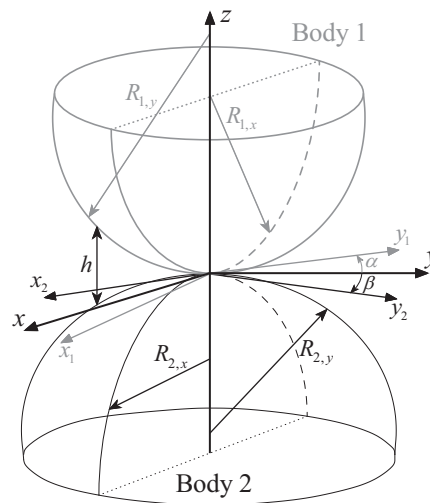

Figure 4.10 - Two bodies in contact and their respective principal directions and radii of curvature.

Considering the principal radii of curvature of the surfaces (see Figure 4.10), equations (4.26) and (4.28) are rewritten in the form

$$z_1 = \frac{1}{2\,R_{1,x}}\,x_1^2 + \frac{1}{2\,R_{1,y}}\,y_1^2 \tag{4.29a}$$

$$z_2 = \frac{1}{2\,R_{2,x}}\,x_2^2 + \frac{1}{2\,R_{2,y}}\,y_2^2 \tag{4.29b}$$

$$h = \frac{1}{2\,R_x}\,x^2 + \frac{1}{2\,R_y}\,y^2 + C\,xy \tag{4.30}$$

where $R_{i,x}$ and $R_{i,y}$ are the principal radii of curvature of the body i ($i = 1, 2$) and R_x and R_y are the principal relative radius of curvature.

The angles α and β may be calculated by eliminating the quadratic term xy from equation (4.30). Using this, in addition to the equation (4.29), the following relations are obtained (Hertz, 1882; Johnson, 1985; Shabana et al., 2008)

$$B - A = \frac{1}{2}\left(\frac{1}{R_{1,x}} - \frac{1}{R_{1,y}}\right)\cos(2\alpha) + \frac{1}{2}\left(\frac{1}{R_{2,x}} - \frac{1}{R_{2,y}}\right)\cos(2\beta) \tag{4.31a}$$

$$A + B = \frac{1}{2}\left(\frac{1}{R_{1,x}} + \frac{1}{R_{2,x}} + \frac{1}{R_{1,y}} + \frac{1}{R_{2,y}}\right) \tag{4.31b}$$

When the relative yaw rotations between wheel and rail are small, which occurs in the majority of the wheel-rail contact problems, the α and β angles may be neglected (Antolín, 2013). With this assumption, the geometric parameters A and B are given by

$$A = \frac{1}{2}\left(\frac{1}{R_{1,x}} + \frac{1}{R_{2,x}}\right) \tag{4.32a}$$

$$B = \frac{1}{2}\left(\frac{1}{R_{1,y}} + \frac{1}{R_{2,y}}\right) \tag{4.32b}$$

Note that in this case, the principal directions x and y coincide with the principal directions of both contacting bodies.

The radius of curvature is defined as the inverse of the curvature in the respective direction. Thus, taking the body 1 and 2 as the wheel and rail, respectively, and the principal directions x

and y as the directions x_c and y_c of the contact point coordinate system (see Figure 4.2), the principal curvatures κ of both surfaces measured along the longitudinal direction are given by

$$\kappa_{r,x_c} = \frac{1}{R_{r,x_c}} = \frac{\cos(\gamma - \phi_w)}{R} \tag{4.33a}$$

$$\kappa_{w,x_c} = \frac{1}{R_{w,x_c}} \approx 0 \tag{4.33b}$$

where γ and ϕ_w are, respectively, the contact angle defined in equation (4.14) and the roll rotation between the wheel profile coordinate system and the target element coordinate system (see Section 4.3.1.1), and R is the instantaneous radius of the wheel. Notice that the curvature of the rail in the longitudinal direction is null due to its prismatic shape.

The curvatures of the wheel and rail surfaces measured along the lateral direction at the contact point are calculated using the parameterization functions $f_r(s_r)$ and $f_w(s_w)$ defined in equations (4.10) and (4.16), respectively. The curvature of a plane curve defined parametrically in a Cartesian system (x, y) is given by (Kreyszig, 1991)

$$\kappa = \frac{d^2 y / d x^2}{\left[1 + (d y / d x)^2\right]^{3/2}} \tag{4.34}$$

Thus, the principal curvatures of both surfaces in the lateral direction are expressed as

$$\kappa_{r,y_c} = \frac{1}{R_{r,y_c}} = \frac{d^2 f_r(s_r) / d s_r^2}{\left[1 + (d f_r(s_r) / d s_r)^2\right]^{3/2}} \tag{4.35a}$$

$$\kappa_{w,y_c} = \frac{1}{R_{w,y_c}} = \frac{d^2 f_w(s_w) / d s_w^2}{\left[1 + (d f_w(s_w) / d s_w)^2\right]^{3/2}} \tag{4.35b}$$

The radius of curvature of a surface is considered to be positive if the corresponding center of curvature is within the body, i.e., if the surface is convex (Garg and Dukkipati, 1984).

4.4.3   Normal contact pressure

According to the Hertz solution, the contact area has an elliptical shape with semi-axes a and b in the longitudinal and lateral directions, respectively, being the pressure distribution σ defined as a semi-ellipsoid function given by (Hertz, 1882; Johnson, 1985; Shabana et al., 2008)

$$\sigma(x_c, y_c) = \frac{3F_n}{2\pi\,ab}\sqrt{1-\left(\frac{x_c}{a}\right)^2 - \left(\frac{y_c}{b}\right)^2} \tag{4.36}$$

where x_c and y_c are the coordinates of each point of the contact area with respect to the contact point coordinate system, and F_n is the normal contact force applied at the contact interface when the two bodies are compressed against each other. The semi-axes of the contact ellipse can be calculated as

$$a = m\sqrt[3]{\frac{3}{2}F_n\frac{1-v^2}{E}\frac{1}{A+B}} \tag{4.37a}$$

$$b = n\sqrt[3]{\frac{3}{2}F_n\frac{1-v^2}{E}\frac{1}{A+B}} \tag{4.37b}$$

where E and v are the Young modulus and the Poisson's ratio of the contacting bodies, respectively, and A and B are the geometric parameters given by equation (4.32). Note that the semi-axes calculated using equation (4.37) correspond to the particular case in which the bodies are made from the same material, which is reasonable in wheel-rail contact applications since both the wheel and the rail are made from steel. The coefficients m and n may be found in Appendix B as a function of the angular parameter θ, defined as

$$\theta = \cos^{-1}\left(\frac{B-A}{A+B}\right) \tag{4.38}$$

Finally, the nonlinear Hertz contact law can be defined as follows

$$F_n = K_h\,d^{3/2} \tag{4.39}$$

where d is the penetration between the two contacting bodies given by equations (4.21) or (4.25), depending on the contact search algorithm used, and K_h is a generalized stiffness coefficient given by (Goldsmith, 1960)

$$K_h = \frac{2}{3}\frac{C_h}{\left(\dfrac{1-v^2}{\pi E}\right)\sqrt{A+B}} \tag{4.40}$$

in which C_h is a Hertz constant that may be found in Appendix B as a function of the ratio A/B. The generalized stiffness coefficient expressed in equation (4.40) corresponds to the particular case in which the bodies are made from the same material.

4.5 TANGENTIAL CONTACT PROBLEM

4.5.1 Creep phenomenon

If two bodies that are compressed against each other are allowed to roll over each other, some points on the contact area may slip while others may adhere (see Figure 4.11). The difference between the tangential strains of the bodies in the adhesion area leads to a small apparent slip, called creep. The creep, which depends on the relative velocities of the two bodies at the contact point, is crucial for the determination of the tangential forces that develop in the contact area, called creep forces. Hence, the creep may be defined as a combined elastic and frictional behavior in which two elastic bodies that roll over each other share a contact area where both slip and adhesion occur simultaneously. This phenomenon was recognized for the first time by Carter (1926).

A typical distribution of normal and tangential stresses inside an elliptical contact area Γ defined by the Hertz theory is illustrated in Figure 4.11.
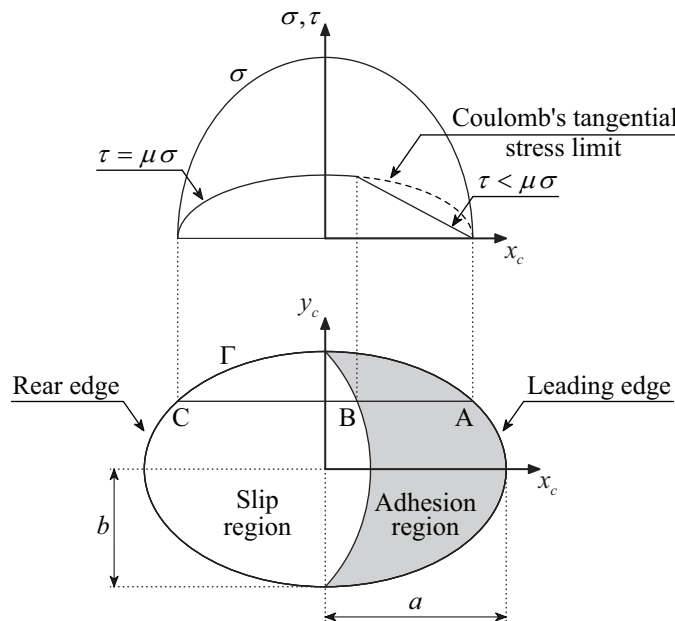

Figure 4.11 - Distribution of normal and tangential stresses inside the contact area.

Let ABC be a line inside the contact ellipse along the longitudinal direction. The tangential stresses τ, which are null in the leading edge (point A), tend to grow as approaching the limit of the Coulomb law τ_{lim} in point B, given by

$$\tau_{\text{lim}} = \mu \sigma \qquad (4.41)$$

where μ is the friction coefficient and σ the normal stresses given by equation (4.36). In this region of the contact area, called adhesion region, the wheel and rail stick to each other, being their relative displacements fully compensated by the elastic strain of the bodies. However, from point B to point C, the normal stresses are no longer capable of supporting the strains and the wheel and rail start to slide, forming the slip region of the contact area in which relative motions between the two bodies occur.

4.5.2 Basic equations of the rolling contact

The relative velocity between wheel and rail at the contact area may be determined as a function of three dimensionless parameters, called creepages, defined with respect to the contact point coordinate system presented in Figure 4.2. These are the longitudinal creepage υ_ξ, the lateral creepage υ_η and the angular slip velocity around an axis perpendicular to the contact area, called spin creepage υ_ϕ, as depicted in Figure 4.12. The creepages are necessary for the calculation of the tangential forces that develop in the contact area, called creep forces.
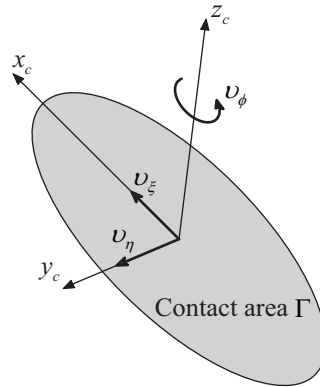

Figure 4.12 - Orientation of the creepages with respect to the contact point coordinate system.

The longitudinal and the lateral creepages are the relative velocities between the wheel and rail at the contact point along the x_c and y_c axes, respectively, normalized to the vehicle's speed V, given by

$$\upsilon_\xi = \frac{\left(\dot{\mathbf{a}}_w - \dot{\mathbf{a}}_r\right)\cdot\mathbf{e}_{x_c}}{V} \tag{4.42a}$$

$$\upsilon_\eta = \frac{\left(\dot{\mathbf{a}}_w - \dot{\mathbf{a}}_r\right)\cdot\mathbf{e}_{y_c}}{V} \tag{4.42b}$$

where $\dot{\mathbf{a}}_w$ and $\dot{\mathbf{a}}_r$ are the vectors of translational velocities of the wheel and rail at the contact point, respectively, defined with respect to the global coordinate system, and $\mathbf{e}_{x_c}$ and $\mathbf{e}_{y_c}$ are unit base vectors of the contact point coordinate system.

The spin creepage is the relative angular velocity between the wheel and rail at the contact point about the z_c axis normalized to the vehicle's speed, given by

$$v_\phi = \frac{(\dot{\boldsymbol{\omega}}_w - \dot{\boldsymbol{\omega}}_r) \cdot \mathbf{e}_{z_c}}{V} \tag{4.43}$$

in which $\dot{\boldsymbol{\omega}}_w$ and $\dot{\boldsymbol{\omega}}_r$ are the vectors of rotational velocities of the wheel and rail at the contact point, respectively, defined with respect to the global coordinate system, and $\mathbf{e}_{z_c}$ is a unit base vector of the contact point coordinate system.

Using the creepages defined in equations (4.42) and (4.43), the rigid body slip $\dot{\mathbf{r}}$ at each point of the contact area is found to be (Garg and Dukkipati, 1984; Kalker, 1990)

$$\dot{\mathbf{r}}(x_c, y_c) = \begin{bmatrix} \dot{r}_{x_c} \\ \dot{r}_{y_c} \end{bmatrix} = \begin{bmatrix} V(v_\xi - v_\phi y_c) \\ V(v_\eta + v_\phi x_c) \end{bmatrix} \tag{4.44}$$

where x_c and y_c are the coordinates of an arbitrary point of the contact area with respect to the contact point coordinate system. Furthermore, as a consequence of compressive and frictional forces in the contact area, local elastic deformations occur in the wheel and rail surfaces. Thus, the relative tangential elastic displacements $\mathbf{v}$ at each point of the contact area may be expressed as (Kalker, 1990)

$$\mathbf{v}(x_c, y_c) = \begin{bmatrix} v_{x_c} \\ v_{y_c} \end{bmatrix} = \mathbf{v}_w(x_c, y_c) - \mathbf{v}_r(x_c, y_c) \tag{4.45}$$

where $\mathbf{v}_w$ and $\mathbf{v}_r$ are, respectively, the elastic surface displacements of the wheel and rail at the contact area. Hence, the actual slip $\dot{\mathbf{s}}$, which represents the relative velocity between a particle of the wheel inside the contact area and the corresponding contact particle of the rail, is given by (Garg and Dukkipati, 1984; Kalker, 1990)

$$\dot{\mathbf{s}} = \dot{\mathbf{r}} + \dot{\mathbf{v}} \tag{4.46}$$

where $\dot{\mathbf{v}}$ is the derivative of $\mathbf{v}$ with respect to time. Considering that the contact area moves with the wheel in the longitudinal direction x_c, equation (4.46) may be rewritten as

$$\dot{\mathbf{s}} = \dot{\mathbf{r}} - \frac{\partial \mathbf{v}}{\partial x_c} V + \frac{\partial \mathbf{v}}{\partial t} \tag{4.47}$$

which in the case of steady-state rolling, the component $\partial \mathbf{v}/\partial t$ is null. In the wheel-rail contact area, the actual slip $\dot{\mathbf{s}}$, the tangential stress $\boldsymbol{\tau}$ and the normal pressure σ are related by the Coulomb law as (Kalker, 1990)

$$\begin{cases} |\boldsymbol{\tau}| \leq \mu & \text{if} \quad |\dot{\mathbf{s}}| = 0 \quad \text{(adhesion region)} \\ |\boldsymbol{\tau}| = \mu\sigma & \text{if} \quad |\dot{\mathbf{s}}| \neq 0 \quad \text{(slip region)} \end{cases} \tag{4.48}$$

Finally, the longitudinal F_ξ and lateral F_η creep forces, as well as the spin creep moment M_ϕ, can be calculated by integrating the tangential stresses along the contact area Γ as follows (Kalker, 1990):

$$F_\xi = \iint_\Gamma \tau_{x_c} \, dx_c \, dy_c \tag{4.49a}$$

$$F_\eta = \iint_\Gamma \tau_{y_c} \, dx_c \, dy_c \tag{4.49b}$$

$$M_\phi = \iint_\Gamma \left(x_c \tau_{y_c} - y_c \tau_{x_c} \right) dx_c \, dy_c \tag{4.49c}$$

where τ_{x_c} and τ_{y_c} are the longitudinal and lateral components of the tangential stress vector $\boldsymbol{\tau}$.

4.5.3 Creep force theories

In Section 2.4.3 of Chapter 2, several wheel-rail rolling contact theories, used to calculate the creep forces that develop at the contact interface, are introduced and briefly described. Among these, the Kalker's linear theory (Kalker, 1967), the Polach method (Polach, 1999) and the Kalker's book of tables (Kalker, 1996) are implemented in the vehicle-structure interaction method proposed in the present chapter.

4.5.3.1 Kalker's linear theory

According to Kalker's linear theory (Kalker, 1967), the actual slip $\dot{\mathbf{s}}$ inside the contact area is null (no-slip condition) and the adhesion region is assumed to cover the entire contact area. Thus, by imposing this condition to equation (4.47), one obtains

$$\frac{\partial v_{x_c}}{\partial x_c} = \upsilon_\xi - \upsilon_\phi y_c \tag{4.50a}$$

$$\frac{\partial v_{y_c}}{\partial x_c} = \upsilon_\eta + \upsilon_\phi x_c \tag{4.50b}$$

Integrating equation (4.50) with respect to x_c gives

$$v_{x_c} = \upsilon_\xi x_c - \upsilon_\phi y_c x_c + f_1(y_c) \tag{4.51a}$$

$$v_{y_c} = \upsilon_\eta x_c - \frac{1}{2}\upsilon_\phi x_c^2 + f_2(y_c) \tag{4.51b}$$

where $f_1(y_c)$ and $f_2(y_c)$ are arbitrary functions that arise from the integration process.

For an elliptical contact area, and according to the Galin theorem (Kalker, 1967), if the distribution of the relative tangential elastic displacements **v** is described by a polynomial function, the tangential stresses can be as well, but multiplied by

$$J(x_c, y_c) = \frac{1}{\sqrt{1 - \left(\dfrac{x_c}{a}\right)^2 - \left(\dfrac{y_c}{b}\right)^2}} \tag{4.52}$$

As a consequence of the no-slip condition, the tangential stresses must be continuous at the leading edge of the contact area, which implies that it vanishes at that point. Hence, according to the aforementioned distribution of the tangential stresses, the creep forces law expressed in equation (4.49) may be defined as

$$F_\xi = -G\,a\,b\,c_{11}\,\upsilon_\xi \tag{4.53a}$$

$$F_\eta = -Gab\left(c_{22}\,\upsilon_\eta + \sqrt{ab}\,c_{23}\,\upsilon_\phi\right) \tag{4.53b}$$

$$M_\phi = -Gab\left(-\sqrt{ab}\,c_{23}\,\upsilon_\eta + ab\,c_{33}\,\upsilon_\phi\right) \tag{4.53c}$$

where G is the combined shear modulus of rigidity of wheel and rail materials and c_{ij} are Kalker's creepage coefficients that depend on the semi-axes ratio a/b and on the Poisson's ratio of the wheel and rail materials. These coefficients can be found in Appendix B

Note that the linear theory is an approximation, since for large creepages the condition given by the Coulomb's law can be violated. Nevertheless, due to its low computational cost, the linear theory may be useful to study scenarios in which the creepages remain low, such as railway operations in ordinary conditions.

4.5.3.2 Polach method

Polach (1999) proposed an algorithm to compute the wheel-rail creep forces based on the Hertz assumption of an elliptical contact area, in which the relative displacements between the bodies in the adhesion region increase linearly from the leading to the rear edge. Thus, the tangential stress also grows linearly with the distance from the leading edge, being its maximum limited by the Coulomb's law, as stated in equation (4.41). If the tangential stress in the adhesion region reaches the maximum value, sliding takes place and a slip region begins to form, as depicted in Figure 4.11.

According to Polach (1999), the tangential contact force F_{tr} due to the translational creepages v_ξ and v_η is given by

$$F_{tr} = -\frac{2\mu F_n}{\pi}\left(\frac{\varepsilon_{tr}}{1+\varepsilon_{tr}^2} + \tan^{-1}\varepsilon_{tr}\right) \tag{4.54}$$

in which ε_{tr} is the gradient of tangential stress in the adhesion region given by

$$\varepsilon_{tr} = \frac{1}{4}\frac{G\pi a b c_C}{\mu F_n}v_{trC} \tag{4.55}$$

where c_C is a constant that depends on the Kalker's creepage coefficients c_{11} and c_{22} as follows

$$c_C = \sqrt{\left(c_{11}\frac{v_\xi}{v_{tr}}\right)^2 + \left(c_{22}\frac{v_\eta}{v_{tr}}\right)^2} \tag{4.56}$$

and v_{trC} is the modified translational creepage, which accounts for the effect of the spin creepage, that can be written as

$$v_{trC} = \sqrt{v_\xi^2 + v_{\eta C}^2} \tag{4.57}$$

In equation (4.56), the parameter v_{tr} is the magnitude of the translational creepage given by

$$v_{tr} = \sqrt{v_\xi^2 + v_\eta^2} \tag{4.58}$$

while $v_{\eta C}$, presented in equation (4.57), is the modified lateral creepage defined as

$$v_{\eta C} = \begin{cases} v_\eta & \text{if} \quad \left|v_\eta + v_\phi a\right| \leq \left|v_\eta\right| \\ v_\eta + v_\phi a & \text{if} \quad \left|v_\eta + v_\phi a\right| > \left|v_\eta\right| \end{cases} \tag{4.59}$$

Assuming that the creep moments are small when compared to other moments acting on the system, the lateral tangential contact force $F_{\eta S}$ caused by pure spin is found to be

$$F_{\eta S} = -\frac{9}{16} a\,\mu\,F_n\,K_M\left[1+6.3\left(1-e^{-a/b}\right)\right] \tag{4.60}$$

where K_M is defined as

$$K_M = |\varepsilon_S|\left(\frac{\delta^3}{3}-\frac{\delta^2}{2}+\frac{1}{6}\right)-\frac{1}{3}\sqrt{\left(1-\delta^2\right)^3} \tag{4.61}$$

and δ is given by

$$\delta = \frac{\varepsilon_S^2-1}{\varepsilon_S^2+1} \tag{4.62}$$

The parameter ε_S is the gradient of tangential stress to account for the spin influence that is given by

$$\varepsilon_S = \frac{8}{3}\frac{Gb\sqrt{ab}}{\mu F_n}\frac{c_{23}\,\upsilon_{\eta C}}{1+6.3\left(1-e^{-a/b}\right)} \tag{4.63}$$

in which c_{23} is one of the Kalker's creepage coefficient.

Finally, the creep forces according to the Polach's method are defined as

$$F_\xi = F_{tr}\frac{\upsilon_\xi}{\upsilon_{trC}} \tag{4.64a}$$

$$F_\eta = \frac{1}{\upsilon_{trC}}\left(F_{tr}\,\upsilon_\eta + F_{\eta S}\,\upsilon_\phi\right) \tag{4.64b}$$

Note that the contribution of spin is accounted for in the lateral creep force. According to Polach (1999), the moment caused by the spin and lateral creepages can be neglected, since it is small when compared to other moments acting on the system.

4.5.3.3 Kalker's book of tables

Kalker (1996) proposed a methodology based on precalculated lookup tables, named book of tables, in which several values of creep forces are stored to be later interpolated during the dynamic analysis as a function of the creepages and the semi-axes ratio of the contact ellipse.

The tables, along with the algorithm to interpolate them, were implemented in a computer code called USETAB.

The lookup table uses an effective layout, exploiting all possible symmetries between the contact forces and creepages (Kalker, 1967). The values from the table are normalized and calculated according to the following criteria: 1) the combined shear modulus of the wheel and rail materials G is 1; 2) the Coulomb's friction limit given by μF_n is 1 and 3) the square root of the ellipse's semi-axes product $\sqrt{ab}$ is 1. The table inputs are the semi-axes ratio of the contact ellipse and the normalized creepages, defined as

$$\upsilon'_\xi = \frac{abG}{3\mu F_n} c_{11} \upsilon_\xi \tag{4.65a}$$

$$\upsilon'_\eta = \frac{abG}{3\mu F_n} c_{22} \upsilon_\eta \tag{4.65b}$$

$$\upsilon'_\phi = \frac{(ab)^{3/2}G}{\mu F_n} c_{23} \upsilon_\phi \tag{4.65c}$$

The outputs consist in the normalized longitudinal creep force F'_ξ, the normalized lateral creep force F'_η and the normalized spin creep moment M'_ϕ, which are linearly interpolated during the dynamic analysis. Hence, the absolute value of the creep forces are given by

$$F_\xi = F'_\xi \mu F_n \tag{4.66a}$$

$$F_\eta = F'_\eta \mu F_n \tag{4.66b}$$

$$M_\phi = M'_\phi \mu F_n \sqrt{ab} \tag{4.66c}$$

In the present thesis, the table is calculated using the software CONTACT (2011) which is based on Kalker's exact three-dimensional rolling contact theory (Kalker, 1979). The normalized creepages and semi-axes ratios were discretized in two intervals as in the original USETAB, namely $0 \le x \le 1$ and $1 \le x < \infty$, where x is the input of the table. However, a linear and a logarithmic distribution of ten values were used for the discretization of the first and second intervals, respectively, instead of the original linear intervals with seven values. Adopting a 40×40 element discretization of the contact ellipse, and by considering all possible combinations of the creepages and semi-axes ratios, a total of 320000 calculations were performed using the software CONTACT.

An important point is the consideration of an upper limit for the table to avoid inaccurate extrapolations. Furthermore, according to Kalker (1996), the linear interpolations with semi-axes ratios close to zero or infinite should be avoided, since the creepage coefficients are singular in these cases. Therefore, an upper limit of 10^3 and a lower limit of 10^{-3} are used for the semi-axes ratios and an upper limit of 10^3 is adopted for the normalized creepages. If a combination of creepages and semi-axes ratio falls outside these intervals, the Polach method is used to solve the mentioned singularities.

4.6 FORMULATION OF THE TRAIN-STRUCTURE COUPLING SYSTEM

Neves et al. (2012) developed an algorithm, referred to as the direct method, in which the governing equilibrium equations of the vehicle and structure are complemented with additional constraint equations that relate the displacements of the contact nodes of the vehicle with the corresponding nodal displacements of the structure, with no separation being allowed. These equations form a single system, with displacements and contact forces as unknowns, that is solved directly using an optimized block factorization algorithm. Later, Neves et al. (2014) extended the algorithm to deal with wheel-rail separation. In this approach, a search algorithm is used to detect which wheels are in contact, being the constraint equations only imposed when contact occurs. Finally, Montenegro et al. (2015b) included the lateral dynamic effects between railway vehicles and structures by incorporating the wheel-rail contact model described above.

4.6.1 Governing equations of motion

4.6.1.1 Force equilibrium

Considering the α method (Hughes, 2000), the equations of motion of the vehicle-structure system can be written as

$$\mathbf{M}\,\ddot{\mathbf{a}}^{t+\Delta t} + (1+\alpha)\,\mathbf{R}^{t+\Delta t} - \alpha\,\mathbf{R}^t = (1+\alpha)\,\mathbf{F}^{t+\Delta t} - \alpha\,\mathbf{F}^t \tag{4.67}$$

where $\mathbf{M}$ is the mass matrix, $\mathbf{R}$ are the nodal forces corresponding to the internal element stresses, $\mathbf{F}$ are the externally applied nodal loads and $\mathbf{a}$ are the nodal displacements. The elastic and damping forces depend nonlinearly on the nodal displacements and velocities due to the several nonlinearities considered in the present formulation, such as the wheel-rail contact and the nonlinear suspensions. In the present work, the nonlinear inertia effects, such as the

centrifugal and gyroscopic effects, are neglected. The superscripts t and $t+\Delta t$ indicate the previous and current time step, respectively.

To solve equation (4.67) let the F type degrees of freedom (DOF) represent the free nodal DOF, whose values are unknown, and the P type DOF represent the prescribed nodal DOF, whose values are known. Thus, the load vector can be expressed as

$$\mathbf{F}_F = \mathbf{P}_F + \mathbf{D}_{FX}^{ce}\, \mathbf{X}^{ce} + \mathbf{D}_{FX}^{te}\, \mathbf{X}^{te} \tag{4.68a}$$

$$\mathbf{F}_P = \mathbf{P}_P + \mathbf{D}_{PX}^{te}\, \mathbf{X}^{te} + \mathbf{S} \tag{4.68b}$$

where $\mathbf{P}$ corresponds to the externally applied nodal loads whose values are known, $\mathbf{S}$ are the support reactions and $\mathbf{X}$ are the forces acting at the contact interface shown in Figure 4.1. Each matrix $\mathbf{D}$ relates the contact forces, defined with respect to the target element coordinate system, with the nodal forces defined in the global coordinate system.

According to Newton's third law, the forces acting at the contact interface must be of equal magnitude and opposite direction (see Figure 4.1), i.e.,

$$\mathbf{X}^{ce} + \mathbf{X}^{te} = \mathbf{0} \tag{4.69}$$

Substituting equation (4.69) into equation (4.68) leads to

$$\mathbf{F}_F = \mathbf{P}_F + \mathbf{D}_{FX}\, \mathbf{X} \tag{4.70a}$$

$$\mathbf{F}_P = \mathbf{P}_P + \mathbf{D}_{PX}\, \mathbf{X} + \mathbf{S} \tag{4.70b}$$

where

$$\mathbf{X} = \mathbf{X}^{ce} \tag{4.71}$$

$$\mathbf{D}_{FX} = \mathbf{D}_{FX}^{ce} - \mathbf{D}_{FX}^{te} \tag{4.72}$$

$$\mathbf{D}_{PX} = -\mathbf{D}_{PX}^{te} \tag{4.73}$$

Substituting equation (4.70) into equation (4.67), and partitioning into F and P type DOF, gives

$$\begin{bmatrix} \mathbf{M}_{FF} & \mathbf{M}_{FP} \\ \mathbf{M}_{PF} & \mathbf{M}_{PP} \end{bmatrix} \begin{bmatrix} \ddot{\mathbf{a}}_F^{t+\Delta t} \\ \ddot{\mathbf{a}}_P^{t+\Delta t} \end{bmatrix} + (1+\alpha) \begin{bmatrix} \mathbf{R}_F^{t+\Delta t} \\ \mathbf{R}_P^{t+\Delta t} \end{bmatrix} - \alpha \begin{bmatrix} \mathbf{R}_F^{t} \\ \mathbf{R}_P^{t} \end{bmatrix}$$
$$= (1+\alpha) \begin{bmatrix} \mathbf{P}_F^{t+\Delta t} + \mathbf{D}_{FX}^{t+\Delta t}\, \mathbf{X}^{t+\Delta t} \\ \mathbf{P}_P^{t+\Delta t} + \mathbf{D}_{PX}^{t+\Delta t}\, \mathbf{X}^{t+\Delta t} + \mathbf{S}^{t+\Delta t} \end{bmatrix} - \alpha \begin{bmatrix} \mathbf{P}_F^{t} + \mathbf{D}_{FX}^{t}\, \mathbf{X}^{t} \\ \mathbf{P}_P^{t} + \mathbf{D}_{PX}^{t}\, \mathbf{X}^{t} + \mathbf{S}^{t} \end{bmatrix} \tag{4.74}$$

101

Considering only the first row of equation (4.74) and transferring the unknowns to the left-hand size leads to

$$\mathbf{M}_{FF}\,\ddot{\mathbf{a}}_F^{t+\Delta t}+(1+\alpha)\mathbf{R}_F^{t+\Delta t}-(1+\alpha)\mathbf{D}_{FX}^{t+\Delta t}\,\mathbf{X}^{t+\Delta t}=\overline{\mathbf{F}}_F \tag{4.75}$$

where

$$\overline{\mathbf{F}}_F=(1+\alpha)\mathbf{P}_F^{t+\Delta t}-\alpha\mathbf{P}_F^t-\alpha\,\mathbf{D}_{FX}^t\,\mathbf{X}^t-\mathbf{M}_{FP}\,\ddot{\mathbf{a}}_P^{t+\Delta t}+\alpha\,\mathbf{R}_F^t \tag{4.76}$$

4.6.1.2 Incremental formulation for nonlinear analysis

Since the present problem has a nonlinear nature, equation (4.75) is rewritten in the form

$$\mathbf{\psi}_F\left(\mathbf{a}_F^{t+\Delta t},\mathbf{X}^{t+\Delta t}\right)=\mathbf{0} \tag{4.77}$$

where $\mathbf{\psi}_F$ is the residual force vector, given by

$$\mathbf{\psi}_F\left(\mathbf{a}_F^{t+\Delta t},\mathbf{X}^{t+\Delta t}\right)=\overline{\mathbf{F}}_F-\mathbf{M}_{FF}\,\ddot{\mathbf{a}}_F^{t+\Delta t}-(1+\alpha)\mathbf{R}_F^{t+\Delta t}+(1+\alpha)\mathbf{D}_{FX}^{t+\Delta t}\,\mathbf{X}^{t+\Delta t} \tag{4.78}$$

The nodal velocities and accelerations depend on the nodal displacements and for this reason are not independent unknowns. According to the *α* method, the following approximations for the acceleration and velocity at the current time step can be obtained (Neves et al., 2014):

$$\ddot{a}^{t+\Delta t}=\frac{1}{\beta\Delta t^2}\left(a^{t+\Delta t}-a^t\right)-\frac{1}{\beta\Delta t}\,\dot{a}^t-\left(\frac{1}{2\beta}-1\right)\ddot{a}^t \tag{4.79}$$

$$\dot{a}^{t+\Delta t}=\frac{\gamma}{\beta\Delta t}\left(a^{t+\Delta t}-a^t\right)+\left(1-\frac{\gamma}{\beta}\right)\dot{a}^t+\Delta t\left(1-\frac{\gamma}{2\beta}\right)\ddot{a}^t \tag{4.80}$$

where *β* and *γ* are parameters that control the stability and accuracy of the method.

An iterative scheme based on the Newton method (Owen and Hinton, 1980) is used to solve equation (4.77). Assuming that the solution at the *i*th Newton iteration has been evaluated and neglecting second and higher order terms, the Taylor series for $\mathbf{\psi}_F$ about $\left(\mathbf{a}_F^{t+\Delta t,i},\mathbf{X}^{t+\Delta t,i}\right)$ is given by

$$\begin{aligned}
\mathbf{\psi}_F\left(\mathbf{a}_F^{t+\Delta t,i+1},\mathbf{X}^{t+\Delta t,i+1}\right)=\mathbf{\psi}_F\left(\mathbf{a}_F^{t+\Delta t,i},\mathbf{X}^{t+\Delta t,i}\right)&+\left[\frac{\partial\mathbf{\psi}_F}{\partial\mathbf{a}_F^{t+\Delta t}}\bigg|_{\left(\mathbf{a}_F^{t+\Delta t,i},\mathbf{X}^{t+\Delta t,i}\right)}\right]\left(\mathbf{a}_F^{t+\Delta t,i+1}-\mathbf{a}_F^{t+\Delta t,i}\right)\\
&+\left[\frac{\partial\mathbf{\psi}_F}{\partial\mathbf{X}^{t+\Delta t}}\bigg|_{\left(\mathbf{a}_F^{t+\Delta t,i},\mathbf{X}^{t+\Delta t,i}\right)}\right]\left(\mathbf{X}^{t+\Delta t,i+1}-\mathbf{X}^{t+\Delta t,i}\right)
\end{aligned} \tag{4.81}$$

Substituting equations (4.78) to (4.80) into equation (4.81), and assuming that the residual force vector at iteration $i+1$ fulfils the condition given by equation (4.77), leads to

$$\boldsymbol{\psi}_F\left(\mathbf{a}_F^{t+\Delta t,i},\mathbf{X}^{t+\Delta t,i}\right)+\left[-\frac{1}{\beta\Delta t^2}\mathbf{M}_{FF}-(1+\alpha)\left[\frac{\partial\mathbf{R}_F}{\partial\mathbf{a}_F^{t+\Delta t}}\bigg|_{\mathbf{a}_F^{t+\Delta t,i}}\right]\right]\left(\mathbf{a}_F^{t+\Delta t,i+1}-\mathbf{a}_F^{t+\Delta t,i}\right) \\ +(1+\alpha)\mathbf{D}_{FX}^{t+\Delta t,i}\left(\mathbf{X}^{t+\Delta t,i+1}-\mathbf{X}^{t+\Delta t,i}\right)=\mathbf{0}$$

(4.82)

Transforming equation (4.82) into an incremental form leads to

$$\overline{\mathbf{K}}_{FF}\,\Delta\mathbf{a}_F^{i+1}-(1+\alpha)\mathbf{D}_{FX}^{t+\Delta t,i}\,\Delta\mathbf{X}^{i+1}=\boldsymbol{\psi}_F^i$$

(4.83)

where $\overline{\mathbf{K}}_{FF}$ is the current effective stiffness matrix defined by

$$\overline{\mathbf{K}}_{FF}=\frac{1}{\beta\Delta t^2}\mathbf{M}_{FF}+(1+\alpha)\left[\frac{\partial\mathbf{R}_F}{\partial\mathbf{a}_F^{t+\Delta t}}\bigg|_{\mathbf{a}_F^{t+\Delta t,i}}\right]$$

(4.84)

and

$$\Delta\mathbf{a}_F^{i+1}=\mathbf{a}_F^{t+\Delta t,i+1}-\mathbf{a}_F^{t+\Delta t,i}$$

(4.85)

$$\Delta\mathbf{X}^{i+1}=\mathbf{X}^{t+\Delta t,i+1}-\mathbf{X}^{t+\Delta t,i}$$

(4.86)

$$\boldsymbol{\psi}_F^i=\boldsymbol{\psi}_F\left(\mathbf{a}_F^{t+\Delta t,i},\mathbf{X}^{t+\Delta t,i}\right)$$

(4.87)

In matrix notation, equation (4.83) can be expressed as

$$\left[\overline{\mathbf{K}}_{FF}\quad\overline{\mathbf{D}}_{FX}\right]\begin{bmatrix}\Delta\mathbf{a}_F^{i+1}\\\Delta\mathbf{X}^{i+1}\end{bmatrix}=\boldsymbol{\psi}_F^i$$

(4.88)

being

$$\mathbf{D}_{FX}=-(1+\alpha)\mathbf{D}_{FX}^{t+\Delta t,i}$$

(4.89)

After evaluating the solution at iteration $i+1$, the residual force vector is calculated using equation (4.78). The iteration scheme continues until the following condition is fulfilled:

$$\frac{\left\|\boldsymbol{\psi}_F^{i+1}\right\|}{\left\|\mathbf{P}_F^{t+\Delta t}\right\|}\leq\varepsilon$$

(4.90)

where ε is a specified tolerance.

4.6.1.3 Updating of the effective stiffness matrix

According to Owen and Hinton (1980), the complete factorization of the global effective stiffness matrix (full Newton-Raphson method) can be avoided if the stiffness corresponding to the initial trial of the iterative process is kept constant. This procedure, called initial stiffness method, has the immediate advantage of significantly reducing the computational cost of each iteration but reduces the convergence rate of the step, since more iterations are required to achieve the necessary convergence expressed in equation (4.90). Thus, the optimal algorithm is generally provided by a combination of these two processes, depending on the degree of nonlinearity inherent in the problem.

In the present work, the main nonlinearities inherent to the problem are concentrated at the wheel-rail contact elements described in Section 4.2. Regarding the stiffness of these elements, since the Hertz law (Hertz, 1882) is given by the close-form expression presented in equation (4.39), which has an analytic derivative, the tangent stiffness matrix **K** can be updated at each iteration in order to take advantage of the full Newton-Raphson method. However, the same is not true regarding the damping, since the contact laws based on Kalker's exact theory of rolling contact (Kalker, 1979) or on Polach's method (Polach, 1999) cannot be defined with a closed-form expression. Therefore, since the calculation of numerical derivatives with respect to the nodal velocities can be computationally expensive, the initial tangent damping matrix **C** of the contact element is calculated based on the Kalker's linear theory (Kalker, 1967) and is kept constant throughout the analysis.

4.6.2 Contact constraint equations

When contact occurs, the additional internal node of the contact element and the auxiliary point belonging to the rigid surface of the target element are coupled in the three directions (see Section 4.2). Thus, the following constraint equations must be imposed:

$$\mathbf{v}^{ce} - \mathbf{v}^{te} = \mathbf{r} \tag{4.91}$$

where **r** are the irregularities between the contact and target elements in the vertical and lateral directions. The displacements of the additional internal nodes (see Figure 4.1) are given by

$$\mathbf{v}^{ce} = \mathbf{H}_{XF}^{ce} \, \mathbf{a}_F^{t+\Delta t, i+1} \tag{4.92}$$

where the transformation matrix **H** relates the displacements of the additional internal nodes of the contact element, defined in the global coordinate system, with the displacements defined in

the local coordinate system of the corresponding target element. The displacements of the auxiliary points of the target elements are given by

$$\mathbf{v}^{te} = \mathbf{H}_{XF}^{te} \, \mathbf{a}_F^{t+\Delta t, i+1} + \mathbf{H}_{XP}^{te} \, \mathbf{a}_P^{t+\Delta t} \tag{4.93}$$

where each transformation matrix $\mathbf{H}$ relates the displacements of the nodes of the target elements, defined in the global coordinate system, to the displacements of the auxiliary points defined in the target element coordinate system.

Substituting equations (4.92) and (4.93) into equation (4.91) yields

$$\mathbf{H}_{XF} \, \mathbf{a}_F^{t+\Delta t, i+1} = \mathbf{r} - \mathbf{H}_{XP} \, \mathbf{a}_P^{t+\Delta t} \tag{4.94}$$

where

$$\mathbf{H}_{XF} = \mathbf{H}_{XF}^{ce} - \mathbf{H}_{XF}^{te} \tag{4.95}$$

$$\mathbf{H}_{XP} = -\mathbf{H}_{XP}^{te} \tag{4.96}$$

Rearranging equation (4.85) in terms of $\mathbf{a}_F^{t+\Delta t, i+1}$ and substituting into equation (4.94) leads to

$$\mathbf{H}_{XF} \, \Delta \mathbf{a}_F^{i+1} = \mathbf{r} - \mathbf{H}_{XP} \, \mathbf{a}_P^{t+\Delta t} - \mathbf{H}_{XF} \, \mathbf{a}_F^{t+\Delta t, i} \tag{4.97}$$

Multiplying equation (4.97) by $-(1+\alpha)$ gives

$$\overline{\mathbf{H}}_{XF} \, \Delta \mathbf{a}_F^{i+1} = \overline{\mathbf{r}} \tag{4.98}$$

where

$$\overline{\mathbf{H}}_{XF} = -(1+\alpha) \, \mathbf{H}_{XF} \tag{4.99}$$

and

$$\overline{\mathbf{r}} = -(1+\alpha) \left(\mathbf{r} - \mathbf{H}_{XP} \, \mathbf{a}_P^{t+\Delta t} - \mathbf{H}_{XF} \, \mathbf{a}_F^{t+\Delta t, i} \right) \tag{4.100}$$

4.6.3 Complete system of equations

The incremental formulation of the governing equations of motion of the vehicle-structure system is applicable to either linear or nonlinear analyses. These equations and the contact constraints form a complete system whose unknowns are incremental nodal displacements and incremental contact forces. Equations (4.88) and (4.98) can be expressed in matrix form leading to the following system of equations:

$$\begin{bmatrix} \overline{\mathbf{K}}_{FF} & \overline{\mathbf{D}}_{FX} \\ \overline{\mathbf{H}}_{XF} & \mathbf{0} \end{bmatrix} \begin{bmatrix} \Delta \mathbf{a}_F^{i+1} \\ \Delta \mathbf{X}^{i+1} \end{bmatrix} = \begin{bmatrix} \boldsymbol{\psi}_F^i \\ \overline{\mathbf{r}} \end{bmatrix} \tag{4.101}$$

Using Betti's theorem, it can be demonstrated that the matrix in equation (4.101) is symmetric. Since the time required to solve the system of linear equations presented in equation (4.101) may represent a significant percentage of the total solution time, the efficiency of the solver is very important. The system matrix is partitioned into the following form in order to improve the efficiency of the solver.

$$
\begin{bmatrix}
\overline{\mathbf{K}}_{II} & \overline{\mathbf{K}}_{IR} & \overline{\mathbf{K}}_{IY} & \overline{\mathbf{D}}_{IX} \\
\overline{\mathbf{K}}_{RI} & \overline{\mathbf{K}}_{RR} & \overline{\mathbf{K}}_{RY} & \overline{\mathbf{D}}_{RX} \\
\overline{\mathbf{K}}_{YI} & \overline{\mathbf{K}}_{YR} & \overline{\mathbf{K}}_{YY} & \overline{\mathbf{D}}_{YX} \\
\overline{\mathbf{H}}_{XI} & \overline{\mathbf{H}}_{XR} & \overline{\mathbf{H}}_{XY} & \mathbf{0}
\end{bmatrix}
\begin{bmatrix}
\Delta \mathbf{a}_I^{i+1} \\
\Delta \mathbf{a}_R^{i+1} \\
\Delta \mathbf{a}_Y^{i+1} \\
\Delta \mathbf{X}^{i+1}
\end{bmatrix}
=
\begin{bmatrix}
\mathbf{\psi}_I^i \\
\mathbf{\psi}_R^i \\
\mathbf{\psi}_Y^i \\
\overline{\mathbf{r}}
\end{bmatrix}
\tag{4.102}
$$

The *F* type DOF is partitioned into *I*, *R* and *Y* type DOF. The *Y* type DOF corresponds to the DOF of the internal nodes added by the contact elements (see node C_3 in Figure 4.1). These DOF have to be grouped together because they are only active when contact occurs, and so the size of the matrices relating these DOF is time-dependent. Since the laws for the contact interface are nonlinear, the matrices of the contact elements are also time-dependent. The *R* type DOF correspond to all the nodal DOF of the contact elements, except for the *Y* type DOF, which have already been grouped separately (see node C_1 in Figure 4.1). The *I* type DOF are all the remaining *F* type DOF. The *R* type DOF can also include DOF belonging to other nonlinear finite elements such as the spring-dampers used to model the vehicle's suspensions. The present method adopts a block factorization algorithm (see Appendix C), based on that developed by Neves et al. (2012) and later extended by Montenegro et al. (2015b) to deal with 3D contact.

4.6.4 Algorithm for solving the train-structure interaction problem

The proposed train-structure interaction method is implemented in MATLAB, being the vehicles and structures modeled with ANSYS. All the data regarding these models, such as the structural matrices, the definition of the target elements, the contact nodes of the vehicle and the support conditions are exported using ANSYS in batch mode and subsequently imported by MATLAB. The remaining data, namely the irregularities between the wheel and rail, the contact lookup table and the control points defining the rail and wheel profiles are stored in an external database and imported directly by MATLAB.

After all the data is imported and processed, an initial static analysis is performed in order to obtain the initial conditions of the dynamic problem. The flowchart depicted in Figure 4.13 illustrates all the aspects regarding the dynamic analysis of the train-structure interaction.

Start

Estimate $(s_r, s_w)^0_{tread}$

$t = 0$

Calculate $\mathbf{P}^{t+\Delta t}$

Predict: a) $\ddot{\mathbf{a}}_F^{t+\Delta t} = \mathbf{0}$; b) $\mathbf{X}^{t+\Delta t} = \mathbf{X}^t$

$\mathbf{a}_F^{t+\Delta t} = \mathbf{a}_F^t + \dot{\mathbf{a}}_F^t\,\Delta t + \left(1/2 - \beta\right)\ddot{\mathbf{a}}_F^t\,\Delta t^2$
$\dot{\mathbf{a}}_F^{t+\Delta t} = \dot{\mathbf{a}}_F^t + \left(1 - \gamma\right)\ddot{\mathbf{a}}_F^t\,\Delta t$

$i = 0$

$i\,\text{Wheel} = 1$

$(s_r, s_w)^{i+1}_{tread} = (s_r, s_w)^{i}_{tread}$
$(s_r, s_w)^{i+1}_{flange} = (s_r, s_w)^{i}_{flange}$ or contact tables

$i\,\text{Wheel} = i\,\text{Wheel} + 1$

$\kappa_{w,y_c} > 0$
(Eq. 4.19)

No   Yes

No contact occurs
Update matrices $\mathbf{D}$ and $\mathbf{H}$

Convex contact
search (Section 4.3.2.1)

Concave contact
search (Section 4.3.2.2)

Contact status
(Eq. 4.20 or 4.23)   False

$t = t + \Delta t$

$i\,\text{Wheel} = i\,\text{Wheel} + 1$

$i = i + 1$

True

Contact occurs
Update matrices $\mathbf{D}$ and $\mathbf{H}$

Calculate the internal resisting
forces in the normal direction

Calculate creepages (Eq. 4.42 and 4.43)
and ellipse's semi-axes (Eq. 4.37)

Calculate the internal resisting
forces in the tangential directions

Update:
a) $\mathbf{a}_F^{t+\Delta t,i+1} = \mathbf{a}_F^{t+\Delta t,i} + \Delta\mathbf{a}_F^{i+1}$
b) $\dot{\mathbf{a}}_F^{t+\Delta t,i+1}$ (Eq. 4.80)
c) $\ddot{\mathbf{a}}_F^{t+\Delta t,i+1}$ (Eq. 4.79)
d) $\mathbf{X}^{t+\Delta t,i+1} = \mathbf{X}^{t+\Delta t,i} + \Delta\mathbf{X}^{i+1}$

No $i\,\text{Wheel} = n\,\text{Wheel}$

Solve system of equations (4.102)
(see Appendix B)

Yes

Calculate $\boldsymbol{\psi}_F\left(\mathbf{a}_F^{t+\Delta t}, \mathbf{X}^{t+\Delta t}\right)$ (Eq. 4.78)

Update $\bar{\mathbf{K}}_{FF}$ (Eq. 4.84)

$\left\|\boldsymbol{\psi}_F^{i+1}\right\| / \left\|\mathbf{P}_F^{t+\Delta t}\right\| \le \varepsilon$
(Eq. 4.90)   No

Yes

No $t = t_{end}$

Yes

End

Figure 4.13 - Flowchart of the algorithm for analyzing the train-structure dynamic interaction.

4.7 CONCLUDING REMARKS

A method for analyzing the nonlinear dynamic interaction between the train and structure is proposed and implemented (Montenegro et al., 2015b). The method takes into account the geometry of the wheel and rail surfaces in order to accurately evaluate the lateral interaction.

In the majority of the currently available methods for analyzing the train-structure interaction, the normal and tangential contact forces are treated as external forces. However, it is generally more efficient to use a finite element formulation based on the contact laws for the normal and tangential directions. Therefore, a wheel-rail contact finite element specially developed for modeling the behavior of the contact interface in the normal and tangential directions is proposed. This behavior is reproduced by a wheel-rail contact model whose formulation is divided in three main parts: the geometric problem, the normal problem and the tangential problem.

The geometric problem, which consists of detecting the position of the contact points between wheel and rail, is solved online, i.e., during the dynamic analysis. Although this procedure is computationally more expensive than an offline contact approach, in which the location of the contact points is precalculated as a function of the relative displacements between wheel and rail, its higher accuracy outweighs this drawback. The proposed method is able to look for potential contact points in any type of geometric surfaces (convex or concave) at the tread and the flange of the wheel. Thus, the formulation is suitable to investigate not only scenarios related to ordinary railway operation, but also derailment situations, in which the flange contact plays an important role.

Regarding the normal contact problem, the nonlinear Hertz theory is used to compute the normal contact forces between wheel and rail. Although this theory rests on a series of assumptions that may limit its range of application, it offers a good compromise between computational efficiency and accuracy for dealing with the dynamic analysis of railway vehicles. However, for the study of local phenomena, such as wear, a more accurate procedure based on multi-Hertzian or non-Hertzian formulations may be adopted.

For dealing with the tangential contact problem, three different approaches are adopted. Since the exact theory of rolling contact proposed by Kalker (1979) is impracticable to be used in dynamic analysis of railway vehicles due to its excessive computational cost, the Polach method (Polach, 1999), the Kalker's book of tables (Kalker, 1996) and the Kalker's linear

theory (Kalker, 1967) are implemented in the proposed formulation. The first two methods combine accuracy with computational efficiency, while the latter is limited to scenarios with small creepages. However, due to its excellent computational performance, the Kalker's linear theory is also implemented for being used in ordinary operation scenarios.

Finally, the coupling between the vehicle and the structure is accomplished using the direct method (Neves et al., 2012; Neves et al., 2014), which complements the governing equilibrium equations of the vehicle and structure with additional constraint equations that relate the displacements of the contact nodes of the vehicle with the corresponding nodal displacements of the structure. These equations form a single system, with displacements and contact forces as unknowns, that is solved directly using an optimized block factorization algorithm. The proposed method is based on the finite element method, which allows the analysis of structures and vehicles with any degree of complexity and the consideration of the deformations undergone by the two systems.

Chapter 5

VALIDATION OF THE TRAIN-STRUCTURE INTERACTION METHOD

5.1   INTRODUCTION

In the present chapter, the train-structure interaction method developed in the present thesis and described in Chapter 4 is validated with three numerical applications and one experimental test. First, the results obtained with the creep force models implemented in the proposed method are compared with those obtained with the Kalker's exact theory of rolling contact (ANSYS (1979)) implemented in the software CONTACT (2011). In the second application, the Manchester Benchmark proposed by Shackleton and Iwnicki (2006) is revisited. The benchmark consisted of a series of tests simulated with ten different softwares with the aim of allowing an informed choice when selecting a contact model for a particular railway vehicle simulation scenario. The third numerical application consists of the hunting stability analysis of a suspended wheelset. The results obtained with the proposed method for the lateral displacements and yaw rotations of the wheelset are compared with those obtained with semi-analytical models described by Knothe and Böhm (1999) and Valtorta et al. (2001). Finally, an experimental test conducted in the rolling stock test plant of the RTRI in Japan (Sogabe et al., 2006), in which a full scale railway vehicle runs over a test rig with vertical and lateral deviations, is reproduced numerically (Montenegro et al., 2015b). The results obtained

with the proposed method are compared with the experimental results, and also with the results obtained using the software DIASTARS developed by Tanabe et al. (2008).

5.2 VALIDATION OF THE IMPLEMENTED CREEP FORCE MODELS

5.2.1 Description of the analyzed cases

In the present section, the results obtained with the implemented creep force models using elliptical contact areas are compared with those obtained with the software CONTACT. The test cases shown in this section are based on the examples presented in Kalker (1990), in which the longitudinal and lateral creep forces are computed for distinct ranges of creepages and semi-axes ratios of the contact ellipse.

The comparisons are made between the following methods:

a) Kalker's exact theory of rolling contact (Kalker, 1979), implemented in the software CONTACT. This method is used as a reference due to its high level of accuracy to solve rolling contact problems;

b) Kalker's linear theory (Kalker, 1967) implemented in this work (see Section 4.5.3.1 of Chapter 4);

c) Polach method (Polach, 1999) implemented in this work (see Section 4.5.3.2 of Chapter 4);

d) Kalker's book of tables (Kalker, 1996) implemented in this work (see Section 4.5.3.3 of Chapter 4).

Four different test cases are analyzed, each of them for semi-axes ratios *a/b* of 0.1, 1 and 10. The longitudinal v_ξ, lateral v_η and spin v_ϕ creepages are normalized according to equation (4.65), while the longitudinal F_ξ and lateral F_η creep forces are normalized with respect to the product between the friction coefficient and the normal contact force μF_n (see equation (4.66)). The analyzed cases are therefore:

a) Case 1: Longitudinal and lateral creep forces for $v_\xi' = v_\eta'$ and $v_\phi' = 0$;

b) Case 2: Longitudinal and lateral creep forces for $v_\xi' = v_\phi'$ and $v_\eta' = 0$;

c) Case 3: Lateral creep forces for $v_\eta' = -v_\phi'$ and $v_\xi' = 0$;

d) Case 4: Lateral creep forces for a range of values of υ'_ϕ and $\upsilon'_\xi = \upsilon'_\eta = 0$.

5.2.2 Comparison between the creep force models

The results obtained for the Cases 1, 2, 3 and 4 described in Section 5.2.1 are plotted in Figures 5.1, 5.2, 5.3 and 5.4, respectively. All the implemented methods for computing the contact forces are suitable to deal with scenarios with small creepages. However, as the creepages become higher, the tangential stresses tend to reach the saturation limit and the Kalker's linear theory is no longer valid.

The Polach method seems to be accurate for low values of spin, but it starts to lose precision as the spin creepages increase. Nevertheless, the method takes into consideration the saturation limit of the tangential stresses, making it much more accurate than the Kalker's linear theory for high values of creepages.

Finally, the implemented book of tables based on Kalker's USETAB predicts very accurate results when compared to the exact theory. Furthermore, the computational efficiency of this method is very high, since it is based on simple linear interpolations carried out during the dynamic analysis. Hence, despite the minor errors due to the discretization of the table, that can be observed when the input values are far from the combinations of creepages and semi-axes ratios used to compute the table (see Figure 5.3), the book of tables is the most adequate method to compute the creep forces.

For all the reasons discussed above, unless otherwise stated, the implemented book of tables is used in all the dynamic simulations presented in this thesis.

(a) F_ξ' with $a/b = 0.1$

(b) F_η' with $a/b = 0.1$

(c) F_ξ' with $a/b = 1$

(d) F_η' with $a/b = 1$
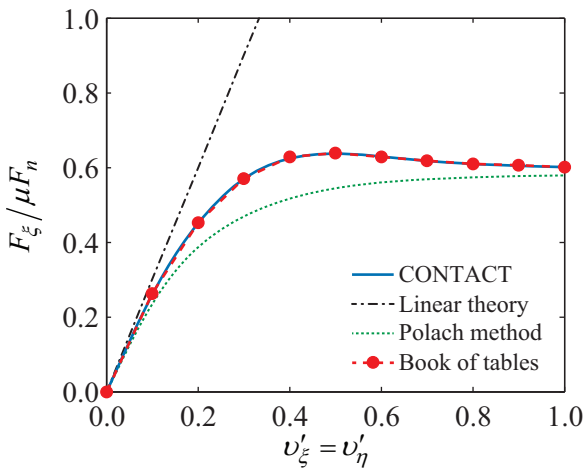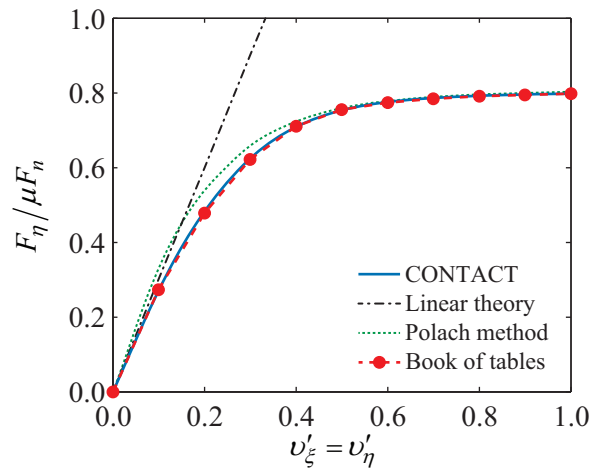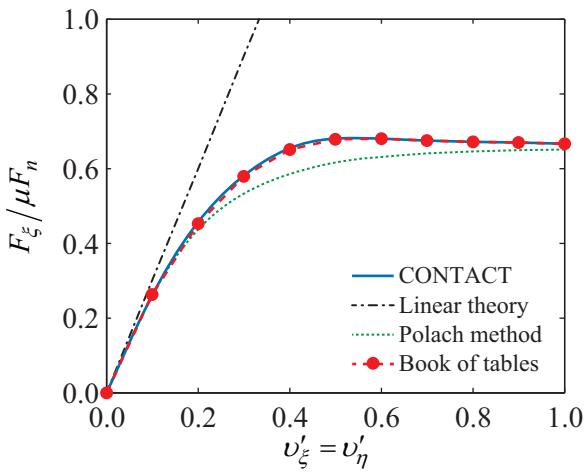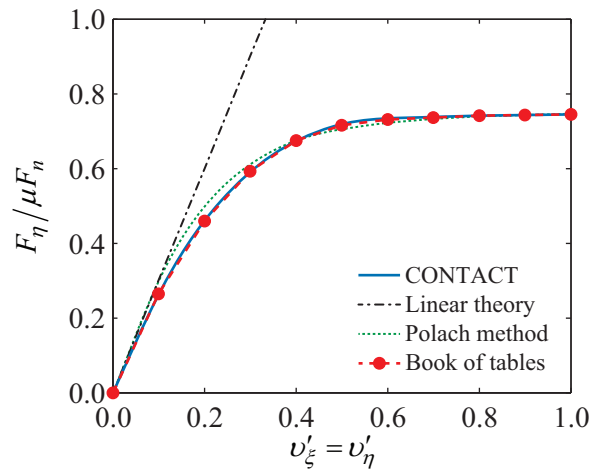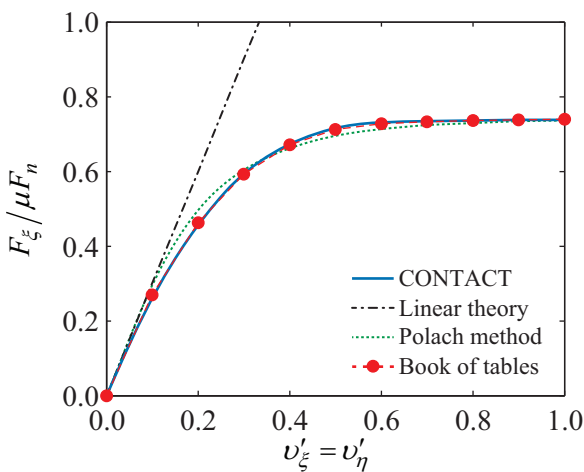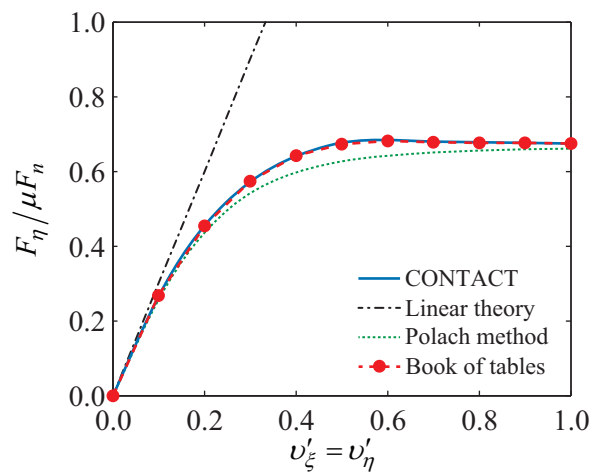
(e) F_ξ' with $a/b = 10$

(f) F_η' with $a/b = 10$

Figure 5.1 - Case 1: Longitudinal and lateral creep forces for $\upsilon_\xi' = \upsilon_\eta'$ and $\upsilon_\phi' = 0$.

(a) F'_ξ with $a/b = 0.1$

(b) F'_η with $a/b = 0.1$

(c) F'_ξ with $a/b = 1$

(d) F'_η with $a/b = 1$
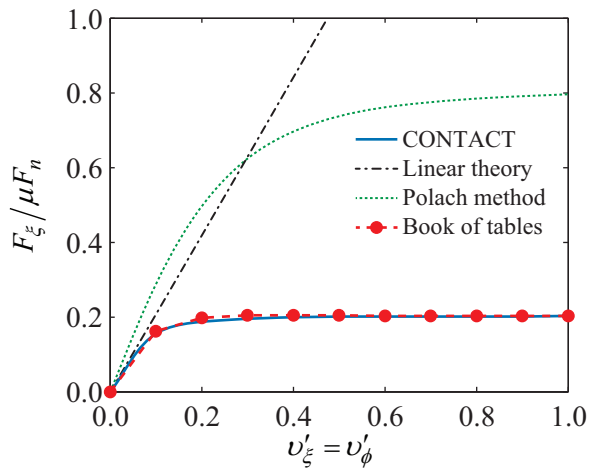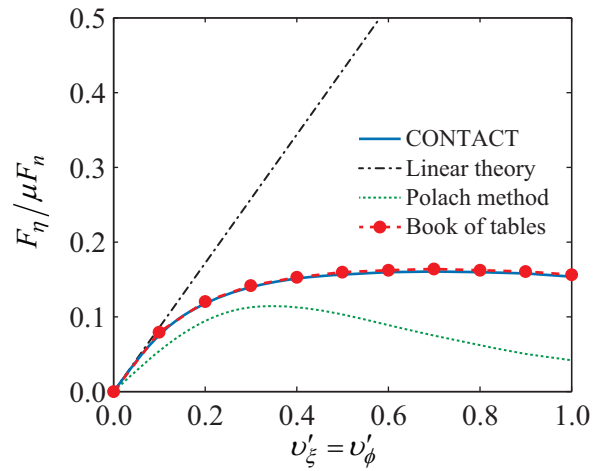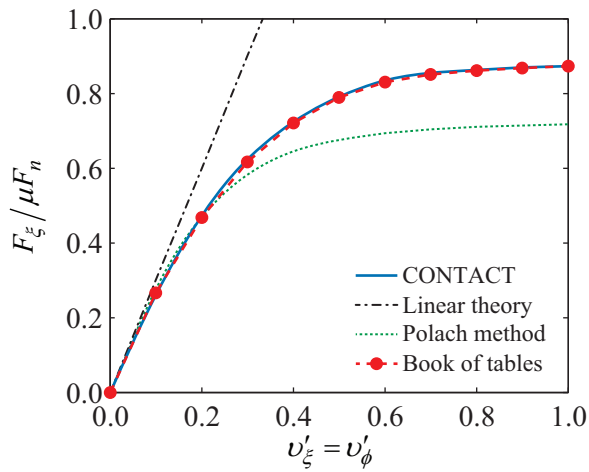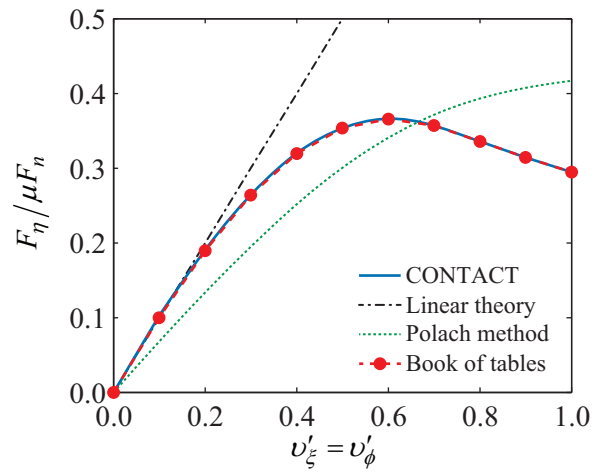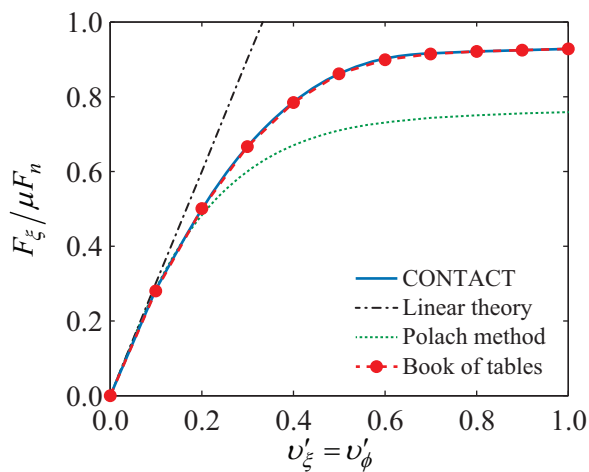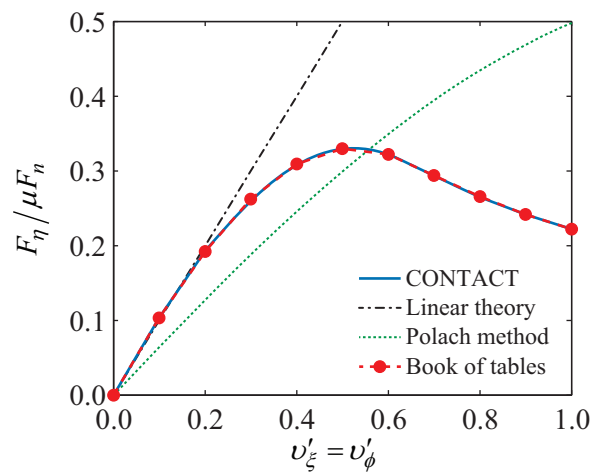
(e) F'_ξ with $a/b = 10$

(f) F'_η with $a/b = 10$

Figure 5.2 - Case 2: Longitudinal and lateral creep forces for $\upsilon'_\xi = \upsilon'_\phi$ and $\upsilon'_\eta = 0$.

(a) F'_η with $a/b = 0.1$

(b) F'_η with $a/b = 1$
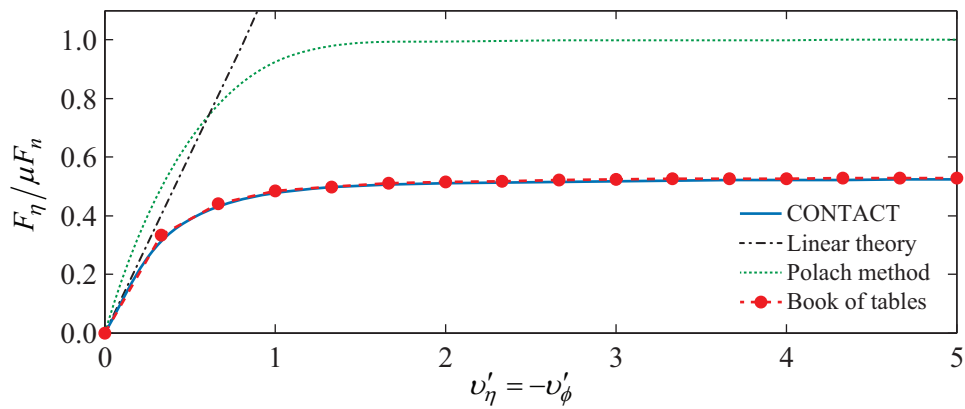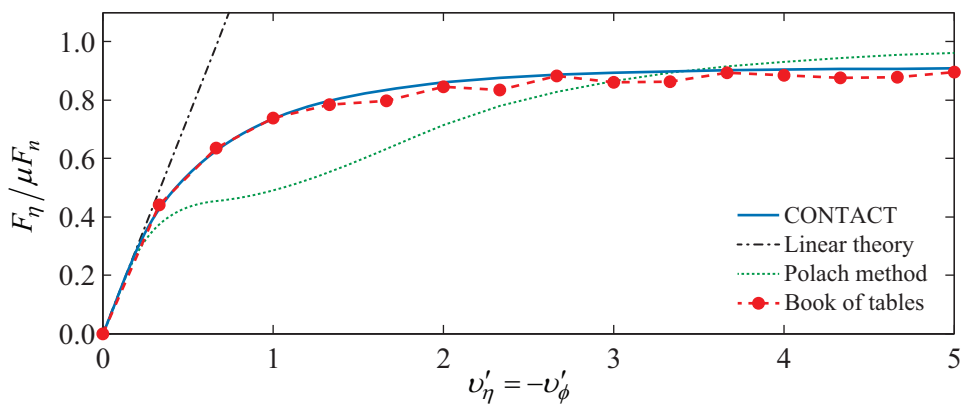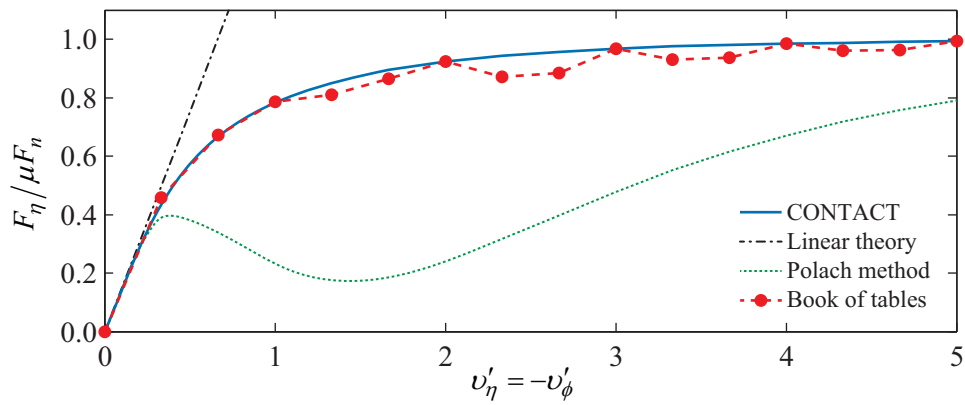
(c) F'_η with $a/b = 10$

Figure 5.3 - Case 3: Lateral creep forces for $\upsilon'_\eta = -\upsilon'_\phi$ and $\upsilon'_\xi = 0$.

(a) F_η' with $a/b = 0.1$

(b) F_η' with $a/b = 1$
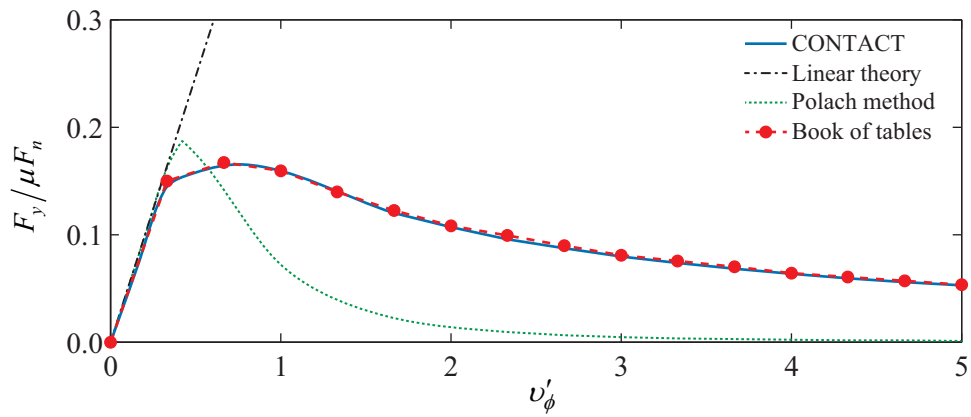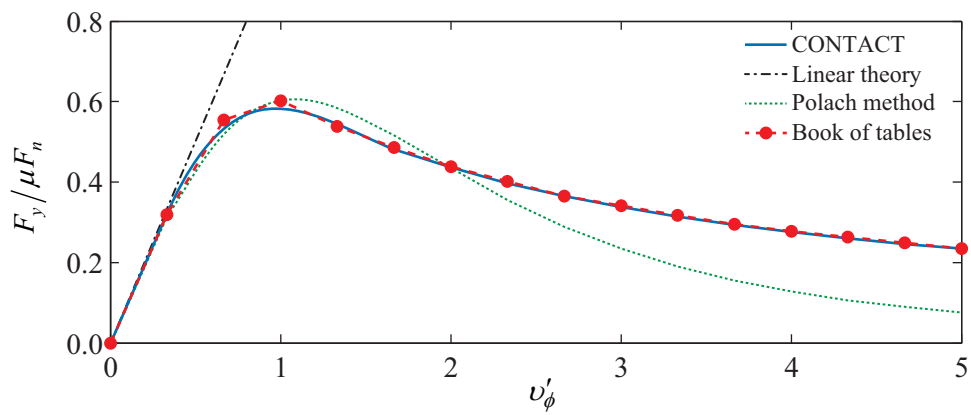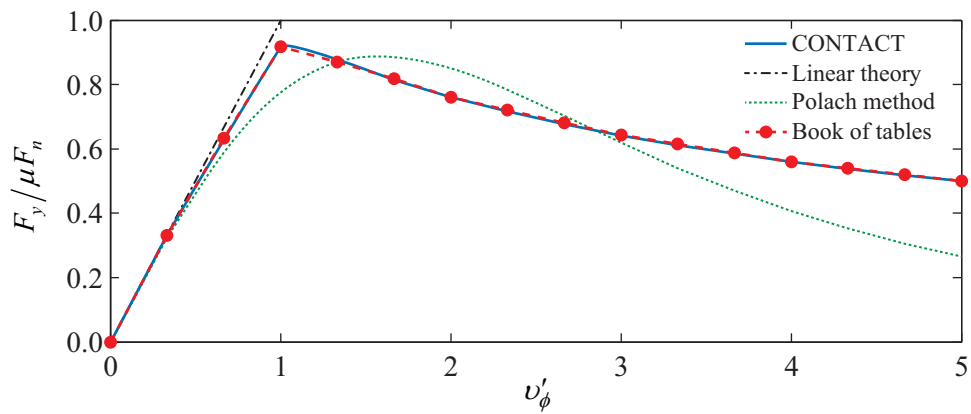
(c) F_η' with $a/b = 10$

Figure 5.4 - Case 4: Lateral creep forces for a range of values of υ_ϕ' and $\upsilon_\xi' = \upsilon_\eta' = 0$.

5.3 THE MANCHESTER BENCHMARK

5.3.1 Description of the benchmark

Shackleton and Iwnicki (2006) proposed a benchmark with the aim of allowing an informed choice when selecting a contact model for a particular railway vehicle simulation scenario. There is a wide range of wheel-rail contact models in the vehicle simulation softwares and, to achieve acceptable computational times, all of them make simplifying assumptions. As a result, each model has a limit of its validity and restrictions to its applications that are not always apparent to the user. Thus, the Manchester Metropolitan University conducted a series of tests with ten railway vehicle simulation softwares and compared the results. These softwares vary in the way they establish the position of the contact point between the wheel and the rail, in the manner in which they predict the size and shape of the contact area and in terms of the methods used to simulate the forces that are generated in the contact interface. Table 5.1 summarizes the formulations adopted by each software to solve the contact problem.

Table 5.1 - Formulations adopted by each tested software in the Manchester Benchmark to solve the normal and tangential contact problems (Shackleton and Iwnicki, 2008).

Software	Normal contact formulation	Tangential contact formulation
CONPOL	Hertzian	FASTSIM
CONTACT PC92	CONTACT	CONTACT
DYNARAIL	Hertzian and Multi-Hertzian	USETAB
GENSYS	Non-Hertzian (equivalent contact ellipses)	FASTSIM
LaGer	CONTACT	CONTACT
OCREC	Multi-Hertzian	FASTSIM
NUCARS	Multi-Hertzian	Lookup tables based on DUVOROL
TDS CONTACT	Hertzian	FASTSIM
VAMPIRE	Hertzian	Lookup tables based on DUVOROL
VOCOLIN	Semi-Hertzian	FASTSIM

The tests consisted of prescribing, both statically and dynamically, lateral displacements and yaw rotations to a single wheelset in order to analyze its behavior. Four case studies were conducted during the benchmark with real wheel and rail profiles, S1002 wheel and UIC60 rail with a 1:40 inclination, as depicted in Figure 5.5, and a vertical load of 20 kN applied at the center of mass of the wheelset. These case studies are the following:

a) Case A1.1: the wheelset is subjected to a prescribed lateral displacement from 0 to 10 mm with 0.5 mm increments. A static analysis is performed in each position and the normal contact is evaluated;

b) Case A1.2: the wheelset is subjected to the previously described lateral displacements combined with a yaw rotation from 0 to 24 mrad with 1.2 mrad increments. A static analysis is performed in each position and the normal contact are evaluated;

c) Case A2.1: forward speed of 2 m.s^{-1} is given to the wheelset on straight track while it is subjected to the previously described lateral displacements. A dynamic analysis is performed and both the normal and tangential contact are evaluated;

d) Case A2.2: the wheelset is subjected to the combinations of lateral displacements and yaw rotations described in the case A1.2. The dynamic conditions are the same as for the case A2.1 and both the normal and tangential contact is evaluated.
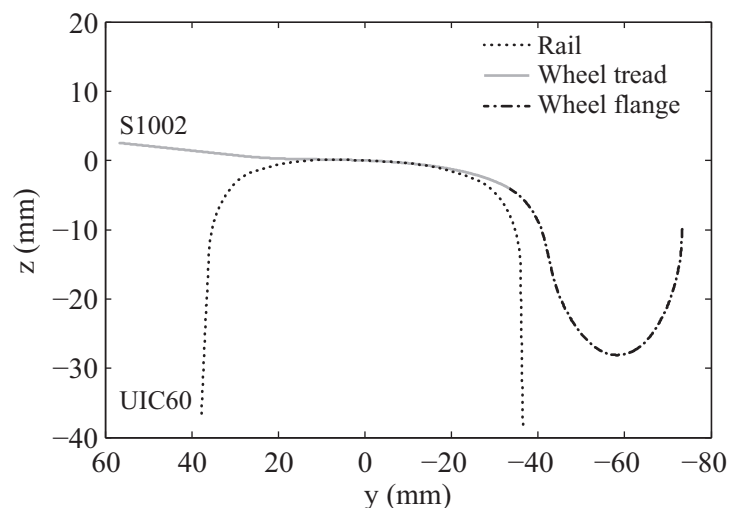
Figure 5.5 - Wheel and rail profiles used in the benchmark.

5.3.2 Analysis results

The results obtained with the proposed method described in Chapter 4 are compared with those obtained with the tested softwares. The local coordinate systems considered in the benchmark, as well as the adopted conventions, are described in Shackleton and Iwnicki (2006) and in the Appendix B of Shackleton and Iwnicki (2008). Each tested code has been assigned a line/marker style, being the results obtained with the proposed method superimposed over those codes.

5.3.2.1 Contact point positions

Figures 5.6 and 5.7 shows the lateral position of the contact point in the rails and wheels, respectively, defined in the local coordinate systems adopted in the benchmark, for the case A1.1 and for each wheelset lateral position y_{ws}. The solid line without a marker illustrates the rail and wheel profile. The proposed method shows a good agreement with the majority of the tested codes in both the convex and the concave regions of the wheel, validating the contact search approaches presented in Section 4.3.2 of Chapter 4, respectively.
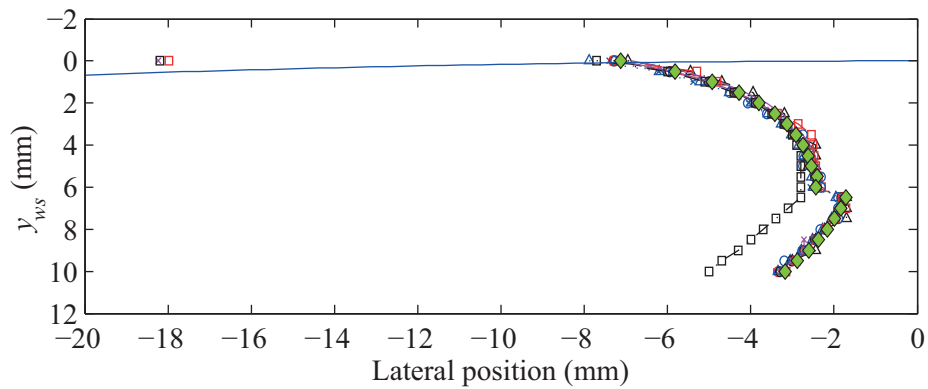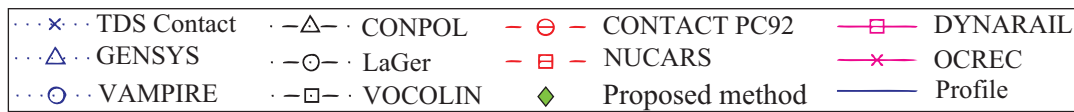
(a)
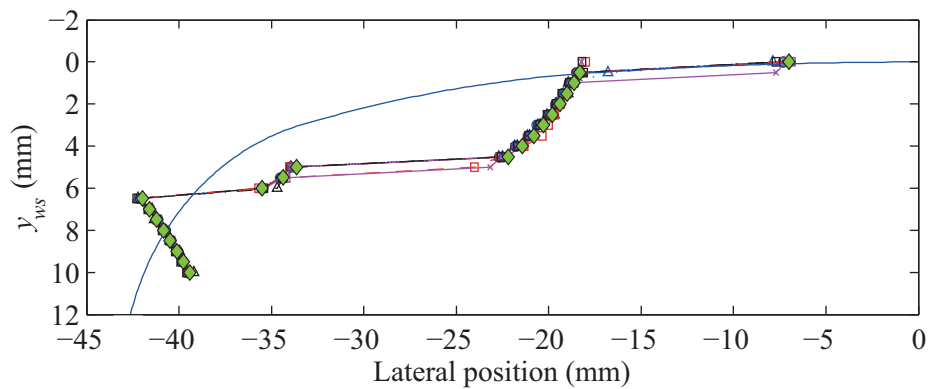
(b)

Figure 5.6 - Rail lateral contact positions in case A1.1: (a) left and (b) right rails (adapted from Shackleton and Iwnicki (2008)).
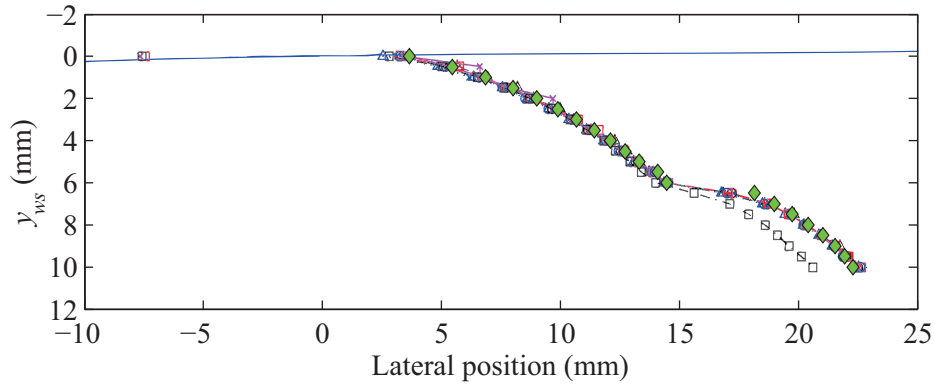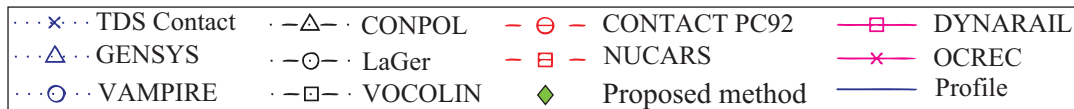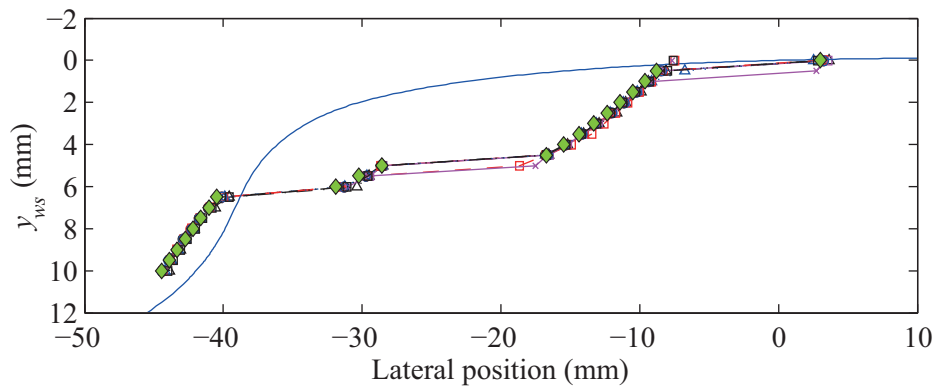
Figure 5.7 - Wheel lateral contact positions in case A1.1: (a) left and (b) right wheels (adapted from Shackleton and Iwnicki (2008)).

5.3.2.2 *Rolling radius difference*

The rolling radius difference $\varDelta R$ between the left and right wheels obtained in the test case A1.1 is plotted in Figure 5.8. Again, a good agreement can be observed between the proposed method and the tested softwares. It can be seen that for lateral displacements between 4.5 and 6 mm, the contact occurs in the tread/flange transition of the right wheel, causing a small increase in the rolling radius. After 6 mm, however, the contact point jumps to the flange, leading to an abrupt increase in the right rolling radius and, consequently, in the rolling radius difference between the two wheels.
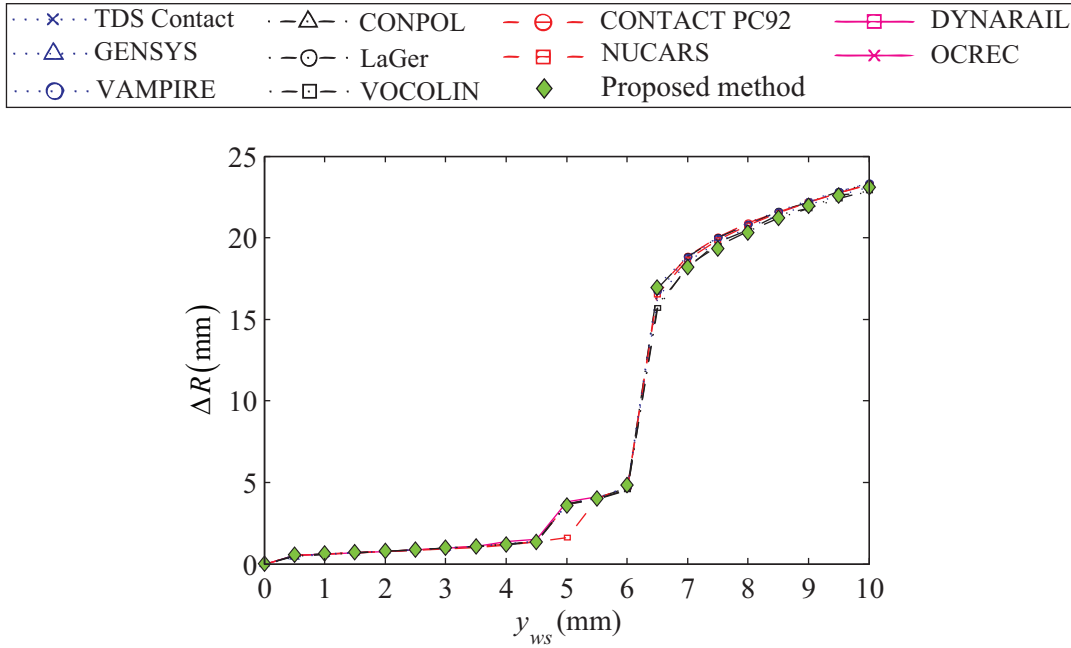
Figure 5.8 - Rolling radius difference between right and left wheels in case A1.1 (adapted from Shackleton and Iwnicki (2008)).

5.3.2.3 Contact angles

Figure 5.9 presents the contact angles in the left γ_{lft} and right γ_{rht} wheels obtained in the test case A1.2, in which the lateral displacement of the wheelset is combined with yaw rotations. The contact angle in the right wheel reaches the maximum value for a lateral displacement of 6.5 mm accompanied by a yaw rotation of 15.6 mrad and, like the rolling radius difference, suffers an abrupt increase when the contact point jumps to the flange. The results obtained with the proposed method for the right contact angle show a good match with those obtained with all the tested softwares. Regarding the left contact angle, the proposed method follows the same trend as the softwares GENSYS, NUCARS and VAMPIRE, which are widely used in railway vehicle simulations. The other two trends are followed by VOCOLIN and by the softwares LaGer and CONTACT PC92. The discrepancies obtained with VOCOLIN derive from the non-consideration of the roll rotation of the wheelset to locate the contact point, while the trend followed by LaGer and CONTACT PC92 is justified by the fact that the output given by these codes are related to the wheelset coordinate system rather than to the track centerline coordinate system (see Appendix A for the definition of these coordinate systems).
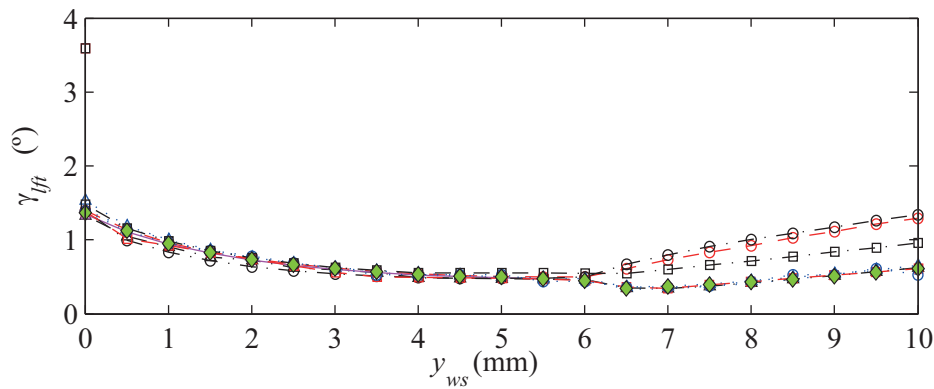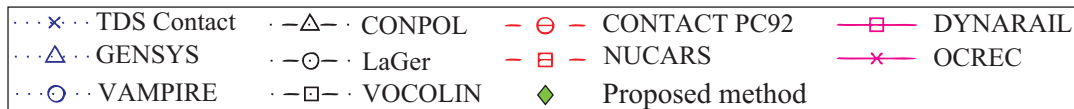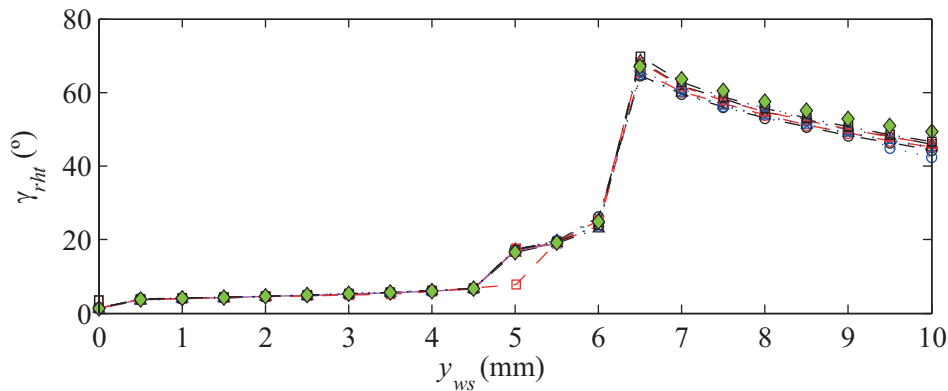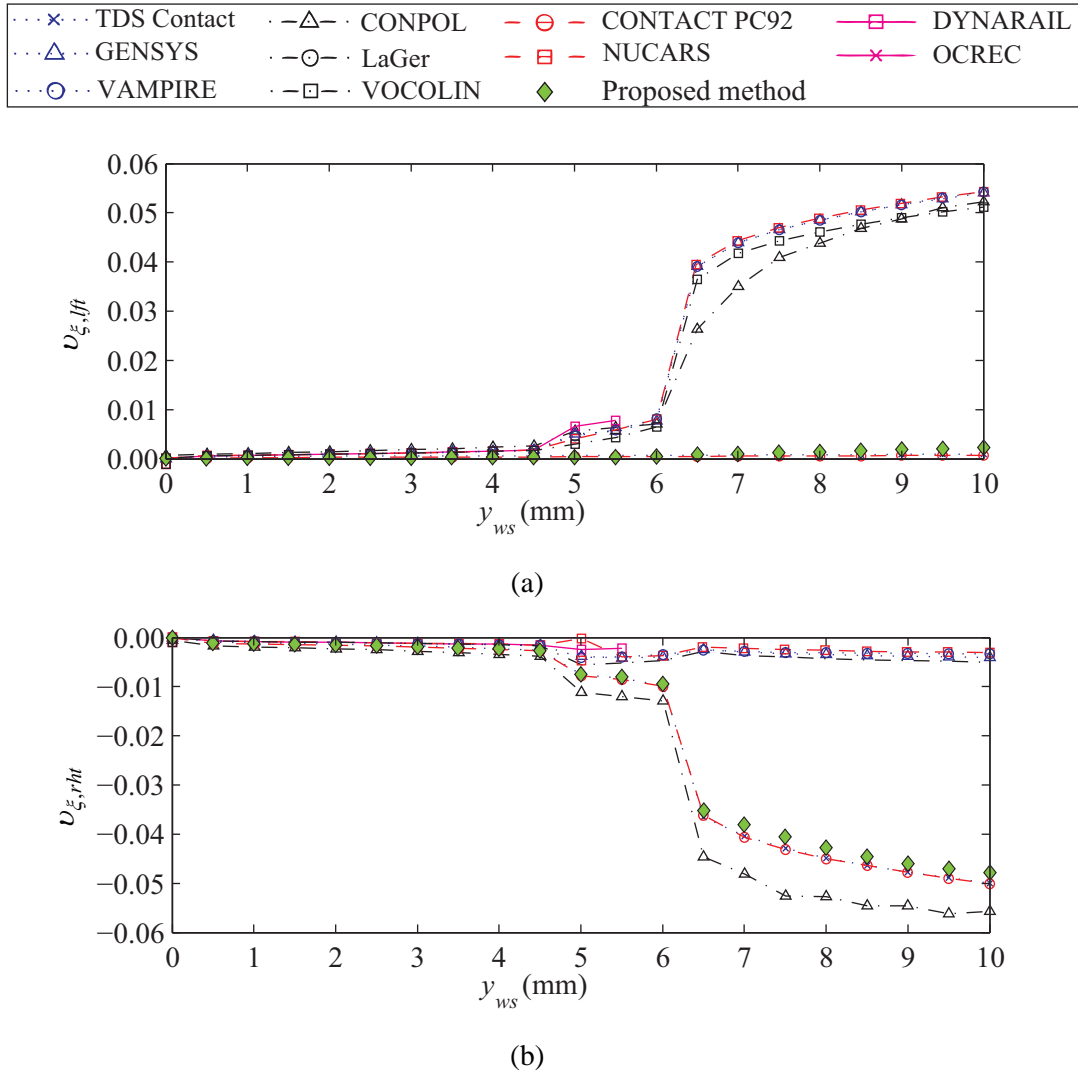
Figure 5.9 - Contact angle in case A1.2: (a) left and (b) right contact interfaces (adapted from Shackleton and Iwnicki (2008)).

5.3.2.4 Longitudinal creepages

The longitudinal creepages in the left and right contact interfaces obtained in the dynamic test case A2.1 are plotted in Figure 5.10. According to Shackleton and Iwnicki (2008), the lack of conformity between the results predicted by the several codes is due to differences in the way the total longitudinal creepage is distributed between the left and right contact interfaces. Therefore, in absolute terms, the output of the proposed method is in agreement with the outputs obtained with the softwares tested during the benchmark, except CONPOL, which follows an isolated trend.

(a)

(b)

Figure 5.10 - Longitudinal creepages in case A2.1: (a) left and (b) right contact interfaces (adapted from Shackleton and Iwnicki (2008)).

5.3.2.5 *Lateral creepages*

The lateral creepages calculated in the test case A2.2 are presented in Figure 5.11. Since the lateral creepages obtained in the left contact interface have not been published in Shackleton and Iwnicki (2008), only the results of the right interface are presented. As can be seen in Figure 5.11, the results given by the proposed method accompanies the main trend followed by all codes, except CONPOL, which again shows a different output. These differences are justified by the fact that CONPOL neglects the effects of the yaw angle of the wheelset in the calculation of the creepages. This important limitation also affects the spin creepages, as will be shown in the next section.
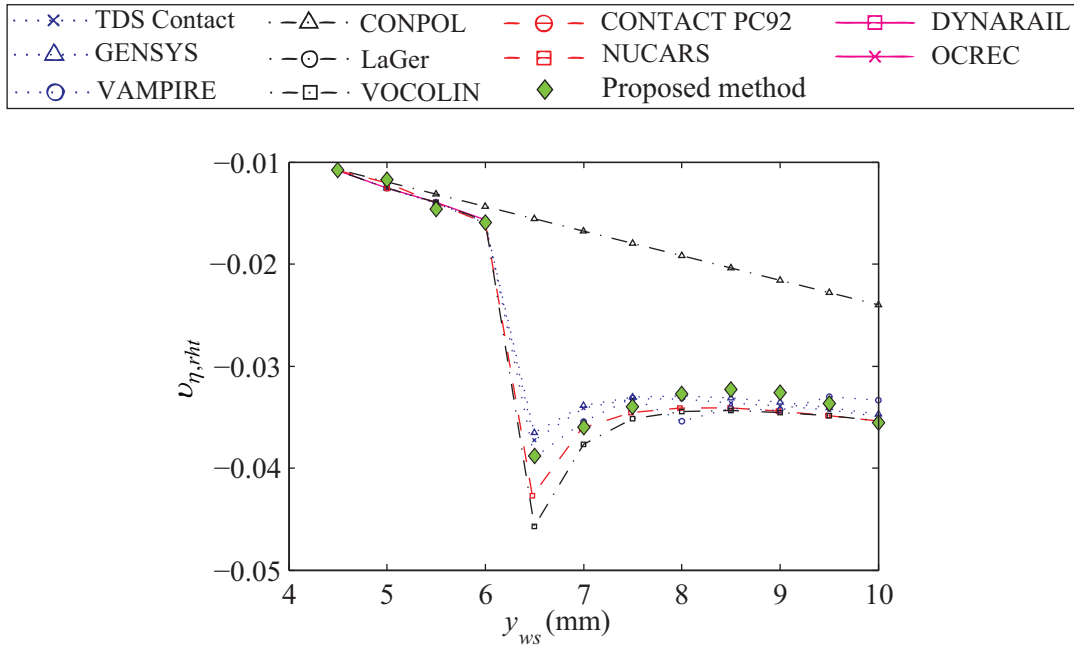
Figure 5.11 - Lateral creepages at the right contact interface in case A2.2 (adapted from Shackleton and Iwnicki (2008)).

5.3.2.6 Spin creepages

Finally, the spin creepages in the left and right contact interfaces obtained in the test case A2.2 are plotted in Figure 5.12. The spin creepages follows the same trend as the contact angle (see Figure 5.9), since they depend directly on it. Therefore, the different trends observed in the left side are justified by the same reasons presented in Section 5.3.2.3, while the discrepancies obtained with CONPOL in the right side are, once more, due to the non-consideration of the yaw angle effects in the calculation of the creepages.

Regarding the proposed method, a good agreement is observed between the results obtained with it in the right contact interface and those obtained with the softwares tested during the benchmark, with exception to CONPOL for the reasons stated above. In the left side, the proposed method follows again the same trend as GENSYS and VAMPIRE.
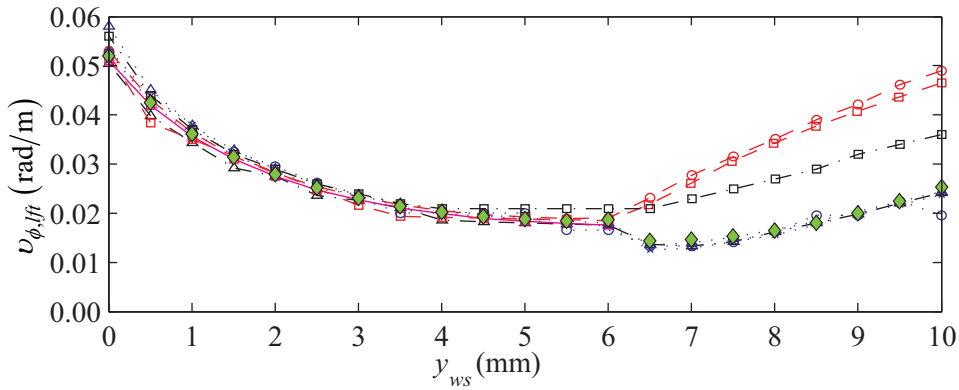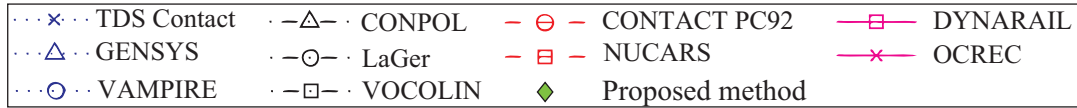
(a)
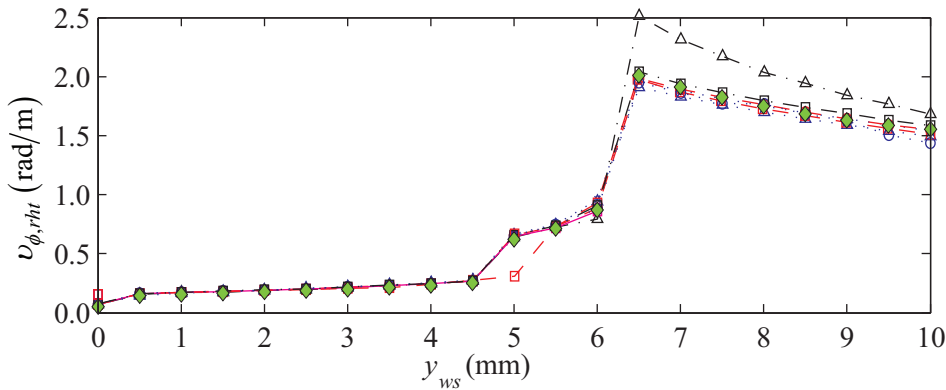
(b)

Figure 5.12 - Spin creepages in case A2.2: (a) left and (b) right contact interfaces (adapted from Shackleton and Iwnicki (2008)).

5.3.2.7 Conclusions

Although a general agreement between the tested softwares and the proposed method is observed, there are, in some cases, notable discrepancies. However, the main discrepancies are mainly justified by limitations of the contact models adopted by some of the tested softwares, especially CONPOL and VOCOLIN, rather than by limitations of the proposed method. Moreover, the results obtained with the proposed method are, in most cases, in an excellent agreement with those obtained with GENSYS, NUCARS and VAMPIRE, which are widely used in dynamic simulations of railway vehicles. Therefore, it can be concluded that the wheel-rail contact model developed in this work is suitable for being used in railway dynamics applications.

5.4   HUNTING STABILITY ANALYSIS OF A SUSPENDED WHEELSET

5.4.1   The hunting phenomenon

Due to the specific conic shape of the train wheels, when a wheelset is running on a straight track and is subjected to a lateral perturbation, the rolling radii of the left and right wheel differ from each other. Hence, since both wheels have the same angular velocity if the wheelset is running with a constant speed, the wheel with larger radius will experiment a higher velocity than the opposite wheel. This phenomenon will force the wheelset to yaw and go back to the centered position, making the rolling radius of the opposite wheel to become larger. This process, called hunting motion (see Figure 5.13), tends to continue indefinitely in an unsuspended wheelset making it unstable (Garg and Dukkipati, 1984; Andersson et al., 1999; Wickens, 2003). However, the creep forces that arise in the contact interface act as damping forces that dissipate energy and ensure the existence of a certain range of speeds where the wheelset is stable. The speed above which the wheelset become unstable is called critical speed. In addition to the creep forces, the critical speed of a wheelset also depends on the wheel conicity, wheelset mechanical properties and suspensions. The last one is particularly important to ensure that the wheelset instability occurs only at higher ranges of speeds.
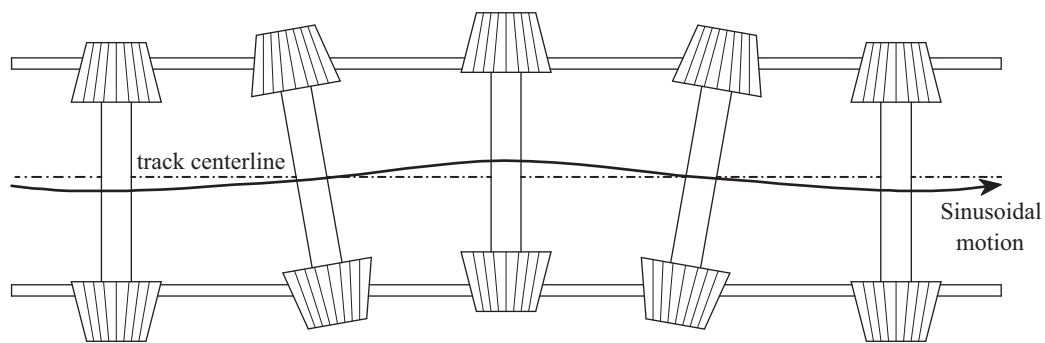
Figure 5.13 - Schematic representation of the hunting motion.

When a wheelset experiences the hunting motion, its center of gravity follows an almost sinusoidal lateral motion around the track centerline, as illustrated in Figure 5.13. Klingel (1883) was the first author to derive an expression which describes this motion on a non-suspended wheelset. Based on purely kinematic relationships, Klingel proposed the following expression for the wavelength $\lambda_{Klingel}$ of the hunting motion:

$$\lambda_{Klingel} = 2\pi \sqrt{\frac{L_{cp} R_0}{\gamma_0}} \tag{5.1}$$

127

where R_0 the initial rolling radius of the wheel, L_{cp} is the half lateral distance between contact points and γ_0 is the conicity of the wheels. However, as aforementioned, this expression only considers the kinematic components of the movement, ignoring the inertial effects due to the mass of the wheelset, the influence of the suspensions flexibility, the creep forces that arise in the contact interface and the real shape of the wheels (the wheels are perfectly conical in the Klingel's model). Hence, in order to allow a reliable validation of the proposed method, a fully dynamic model of the wheelset is adopted.

5.4.2 Numerical model

The numerical model consists of a single suspended wheelset connected to a moving frame by lateral and longitudinal suspensions, as shown in Figure 5.14.
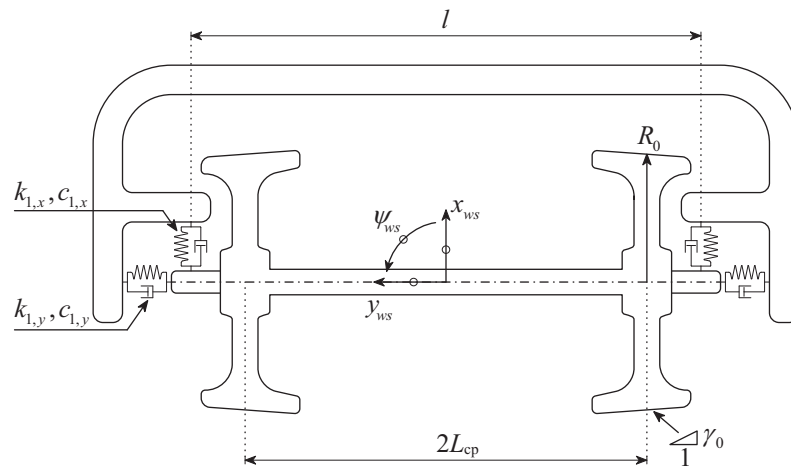
Figure 5.14 - Dynamic model of a suspended wheelset connected to a moving frame (top view).

The geometrical and mechanical properties of the model, which are based on those defined by Valtorta et al. (2001), are presented in Table 5.2. Note that the contact ellipse semi-axes a and b, as well as the Kalker creepage coefficients c_{11} and c_{22}, are calculated for a static position of the wheelset centered with the track and maintained constant throughout the analysis.

Table 5.2 - Geometrical and mechanical properties of the suspended wheelset model (based on Valtorta et al. (2001)).

Variable	Description	Value
m_{ws}	Wheelset mass	1568 kg
$I_{x,ws}$	Roll mass moment of wheelset	656 kg.m^2
$I_{y,ws}$	Pitch mass moment of wheelset	168 kg.m^2
$I_{z,ws}$	Yaw mass moment of wheelset	656 kg.m^2
$k_{1,x}$	Stiffness of the longitudinal primary suspensions	135 kN/m
$k_{1,y}$	Stiffness of the lateral primary suspensions	250 kN/m
$c_{1,x}$	Damping of the longitudinal primary suspensions	0 kN/m.s
$c_{1,y}$	Damping of the lateral primary suspensions	0 kN/m.s
P_{ws}	Applied vertical load	98 kN
a	Contact ellipse longitudinal semi-axis	5.667 mm
b	Contact ellipse lateral semi-axis	4.284 mm
c_{11}	Longitudinal creepage coefficient	4.523
c_{22}	Lateral creepage coefficient	4.121
R_0	Initial rolling radius	456.6 mm
γ_0	Conicity	0.025
$2L_{cp}$	Lateral distance between initial contact points	1435 mm
l	Distance between longitudinal suspensions	1800 mm

5.4.3 Governing equations of motion of the semi-analytical model

The results obtained with the proposed method are compared with those obtained with a semi-analytical model described by several authors (Knothe and Böhm, 1999; Valtorta et al., 2001; Wickens, 2003). Wickens (2003) considered a number of simplifying assumptions in the model, which are also adopted in the present work for validation purposes. These are:

a) The wheelset is rigid and is connected to a reference moving frame by lateral and longitudinal suspensions;

b) The running speed of the wheelset is constant;

c) The wheelset movement is characterized exclusively by two degrees of freedom: the lateral displacement y_{ws} and the yaw rotation ψ_{ws} (see Figure 5.14);

d) The profile of the wheels is perfectly conic;

e) The assumptions of the Hertz theory (see Section 4.4.1 of Chapter 4) are valid and the dimensions of contact area remain constant throughout the analysis;

f) The slip inside the contact area is neglected, being the tangential contact problem solved with the Kalker's linear theory (see Section 4.5.3.1 of Chapter 4).

Based on these assumptions, the linear equations of motions that governs the dynamics of the system can be written as

$$
\begin{bmatrix} m_{ws} & 0 \\ 0 & I_{z,ws} \end{bmatrix} \begin{bmatrix} \ddot{y}_{ws} \\ \ddot{\psi}_{ws} \end{bmatrix} + \frac{2}{V} \begin{bmatrix} f_y & 0 \\ 0 & L_{cp}^2 f_x \end{bmatrix} \begin{bmatrix} \dot{y}_{ws} \\ \dot{\psi}_{ws} \end{bmatrix} + 2 \begin{bmatrix} k_y & -f_y \\ \dfrac{L_{cp}\gamma_0}{R_0} f_x & k_x l^2 \end{bmatrix} \begin{bmatrix} y_{ws} \\ \psi_{ws} \end{bmatrix} = \begin{bmatrix} 0 \\ 0 \end{bmatrix} \tag{5.2}
$$

where V is the forward speed of the wheelset, $f_x = G c_{11} ab$ and $f_y = G c_{22} ab$. The remaining variables present in equation (5.2) are described in Table 5.2. The secondary effects, such as gravitational stiffness, gyroscopic effects and spin creep, are neglected in the present study. The system of linear differential equations (5.2) can be solved using a direct integration method, such as Newmark (Clough and Penzien, 2003) or α method (Hughes, 2000).

The speed above which the wheelset become unstable, called critical speed V_{crit}, can be determined from a stability study described in detail in Antolín (2013) and is given by

$$
V_{crit} = \sqrt{ \dfrac{ 2l^2 \left(\dfrac{k_{1x}}{f_x} + \dfrac{k_{1y}}{f_y} \right) \left(\dfrac{m_{ws} l^2}{f_y} + \dfrac{I_{z,ws}}{f_x} \right) }{ \left(\dfrac{m_{ws} l^2}{f_y} + \dfrac{I_{z,ws}}{f_x} \right)^2 \dfrac{\gamma_0}{L_{cp} R_0} - \left(\dfrac{m_{ws} l^2}{f_y} \dfrac{k_{1x}}{f_x} + \dfrac{I_{z,ws}}{f_x} \dfrac{k_{1y}}{f_y} \right)^2 } } \tag{5.3}
$$

For running speeds below the critical value, the wheelset experiences a sinusoidal lateral motion that tends to damp out if no further disturbances occur. However, if the critical speed is exceeded, the wheelset undergoes an increasing oscillatory motion that makes it unstable.

The hunting wavelength is also a characteristic of the hunting motion of the wheelset, since is independent from the running speed. By performing a quasi-static analysis of the dynamic equations of motion, the theoretical hunting wavelength λ_{theory} is found to be (Antolín, 2013)

$$
\lambda_{theory} = 2\pi \sqrt{ \left[\dfrac{\gamma_0}{L_{cp} R_0} - \left(\dfrac{k_{1x}}{2f_x} - \dfrac{k_{1y}}{2f_y} \right)^2 \right]^{-1} } \tag{5.4}
$$

Notice that the theoretical hunting wavelength expressed in equation (5.4) becomes equal to the wavelength proposed by Klingel, defined in equation (5.1), if the dynamic terms are neglected.

5.4.4   Analysis results

The results obtained with the numerical integration of the system of equations (5.2) are compared with those obtained with the proposed train-structure interaction method described in Chapter 4. The time step used in all the analysis with both the numerical and semi-analytical models is $\Delta t = 0.001 \text{s}$ and the total number of time steps is 8000. The Newmark integration scheme (Clough and Penzien, 2003) with integration parameters $\alpha = 0$, $\beta = 0.25$ and $\gamma = 0.5$ is used to solve the equations of motion. At the beginning of the dynamic analysis, a lateral impulsive load of 100 N is applied at the center of mass of the wheelset in order to drive the system away from its equilibrium position, causing it to oscillate over the track centerline. Since the equations that govern the dynamic behavior of the analytic model are based on the assumption that there is no slip inside the contact area (see equation (5.2)), the Kalker's linear model is adopted to compute the creep forces in the simulations performed in the present section.

For the wheelset considered in the present problem, the critical speed calculated with equation (5.3) is $V_{crit} = 234.4$ km/h. Thus, the response of the wheelset when it is running at a speed below and above the critical value is evaluated. Figures 5.15 and 5.16 show the comparison between the responses of the wheelset obtained with the proposed method and with the semi-analytical equations of motion expressed by equation (5.2), for a running speed of 100 km/h and 250 km/h, respectively. The results obtained with both formulations show a good agreement, with slight differences observed in the solution regarding the wheelset running above the critical speed. These differences may be justified by the fact that the numerical model accounts for a minimum flexibility to avoid numerical instabilities, since it is developed in a finite element method framework. As expected, when the wheelset runs below the critical speed, the energy dissipation due to the creep forces and the stability provided by the primary suspensions lead to a decrement of the hunting amplitude. On the other hand, when the wheelset travels at 250 km/h the behavior becomes unstable and the system does not return to the centered position.

Regarding the hunting wavelength, which is independent from the running speed, the numerical values obtained for the analysis below and above the critical speed are, respectively, $\lambda_{100} = 22.618$ m and $\lambda_{250} = 22.710$ m. These values are in a good agreement with the theoretical value calculated with equation (5.4), which is found to be $\lambda_{theory} = 22.754$ m.
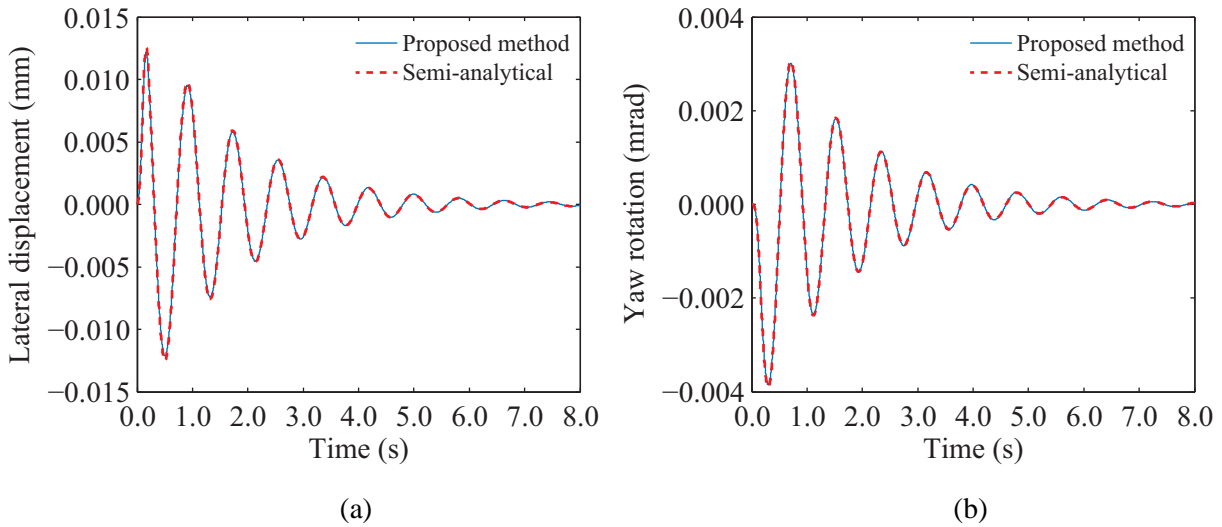

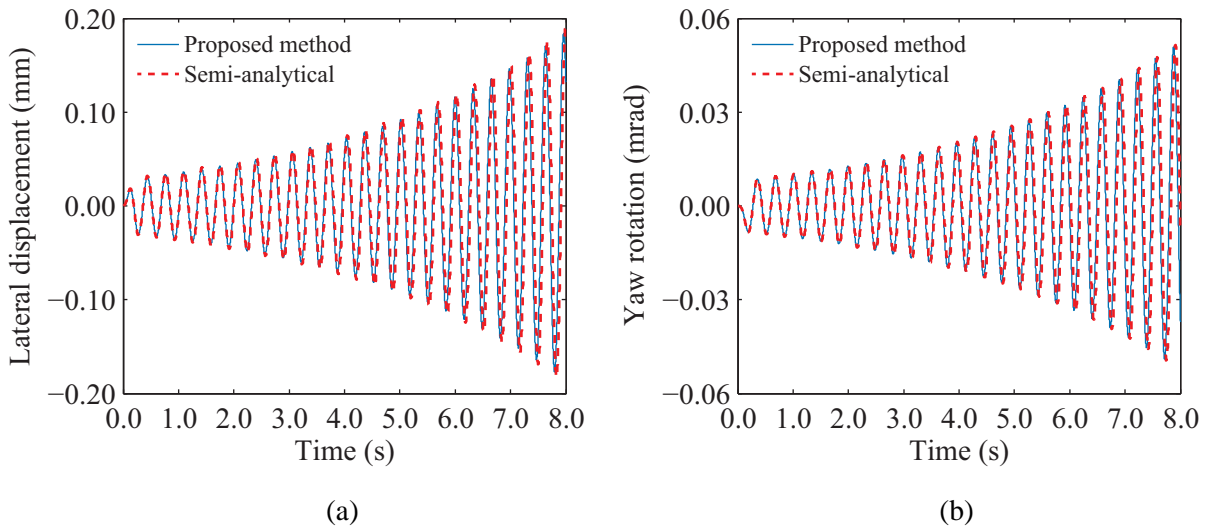Figure 5.15 - Wheelset response for $V = 100$ km/h: (a) lateral displacement and (b) yaw rotation.

Figure 5.16 - Wheelset response for $V = 250$ km/h: (a) lateral displacement and (b) yaw rotation.

The lateral displacement of the wheelset for three different running speeds, including the critical speed, is plotted in Figure 5.17. As the speed increases, the oscillation decay rate tends to decrease, reaching a null value at the critical speed. After that, the hunting motion grows indefinitely and the behavior of the wheelset becomes unstable.
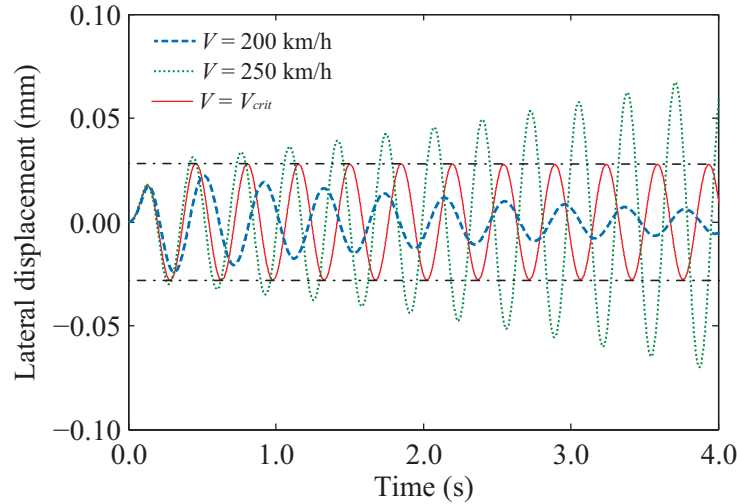
Figure 5.17 - Wheelset lateral displacement for three different running speeds.

The critical speed is therefore a transition in the dynamic behavior of the wheelset that can be analyzed with the logarithmic decrement factor δ_n, given by

$$\delta_n = \frac{1}{n}\ln\left(\frac{y_{ws}(t)}{y_{ws}(t+nT)}\right) \tag{5.5}$$

where $y_{ws}(t)$ and $y_{ws}(t+nT)$ are two peak displacements separated by n consecutive cycles with period T. The logarithmic decrement related to the responses of the wheelset for speeds ranging from 50 km/h to 300 km/h is depicted in Figure 5.18. As expected, the logarithmic decrement for the lower speeds is positive, but starts to decrease as the speed increases. Once the critical speed is reached, the decrement becomes null, since the hunting motion maintains the amplitude throughout the analysis, as shown in Figure 5.17. Then, once the speed exceeds the critical value, the decrement turns negative and the wheelset experiences an unstable behavior.
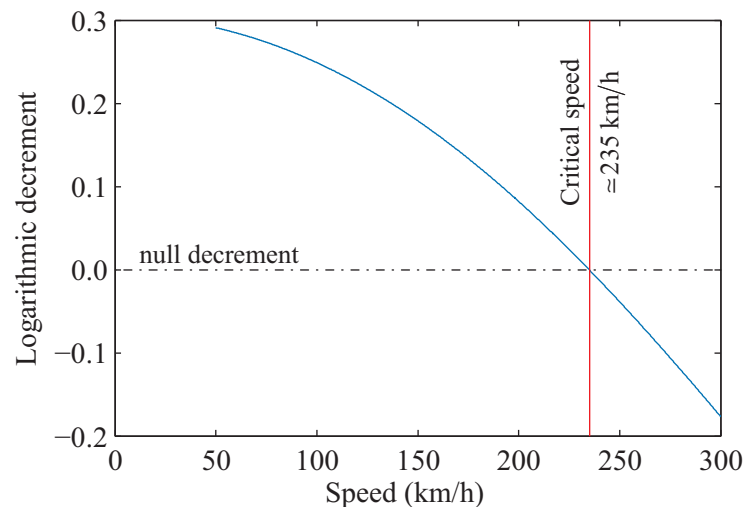
Figure 5.18 - Logarithmic decrement factor as a function of the wheelset speed.

133

5.5 SIMULATION OF AN EXPERIMENTAL TEST CONDUCTED IN A ROLLING STOCK TEST PLANT

5.5.1 Background and description of the experimental test

High-speed railway lines require a more rigorous maintenance when compared with conventional lines. Since the displacements of the structures may contribute to significant track deviations, and subsequently influence the riding comfort or the running safety of the train, deflection limits should be imposed during the design of railway structures. Such precautions are particularly important in countries prone to earthquakes, where large lateral displacements may occur during a seismic event. Japan, with one of the largest railway networks in the world, is one of those countries. Hence, in November 2000, the *Committee on Displacement Limit of Structures Associated with the Runnability of Railway Vehicles*, consisting of engineers and academics specialized in the design of railway structures and in the study of vehicle dynamics, was formed to draw a Displacement Limit Standard for Railway Structures.

Over three years, the committee draft the code provisions based on results obtained in a series of experimental tests, developed in shaking tables and rolling stock test plants using full scale test vehicles, and in numerical simulations regarding the running safety of trains. Finally, in April 2004, the committee approved the final code provision. However, due to the 2004 Mid-Niigata Earthquake that occurred on October 2004, in which a Shinkansen train derailed when running over a bridge at 200 km/h, the publication of the code was postponed, since it also included provisions regarding the running safety of trains under seismic conditions. After taking into consideration a report drawn by the Shinkansen Derailing Countermeasures Council, the Displacement Limit Standard for Railway Structures (RTRI, 2006) was finally published at the beginning of 2006.

One of the experimental tests (Sogabe et al., 2006) used to draft the Displacement Limit Standard is numerically reproduced in the present section (Montenegro et al., 2015b). The test was conducted in the rolling stock test plant in the RTRI and consisted in the analysis of a railway vehicle mounted over a test rig with four wheel-shaped rails controlled by independent actuators that can simulate different types of rail deviations (see Figure 5.19).
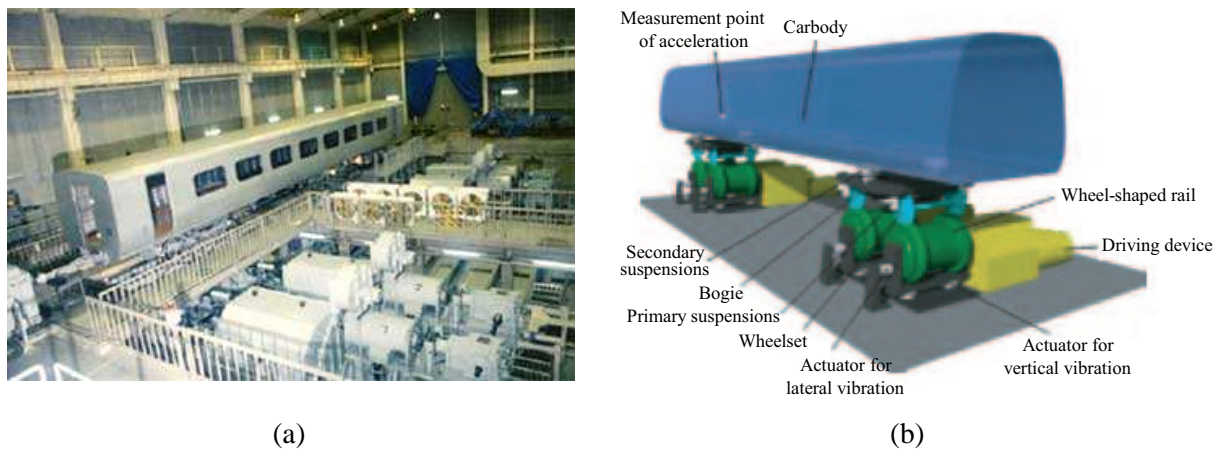
Figure 5.19 - Experimental test: (a) rolling stock test plant (RTRI, 2013) and (b) test setup (adapted from Sogabe et al. (2005)).

Both vertical and lateral deviations were imposed to the track while the vehicle ran over it. These deviations aimed to simulate track misalignments caused by the deflection of a bridge when it is subjected to an earthquake. When these situations occur, the vehicle may experience high levels of vibrations while travelling over the bridge, leading to an increased risk of derailment. The deflection types considered in the test are divided into two: a bending shape (BS), associated with the bending of two consecutive spans, and a translation shape (TS), in which only one span rotates while the other is subjected to a translation, as illustrated in Figure 5.20. Span lengths L ranging from 10 m to 60 m were also considered in the tests, together with transition sections at the ends of each span to guarantee a smooth continuity of rotations of the rail (see Figure 5.20c).
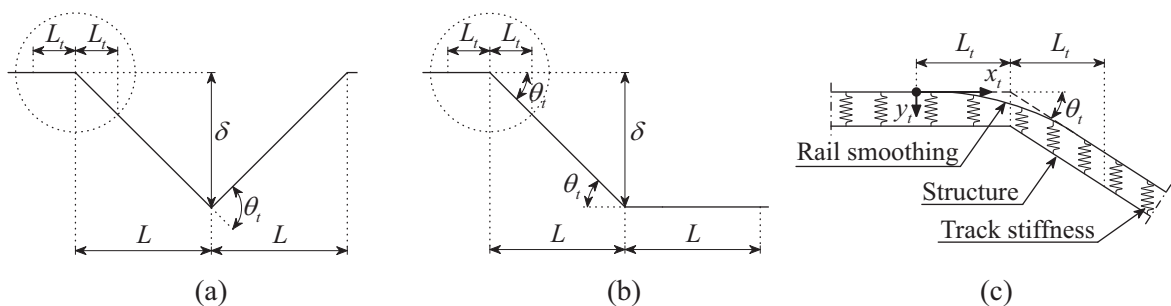
Figure 5.20 - Deflection models: (a) BS, (b) TS and (c) detail of the transition.

During the tests, the vertical and lateral accelerations of the carbody were measured above the rear bogie. The tests were conducted with a full scale railway vehicle running over the test stand at speeds ranging from 100 to 400 km/h. The maximum deflection amplitude considered in all scenarios was $\delta = 8$ mm (see Figure 5.20) for both the vertical and lateral directions.

5.5.2 Numerical model

5.5.2.1 Structure model

The structure shown in Figure 5.20 is modeled with rigid finite elements, being the track deviation introduced as irregularities in the vertical and lateral directions. The half length of the transition zone is denoted by L_t (see Figure 5.20c), the span rotation by θ_t and the distance from the start of the transition zone by x_t. This procedure avoids numerical problems associated with unrealistic impacts that may occur in abrupt transitions. Thus, according to Sogabe et al. (2005; 2006), the track deviation y_t in the transition is given by

$$y_t = \begin{cases} \dfrac{\theta_t}{4\beta_t} e^{\beta_t (x_t - L_t)} \left\{ \cos\left[\beta_t (x_t - L_t)\right] + \sin\left[\beta_t (x_t - L_t)\right] \right\} & \text{if} \quad 0 \le x_t \le L_t \\ \dfrac{\theta_t}{4\beta_t} e^{-\beta_t (x_t - L_t)} \left\{ \cos\left[\beta_t (x_t - L_t)\right] + \sin\left[\beta_t (x_t - L_t)\right] \right\} + \theta(x_t - L_t) & \text{if} \quad L_t < x_t \le 2L_t \end{cases} \tag{5.6}$$

where β_t is the relative bending stiffness of the rails and pads in the lateral direction, given by

$$\beta_t = \sqrt[4]{\frac{k_p}{4EI_r}} \tag{5.7}$$

where k_p is the pad stiffness, E the Young modulus of the steel and I_r the moment of inertia of the rail. The parameters used for defining the transition zones are summarized in Table 5.3.

Table 5.3 - Parameters of the transition zones.

Variable	Track direction	
	Vertical	Lateral
L_t	3 m	3 m
k_p	9.4×10^4 kN/m/m	47.1×10^4 kN/m/m
I_r	3090 cm^4	509 cm^4

5.5.2.2 Vehicle model

The test vehicle consists of a narrow gauge prototype car specially developed for the experimental test, whose properties were provided by the RTRI[1]. A schematic representation of the dynamic model of the test vehicle is illustrated in Figure 5.21. The springs and dampers of the suspensions are denoted by k and c and the masses and rotary inertias are indicated by m

---

[1] The geometrical and mechanical properties of the test vehicle are not published due to confidential matters from the manufacturer.

and *I*. The longitudinal, lateral and vertical distances are denoted by *a*, *b* and *h*, respectively, L_{cp} refers to half of the lateral distance between the initial contact points and R_0 is the nominal rolling radius. The subscripts *cb*, *bg* and *ws* indicate carbody, bogie and wheelset, respectively.
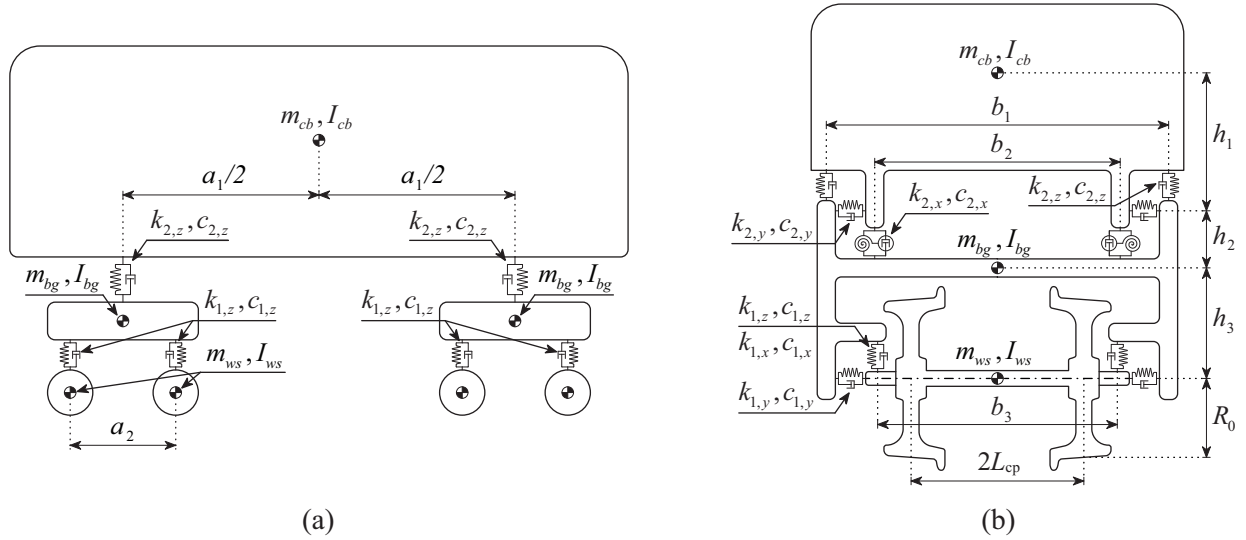

| (a) | (b) |

Figure 5.21 - Dynamic model of the test vehicle: (a) lateral view and (b) front view.

The carbody, bogies and wheelsets are modeled using beam finite elements, and the suspensions are modeled using spring-dampers in the three directions, as depicted in Figure 5.22. The masses and rotary inertias are modeled using mass point elements, located at the center of mass of each component.

| (a) | (b) |
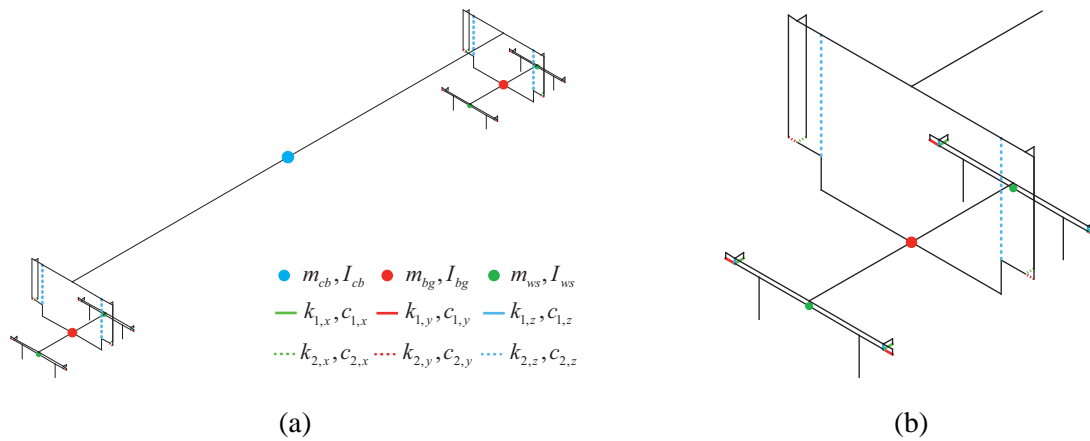
Figure 5.22 - Finite element model of the test vehicle: (a) full perspective and (b) detail of the bogie.

The numerical mode shapes and the corresponding frequencies of the test train presented in Figure 5.23 are computed with ANSYS (2010). The carbody and bogie are denoted by CB and BG, respectively.

(a) CB: 1st rolling - 0.82 Hz   (b) CB: bouncing - 1.71 Hz   (c) CB: yawing - 2.03 Hz

(d) CB: pitching - 2.08 Hz   (e) CB: 2nd rolling - 2.15 Hz   (f) BG: bouncing - 11.64 Hz

(g) BG: rolling - 12.21 Hz   (h) BG: pitching - 14.29 Hz   (i) BG: yawing - 29.95 Hz
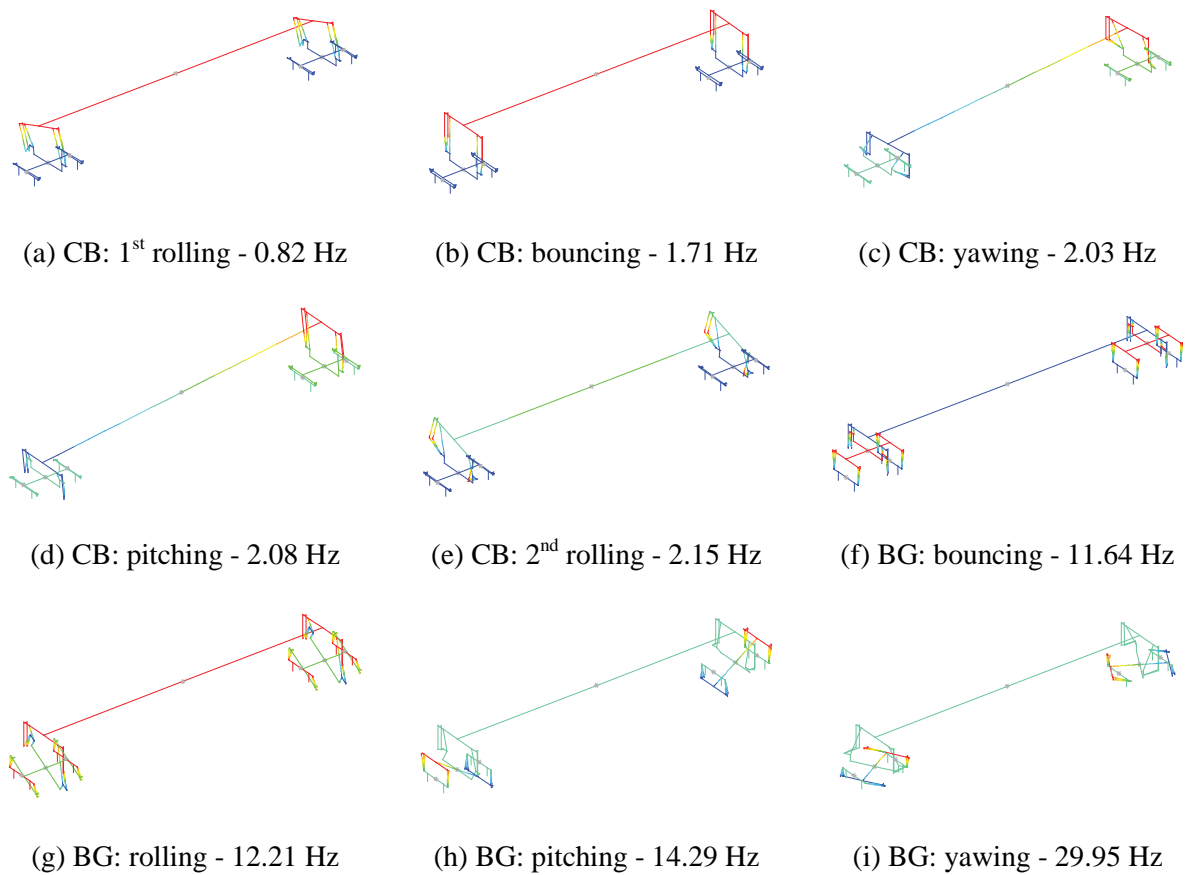
Figure 5.23 - Numerical frequencies and mode shapes of the railway vehicle.

The rail profile used in the analysis is the JIS60 profile (JFE Steel Corporation, 2014), while the wheel is a conic and arc profile wheel with diameter of 860 mm (Matsumoto, 2001), same as that used in the Shinkansen trains. Figure 5.24 shows the geometry of the profiles.
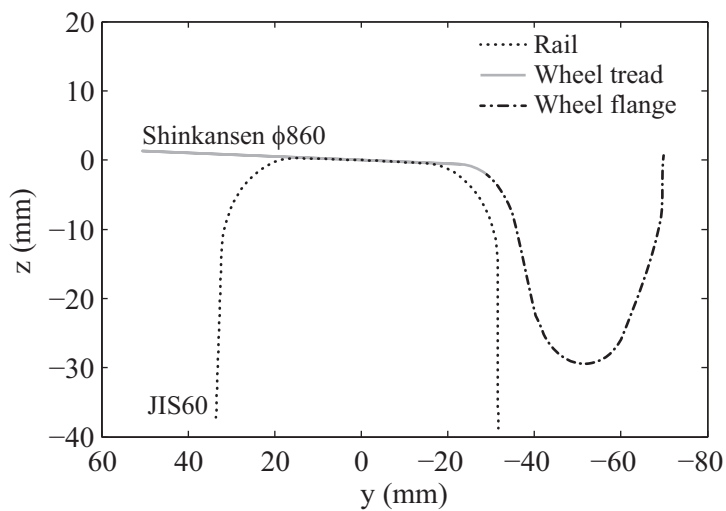
Figure 5.24 - Wheel and rail profiles used in the simulation.

5.5.3 Analysis results

The results obtained with the train-structure interaction method described in Chapter 4 are compared with those obtained in the experimental test and with DIASTARS. The time step used in all the performed analysis is $\Delta t = 0.001\text{s}$ and the total number of time steps is 2500. Since DIASTARS uses the Newmark integration scheme (Clough and Penzien, 2003) to solve the equations of motion, no numerical dissipation is considered in the α method in order to establish a more reliable comparison. Therefore, the integration parameters $\alpha = 0$, $\beta = 0.25$ and $\gamma = 0.5$ are adopted. All the results presented in this section regarding the vertical direction are obtained exclusively with the imposition of vertical deflections to the track, while the results relative to the lateral direction are obtained with the imposition of transversal deflections (see Section 5.5.1).

The comparison between the vertical accelerations measured in the carbody above the rear bogie and the results obtained with the proposed method and DIASTARS is depicted in Figure 5.25. The same comparison, but for the lateral accelerations measured at the same point, is plotted in Figure 5.26. The results shown on both figures correspond to an analysis in which the vehicle is running at $V = 300\,\text{km/h}$ and the letters y and z presented in the deflection schemes of those figures indicate lateral and vertical deflection shapes, respectively. A good agreement can be observed between the measured data and the numerical results. The differences observed may be justified by the fact that the numerical model of the vehicle does not consider the flexibility of some components, especially the carbody, where the accelerations were measured. The lack of additional experimental data to calibrate the vehicle model may also contribute to these differences. When comparing the numerical results obtained with the proposed method and with DIASTARS an excellent agreement can be observed. The slight differences may be due to the fact that the two numerical formulations are based on different wheel-rail contact models. The DIASTARS uses an offline contact search algorithm and a creep model based on Kalker's linear theory with a saturation limit for high creepages, whereas the proposed method uses an online contact search formulation and the Kalker's book of tables to compute the creep forces.
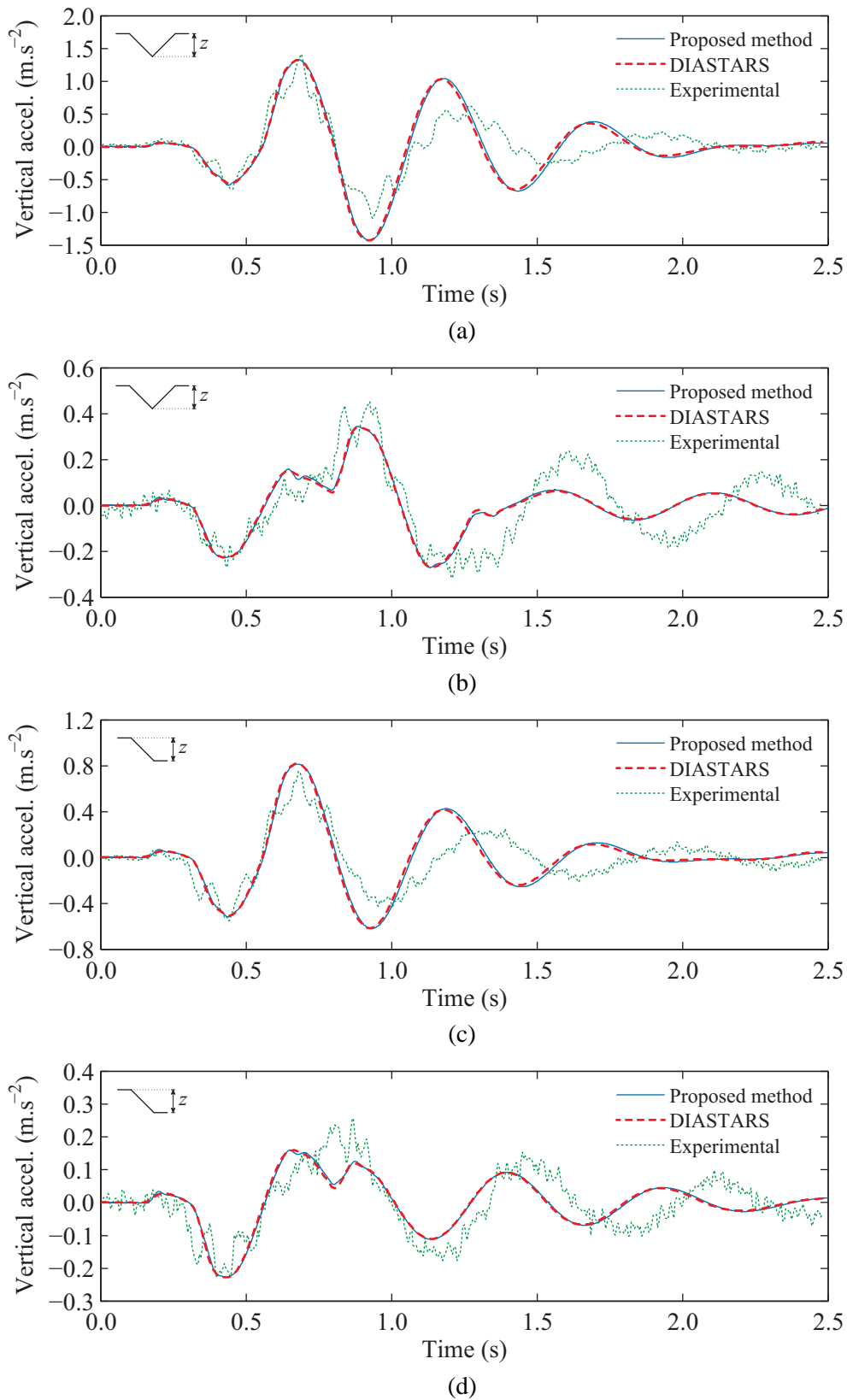
Figure 5.25 - Vertical accelerations in the carbody above the rear bogie for $V = 300$ km/h: (a) BS - 20 m span; (b) BS - 40 m span; (c) TS - 20 m span; (d) TS - 40 m span.
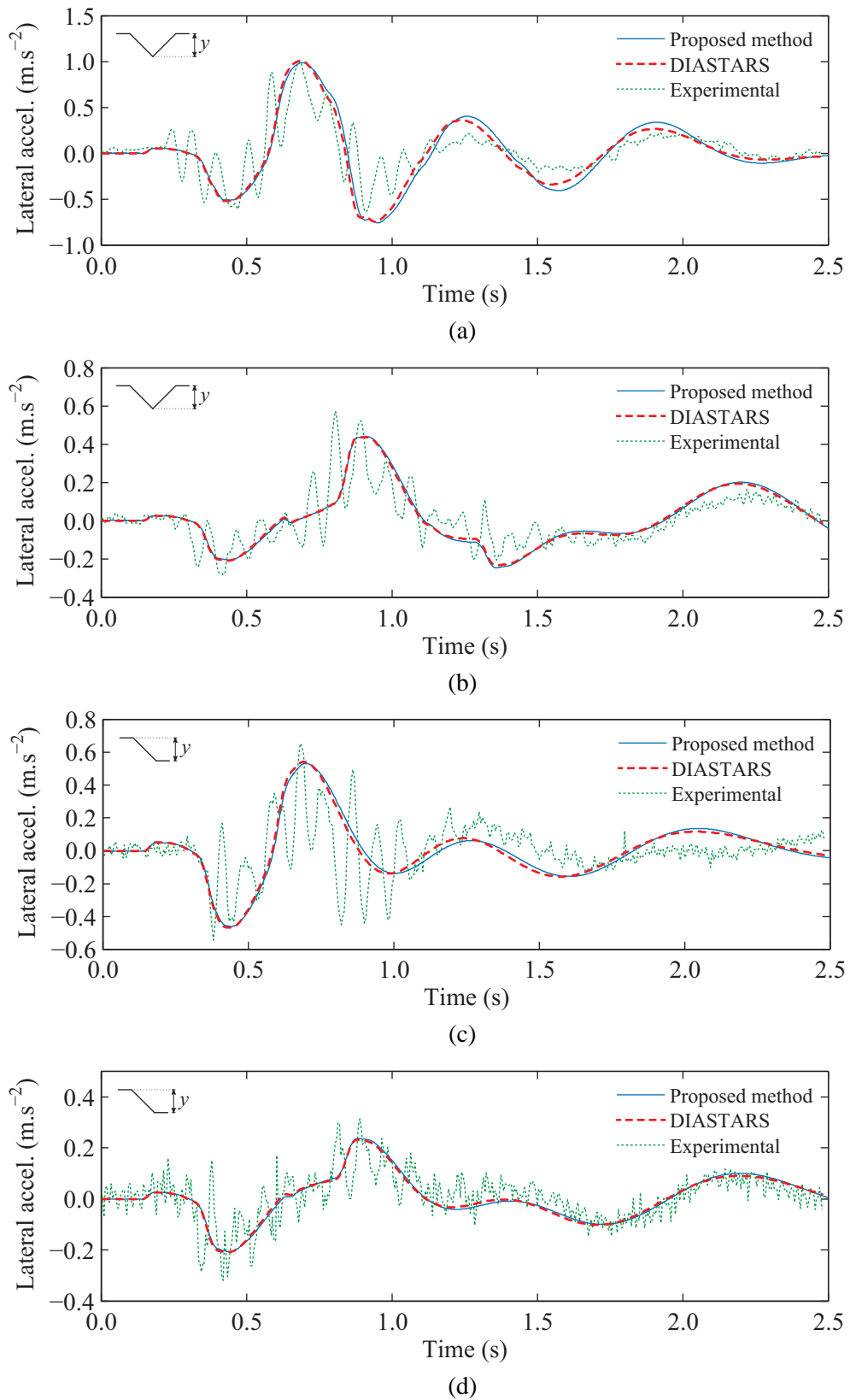
Figure 5.26 - Lateral accelerations in the carbody above the rear bogie for $V = 300$ km/h: (a) BS - 40 m span; (b) BS - 20 m span; (c) TS - 40 m span; (d) TS - 20 m span.

Figures 5.27 and 5.28 show, respectively, the maximum vertical and lateral accelerations in the carbody, obtained in the experimental tests and with the proposed method. The results refer to span lengths of 10, 20, 40 and 60 m and vehicle speeds ranging from 100 km/h to 400 km/h with steps of 50 km/h. In most of the cases, the numerical results show a good agreement with the experimental results. Some discrepancies may be justified by the incapacity of the actuators to reproduce with precision the track rotations (Sogabe et al., 2006).
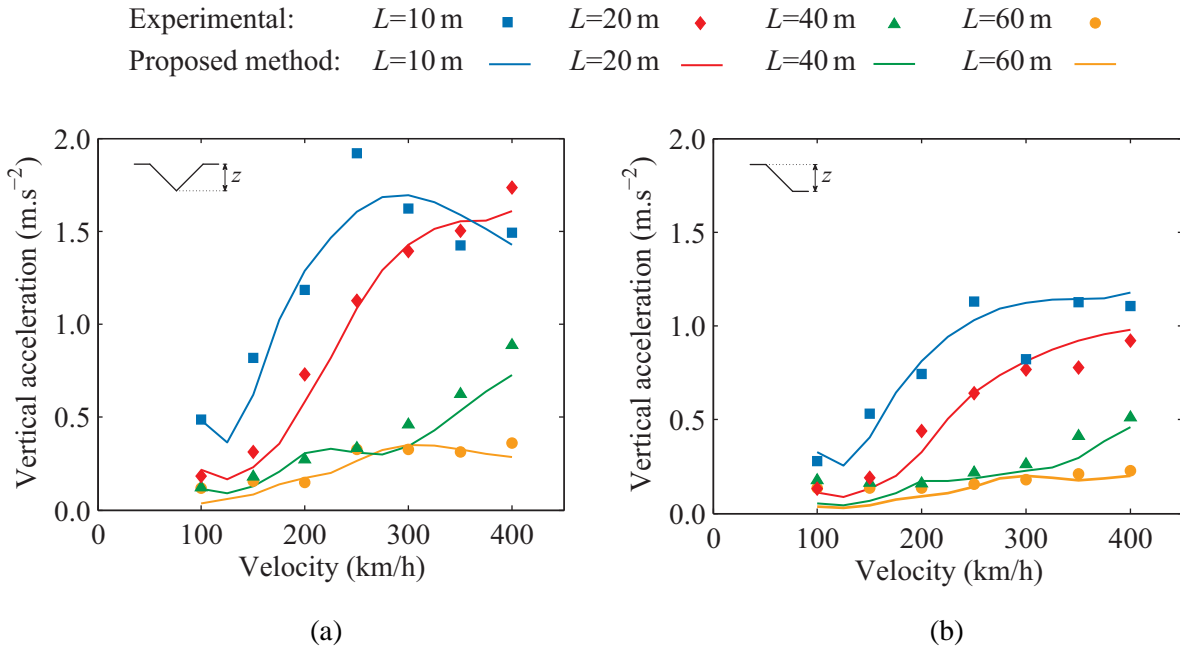
Figure 5.27 - Maximum vertical accelerations in the carbody above rear bogie: (a) BS and (b) TS tests.
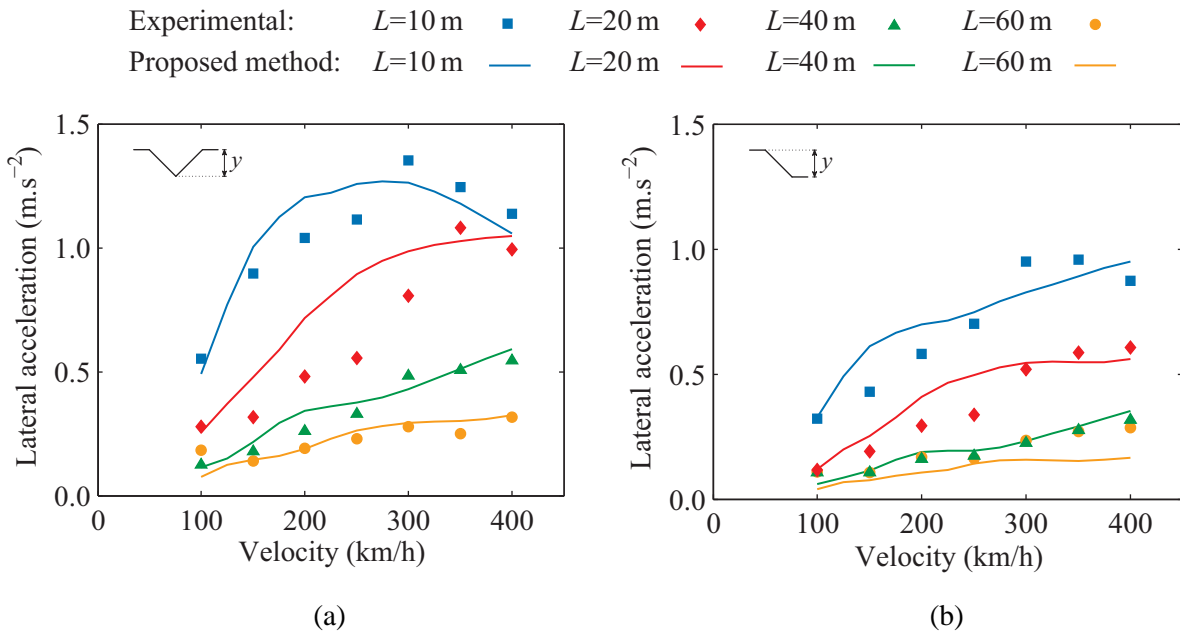
Figure 5.28 - Maximum lateral accelerations in the carbody above rear bogie: (a) BS and (b) TS tests.

As mentioned earlier, the experimental data is restricted to the acceleration in the carbody above the rear bogie. Nevertheless, for a more accurate validation, the responses obtained with the proposed method in other components of the railway vehicle are compared with those obtained with DIASTARS. Only results regarding the BS test with a 20 m span and the TS test with a 40 m span are presented hereafter.

The vertical displacements at the center of mass of the first wheelset and front bogie obtained in the BS test are plotted in Figure 5.29. The results obtained with both the proposed method and with DIASTARS are in an excellent agreement. It can be observed that the wheelset follows the vertical irregularity almost exactly, since the response of this component of the vehicle is not filtered by the suspensions. Notice that the initial displacement is different than zero due to the effect of gravity. Regarding the wheelset, the displacement is almost exclusively due to the wheel-rail static penetration, while in the case of the bogie, the displacement is already affected by the primary suspensions.
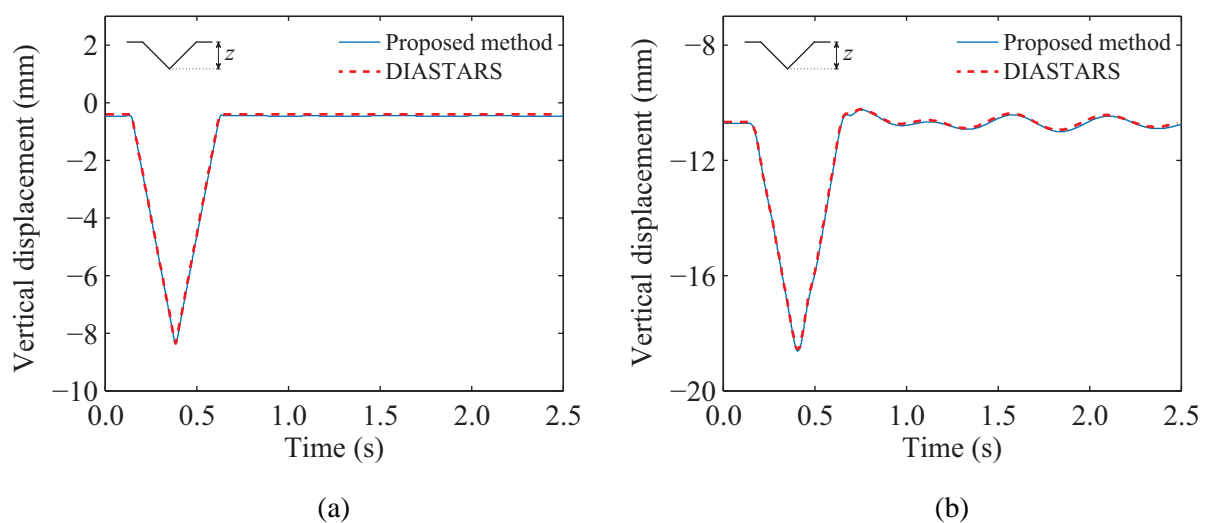
Figure 5.29 - Vertical displacements obtained in the BS test ($L = 20$ m): (a) wheelset and (b) bogie.

Figure 5.30 shows the response obtained at the same points but in terms of vertical acceleration. The solution obtained with the proposed method show numerical instabilities due to the stiff properties adopted to model the wheelset. Such instabilities are not visible in the DIASTARS solution, since it uses a pure multibody formulation to model the vehicle. A better agreement, however, can be observed in the accelerations of the center of mass of the bogie, since the primary suspensions filter most of the high frequencies that occur in the wheelset.
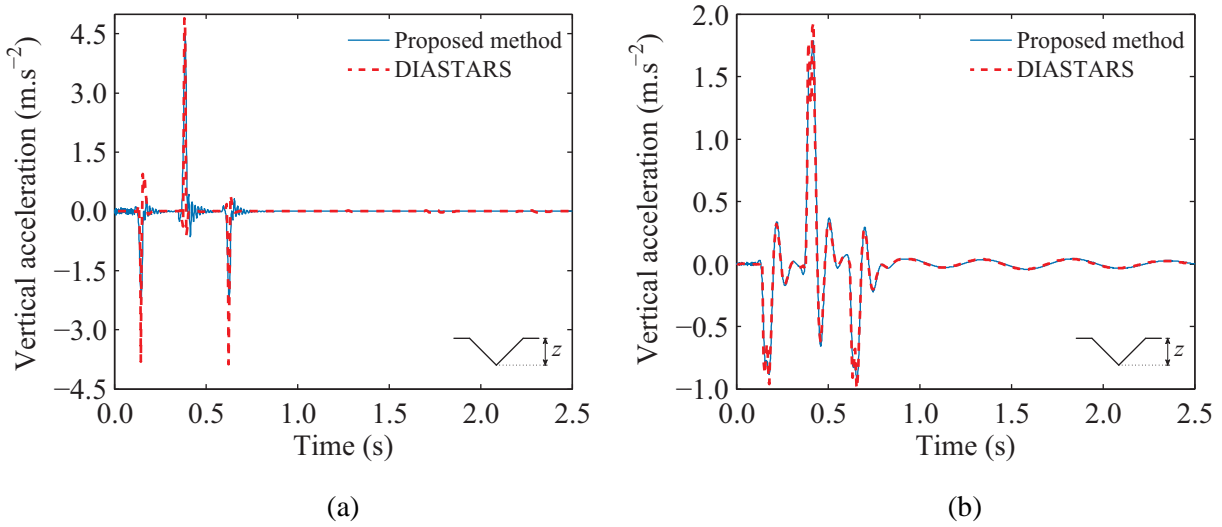
(a)   (b)

Figure 5.30 - Vertical accelerations obtained in the BS test (*L* = 20 m): (a) wheelset and (b) bogie.

The lateral displacements at the center of mass of the first wheelset and front bogie obtained in the BS test are depicted in Figure 5.31. Again, a very good agreement can be observed between the results obtained with the two methodologies. Note that the displacements in the bogie are practically identical to the displacements in the wheelset due to the high stiffness of the primary lateral suspensions.

(a)   (b)
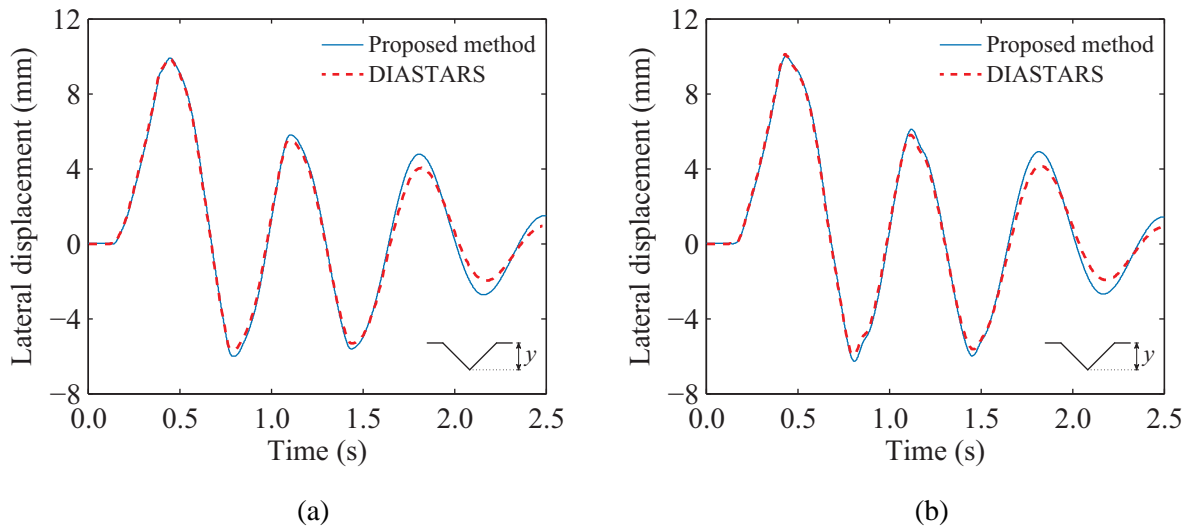
Figure 5.31 - Lateral displacements obtained in the BS test (*L* = 20 m): (a) wheelset and (b) bogie.

The lateral accelerations calculated at the center of mass of the first wheelset and front bogie obtained in the BS test are shown in Figure 5.32. It can be observed that the highest peaks of acceleration observed in the wheelset are filtered by the primary suspensions.
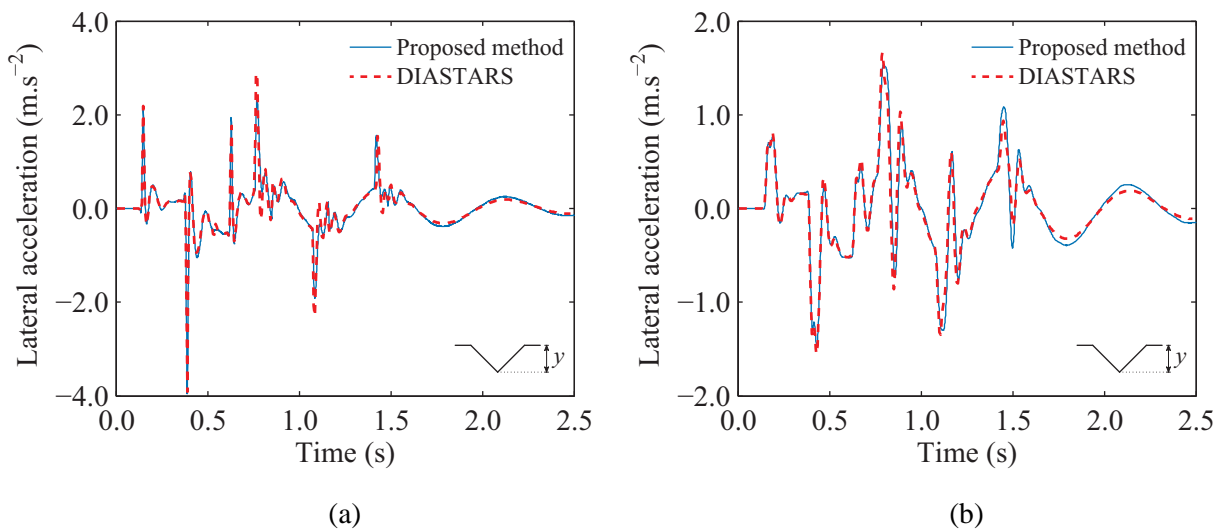
Figure 5.32 - Lateral accelerations obtained in the BS test ($L = 20$ m): (a) wheelset and (b) bogie.

The vertical contact forces in the wheels of the first wheelset for the BS and TS tests are plotted in Figure 5.33. Since the contact forces are similar in both wheels, only the results obtained for the left wheel are presented. There is, once more, a very good agreement between the two numerical tools. The differences observed in the peak forces may be justified by the fact that DIASTARS uses a linearized Hertz model for the normal contact, while the proposed method adopts the nonlinear formulation.
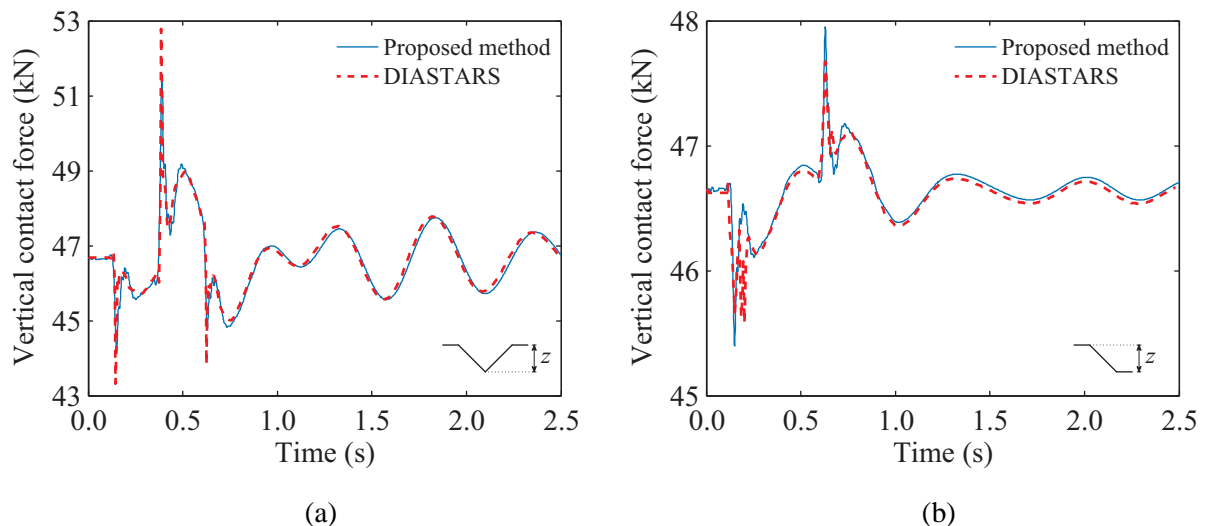
Figure 5.33 - Vertical contact force in the left wheel of the first wheelset: (a) BS ($L = 20$ m) and (b) TS ($L = 40$ m) tests.

Finally, the lateral contact forces in the wheels of the first wheelset for the BS and TS tests are plotted in Figures 5.34 and 5.35, respectively. In the BS test, three flange impacts can be

observed when the contact force suddenly increases: one in the left wheel, approximately at 1.1 s, and two in the right wheel, at 0.8 s and 1.4 s. The functions defining the BS and TS deflection models are the same for the first span (see Figure 5.20). Therefore, the higher contact forces obtained in the BS test, when the wheelset enters the first span, are due the fact that span deviation is more abrupt in the BS test, .i.e., the maximum deflection amplitude is the same in both tests but the span lengths are different. Once more, the results obtained with both numerical methods show an excellent agreement.

(a) (b)
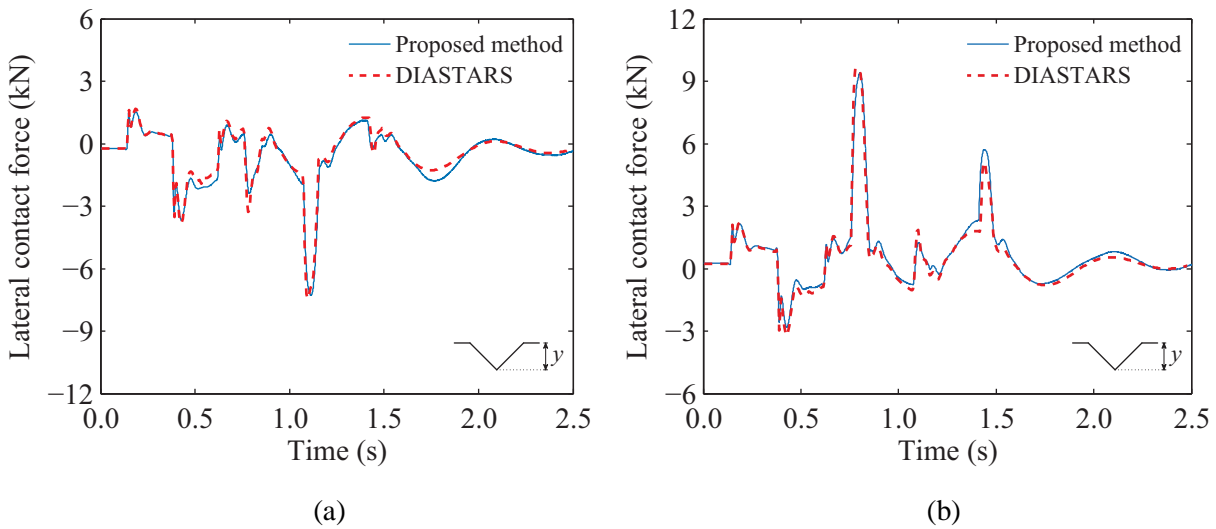
Figure 5.34 - Lateral contact force obtained in the BS test ($L = 20$ m): (a) left wheel and (b) right wheel of the first wheelset.

(a) (b)
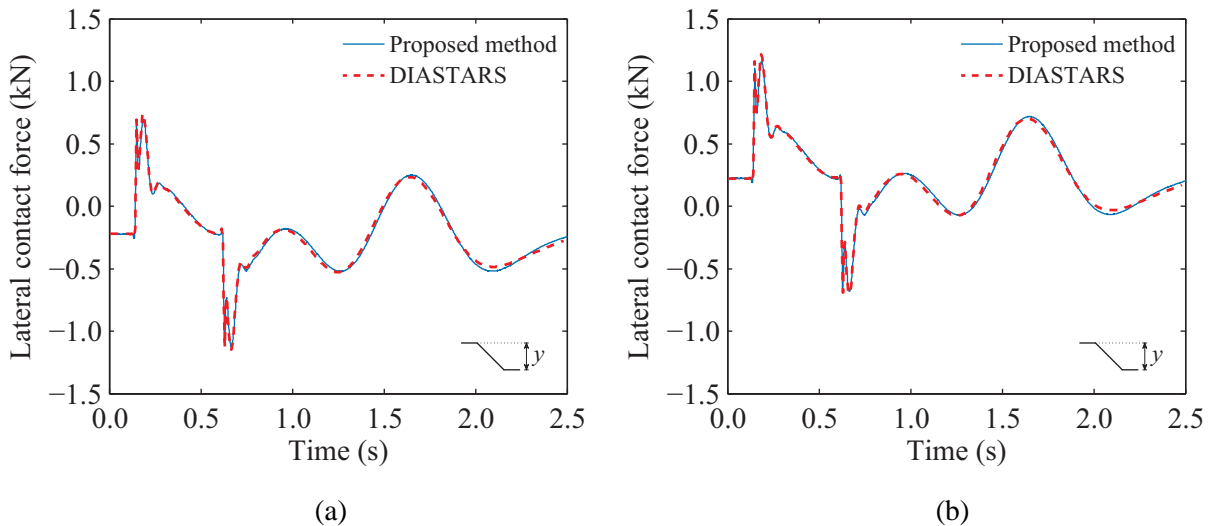
Figure 5.35 - Lateral contact force obtained in the TS test ($L = 40$ m): (a) left wheel and (b) right wheel of the first wheelset.

5.6   CONCLUDING REMARKS

The train-structure interaction method developed in the present thesis is validated with three numerical applications and one experimental test.

The first application consists of reproducing four test cases based on examples presented in Kalker (1990), in which the longitudinal and lateral creep forces are computed for distinct ranges of creepages and semi-axes ratios of the contact ellipse. This application aims to validate the implemented creep force models used to compute the tangential forces that appear in the contact interface due to the rolling friction contact between wheel and rail. All the three methods implemented in the present work proved to be adequate to deal with scenarios with small creepages. However, the Kalker's linear model cannot predict reasonable values of the creep forces when the creepages increase and the tangential stresses approach the saturation limit. For higher values of translational creepages and low values of spin, both the Polach method and the Kalker's book of tables provide adequate results, but only the latter is sufficiently accurate for situations where the spin creepage is also higher. For these reasons, the implemented book of tables is used in the majority of the dynamic simulations presented in this thesis.

In the second application, the Manchester Benchmark proposed by Shackleton and Iwnicki (2006) is revisited. The benchmark comprised a series of tests simulated with ten different softwares with the aim of allowing an informed choice when selecting a contact model for a particular railway vehicle simulation scenario. The tests consisted of prescribing, both statically and dynamically, lateral displacements and yaw rotations to a single wheelset in order to analyze its behavior. Several contact characteristics were analyzed during the benchmark, namely the contact point positions on both wheels of the wheelset, the rolling radius difference between wheels, the contact angles and the creepages. Generally, the results obtained with the proposed method for all the analyzed quantities show an excellent agreement with those obtained with widely used softwares in railway vehicle dynamics, such as GENSYS, NUCARS and VAMPIRE. The few discrepancies observed are mainly justified by limitations of the contact models adopted by some of the tested softwares, especially CONPOL and VOCOLIN, rather than by limitations of the proposed method.

The third numerical example consists of evaluating the lateral stability of a single wheelset running at several speeds. The dynamic response of the wheelset calculated with the proposed

method is compared with that obtained using a semi-analytical model with two degrees of freedom available in the literature (Knothe and Böhm, 1999; Valtorta et al., 2001; Wickens, 2003). The model follows a number of simplifying assumptions whereby the dynamics of the wheelset can be described by simple linear differential equations. A good agreement between the responses obtained with the proposed method and those obtained by the integration of the equations of motion of the semi-analytical model is observed. As expected, for speeds below the critical limit, both the lateral displacement and the yaw rotation of the wheelset tend to damp out after being driven away by a lateral disturbance. This is due to the energy dissipation provided by the creep forces and to the stability provided by the suspensions. However, when the speed exceeds the critical value, the behavior of the wheelset becomes unstable, leading to a hunting motion that grows indefinitely. The critical speed predicted by the proposed formulation using a logarithmic decrement factor is also in a good agreement with the theoretical value determined from a stability study described in Antolín (2013).

Finally, an experimental test conducted in the rolling stock test plant of the RTRI, in which a full scale railway vehicle runs over a track that is subjected to vertical and lateral deviations, is reproduced numerically. The lateral accelerations inside the carbody measured during the test are compared with those obtained with the proposed method and with the train-structure interaction software DIASTARS. The results show a good agreement, especially when the two numerical methods are compared. Regarding the experimental results, the discrepancies observed may be caused by the fact that vehicle is modeled using rigid bars and thus important deformations are not considered. Furthermore, the incapacity of the actuators to reproduce with precision the track rotations may also contribute for the differences between the experimental and numerical results.

Chapter 6

RUNNING SAFETY ANALYSIS OF A HIGH-SPEED TRAIN MOVING ON A VIADUCT UNDER SEISMIC CONDITIONS

6.1 INTRODUCTION

In the present chapter, a study regarding the running safety of a high-speed train moving on a viaduct under seismic conditions is conducted (Montenegro et al., 2015a) using the methodology presented in Chapter 3. The main objective of the present study consists of evaluating the influence of the seismic intensity and track irregularities on the train running safety. First, a description of the case study is exposed in order to introduce the viaduct, the vehicle and the external excitation sources, namely the earthquake and the track irregularities. The viaduct is based on an existing flyover type structure of the Portuguese railway network situated in the city of Alverca and composed by simply supported box girders, while the vehicle consists of a Japanese Shinkansen high-speed train whose mechanical properties were known. The numerical models of both subsystems are developed using the finite element method software ANSYS (2010), being their dynamic properties, namely the mode shape configurations and respective natural frequencies, presented. The seismic action is represented in terms of ground acceleration time-histories using artificial accelerograms that are generated from the elastic spectra described in EN 1998‑1 (2004), with PGA corresponding to moderate events with relatively high probability of occurrence. This type of seismic actions is of the utmost importance, since the running safety of trains might be jeopardized not only by intense

shakings, but also by moderate earthquakes, which may not cause significant damage to the structure. Since no significant nonlinearity is likely to be exhibited in the piers of the viaduct for these levels of seismicity, all the analysis are performed in the elastic domain by considering the effective stiffness of the piers due to concrete cracking. Furthermore, and unlike the majority of the studies in this field, the time offset between the beginning of the earthquake and the entry of the vehicle in the viaduct is taken into account by considering different instants in which the earthquake starts to excite the viaduct. Regarding the track irregularities, they are also based on artificial profiles generated based on analytical PSD functions. Then, the dynamic behavior of both the viaduct and vehicle under seismic conditions is evaluated. For the viaduct, the vertical and lateral dynamic responses in terms of displacements and accelerations obtained with and without earthquake are studied. Moreover, the influence of the reduction in the stiffness of the piers due to concrete cracking on the lateral response of the viaduct is evaluated. Regarding the vehicle, in addition to analyzing the vertical and lateral response in terms of displacements and accelerations, the contact forces between wheel and rail are also assessed. Special attention is given to the strong lateral impacts that occur between the wheel flange and the rail which may lead to derailment. At the end of the section, the influence in the response of the vehicle of both the suspension stoppers and the time offset between the beginning of the earthquake and the entry of the vehicle in the viaduct is analyzed. Finally, the running safety analysis of the railway vehicle running over the viaduct is assessed based on the derailment criteria described in Section 3.5 of Chapter 3. The influence in the running safety of the seismic intensity level, vehicle running speed and track quality is evaluated separately. Next, all the information obtained in the dynamic analyses is condensed in the so-called running safety charts, which consist of the global envelope of each analyzed safety criteria as function of the running speed of the vehicle and of the seismic intensity level. At the end of the chapter, a critical analysis about the running safety criteria adopted in the present work is carried out.

6.2   NUMERICAL MODEL OF THE VIADUCT

6.2.1   Description of the Alverca railway viaduct

The Alverca viaduct is a flyover structure belonging to the Northern Line of the Portuguese railway network that connects Lisbon to Porto. Its construction allowed the separation of the rail traffic flowing in both directions and was designed for a maximum speed of 200 km/h.

Figure 6.1 shows an aerial view of the frame type area located in the middle of the viaduct, which allows the intersection with the other railway lines, along with a perspective view of the current zone in one of the ramps.

(a)   (b)

Figure 6.1 - Alverca viaduct: (a) frame area (Fernandes, 2010) and (b) ramp (Malveiro et al., 2013).

The viaduct has a total length of 1091 m divided into the following parts:

a) South ramp with a total length of 388 m divided into 20 simply supported spans distributed as follows: 4×16.5 m $+ 4 \times 17.5$ m $+ 12 \times 21.0$ m;

b) Middle frame type viaduct with a total length of 176 m divided into 3 continuous spans;

c) North ramp with a total length of 527 m divided into 27 simply supported spans distributed as follows: 5×16.5 m $+ 5 \times 17.5$ m $+ 17 \times 21.0$ m.

The deck of the current zones consists of a prefabricated and prestressed U-shaped beam on which pre-slabs serving as formwork to the concrete upper slab cast *in situ* are placed, forming a single-cell box girder deck. The deck is simply supported on the piers and abutments by elastomeric-reinforced bearings, each one composed of four layers of neoprene with plan dimensions 500×300 mm^2 and 8 mm thick, interspersed with steel plates. Each span is fixed in one extremity and longitudinally guided in the other, being the transverse direction fixed on both edges. Since the spans are all simply supported and disconnected from each other, the deck does not confer any transversal stiffness to the viaduct. The track consists in UIC60 rails with an Iberian gauge of 1.688 m, elastomeric rubber pads, prestressed concrete monoblock sleepers and a 25 cm ballast layer under them. Finally, the piers have a rectangular cross-section with dimensions 2×1 m^2 and heights ranging from, approximately, 5 m to 15 m. Figure 6.2a shows the elevation view of both the South and North ramps, while Figures 6.2b and 6.2c present the cross-section and the deck joint, respectively.
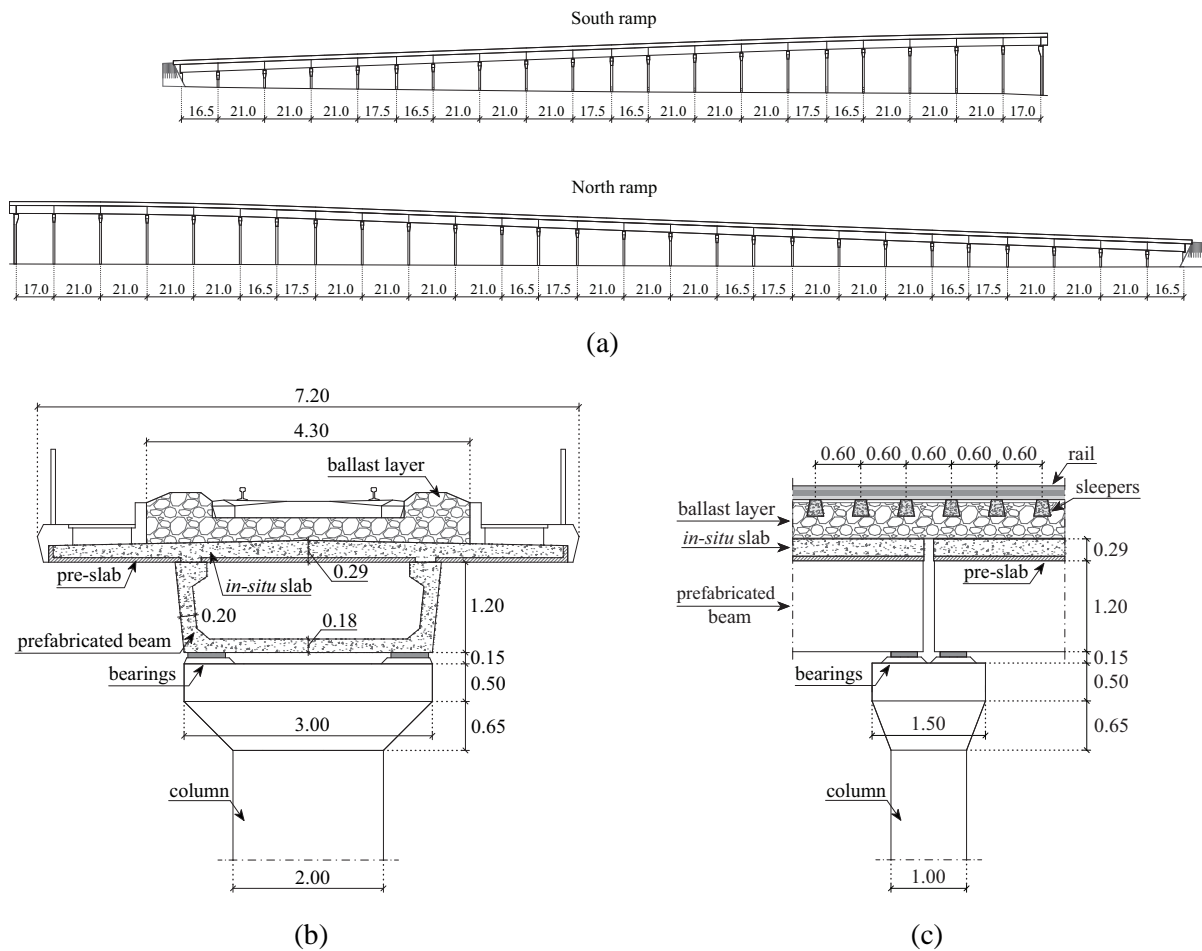
Figure 6.2 - Blueprints of the Alverca viaduct: (a) elevation view of the South and North ramps; (b) cross-section and (c) deck joint above the pier.

6.2.2 Finite element model of the idealized viaduct

The structure used in the present study is based on the Alverca viaduct described in the previous section. However, for simplicity of the model, an idealized structure with a total length of 630 m divided into 30 simply supported spans with 21 m length each and supported by piers with 10 m height is adopted in the present study. The geometrical properties of both the deck and the piers are the same as the original viaduct.

The numerical model of the viaduct is developed in ANSYS. The deck, piers, sleepers and rails are modeled using beam finite elements, while the bearing supports, ballast and pads are modeled using linear spring-dampers. Mass point elements are also used to model the ballast mass and the non-structural elements such as safeguards and edge beams of the deck. The connection between the top of the piers and the deck, as well as the connection between the deck and the track, is accomplished by rigid frame elements. In order to guarantee a correct

representation of the transition zones between the structure and the embankment, an extension of the track is modeled in both extremities of the viaduct.

Special focus is given to the track modeling, since it may strongly influence the behavior of the vehicle. This is one of the advantages of using the finite element method to model the structure, since in the majority of studies performed in multibody platforms the track is considered to be rigid, which is far from reality.

A schematic representation of the numerical model, along with a detail of the cross-section and the deck joint above the piers is illustrated in Figure 6.3 (the track is not included in Figure 6.3a for simplicity), while Figure 6.4 presents a partial overview and two details of the numerical model of the viaduct developed in ANSYS. Although the spans are disconnected from each other, the track mobilizes a certain amount of transversal stiffness when relative movements between adjacent spans occur, as can be seen in the detail of the joint depicted in Figure 6.3c.

(a)

(b)

(c)
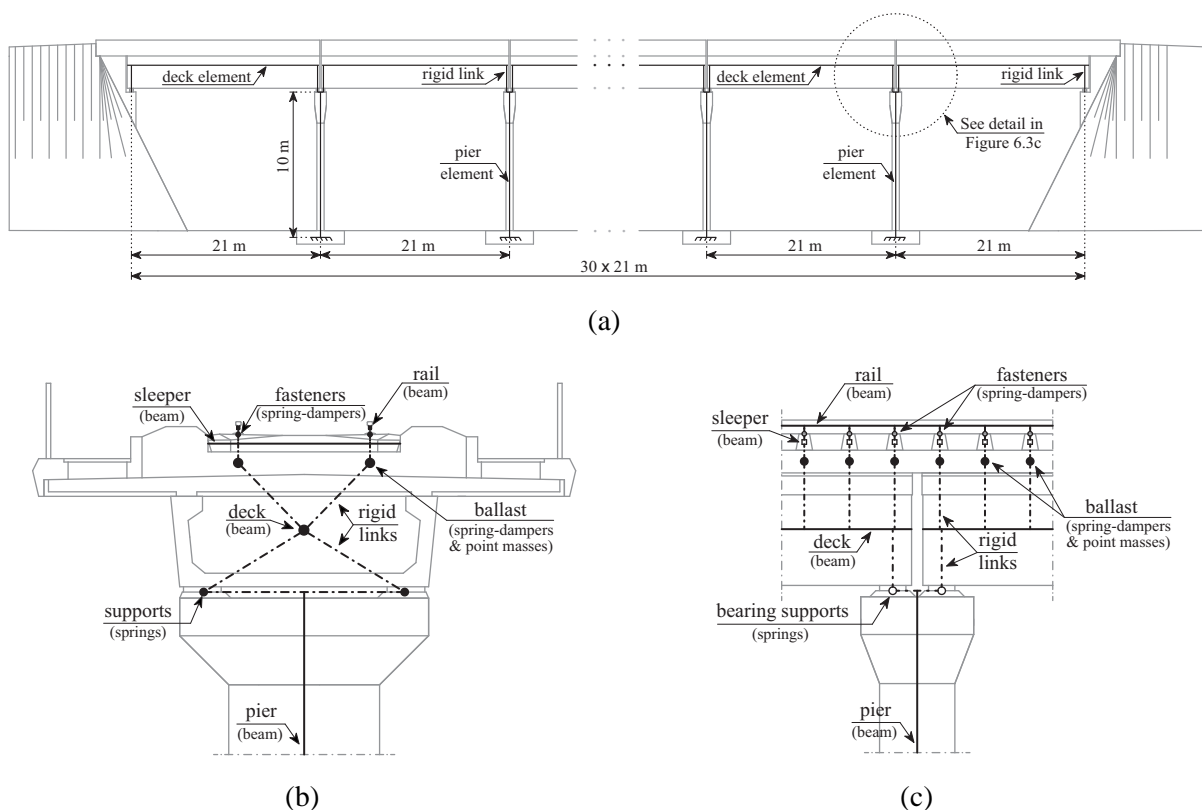
Figure 6.3 - Numerical model of the viaduct: (a) elevation view, (b) cross-section and (c) deck joint.
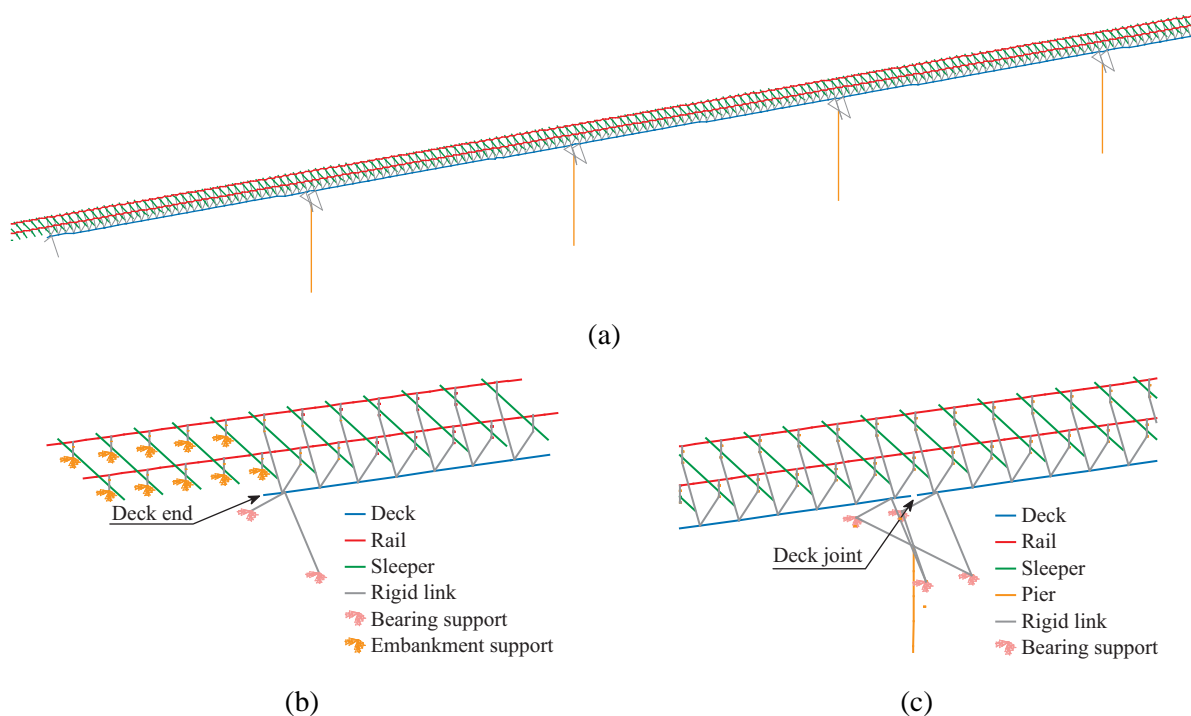
Figure 6.4 - Finite element model of the viaduct developed in ANSYS: (a) overview, (b) detail of the transition and (c) detail of the deck joint.

Table 6.1 presents the main mechanical properties of the numerical model of the viaduct. The mechanical properties used in the numerical model of the deck are those reported by Malveiro et al. (2013). In this study, the authors made a calibration of the mechanical properties of the deck using experimental results of an ambient vibration test. The process involved the application of an iterative procedure based on an optimization technique grounded on a genetic algorithm. The pairing between the numerical and experimental vibration modes was performed using the modal assurance criterion (MAC) parameter (Allemang, 2003), for global modes, and the energy-based modal assurance criterion (EMAC) parameter (Brehm et al., 2010), in the case of local vibration modes. The track properties, namely ballast stiffness and pads/fasteners stiffness and damping, are adopted from the literature, since they could not be estimated with accuracy in the calibration process. Note that the track in the existent viaduct consists in UIC60 rails with an Iberian gauge of 1.688 m. However, since the study is carried out with a Japanese high-speed train, the standard gauge of 1.435 m is considered in the numerical model, as well as the JIS60 rail profiles (JFE Steel Corporation, 2014) used in the Japanese high-speed lines.

Table 6.1 - Mechanical properties of the numerical model of the viaduct.

Parameter	Designation	Value	Unit	Reference
$E_{c,slab}$	Modulus of elasticity of the concrete of the upper slab	33.48	GPa	Malveiro et al. (2013)
$E_{c,beam}$	Modulus of elasticity of the concrete of the prefabricated beam	48.08	GPa	Malveiro et al. (2013)
$E_{c,sleeper}$	Modulus of elasticity of the concrete of the sleeper	40.90	GPa	Malveiro et al. (2013)
$E_{c,pier}$	Modulus of elasticity of the concrete of the pier	33.00	GPa	EN 1992-1-1 (2004)
ρ_c	Density of concrete	2590.4	kg/m^3	Malveiro et al. (2013)
ρ_{bal}	Density of ballast	1995.9	kg/m^3	Malveiro et al. (2013)
$K_{bal,l}$	Ballast's longitudinal stiffness	30	MN/m/m	UIC 774-3-R (2001)
$K_{bal,t}$	Ballast's transversal stiffness	7.5	MN/m/m	ERRI D 202/RP 11 (1999)
$K_{bal,v}$	Ballast's vertical stiffness	100	MN/m/m	ERRI D 202/RP 11 (1999)
C_{bal}	Ballast's damping (3 directions)	50	kN.s/m/m	Wu and Yang (2003)
$K_{fas,l}$	Fastener's longitudinal stiffness	20	MN/m	Zhai et al. (2009)
$K_{fas,t}$	Fastener's transversal stiffness	20	MN/m	Zhai et al. (2009)
$K_{fas,v}$	Fastener's vertical stiffness	500	MN/m	ERRI D 214/RP 5 (1999)
$K_{fas,r}$	Fastener's rotational stiffness	45	kN.m/rad	ERRI D 202/RP 11 (1999)
$C_{fas,l}$	Fastener's longitudinal damping	50	kN.s/m	Zhai et al. (2009)
$C_{fas,t}$	Fastener's transversal damping	50	kN.s/m	Zhai et al. (2009)
$C_{fas,v}$	Fastener's vertical damping	200	kN.s/m	ERRI D 214/RP 5 (1999)
K_l	Longitudinal stiffness of the bearing supports	4.4	MN/m	Malveiro et al. (2013)
K_v	Vertical stiffness of the bearing supports	5200	MN/m	Malveiro et al. (2013)

6.2.3 Dynamic properties of the viaduct

The first mode shapes and natural frequencies of the viaduct are plotted in Figure 6.5. Since all the spans are simply supported and disconnected from each other (see Figure 6.3c), the frequencies of the first modes are identical, i.e., the global frequencies of the viaduct are mainly controlled by the first mode of the piers. The small differences observed are due to the fact that the track confers a slight amount of stiffness to the deck in the transversal direction.
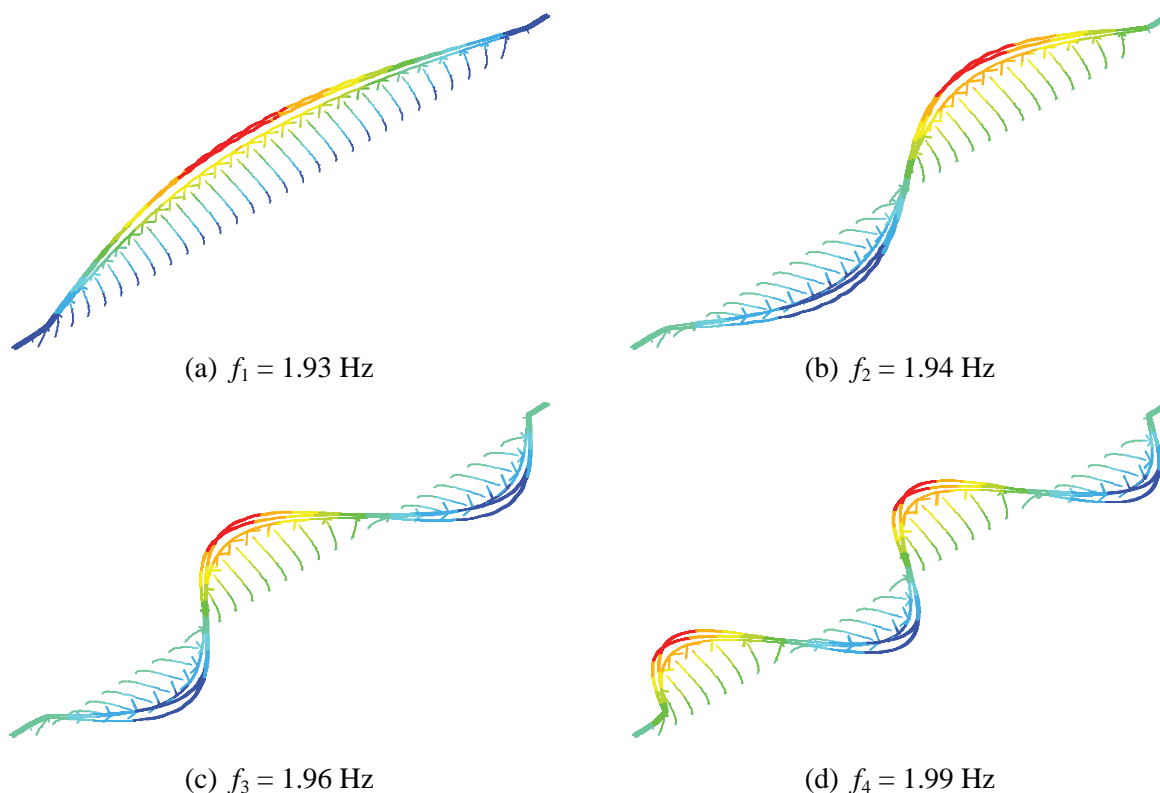
(a) f_1 = 1.93 Hz

(b) f_2 = 1.94 Hz

(c) f_3 = 1.96 Hz

(d) f_4 = 1.99 Hz

Figure 6.5 - Numerical frequencies and mode shapes of the viaduct.

6.3 DEFINITION OF THE SEISMIC ACTION

6.3.1 Artificial accelerograms

The seismic excitations adopted in the present study consist of artificial accelerograms generated from the elastic spectra described in EN 1998-1 (2004), with PGA corresponding to moderate events with return periods less than 475 years, which is the reference return period of the design seismic action associated with the no-collapse requirement. Thus, four levels of seismic intensity with return periods of 95 (proposed return period for the damage limitation requirement of EN 1998-1 (2004)), 150, 225 and 310 years are considered, being the ground motion imposed along the lateral direction.

The artificial accelerograms are generated with the software SeismoArtif (2013), which uses a random process of adjustment by correction in the frequency domain. The method used by SeismoArtif defines the artificial ground motion considering a target spectrum and adapting the frequency content through an iterative process using the Fourrier Transformation Method (see Section 3.3.1 of Chapter 3). The intensity function $I(t)$ used to simulate the transient nature of the earthquake consists of a trapezoidal shape function, with 10 s for the stationary part of the

accelerogram (minimum value according to EN 1998-1 (2004)) and 2 s of slope in each extremity, as shown in Figure 6.6.
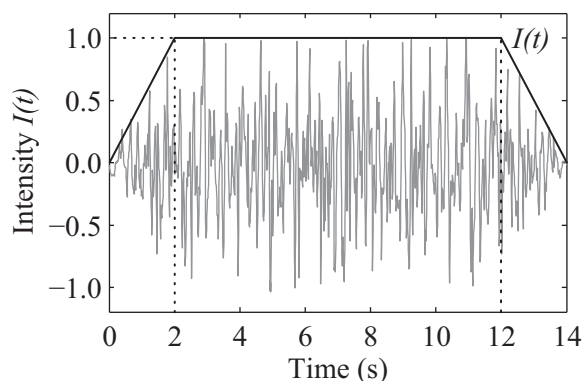
Figure 6.6 - Intensity function adopted in the present study.

The target elastic spectra are defined for the seismic zone 2.3 of the Portuguese territory and for a soil type A (EN 1998-1-NA, 2009), with an importance factor of 1.0, as proposed by EN 1998-2 (2005) for railway bridges, and a viscous damping of 5 %. The PGA corresponding to the return periods T of the seismic actions considered in this work are presented in Table 6.2.

Table 6.2 - PGA corresponding to the return periods of the seismic actions[1].

T (years)	95	150	225	310
PGA (m.s^{-2})	0.862	1.050	1.250	1.420

The artificial ground motions generated with SeismoArtif and the respective response spectrum adjustments to the target spectrum are plotted in Figures 6.7 to 6.10.

(a)

(b)
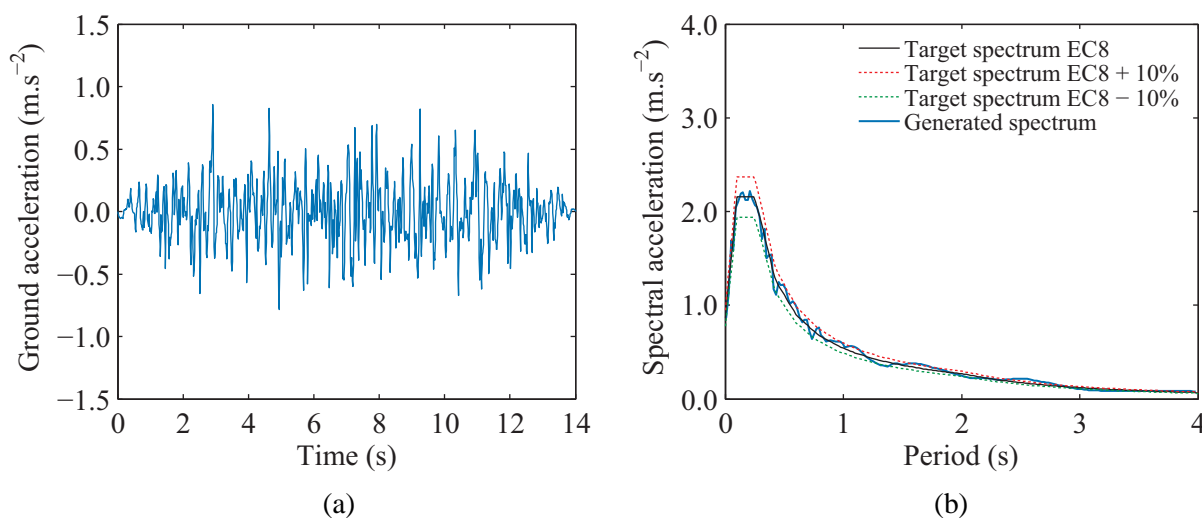
Figure 6.7 - Generated ground motion for $T = 95$ years: (a) accelerogram and (b) spectrum adjustment.

---

[1] The values of the PGA were kindly provided by the National Laboratory for Civil Engineering of Portugal.

(a)

(b)
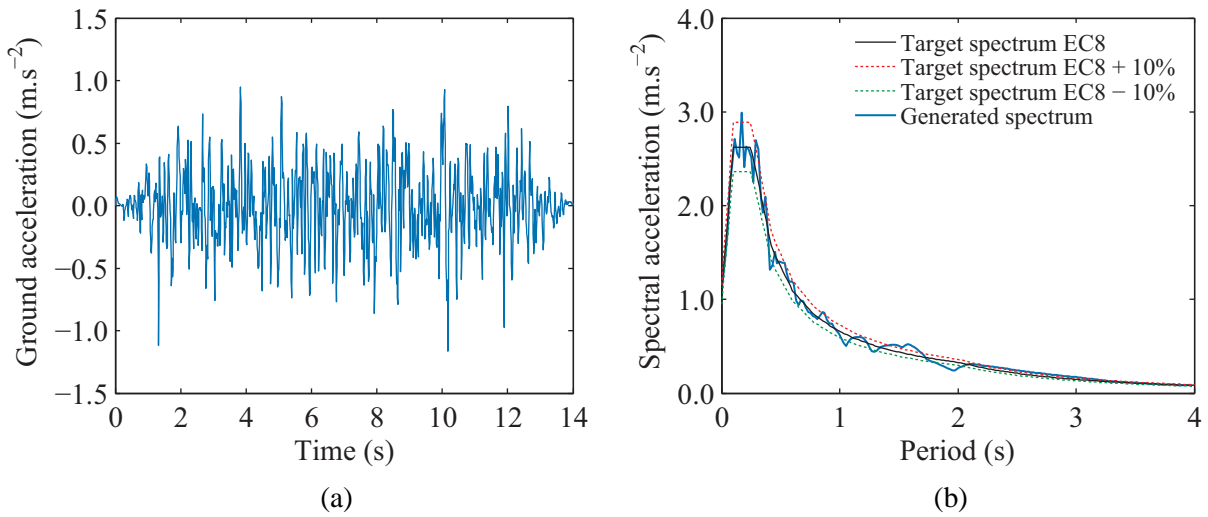
Figure 6.8 - Generated ground motion for $T = 150$ years: (a) accelerogram and (b) spectrum adjustment.

(a)

(b)
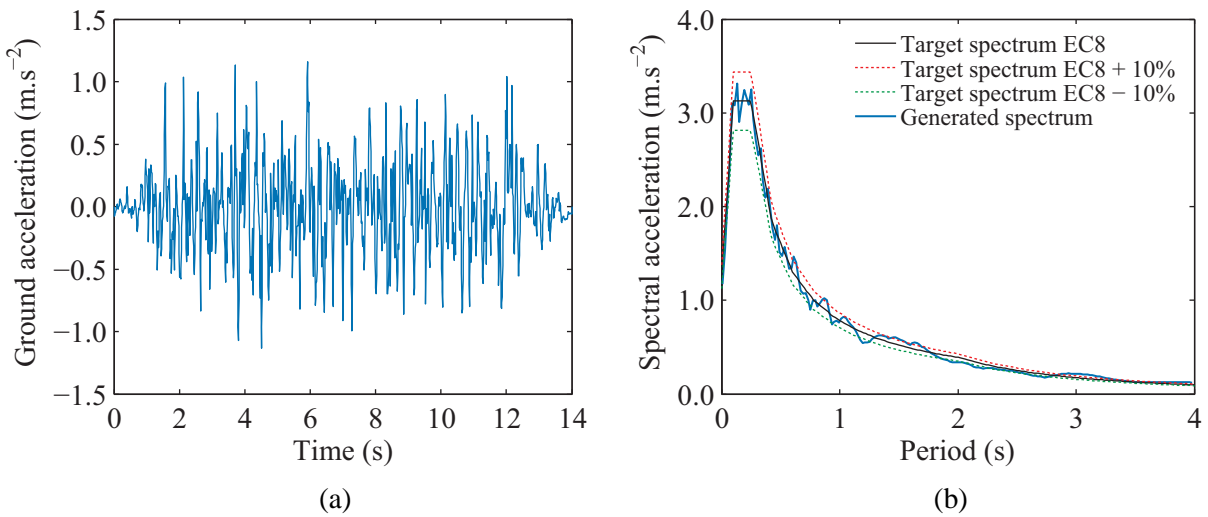
Figure 6.9 - Generated ground motion for $T = 225$ years: (a) accelerogram and (b) spectrum adjustment.
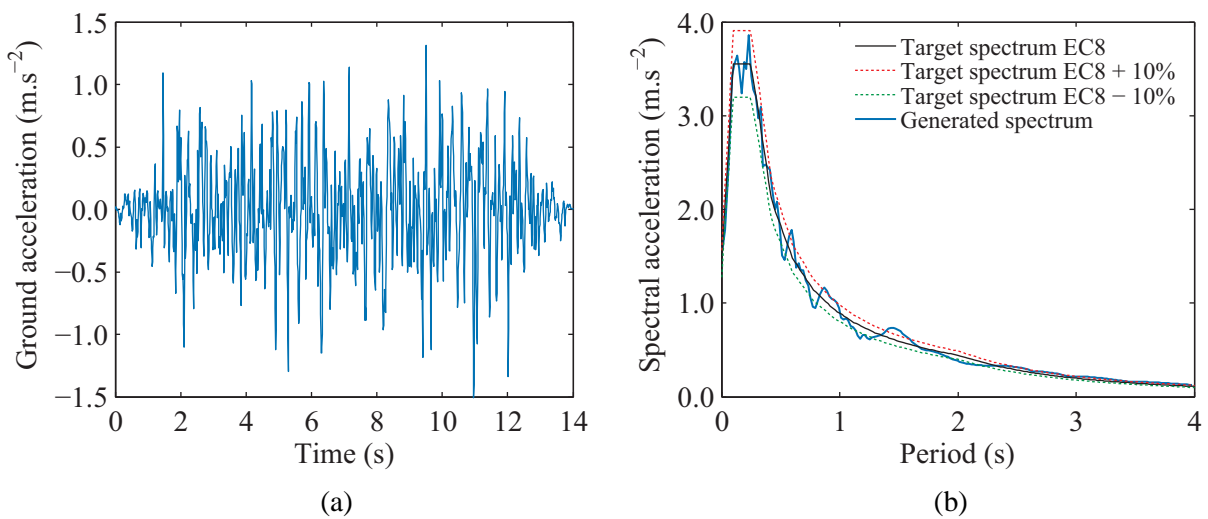

(a)

(b)

Figure 6.10 - Generated ground motion for $T = 310$ years: (a) accelerogram and (b) spectrum adjustment.

6.3.2 Time offset between the beginning of the earthquake and the entry of the vehicle in the viaduct

The random nature of the seismic events makes it impossible to predict the position of the vehicle in the moment the earthquake starts. Therefore, and unlike the majority of studies in this field, in which the earthquake is assumed to start at the instant the train enters the bridge, the time offset between the beginning of the earthquake and the entry of the vehicle in the viaduct is taken into account by considering five scenarios corresponding to different instants in which the earthquake starts to excite the viaduct. This procedure to cover covering a wider range of combinations for a more extensive study.

The coordinate of the first wheelset x_i at the instant the earthquake starts is presented in Figure 6.11. The coordinate x_i is defined with respect to the coordinate system (x, y) positioned at the beginning of the viaduct and the subscripts $i = 1, 2, ..., n$ indicate the scenario number.
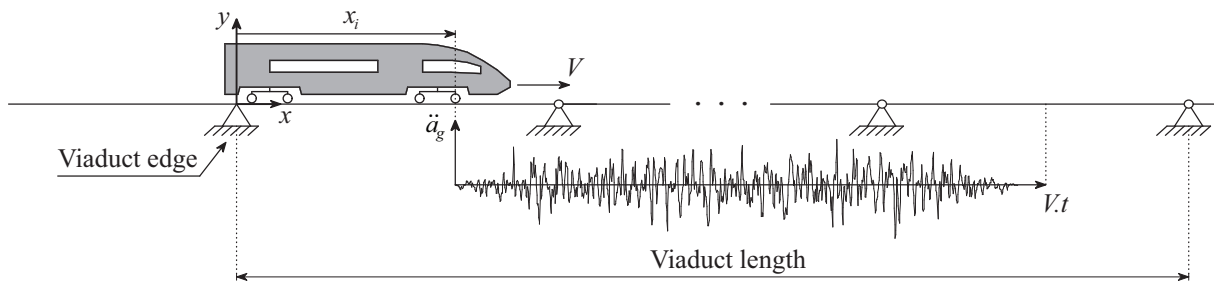
Figure 6.11 - Coordinate of the first wheelset at the instant the earthquake starts.

The first scenario represents the case in which the vehicle enters the viaduct in the instant the earthquake stops, while the last scenario represents a situation in which the earthquake starts in the instant the vehicle leaves the viaduct. The other scenarios will cover the intermediate situations. Hence, for each scenario i, the coordinate of the first wheelset x_i at the instant the earthquake starts is given by

$$x_i = V\left[-t_e + (i-1)\left(\frac{t_e + t_v}{n-1}\right) \right] \tag{6.1}$$

where V is the vehicle speed, t_e is the earthquake duration and t_v is the time that the vehicle takes to cross the viaduct. Note that the coordinate x_i is negative in the scenarios in which the vehicle enters the viaduct after the beginning of the earthquake. This is to ensure that, for these scenarios, the simulations initiate with the beginning of the ground motion. On the other hand, in the scenarios in which the earthquake starts when the vehicle is already on the viaduct, the

simulation begins with the vehicle positioned at its edge. This procedure aims to guarantee that the vehicle is already excited due to the track irregularities and due to the interaction with the structure at the instant the earthquake starts. Figure 6.12 schematizes the position of the vehicle at the start of the simulation for the two aforementioned types of scenarios.
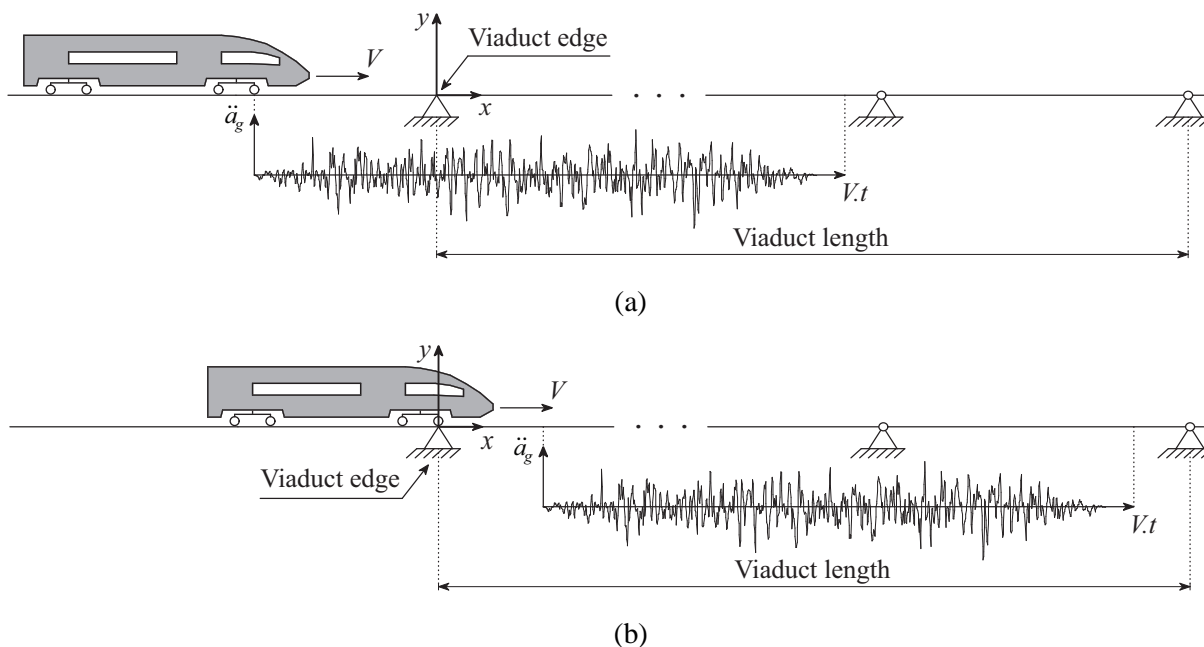

(a)

(b)

Figure 6.12 - Position of the vehicle at the start of the simulation: (a) the vehicle enters the viaduct after the beginning of the earthquake and (b) before the beginning of the earthquake.

6.4 MODELING OF THE SEISMIC BEHAVIOR OF THE PIERS

The seismic actions considered in the present study correspond to moderate events with relatively high probability of occurrence, as shown in Section 6.3.1. Although no significant damage to the structure is expected for these levels of intensity, the reduction in the piers' stiffness due to concrete cracking should be accounted. Thus, the effective stiffness of the piers is evaluated based on the methodology described in Section 3.4 of the Chapter 3.

6.4.1 Monotonic response of the piers

The first step of the methodology consists of performing a nonlinear monotonic static analysis to evaluate the horizontal response of the piers. In this analysis, the idealized representation of the structure is subjected to a constant gravity load and to a monotonically increasing displacement that represent the inertial effects from the earthquake. Since the force is increased until the ultimate capacity of the pier is reached, the model has to account for the effects of both the material inelasticity and the geometric nonlinearity.

In the present work, the monotonic response of the piers is evaluated using the software SeismoStruct (2013). Since all the spans are simply supported and disconnected from each other (see Section 6.2), the monotonic analysis presented in this section is carried out using a single degree of freedom model of one of the piers, as shown in Figure 6.13.

(a)   (b)

Figure 6.13 - Single degree of freedom model of the pier developed in SeismoStruct: (a) initial position and (b) ultimate capacity deflection (5× amplified).

The pier is modeled using frame elements with distributed inelasticity based on the displacement-based formulation, in which the sectional stress-strain state is obtained through the integration of the nonlinear uniaxial material response of the individual fibers used to discretize the cross-section. The uniaxial confinement model proposed by Mander et al. (1988) coupled with the cyclic rules given by Martínez-Rueda and Elnashai (1997) is used to model the concrete, while the steel is modeled using the Menegotto and Pinto (1973) model coupled with the isotropic hardening rules of Filippou et al. (1983). Figure 6.14 shows the stress-strain relationships of both models, whilst the parameters used to define them are given in Table 6.3.

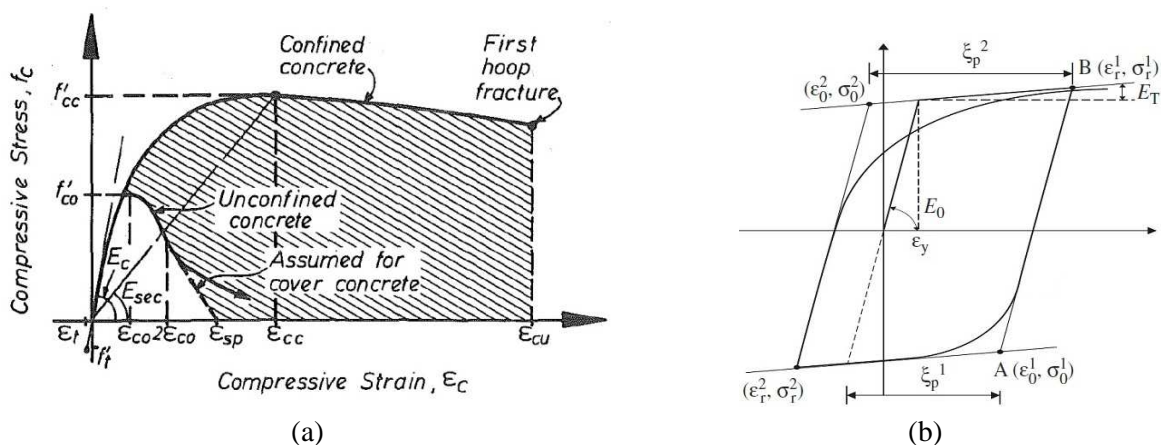(a)   (b)

Figure 6.14 - Stress-strain relationship of the (a) Mander concrete model (Mander et al., 1988) and (b) Menegotto-Pinto steel model (Fragiadakis et al., 2007).

Table 6.3 - Parameters of the nonlinear constitutive material models.

Concrete C30/37		Steel S500	
Parameter	Value	Parameter	Value
Compressive strength	38 MPa	Modulus of elasticity	200 GPa
Tensile strength	2.9 MPa	Yield strength	500 MPa
Strain at peak stress	0.002	Strain hardening parameter	0.005
Specific weight	24 kN/m^3	Specific weight	78 kN/m^3

The piers are designed according to the specifications proposed in the EN 1998-2 (2005) for the seismic zones 1.4 and 2.3 of the Portuguese territory, soil type A (EN 1998-1-NA, 2009) and using a behavior factor of 2.5. The dimensions of the existing cross-sections from the Alverca viaduct (see Section 6.2.1) were adopted, leading to a reinforcement ratio of 0.41 %. Figure 6.15 presents the force-displacement capacity curve of the piers obtained in the monotonic analysis. The piers begin to crack for a base shear force $F_{b,cr}$ of approximately 298 kN and fail for displacements of 0.5 m. The figure also shows the location of the yield region of the pier. The perturbations in the curve are the result of difficulties in reproducing the tensile behavior of the concrete when cracking occurs.
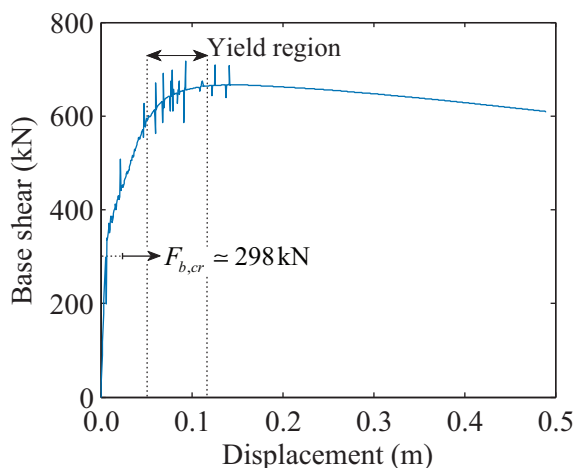
Figure 6.15 - Capacity curve of the piers.

6.4.2 Nonlinear dynamic analysis

The second step for the estimation of the effective stiffness consists of performing a nonlinear dynamic analysis to predict the inelastic response of the piers subjected to the seismic ground motions described in Section 6.3. The finite element model used in this analysis is the same as that presented in the previous section, but with a lumped mass of 281 t positioned above the top of the pier at the center of gravity of the deck cross-section, representing the mass

of the deck. Again, the software SeismoStruct is used to perform the nonlinear dynamic analysis.

The energy dissipation mechanism is accounted by means of Rayleigh damping (Clough and Penzien, 2003), with an equivalent viscous damping ratio of 2 % fixed in $f_{ela} = 1.84$ Hz, corresponding to the frequency obtained with an uncracked cross-section, and in $f_{eff} = 0.76$ Hz, which corresponds to the frequency of the pier with an effective stiffness estimated with the procedure described in the Annex C of EN 1998-2 (2005) for reinforced concrete ductile members. This criterion is based on the fact that the natural frequency of the piers after the calibration of the effective flexural stiffness is somewhere between the two aforementioned frequencies. The Rayleigh damping curve adopted in the present analysis, and also in the train-structure interaction dynamic analyses described later, is plotted in Figure 6.16.
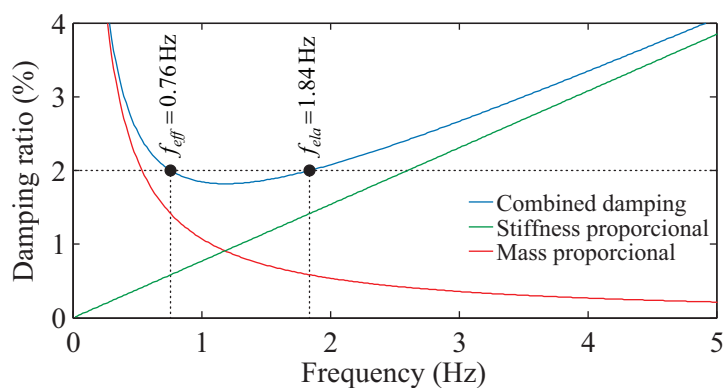
Figure 6.16 - Relation between damping ratio and frequency according to the Rayleigh damping.

The time-history responses at the top of the pier, as well as the base shear force obtained for the seismic load cases with return periods T of 95 and 310 years, are shown in Figure 6.17 for exemplification purposes, being the remaining results summarized in Table 6.4. It can be observed that the piers do not exhibit significant nonlinearity, since the maximum displacements δ_{max} obtained for all the seismic cases adopted in this work are still far from reaching the yield region (see Figure 6.15 and Table 6.4). This behavior was expected, since the piers are designed for a seismic action associated with the no-collapse requirement defined by the EN 1998-1 (2004) ($T = 475$ years). However, the maximum base shear $F_{b,max}$ exceeds $F_{b,cr}$ in all the analyses, making it necessary to use a lower stiffness for the piers in the train-structure dynamic analyses performed in the elastic domain.
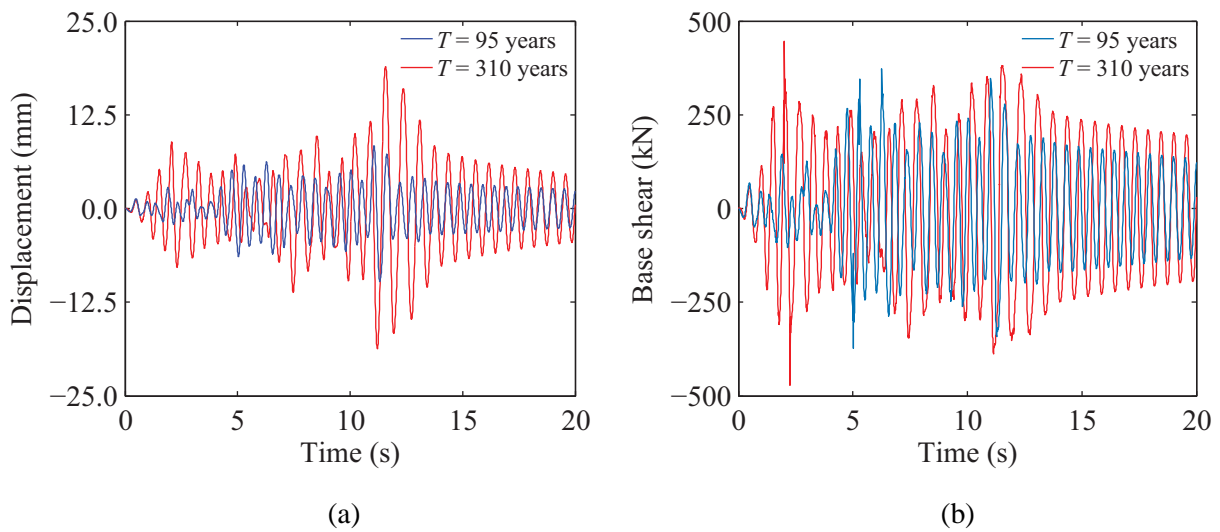
163

Figure 6.17 - Time-history responses of the pier: (a) top displacements and (b) base shear force.

Table 6.4 - Peak values of the responses obtained in the nonlinear dynamic analyses.

Analysis	Quantity	Value
$T = 95$ years	δ_{max}	9.8 mm
	$F_{b,max}$	373 kN
$T = 150$ years	δ_{max}	13.4 mm
	$F_{b,max}$	387 kN
$T = 225$ years	δ_{max}	14.5 mm
	$F_{b,max}$	439 kN
$T = 310$ years	δ_{max}	18.9 mm
	$F_{b,max}$	471 kN

6.4.3 Calibration of the effective stiffness of the piers

The third and final step of the present methodology consists of calibrating the effective stiffness of the piers in order to obtain, with a linear dynamic analysis, levels of displacement similar to those obtained with the nonlinear dynamic analysis presented in Table 6.4. Thus, the base shear force F_b obtained in the pushover curve corresponding to the maximum displacement δ_{max} at the top of the pier computed in the nonlinear dynamic analysis is evaluated (see Section 3.4.4 of Chapter 3). The effective flexural stiffness of the pier will correspond to the secant stiffness at the aforementioned point.

In the present study, since all spans of the viaduct are simply supported and disconnected from each other, the stiffness of the deck does not significantly influence the lateral behavior of the viaduct. Therefore, the effective flexural stiffness of the pier EI_{eff} can be calculated based on the elastic deflection of a cantilever beam subjected to a concentrated load, given by

$$\delta_{max} = \frac{F_b x^2}{6EI_{eff}}(3h-x)$$ (6.2)

where h is the total height of the cantilever, from the base of the pier to the center of gravity of the deck, and x is the position in which the displacement is being computed, which in this case corresponds to the top of the pier.

In order to avoid the dependency of the model on the intensity of the action, the minimum effective flexural stiffness obtained with the strongest excitation is adopted in all calculations. Nevertheless, although the analyses with lower seismic intensities are performed with a more flexible model, the aforementioned assumption ensures an acceptable approximation of the stiffness of the piers, especially in the most critical scenarios when the viaduct is subjected to stronger excitations. Hence, the proposed methodology leads to a value of the effective flexural stiffness EI_{eff} of about 43 % the value of the elastic flexural stiffness EI_0.

The comparison between the responses of the piers subjected to the seismic action with $T = 310$ years, in terms of displacements at the top and shear force at the base, obtained with the nonlinear dynamic analysis described in Section 6.4.2 and with a linear dynamic analysis with effective stiffness, is presented in Figure 6.18. A good agreement can be observed between the linear and nonlinear results in terms of maximum displacements and shear forces. Regarding the global response, the differences were expected, being justified by the fact that, at the beginning of the analysis, the nonlinear model is still with the elastic stiffness, while the linear model is already with a stiffness corresponding to the cracked section. However, when the nonlinear model begins to crack, the responses obtained with both models become similar in terms of maximum values.
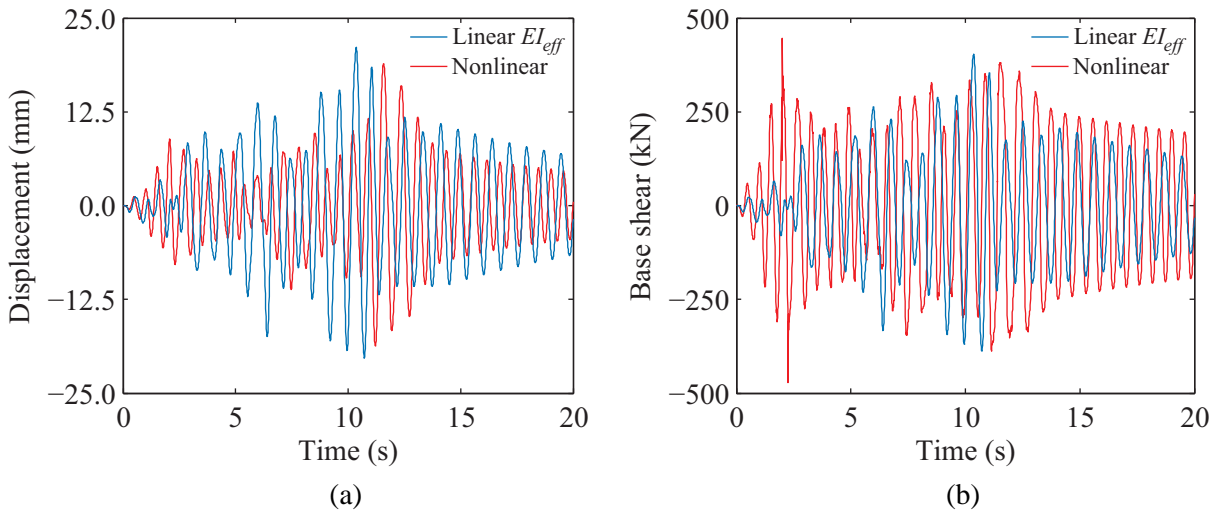
Figure 6.18 - Time-history responses of the pier for the seismic action with $T = 310$ years: (a) top displacements and (b) base shear force.

6.4.4 Dynamic properties of the viaduct considering the effective stiffness of the piers

The mode shapes and natural frequencies of the viaduct considering the effective stiffness of the piers are plotted in Figure 6.19. As expected, the modes are identical to those presented in Figure 6.5, but with lower frequencies due to the reduced stiffness of the piers.
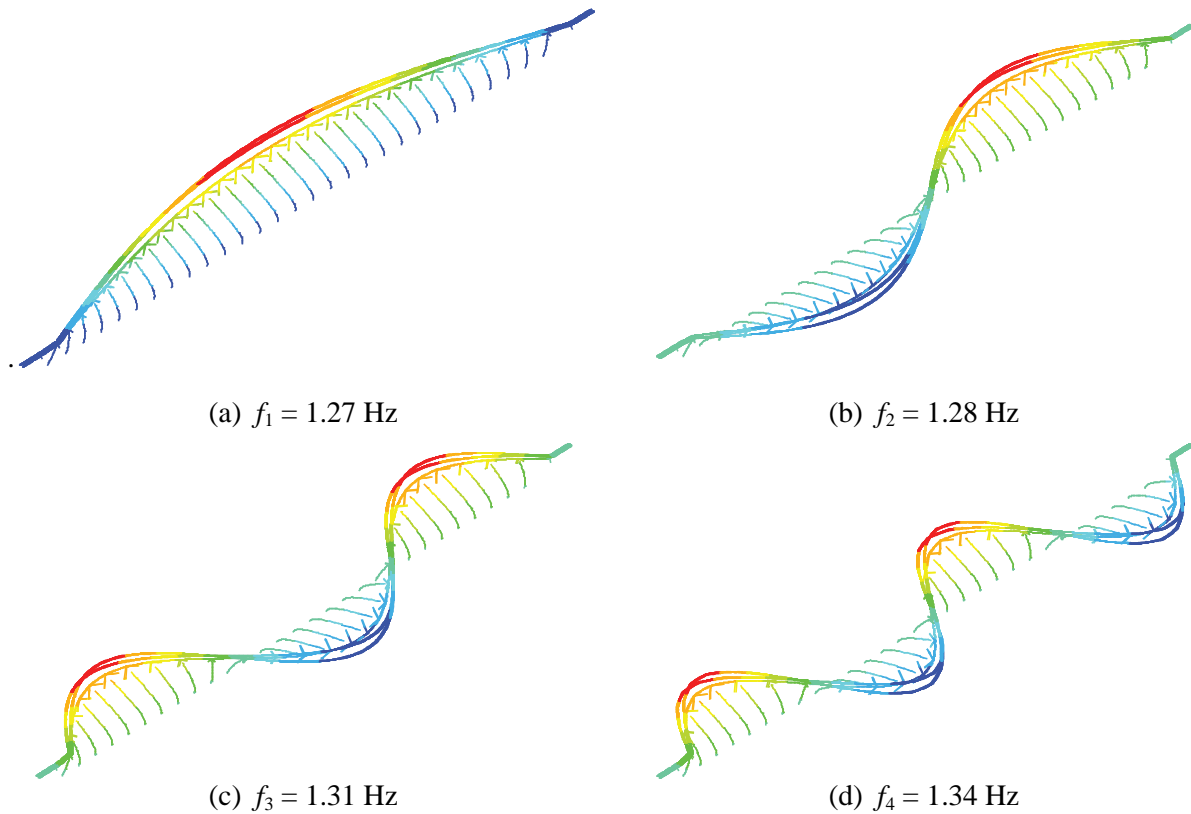

(a) $f_1 = 1.27$ Hz

(b) $f_2 = 1.28$ Hz

(c) $f_3 = 1.31$ Hz

(d) $f_4 = 1.34$ Hz

Figure 6.19 - Numerical frequencies and mode shapes of the viaduct after calibration of the effective stiffness of the piers.

6.5   NUMERICAL MODEL OF THE VEHICLE

6.5.1   Description of the Shinkansen high-speed train

The vehicle used in the present work for the dynamic analysis is based on a Japanese Shinkansen high-speed train (see Figure 6.20). This train was chosen for carrying out the running safety study since its geometrical and mechanical properties were provided by the RTRI[2].
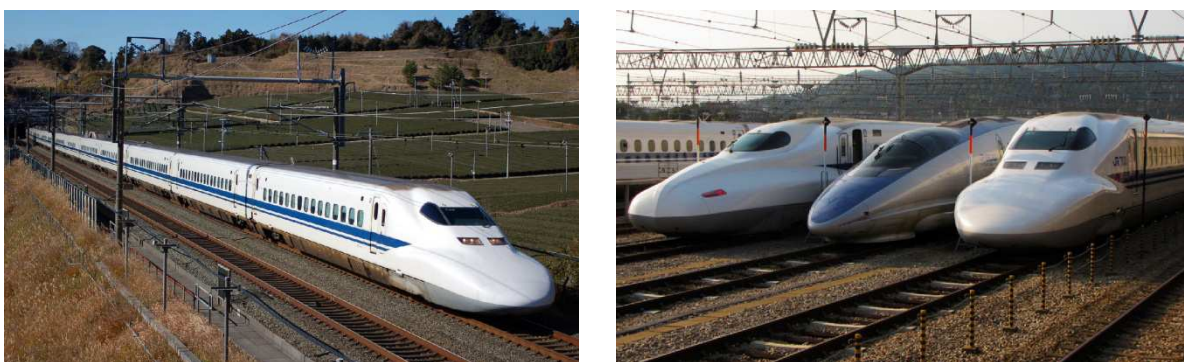
Figure 6.20 - Examples of Shinkansen trains used in Japan (Wikipedia/Shinkansen, 2014).

The train is a conventional type train with all the eight cars independent from each other with 25 m length each. Since the traction is distributed along the whole train, the cars are identical in terms of geometrical and mechanical properties, being the total weight of each car 45 t. Figure 6.21 illustrates the load model of the adopted train, including the static axle load of 110 kN of each wheelset and the longitudinal distances between them.
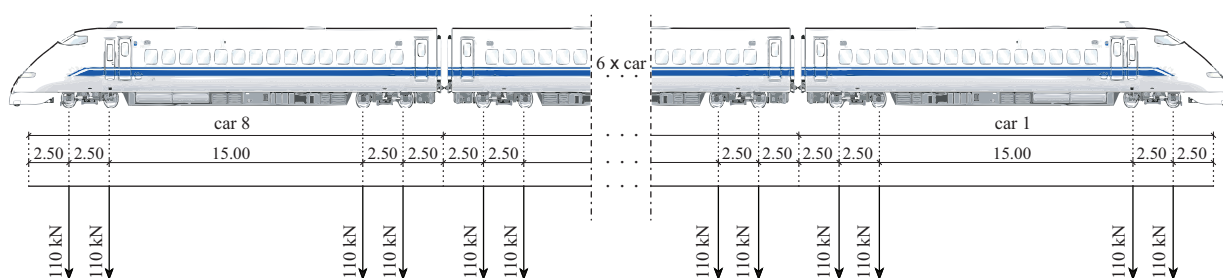
Figure 6.21 - Load model of the Shinkansen high-speed train.

6.5.2   Finite element model of the vehicle

As with the structure, the numerical model of the vehicle is also developed in ANSYS. A schematic representation of the dynamic model of one of the cars is illustrated in Figure 6.22.

---

[2] The geometrical and mechanical properties of the Shinkansen train are not published due to confidential matters from the manufacturer.

The springs and dampers of the suspensions are denoted by *k* and *c* and the masses and rotary inertias are indicated by *m* and *I*. The longitudinal, lateral and vertical distances are denoted by *a*, *b* and *h*, respectively, L_{cp} refers to the lateral distance between the initial contact points and R_0 is the nominal rolling radius. The subscripts *cb*, *bg* and *ws* indicate carbody, bogie and wheelset, respectively.
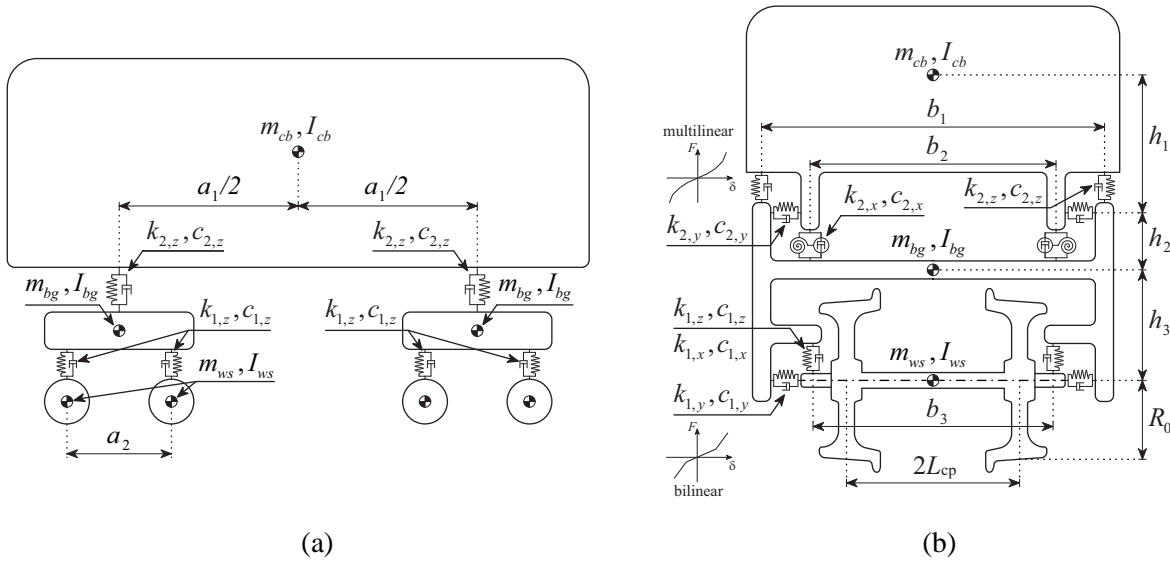

(a)   (b)

Figure 6.22 - Dynamic model of the railway vehicle: (a) lateral view and (b) front view.

The carbody, bogies and wheelsets are modeled using beam finite elements, while the suspensions are modeled using spring-dampers in the three directions, as shown in Figure 6.23. The springs used to model the suspensions are characterized by bilinear laws, as shown in Figure 6.22b, except the one used to model the secondary transversal suspension. This suspension follows a multilinear law to simulate the presence of rubber stoppers whose stiffness increases gradually (Matsumoto et al., 2004). These stoppers are used to avoid large lateral displacements of the carbody, especially during earthquake. Finally, the masses and rotary inertias are modeled using mass point elements, located at the center of mass of each component (see Figure 6.23). The wheel profile adopted in the contact model is the same as that used in the validation application presented in Section 5.5 of Chapter 5.

No material damping is considered in the model, since the flexibility of the several components of the car, such as the carbody, bogies and wheelsets, is not accounted in the beam elements used for modeling them.
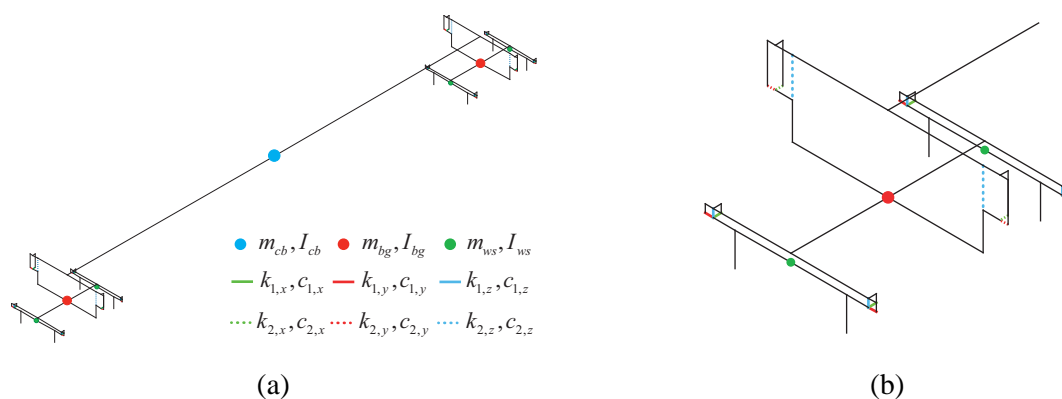
<center>(a)   (b)</center>

Figure 6.23 - Finite element model of the railway vehicle: (a) overview and (b) detail of the bogie.

6.5.3 Dynamic properties of the vehicle

The numerical mode shapes and the corresponding frequencies of one the cars of the train are presented in Figure 6.24. The carbody and bogie are denoted by CB and BG, respectively.
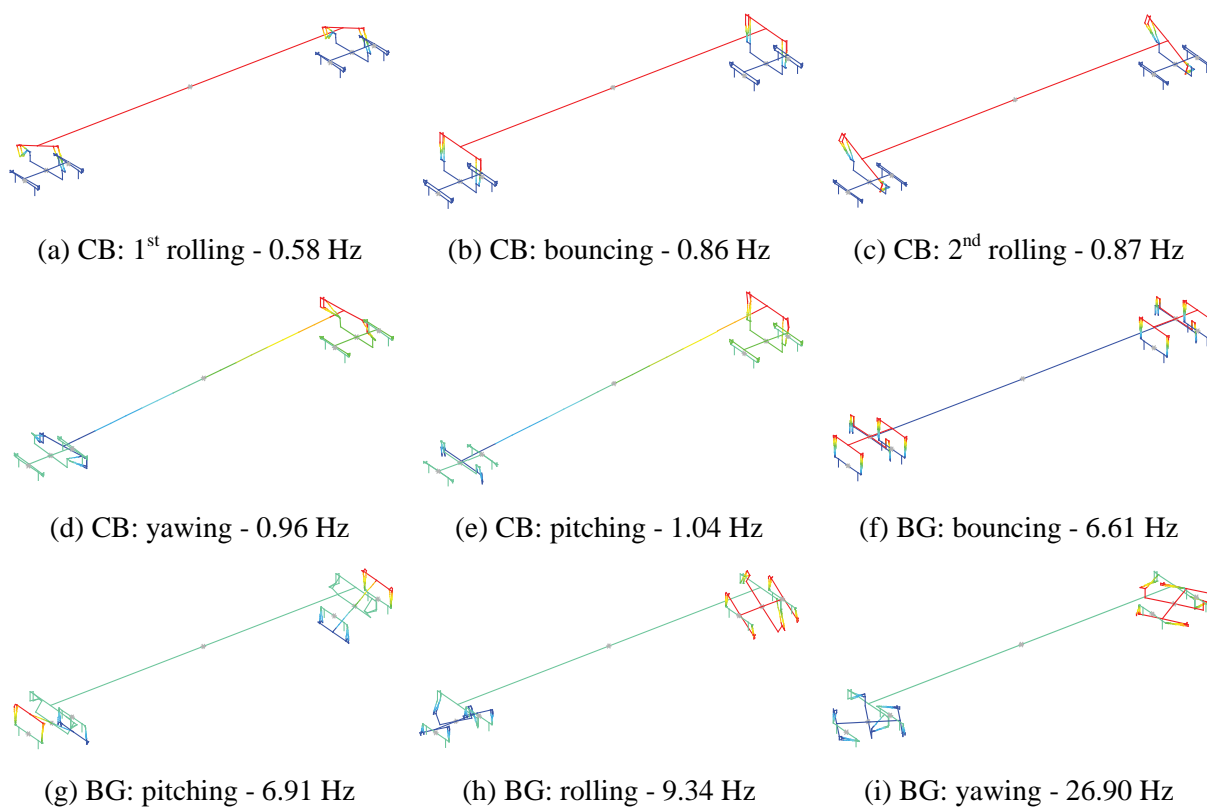

<center>

(a) CB: 1st rolling - 0.58 Hz (b) CB: bouncing - 0.86 Hz (c) CB: 2nd rolling - 0.87 Hz

(d) CB: yawing - 0.96 Hz (e) CB: pitching - 1.04 Hz (f) BG: bouncing - 6.61 Hz

(g) BG: pitching - 6.91 Hz (h) BG: rolling - 9.34 Hz (i) BG: yawing - 26.90 Hz

</center>

Figure 6.24 - Numerical frequencies and mode shapes of the railway vehicle.

6.6 DEFINITION OF THE TRACK IRREGULARITIES

6.6.1 Main characteristic of the generated irregularity profiles

The track irregularities are defined as a stochastic Gaussian ergodic process and artificially generated based on analytical PSD functions (Section 3.3.2 of Chapter 3). In the present study, two levels of track irregularities are considered: 1) regular railway operation limit, according to Claus and Schiehlen (1998) and 2) alert limit defined in EN 13848-5 (2005). The scale factors A_A, A_G, A_V and A_C referred in equation (3.6), the maximum values of each irregularity profile and the standard deviations obtained are presented in Table 6.5. The scale factors used to generate the alert limit profiles were chosen in order to obtain profiles with maximum values close to the limits defined in EN 13848-5 (2005). For both levels of track irregularity, the profiles are generated with 2000 discrete frequencies with wavelengths ranging between 3 m and 25 m (see equation (3.8)), according to EN 13848-5 (2005).

Table 6.5 - Characteristics of the generated irregularity profiles.

Irregularity type	Parameter	Regular operation limit	Alert limit
Alignment	A_A (rad.m)	1.5861×10^{-6}	2.0×10^{-6}
	Peak value (mm)	3.01	3.07
	Standard deviation (mm)	0.80	0.88
Gauge	A_G (rad.m)	1.5861×10^{-6}	2.0×10^{-6}
	Min. peak value (mm)	-3.42	-3.83
	Max. peak value (mm)	3.85	3.88
Elevation level	A_V (rad.m)	1.5861×10^{-6}	5.0×10^{-6}
	Peak value (mm)	2.57	6.03
	Standard deviation (mm)	0.78	1.37
Cross level	A_C (rad.m)	1.5861×10^{-6}	4.0×10^{-6}
	Peak value (mm)	3.85	5.86

6.6.2 Generated irregularity profiles

A 200 m stretch of the generated rail deviations, corresponding to the regular operation limit and to the alert limit level, is depicted in Figures 6.25 and 6.26, respectively. By performing the Fourier transform of the correlation function according to equation (3.5), the PSD functions used to generate the profiles can be obtained, as shown in Figures 6.27 and 6.28. These figures also present the analytic PSD functions defined in equation (3.6) and a good agreement

between both functions can be observed. Note that the PSD functions are only defined within the frequency range used to generate the irregularity profiles.
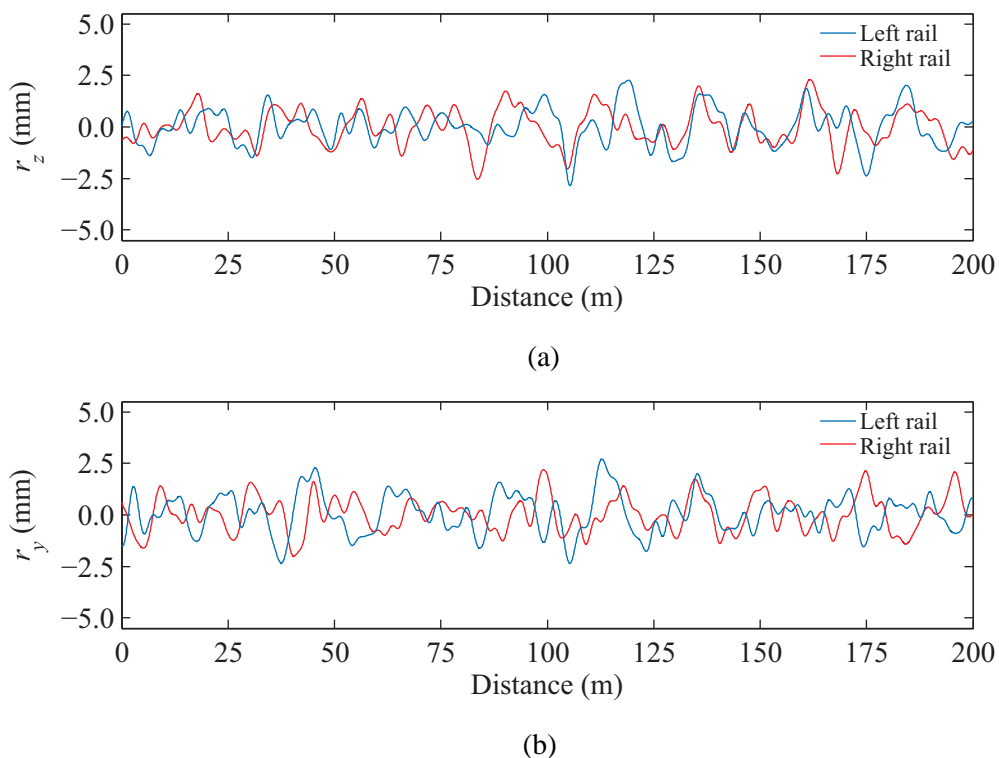

(a)

(b)

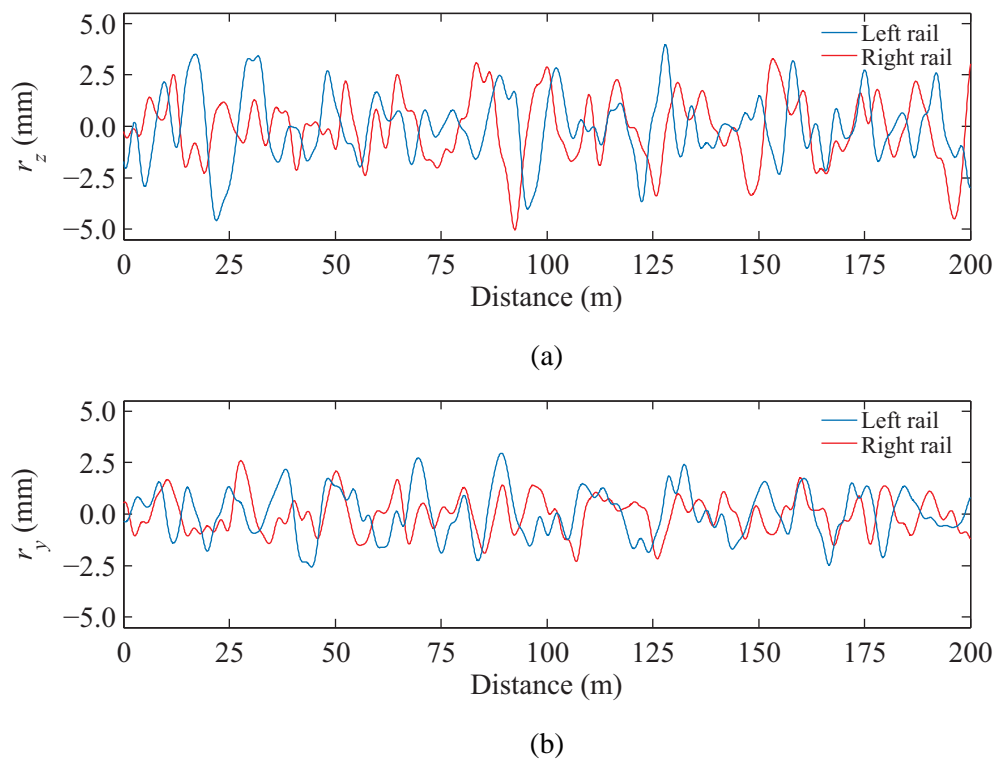Figure 6.25 - Rail deviations corresponding to the regular operation limit: (a) vertical and (b) lateral.

(a)

(b)

Figure 6.26 - Rail deviations corresponding to the alert limit: (a) vertical and (b) lateral.
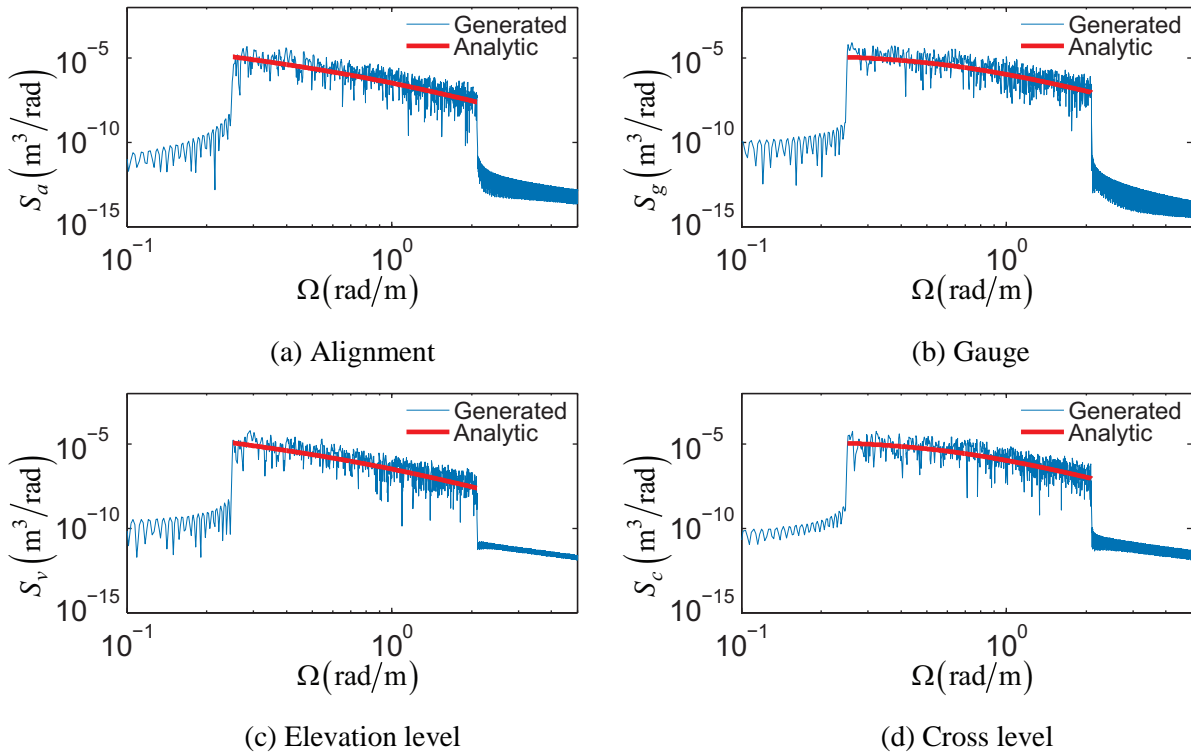
(a) Alignment

(b) Gauge

(c) Elevation level

(d) Cross level

Figure 6.27 - PSD functions of the irregularity profiles corresponding to the regular operation limit.

(a) Alignment

(b) Gauge

(c) Elevation level

(d) Cross level
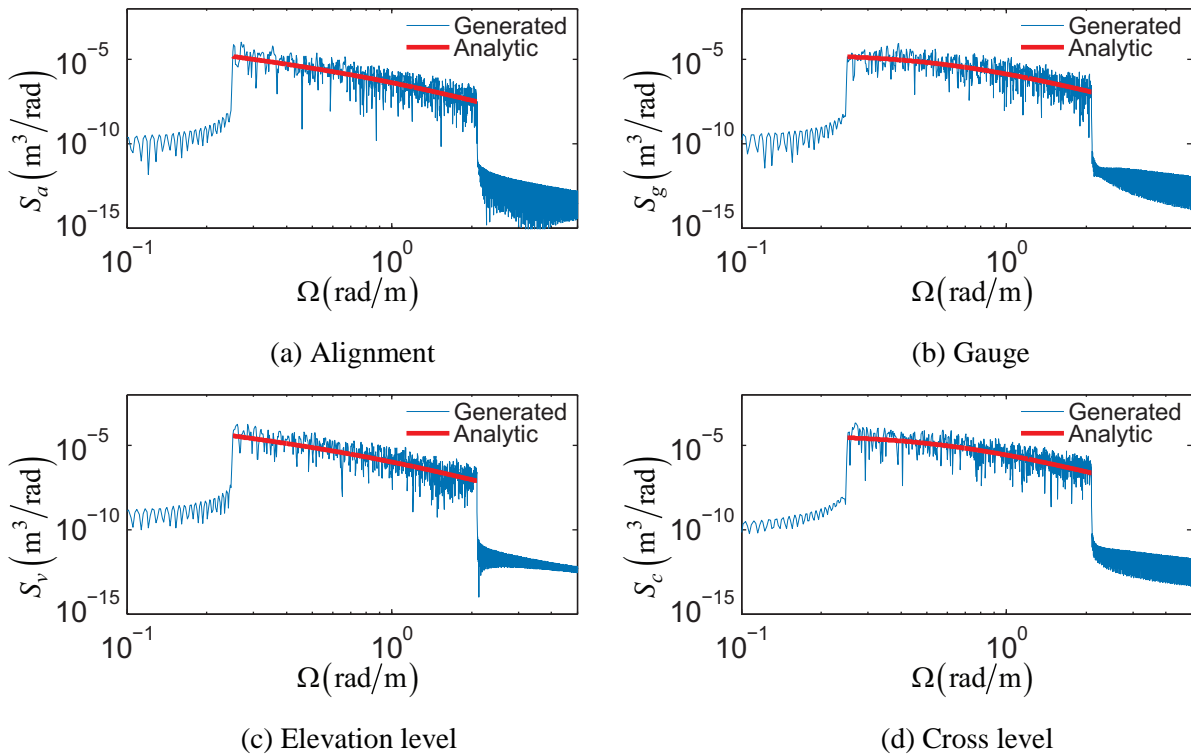
Figure 6.28 - PSD functions of the irregularity profiles corresponding to the alert limit.

6.7 DYNAMIC BEHAVIOR OF THE TRAIN-STRUCTURE SYSTEM

6.7.1 Introduction

In the present section, a preliminary dynamic analysis of the train-structure system performed with the numerical tool described in Chapter 4 is presented. The analysis consists of a Shinkansen train (see Section 6.5) travelling over the idealized Alverca viaduct (see Section 6.2) subjected to the lateral ground motions and to the track irregularities described in Sections 6.3 and 6.6, respectively. Only one car from the whole train is considered, since the train is composed by several independent cars that do not interact significantly with each other (conventional type train). Furthermore, the evaluation of resonance effects that may occur in the viaduct due to the passage of repeated loads is beyond the scope of the present thesis.

The preliminary dynamic analyses are performed for speeds of 200 km/h and 350 km/h, which are the limits of the speed range considered in the running safety analysis presented later in Section 6.8. The results are presented separately for the viaduct (Section 6.7.2) and vehicle (Section 6.7.3). For the first, both the vertical and lateral dynamic responses are evaluated, being the influence of the effective stiffness of the piers due to concrete cracking also discussed. Regarding the vehicle, besides the evaluation of its vertical and lateral behavior, it is also analyzed the influence of the suspension stoppers on the lateral response of the vehicle. Additionally, the adoption of distinct time offsets between the beginning of the earthquake and the entry of the vehicle in the viaduct (see Section 6.3.2) is justified with examples.

Finally, the time step Δt used in the analyses is 0.004 s, which is the maximum value to guarantee that the minimum wavelength of 3 m considered in irregularity generation is discretized with 8 points when the vehicle runs at the maximum speed of 350 km/h. The following parameters for the α method are adopted: $\alpha = -0.1$, $\beta = 0.3025$ and $\gamma = 0.6$. A nonzero value of the α parameter is used to provide numerical dissipation for controlling spurious participation of the higher modes. According to Hughes (2000), values of α in the interval [-1/3, 0] ensure second-order accuracy and unconditional stability to the integration algorithm.

6.7.2 Dynamic response of the viaduct

The present section aims to analyze the dynamic response of the viaduct under seismic conditions. The results correspond to the scenario $i = 3$ and to a running speed $V = 350$ km/h according to equation (6.1), in which the first wheelset of the vehicle is positioned at the coordinate $x_3 = -365.56$ m at the beginning of the simulation (see Figure 6.29).
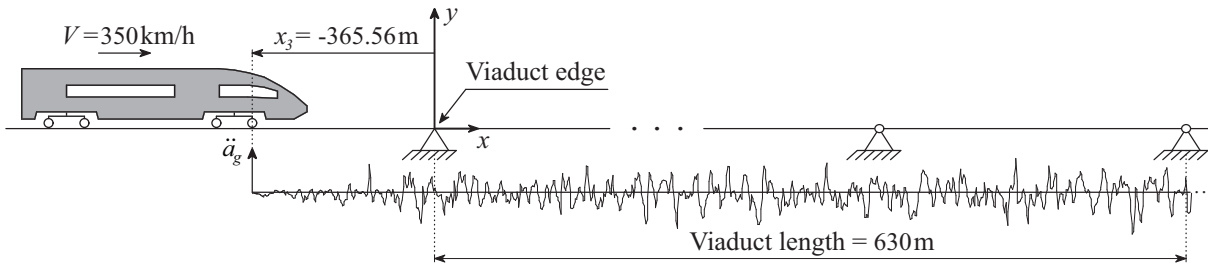
Figure 6.29 - Scenario $i = 3$ according to equation (6.1) for $V = 350$ km/h.

6.7.2.1 Vertical response

The vertical displacements of the deck at the midspan of the first span and 15th span (center span) are plotted in Figure 6.30. The responses are obtained for two distinct scenarios: in the first scenario (Figure 6.30a) the viaduct is subjected exclusively to the load of the vehicle running at $V = 350$ km/h, while in the second scenario (Figure 6.30b) the viaduct is also subjected to the seismic action with $T = 310$ years (see Section 6.3). On both scenarios, the track quality corresponds to the regular operation limit (see Section 6.6). Since only the lateral component of the earthquake is considered, the vertical response of the deck is not affected by the seismic action. As a consequence, and also due to the fact that there is almost no continuity between spans, the vertical excitation in each span is felt only when the vehicle crosses them. A similar conclusion can be drawn from the vertical accelerations presented in Figure 6.31.

(a)

(b)
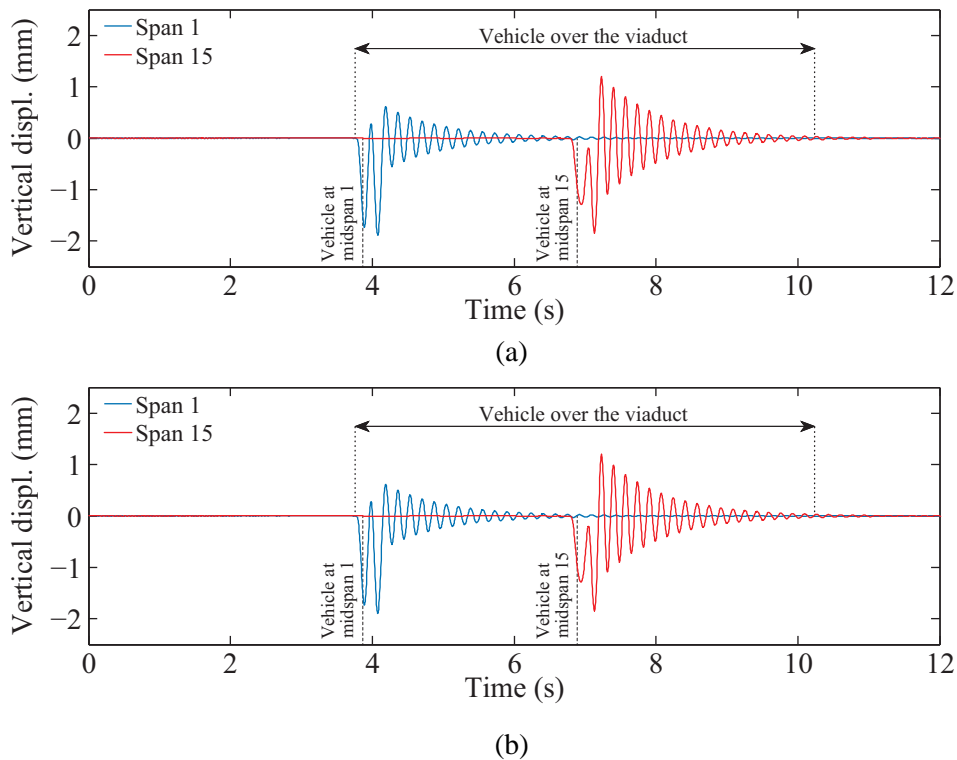
Figure 6.30 - Vertical displacements of the deck at the midspan of span 1 and 15 ($V = 350$ km/h): (a) without earthquake and (b) subjected to the seismic action with $T = 310$ years.
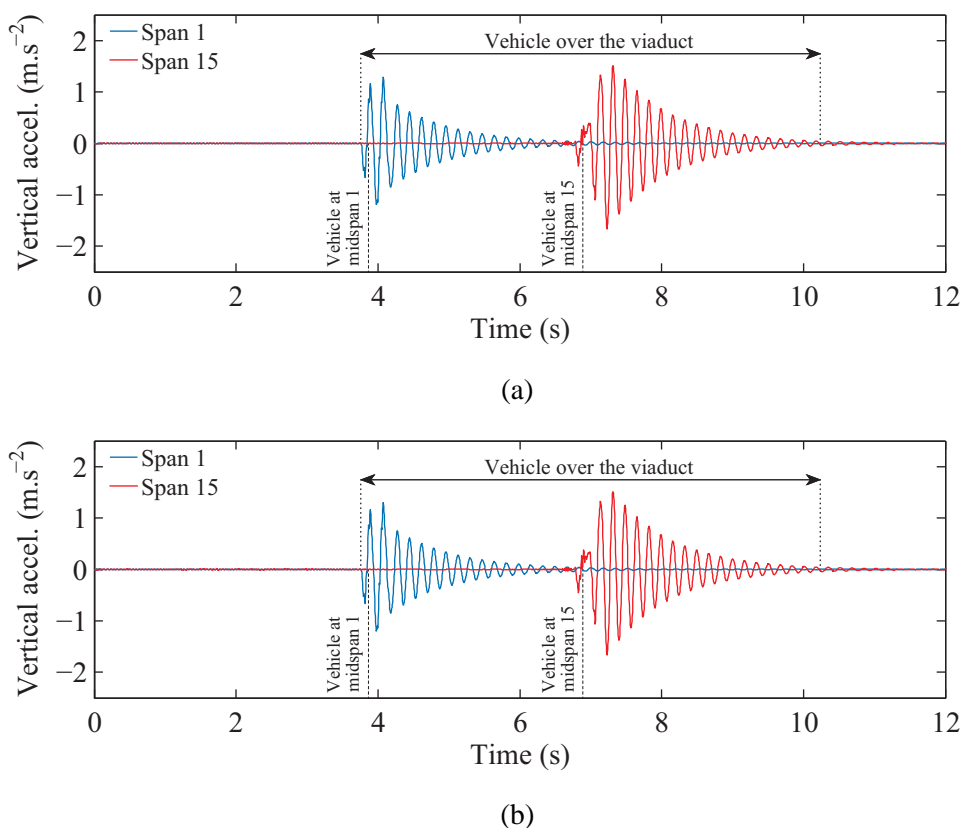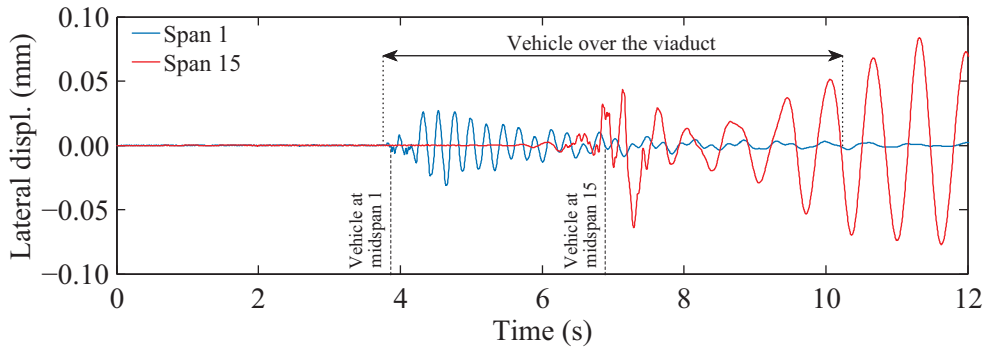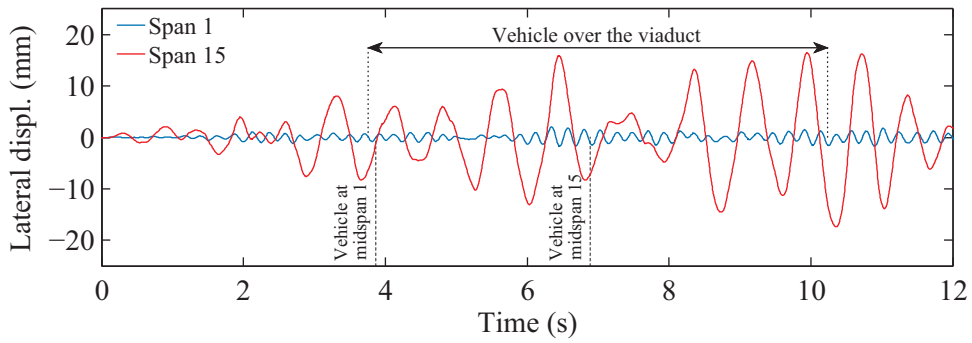
(a)

(b)

Figure 6.31 - Vertical accelerations of the deck at the midspan of span 1 and 15 ($V = 350$ km/h): (a) without earthquake and (b) subjected to the seismic action with $T = 310$ years.

6.7.2.2 Lateral response

Figures 6.32 and 6.33 show the lateral responses of the deck in terms of displacements (the lateral displacement of the deck is relative to the lateral displacement at the base of the piers) and accelerations, respectively, for the same scenario described above. Contrary to what is observed in the vertical direction, the vehicle has a small influence in the lateral response of the viaduct, since the lateral impacts that occur between the wheel and rail are barely reflected in the deck response (the maximum displacement and acceleration is less than 0.10 mm and 0.15 m/s^{-2}, respectively). It can also be observed, especially in the displacements, that the response of the first span has a higher frequency and lower amplitude than the response of the middle span. This is a consequence of the lower flexibility of the viaduct at the ends due to the connection to the abutments. Although the bearing supports are the same in these locations as in the rest of the viaduct, since the flexibility of the abutment and the surrounding embankment is not considered in the model, the edge spans are considerably more constrained than the others.
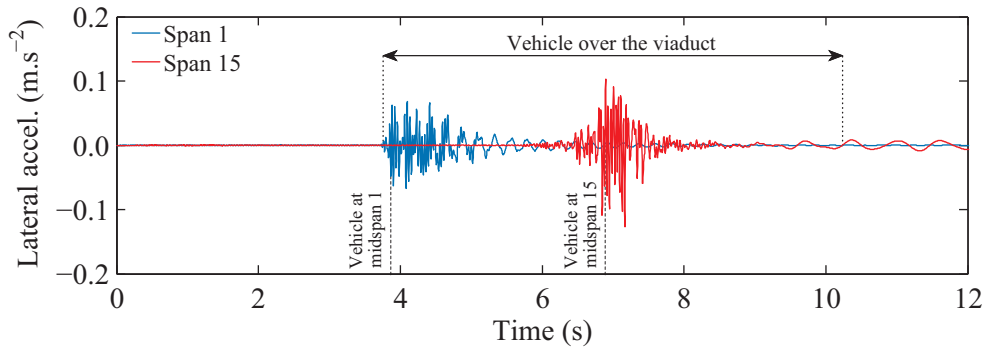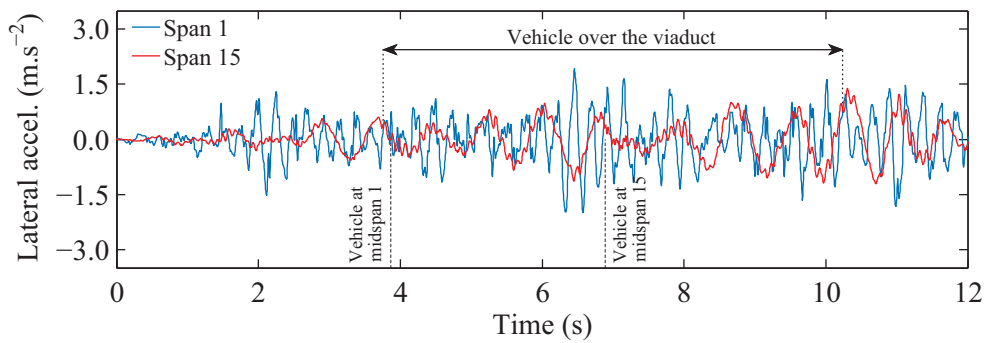
(a)

(b)

Figure 6.32 - Lateral displacements of the deck at the midspan of span 1 and 15 ($V = 350$ km/h): (a) without earthquake and (b) subjected to the seismic action with $T = 310$ years.

(a)

(b)

Figure 6.33 - Lateral accelerations of the deck at the midspan of span 1 and 15 ($V = 350$ km/h): (a) without earthquake and (b) subjected to the seismic action with $T = 310$ years

6.7.2.3 Influence of the effective stiffness of the piers

As mentioned in Section 6.4, although the structure is not expected to experience significant damage for the levels of seismicity considered in the present study, the reduction in the flexural stiffness of the piers should be considered to account for concrete cracking. Therefore, the present section aims to evaluate the effect of this procedure on the lateral response of the viaduct.

The lateral displacements of the deck at the midspan of the 15th (center span) when the viaduct is subjected to the vehicle load, running at $V = 350$ km/h, and to the seismic actions with $T = 95$ years and $T = 310$ years are depicted in Figures 6.34 and 6.35, respectively. The figures also show the response spectra of both accelerograms, together with the representation of the shift in the structural period T due to the reduction in the flexural stiffness of the piers (see Figures 6.5a and 6.19a for the frequencies f_1 of the first mode of vibration of the viaduct considering the elastic and the effective stiffness, respectively). The subscripts *ela* and *eff* indicate elastic and effective stiffness. For both scenarios of seismicity, the frequency of the response become lower after considering the effect of concrete cracking in the piers. On the other hand, although the spectral acceleration decreases due to the increase in the period of the structure (see Figures 6.34b and 6.35b), the amplitude of the response increases. This is due to the fact that the piers are less stiff and therefore may experience larger displacements during the earthquake.
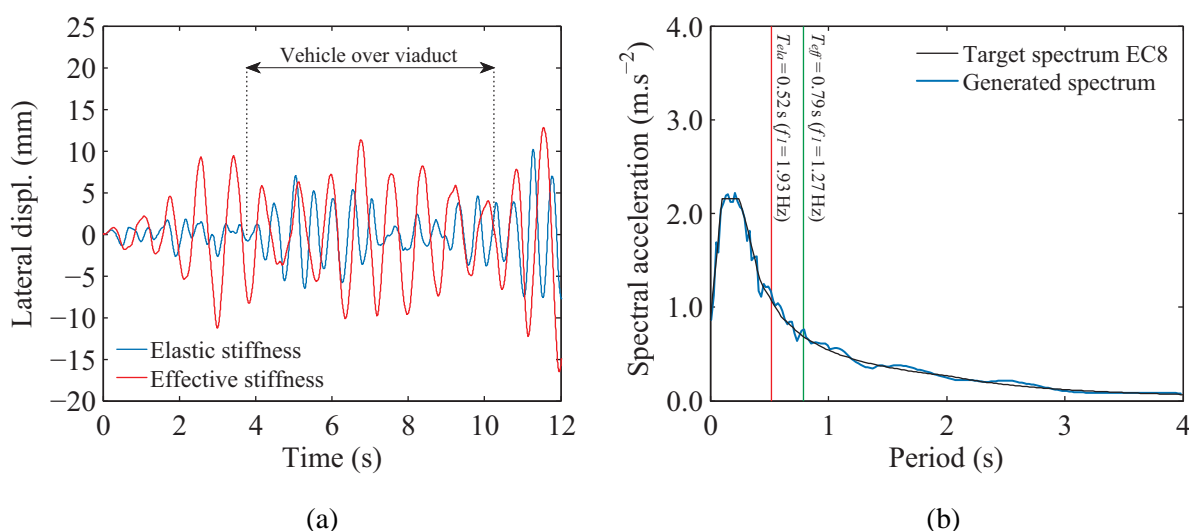

Figure 6.34 - Influence of the effective stiffness of the piers on the response of the structure for the seismic action with $T = 95$ years: (a) lateral displacements of the deck at the midspan of span 15 and (b) shift in the structural period.
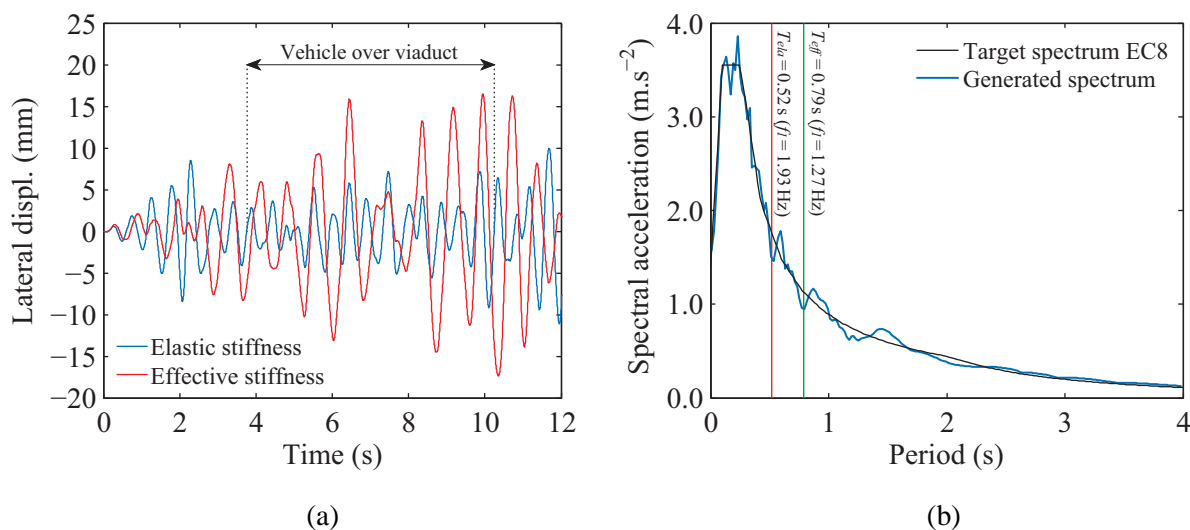
177

Figure 6.35 - Influence of the effective stiffness of the piers on the response of the structure for the seismic action with $T = 310$ years: (a) lateral displacements of the deck at the midspan of span 15 and (b) shift in the structural period.

6.7.3 Dynamic response of the vehicle

The present section aims to assess the dynamic behavior of the Shinkansen high-speed train when travelling on the railway viaduct under seismic conditions. All the results, with the exception of Section 6.7.3.4, correspond to the scenario $i = 3$ according to equation (6.1), in which the first wheelset of the vehicle is positioned at the coordinate $x_3 = -73.89$ m or $x_3 = -365.56$ m at the beginning of the simulation for speeds of 200 and 350 km/h, respectively (see Figure 6.29). In Section 6.7.3.4 the influence of the time offset between the beginning of the earthquake and the entry of the vehicle in the viaduct is discussed, using as an example the scenarios $i = 1$, $i = 2$, $i = 3$ and $i = 4$ (see equation (6.1))

6.7.3.1 Vertical response

Figure 6.36 shows the vertical accelerations at the center of mass of the carbody and second wheelset calculated for speeds of 200 km/h and 350 km/h. On both scenarios the track quality corresponds to the regular operation limit and, since the earthquake does not influence the vertical response of the system (see Section 6.7.2.1), no seismic action is considered. It is perfectly clear that the frequency of the acceleration response of the carbody is much lower than that of the wheelset, which demonstrates the efficiency of the suspensions on filtering the high frequencies arising from the contact between wheel and rail. Regarding the amplitude, the differences are more pronounced when the vehicle runs at higher speeds, since the influence of

the track irregularities on the levels of acceleration become more prominent. Hence, the maximum vertical acceleration at the wheelset increases from 5.4 m/s^2 to 17.5 m/s^2 for speeds of 200 km/h and 350 km/h, respectively, while the acceleration at the carbody remains approximately constant (3.46 m/s^2 and 3.65 m/s^2 for the minimum and maximum speed considered).
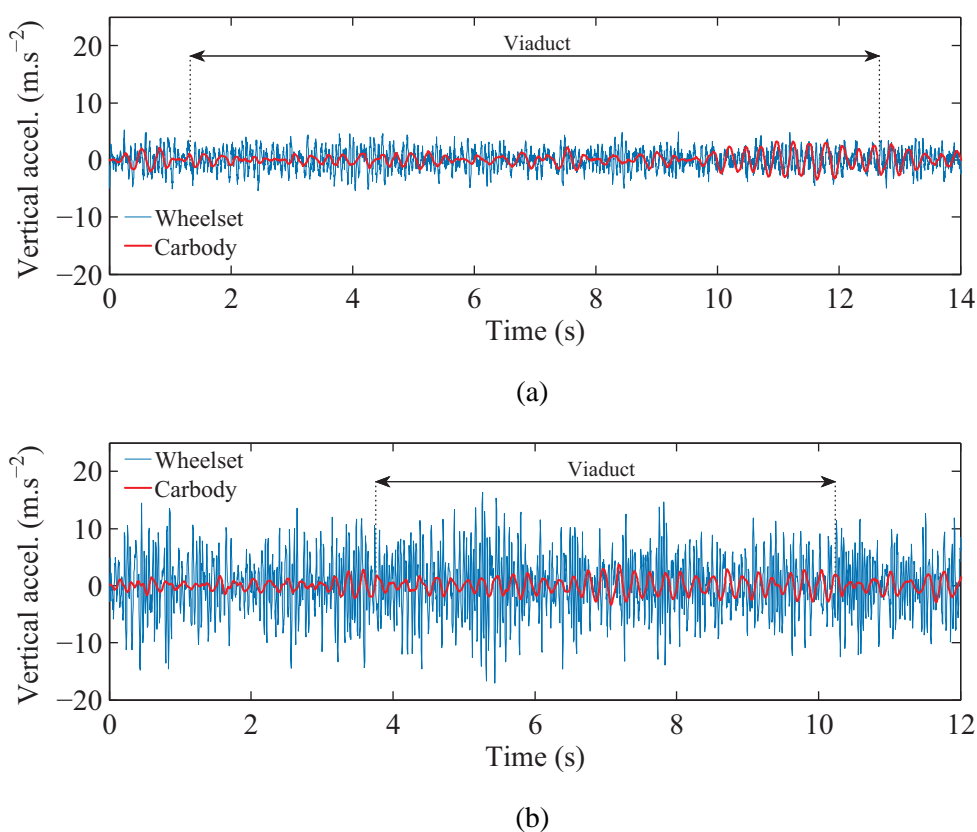

(a)

(b)

Figure 6.36 - Vertical accelerations of the carbody and 2nd wheelset without earthquake and for a track quality corresponding to the regular operation limit: (a) $V = 200$ km/h and (b) $V = 350$ km/h.

The vertical contact forces in the left wheel of the second wheelset calculated for the aforementioned scenario and for speeds of 200 km/h and 350 km/h are plotted in Figure 6.37. Again, the increase in speed has a significant influence in the magnitude of the vertical contact forces due to the stronger impacts that occur between the wheel and the rail caused by the presence of track irregularities. The maximum vertical contact force obtained in this wheel for speeds of 200 km/h and 350 km/h is, approximately, 85 kN and 110 kN, respectively, which represents an increase of about 54 % and 100 % over the static load value of 55 kN of each wheel (see Figure 6.21).
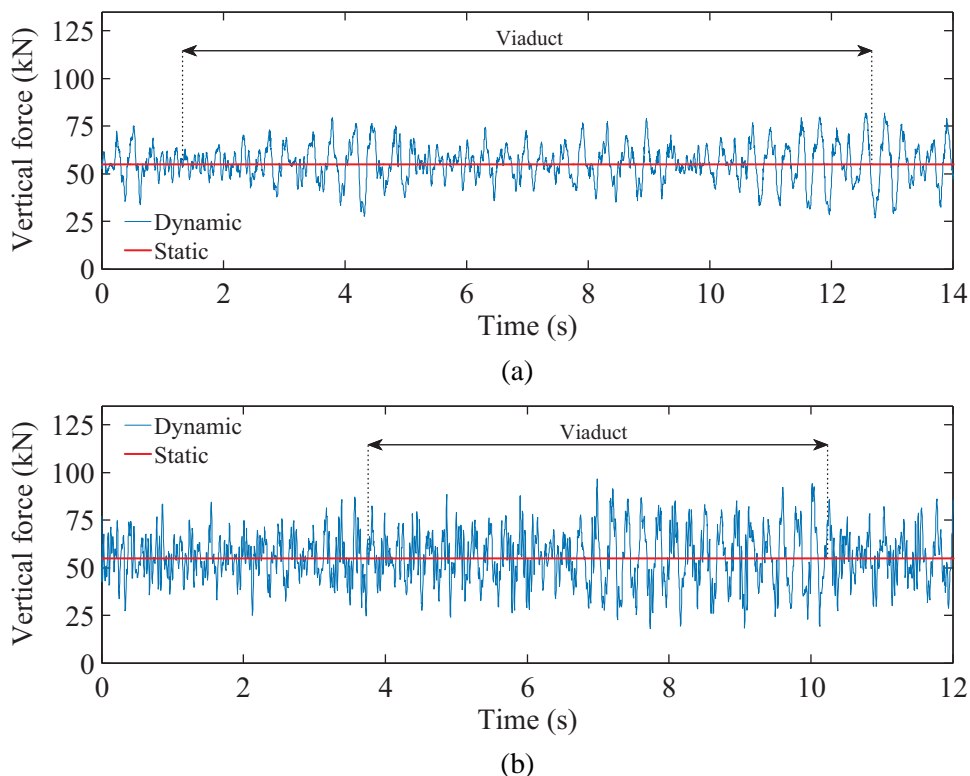
(a)

(b)

Figure 6.37 - Vertical contact forces in the left wheel of the 2nd wheelset without earthquake and for a track quality corresponding to the regular operation limit: (a) $V = 200$ km/h and (b) $V = 350$ km/h.

6.7.3.2 Lateral response

The lateral displacements at the center of mass of the carbody and second wheelset are plotted in Figure 6.38 (the displacements of the vehicle are relative to the lateral displacement of the track centerline). The responses are obtained for two distinct scenarios: in the first scenario (Figure 6.38a) the viaduct is subjected exclusively to the load of the vehicle running at $V = 350$ km/h, while in the second scenario (Figure 6.38b) the viaduct is also subjected to the seismic action with $T = 310$ years. On both scenarios, the track irregularities correspond to the regular operation limit. By comparing Figure 6.38a with Figure 6.38b, it is clear that the earthquake is the main responsible for the large lateral displacements experienced by the carbody, since the track irregularities barely contribute to them, as it can be observed in Figure 6.38a. Under seismic conditions, the maximum lateral displacement of the carbody, relative to the lateral displacement of the track centerline, is approximately six times higher than the maximum displacement of the wheelset.
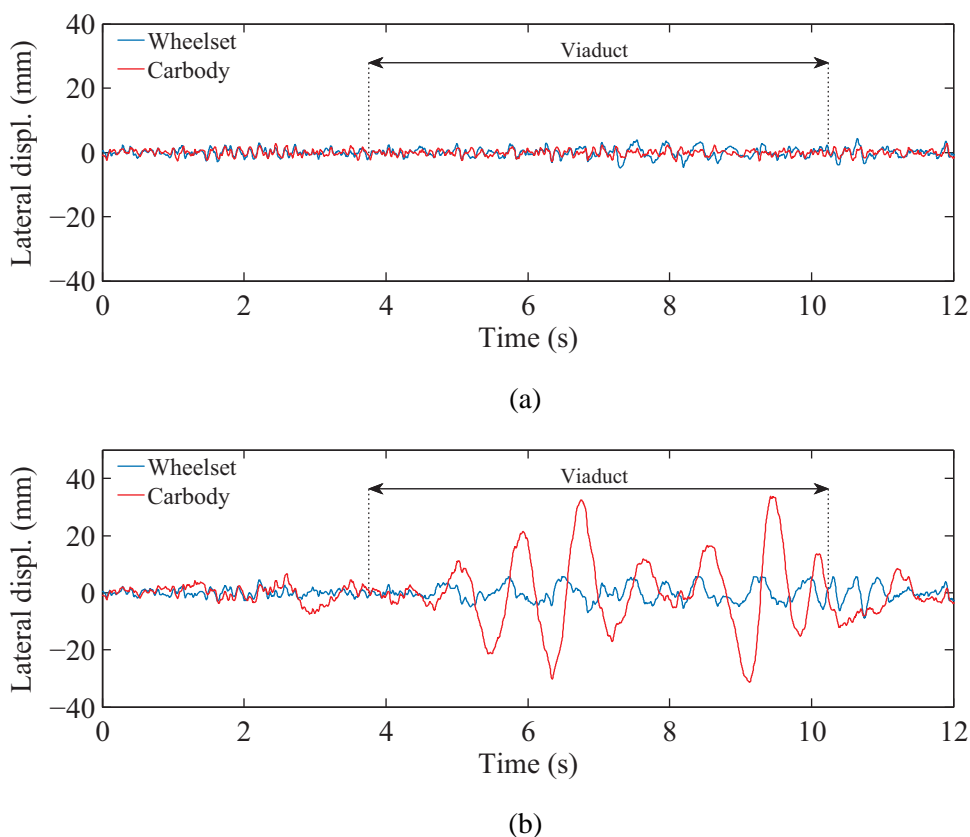
(a)

(b)

Figure 6.38 - Lateral displacements of the carbody and the 2nd wheelset for a track quality corresponding to the regular operation limit ($V = 350$ km/h): (a) without earthquake and (b) subjected to the seismic action with $T = 310$ years.

Figure 6.39 shows the lateral response of the vehicle at the same locations described above, but in terms of accelerations. The response at the wheelset is not significantly affected by the seismic action, since it depends mainly on the contact between wheel and rail and on the track irregularities. However, a considerable difference can be observed between the lateral accelerations at the carbody obtained with and without earthquake, during the period in which the vehicle is crossing the viaduct. Such behavior is expected, since the carbody has a low natural frequency and, therefore, is more susceptible to be excited by the lateral movements of the viaduct imposed by the earthquake. Moreover, when comparing the relatively high frequency observed in the response of the wheelset with the much lower frequency of the response of the carbody, it is clear once again the filtering effect provided by the suspensions, as already shown in Figure 6.36 for the vertical direction.
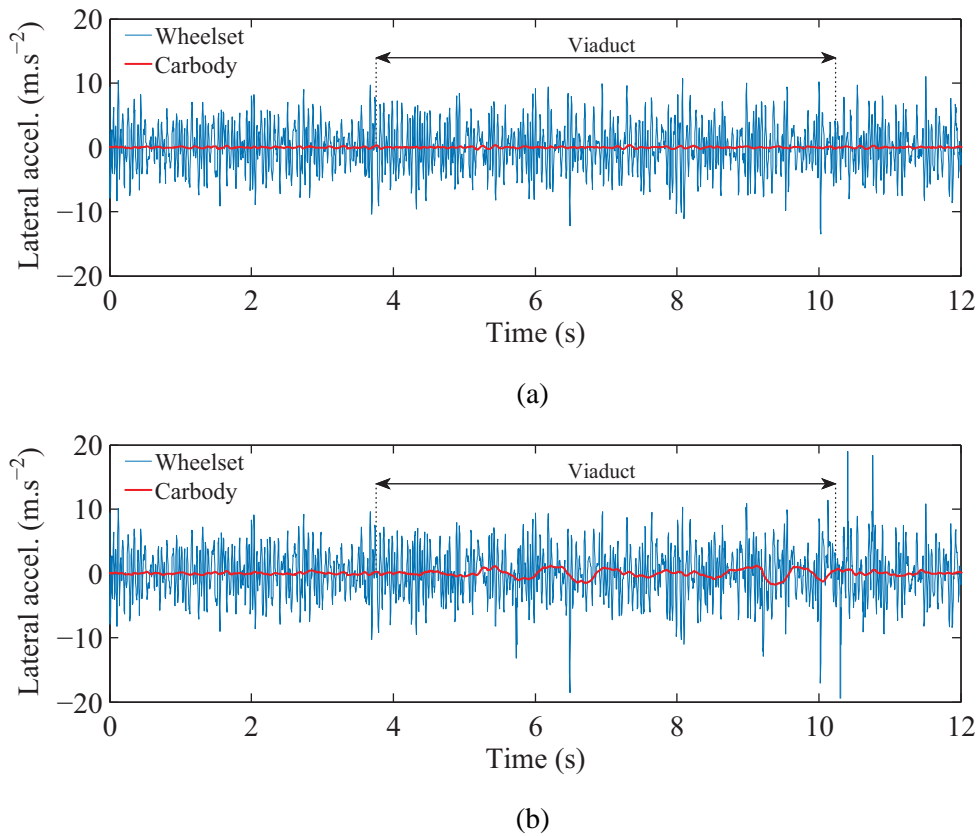
(a)

(b)

Figure 6.39 - Lateral accelerations of the carbody and the 2nd wheelset for a track quality corresponding to the regular operation limit ($V = 350$ km/h): (a) without earthquake and (b) subjected to the seismic action with $T = 310$ years.

Finally, the lateral contact forces obtained in the left wheel of the second wheelset for speeds of 200 km/h and 350 km/h are plotted in Figures 6.40 and 6.41, respectively. On both figures, the lateral contact forces are superimposed on the relative lateral displacements between wheel and rail. It is clear that the peaks observed in the lateral contact forces during the earthquake are due to the wheel flange impacts, since they occur at the same moment as the gap between the flange and rail closes (approximately 6 mm). This is particularly noticeable in Figure 6.41b. When the viaduct is not subjected to any ground motion, the excitations caused solely by the track irregularities are not sufficient to cause lateral impacts between the flange and the rail, leading to a decrease in the levels of contact force. Figure 6.42 illustrates, as an example, the relative position between the wheel and the rail at the instant indicated in Figure 6.41 ($t = 5.7$ s). As expected, in the scenario where the viaduct is not subjected to any ground motion, the flange is still far from the rail and no impact occurs, while in the scenario in which the earthquake action is considered the impact is perfectly visible.
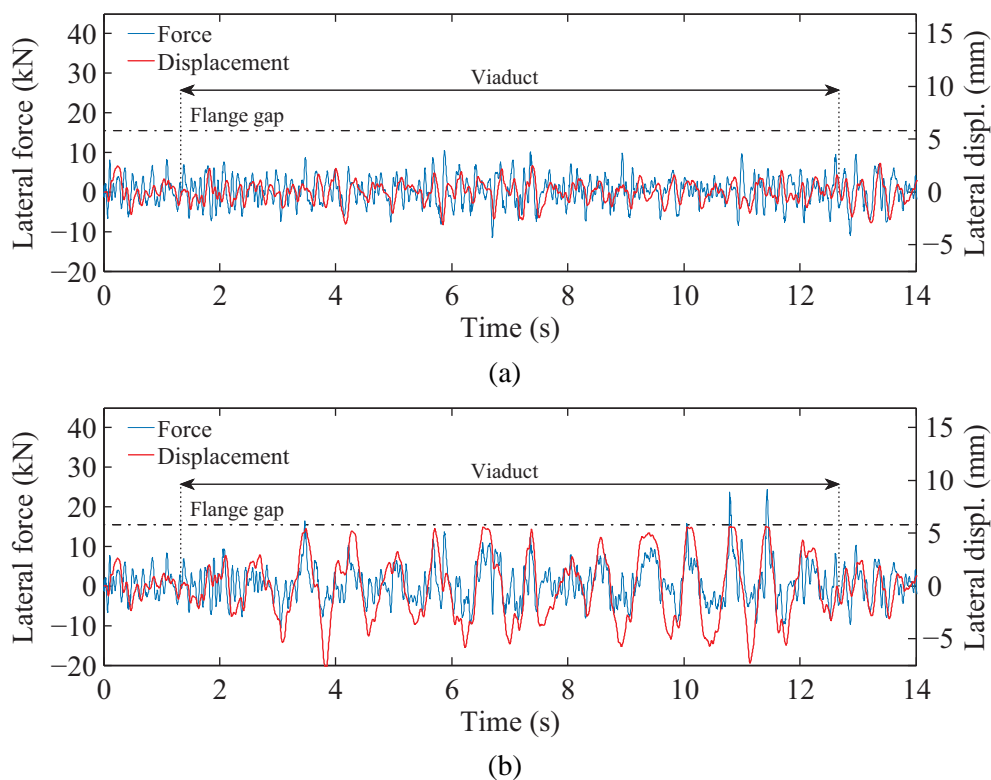
Figure 6.40 - Lateral contact forces and displacements of the left wheel of the second wheelset ($V = 200$ km/h): (a) without earthquake and (b) subjected to the seismic action with $T = 310$ years.
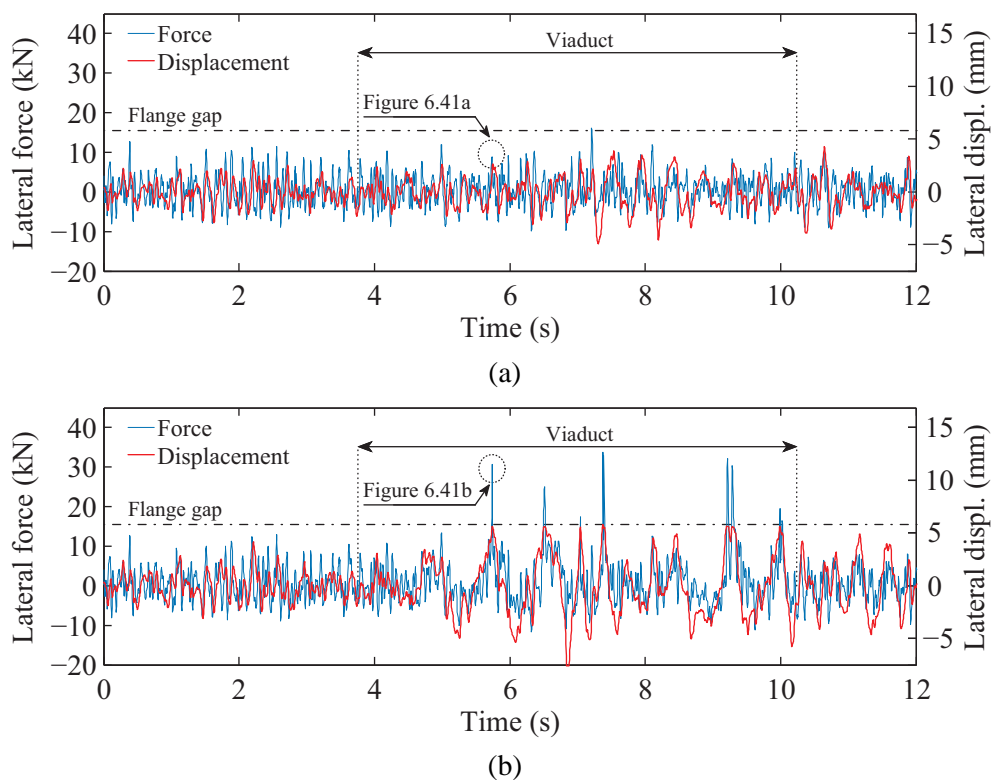

Figure 6.41 - Lateral contact forces and displacements of the left wheel of the 2nd wheelset ($V = 350$ km/h): (a) without earthquake and (b) subjected to the seismic action with $T = 310$ years.
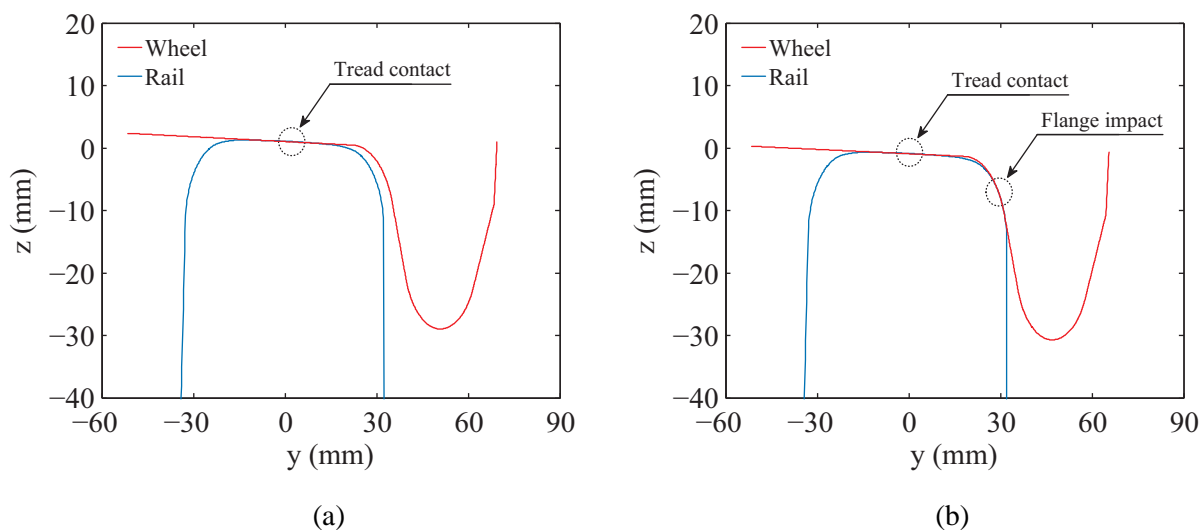
(a)   (b)

Figure 6.42 - Relative position between the left wheel of the 2nd wheelset and rail at t = 5.7 s (V = 350 km/h): (a) without earthquake and (b) subjected to the seismic action with T = 310 years.

6.7.3.3 Influence of the suspension stoppers

Most of the high-speed trains have stoppers installed in the secondary transversal suspensions in order to avoid large lateral displacements of the carbody, especially during earthquake. These devices are characterized by a multilinear force-displacement law that simulates the presence of a rubber pad whose stiffness increases gradually (see Section 6.5.2). Thus, although the importance of the stoppers is unquestionable during intense earthquakes, the present section aims to evaluate if they also influence the behavior of the carbody in the presence of moderate seismic actions as those considered in this work.

The lateral displacements of the carbody at a point above the first bogie relative to the displacements of the center of mass of the first bogie are depicted in Figure 6.43a. The response is obtained for a scenario in which the vehicle runs on the viaduct at V = 350 km/h, subjected to the seismic action with T =310 years and to the track irregularities corresponding to the regular operation limit. In order to evaluate the influence of the stopper on the response of the carbody, the displacements of the actual vehicle are compared with those obtained for the same vehicle but without the presence of this device, i.e., with a secondary lateral suspension characterized by a linear force-displacement law equivalent to the initial stretch of the actual suspension, as shown in Figure 6.43b[3]. It can be observed that the maximum relative displacement δ_{max}

---

[3] As mentioned in Section 6.5, the geometrical and mechanical properties of the Shinkansen train cannot be published due to confidential matters from the manufacturer. Therefore, no details about the multilinear suspension law are given in Figures 6.43b and 6.44b.

between the carbody and the bogie is around 33 mm, which is already above the linear threshold value of 22 mm of the multilinear law. However, although it is notable that the responses start to diverge from each other after the threshold value is reached, the maximum displacements do not show considerable differences. This is due to the fact that the increase in the suspension's stiffness is still not significant for the levels of displacements experienced by the carbody, as can be seen in Figure 6.43b. Thus, for the levels of seismic intensity studied in the present work, the stoppers do not have an important impact in the lateral response of the vehicle.
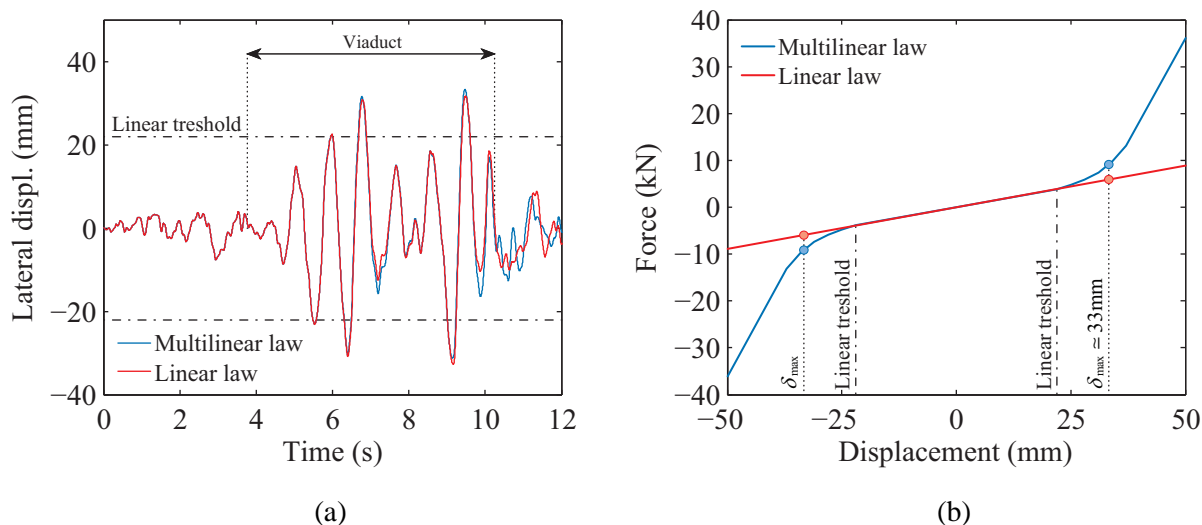

Figure 6.43 - Multilinear vs. Linear law of the secondary transversal suspension: (a) lateral response of the carbody and (b) force-displacement laws of the suspension.

Nevertheless, in order to demonstrate the behavior of the stopper in a situation in which the carbody would experience the impact with the stiff rubber pad, a comparison between the response of the carbody with the actual suspension and with a suspension characterized by a bilinear law whose first and second stretches are equivalent to the first and last stretches of the actual suspension is depicted in Figure 6.44. While in the scenario represented in Figure 6.43 the stiffness of the linear suspension is about 65 % of the value of the actual suspension's stiffness for $\delta_{max} = 33$ mm, in the scenario depicted in Figure 6.44, the stiffness of the bilinear suspension for the same level of displacements is around 265 % of the value of the actual stiffness. Consequently, the sudden increase in stiffness provided by the suspension with a bilinear law significantly restrains the lateral displacements of the carbody, thus demonstrating the importance of these devices in maintaining the stability of the vehicle.
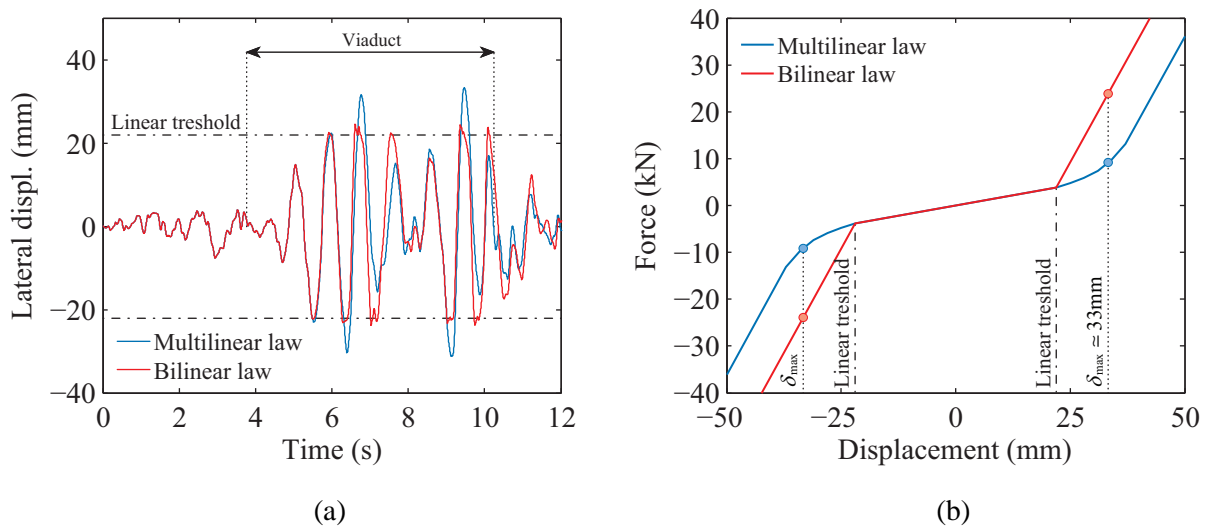
Figure 6.44 - Multilinear vs. Bilinear law of the secondary transversal suspension: (a) lateral response of the carbody and (b) force-displacement laws of the suspension.

6.7.3.4 *Influence of the time offset between the beginning of the earthquake and the entry of the vehicle in the viaduct*

As mentioned earlier, the random nature of the earthquake makes it difficult to predict in advance the most critical scenario for the running safety of the train. Therefore, five scenarios with different time offsets between the beginning of the earthquake and the entry of the vehicle in the viaduct are considered in this study in order to cover a wider range of combinations (see Section 6.3.2). Since the running safety criteria adopted in the present study are based on the wheel-rail contact forces (see Section 3.5 of Chapter 3), the discussion carried out in the present section is mainly focused on the variation of the contact forces, in particular the lateral ones, according to the position x_i given by equation (6.1). As an example to illustrate this point, Figure 6.45 presents the evolution of the lateral contact forces for four scenarios with distinct time offsets between the beginning of the earthquake and the entry of the vehicle in the viaduct. In all scenarios, the characteristics of the analysis are: vehicle's speed $V = 350$ km/h, seismic action with a reference return period $T = 95$ years and track quality corresponding to the regular operation limit. Furthermore, Figure 6.46 shows the equivalent results but for the strongest ground motion considered in this study with a reference return period of $T = 310$ years.
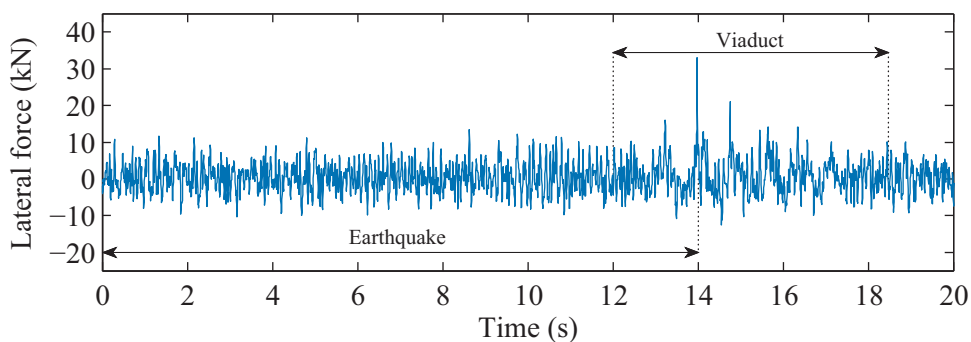
(a) Coordinate x_1 for the scenario $i = 1$
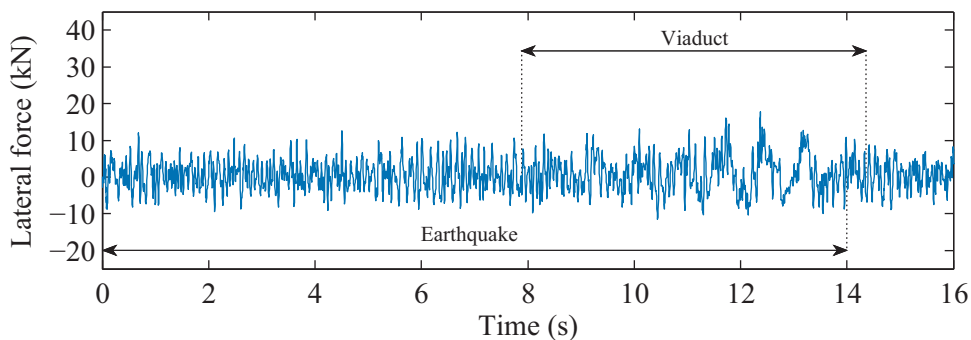
(b) Coordinate x_2 for the scenario $i = 2$
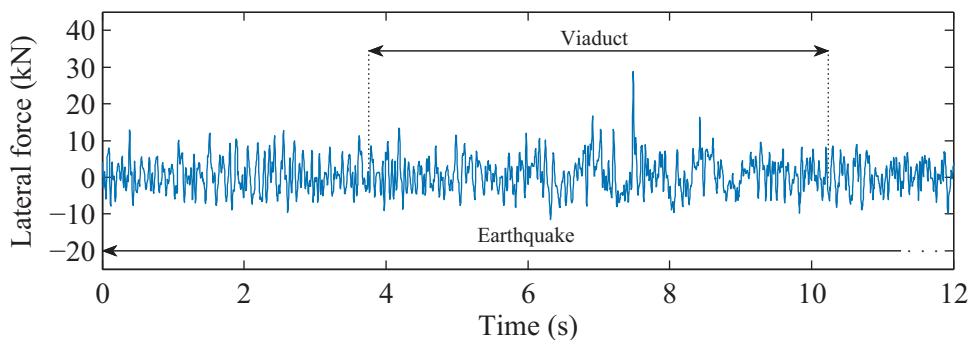
(c) Coordinate x_3 for the scenario $i = 3$

(d) Coordinate x_4 for the scenario $i = 4$

Figure 6.45 - Lateral contact forces in the left wheel of the 2nd wheelset for the seismic action with $T = 95$ years, track quality corresponding to the regular operation limit and $V = 350$ km/h: Coordinates of the first wheelset according to equation (6.1): (a) x_1, (b) x_2, (c) x_3 and (d) x_4.
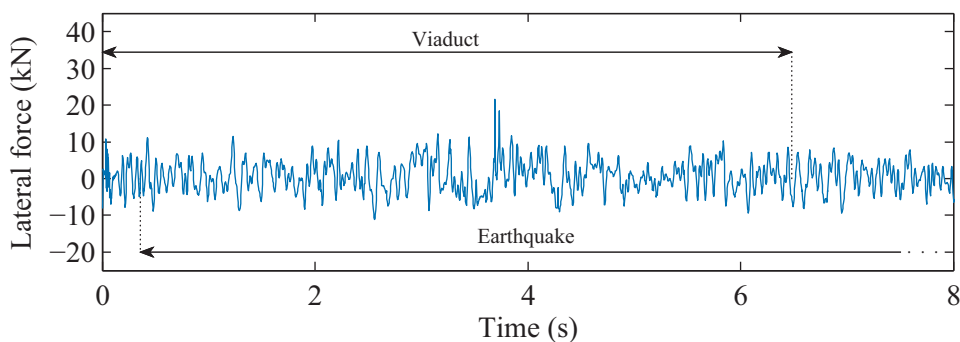
(a) Coordinate x_1 for the scenario $i = 1$

(b) Coordinate x_2 for the scenario $i = 2$

(c) Coordinate x_3 for the scenario $i = 3$

(d) Coordinate x_4 for the scenario $i = 4$

Figure 6.46 - Lateral contact forces in the left wheel of the 2nd wheelset for the seismic action with $T = 310$ years, track quality corresponding to the regular operation limit and $V = 350$ km/h: Coordinates of the first wheelset according to equation (6.1): (a) x_1, (b) x_2, (c) x_3 and (d) x_4.
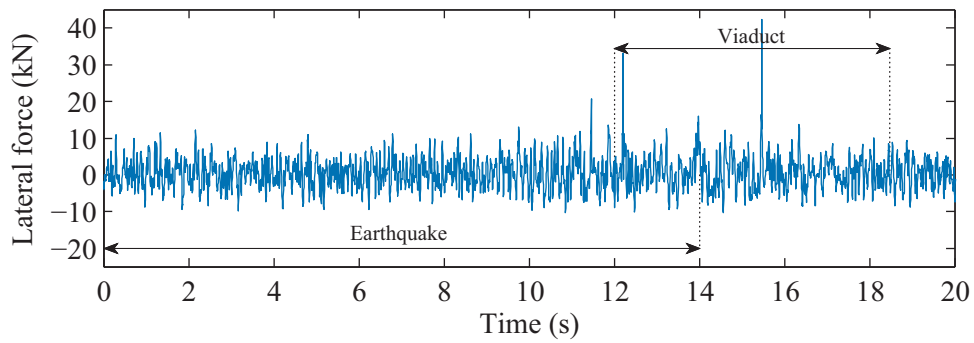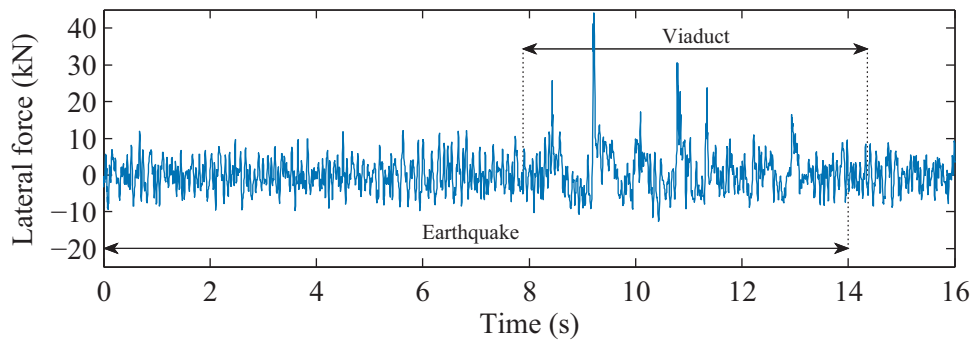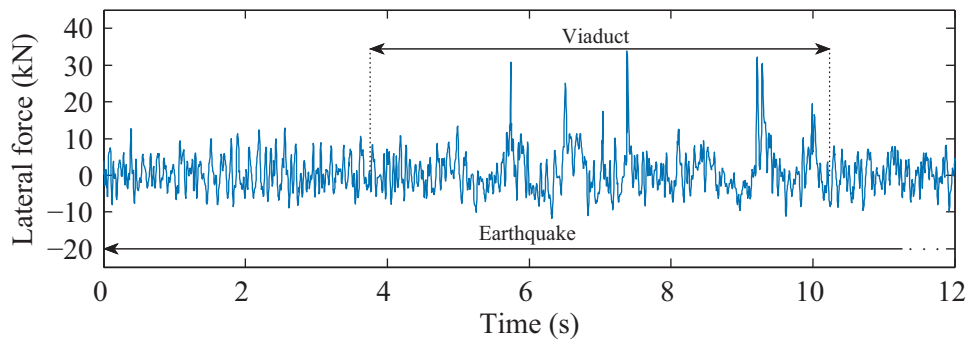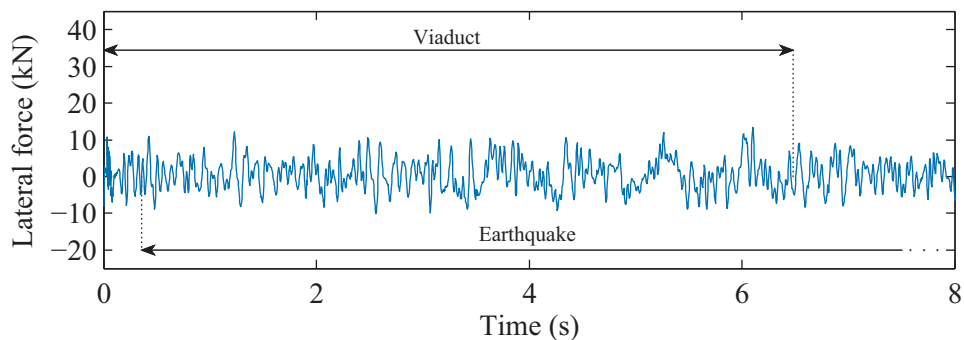
As expected, the most critical scenario is not the same for the two situations depicted in Figures 6.45 and 6.46, since the maximum lateral contact force for the seismic action with $T = 310$ years occurs in the scenario presented in Figure 6.46b (44.5 kN), while for the seismic action with $T = 95$ years this scenario is one of the least conditioning with a maximum lateral force of 17.8 kN. Similar conclusions were drawn for all other scenarios, i.e., the random nature of the seismic action, together with the vast number of possible combinations regarding the time offset between the start of the earthquake and the entry of the vehicle in the viaduct, makes it very difficult to find a unique scenario that could be representative of all possible situations. Therefore, in the running safety study presented in Section 6.8, the outcome of each analysis is the result of the envelope obtained in the five scenarios presented in Section 6.3.2. Nevertheless, a stochastic approach of the problem would be necessary to obtain a more representative range of results.

6.8 RUNNING SAFETY ANALYSIS

6.8.1 Introduction

In the present section, the running safety analysis of one of the Shinkansen cars travelling over the idealized Alverca viaduct under seismic conditions is assessed. As mentioned in Section 6.7, the use of only one car is adequate for the purpose of evaluating the running safety, since the Shinkansen is a conventional type train whose cars do not significantly interact with each other.

For each level of seismic intensity and track irregularity described in Sections 6.3 and 6.6, respectively, the dynamic analyses are performed for speeds ranging from 200 km/h to 350 km/h with steps of 10 km/h. Furthermore, for each speed, five scenarios are considered to account for the time offset between the beginning of the earthquake and the entry of the vehicle in the viaduct, as described in Section 6.3.2. In each scenario, the circulation is considered to be safe as long as none of the safety criteria described in Section 3.5 of Chapter 3 is violated during the whole time that the vehicle is crossing the viaduct. Regarding the derailment due to wheel flange climbing, only the modified Nadal criterion based on the lateral impact duration is used (See Section 3.5.1.4 of Chapter 3).

The time integration parameters adopted for the solution of the dynamic equations of motion of the train-structure system are the same as those considered in Section 6.7. All the analyses finish 2 seconds after the vehicle leaves the viaduct.

### 6.8.2 Influence of the seismic intensity level

The maximum values of the safety criteria obtained for each seismic intensity level in a scenario in which the vehicle crosses the viaduct at 350 km/h with a track quality corresponding to the regular operation limit are listed in Table 6.6. The values presented in this table correspond to an envelope of results regarding all the five scenarios described in Section 6.3.2 and all the wheels of the vehicle. While the Nadal, Prud'homme and rail roll criteria, which depend on the *Y/Q* ratio or on the lateral contact force solely, are significantly affected by the earthquake intensity, the wheel unloading criterion, which depends exclusively on the vertical contact forces, shows less variation. This is due to the fact that only the lateral component of the earthquake is accounted.

In the present scenario, the risk of derailment is null for levels of seismicity corresponding to earthquakes with return periods up to 95 years. Above this level, at least one out of the four criteria is not satisfied. Note that, according to these criteria, the safety of the vehicle may be at risk for levels of seismicity around three times less than the level of the design seismic action defined by the EN 1998-1 (2004) (the reference return period associated with the design seismic action is 475 years). Thus, the results show that the train's safety might be jeopardized even if the structure does not suffer significant damage during the earthquake.

Table 6.6 - Maximum values of the safety criteria for different seismic intensities.

T (years)	Modified Nadal	Prud'homme	Rail roll	Wheel unloading
No earthquake	0.26	0.37	0.16	0.72
95	0.71	0.89	0.41	0.76
150	0.70	1.17	0.69	0.82
225	1.02	1.35	0.69	0.89
310	1.05	1.42	0.72	0.90

As an example to clarify the present discussion, the time-histories of the four safety criteria obtained in the aforementioned scenario for the four seismic intensities considered in this study are plotted in Figures 6.47 to 6.50. All the results correspond to the scenario $i = 2$ according to equation (6.1). The Nadal and wheel unloading criteria correspond to the left wheel of the second wheelset, while the Prud'homme and rail roll criteria are related to the second wheelset and to the left side of the first bogie, respectively. As it can be observed, the Nadal, Prud'homme and rail roll criteria are significantly dependent on the seismic action when the vehicle is crossing the viaduct, while the wheel unloading criterion is barely affected.
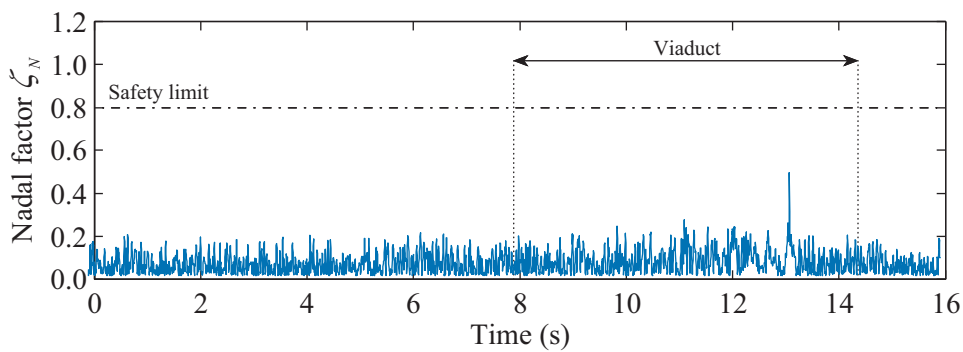
(a) $T = 95$ years
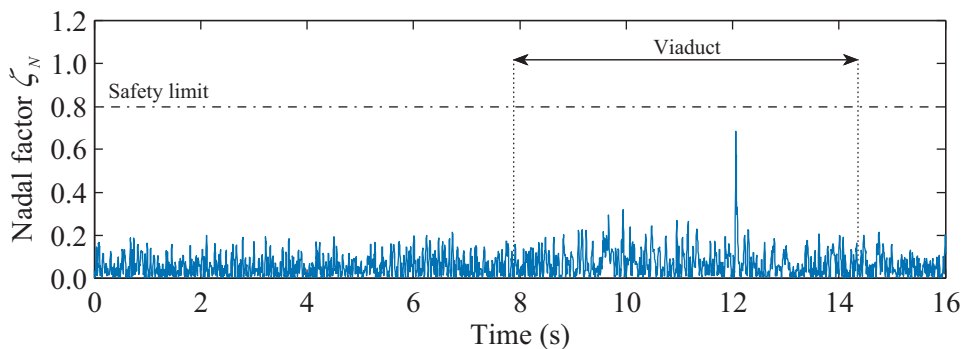
(b) $T = 150$ years
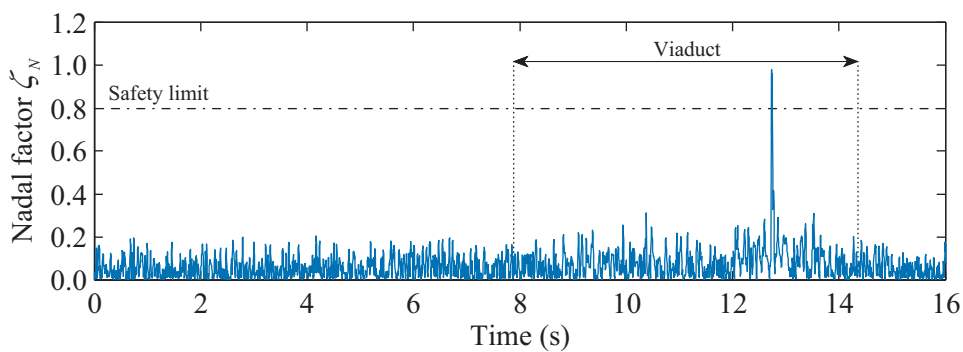
(c) $T = 225$ years

(d) $T = 310$ years

Figure 6.47 - Nadal factor relative to the left wheel of the 2nd wheelset for the scenario $i = 2$ (equation (6.1)), $V = 350$ km/h and track quality corresponding to the regular operation limit.

(a) *T* = 95 years

(b) *T* = 150 years

(c) *T* = 225 years

(d) *T* = 310 years

Figure 6.48 - Prud'homme factor relative to the 2nd wheelset for the scenario $i = 2$ (equation (6.1)), $V = 350$ km/h and track quality corresponding to the regular operation limit.

(a) $T = 95$ years
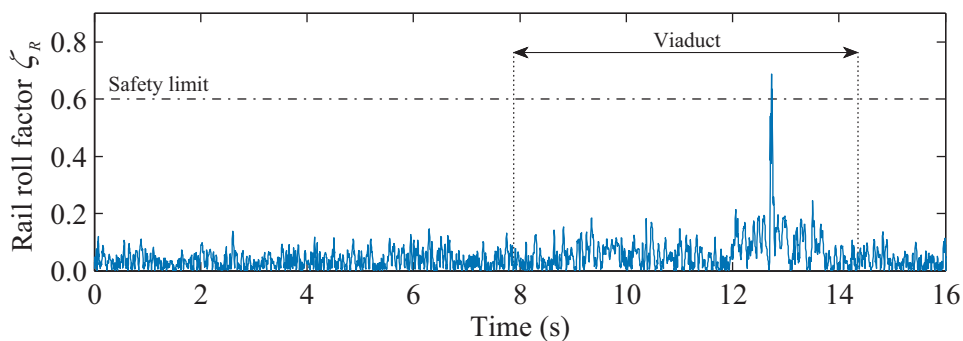
(b) $T = 150$ years

(c) $T = 225$ years

(d) $T = 310$ years

Figure 6.49 - Rail roll factor relative to the left side of the 1st bogie for the scenario $i = 2$ (equation (6.1)), $V = 350$ km/h and track quality corresponding to the regular operation limit.
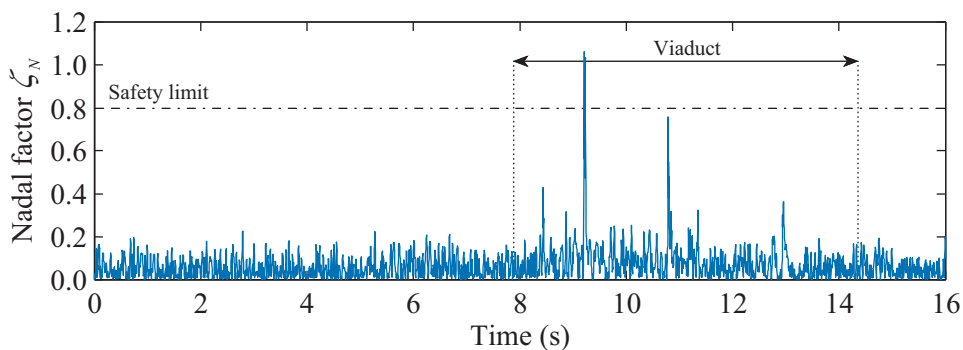
(a) $T = 95$ years
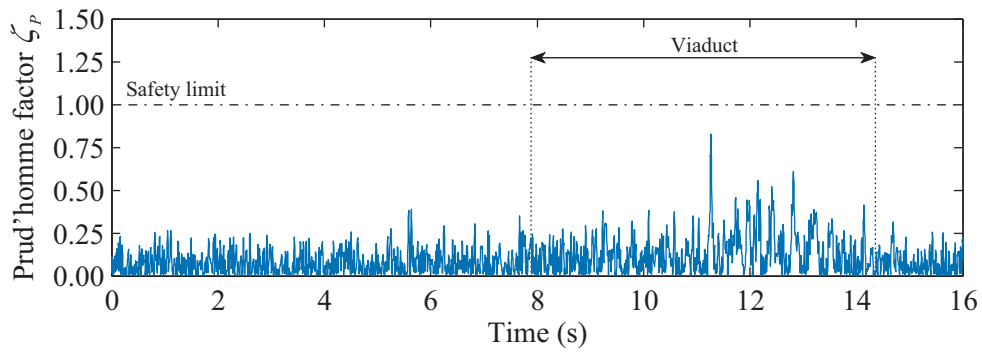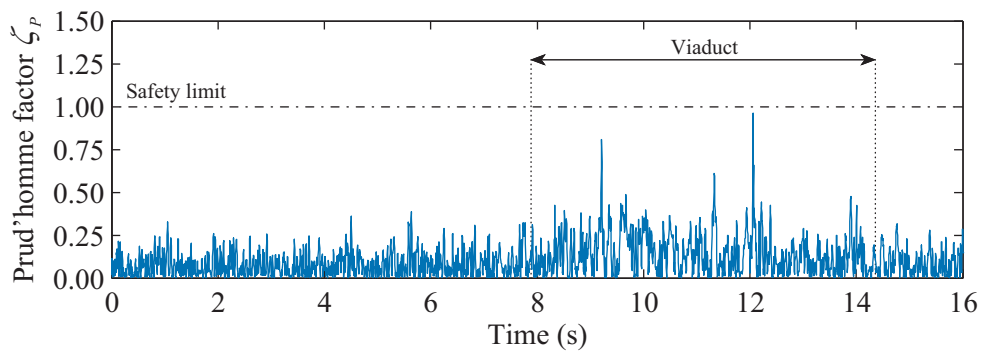

(b) $T = 150$ years
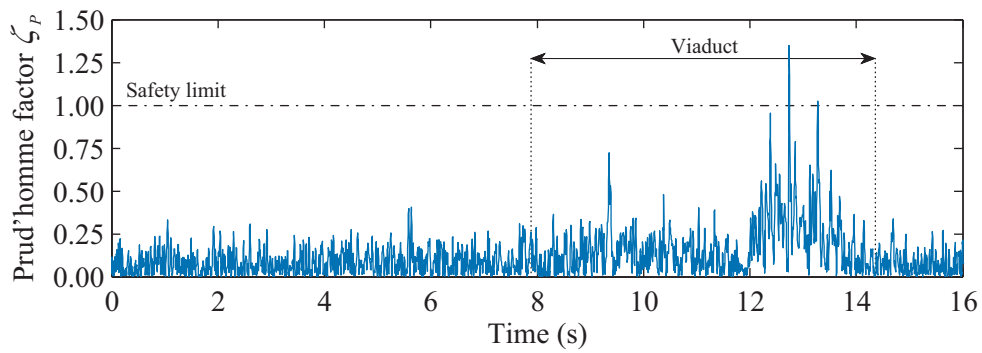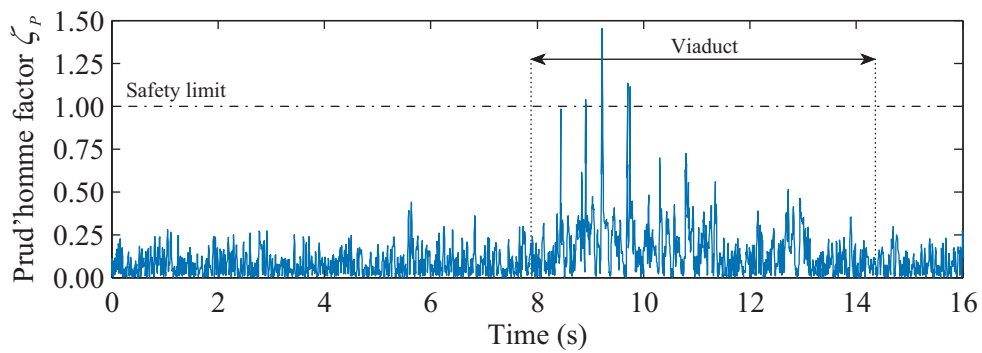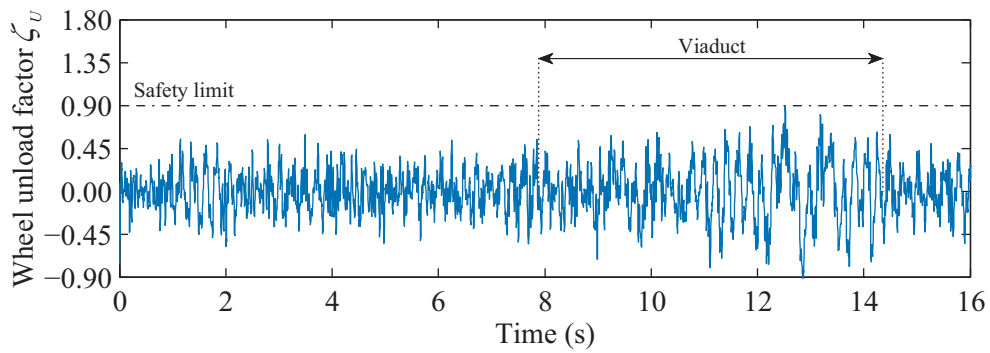

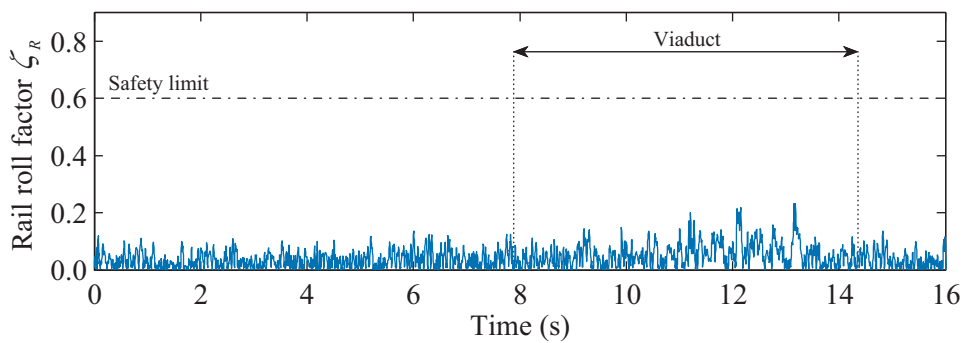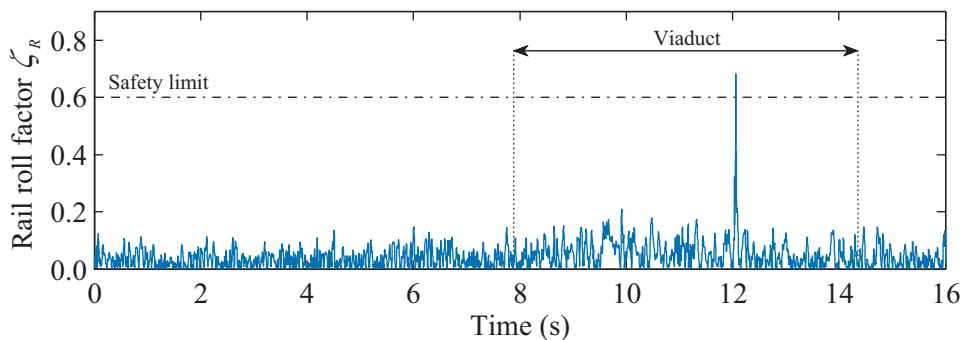(c) $T = 225$ years

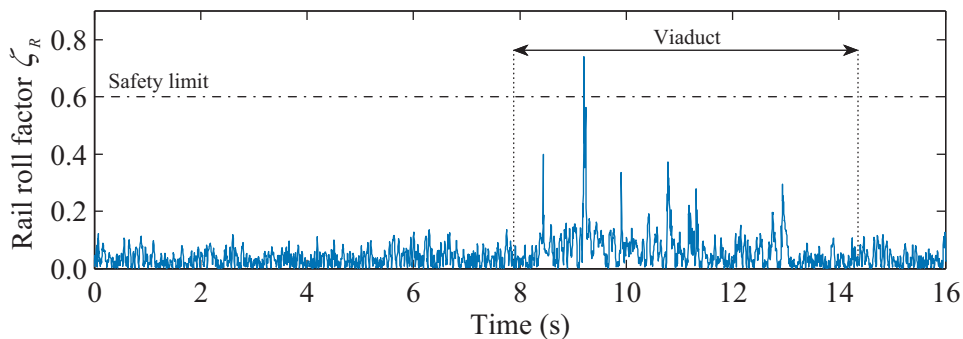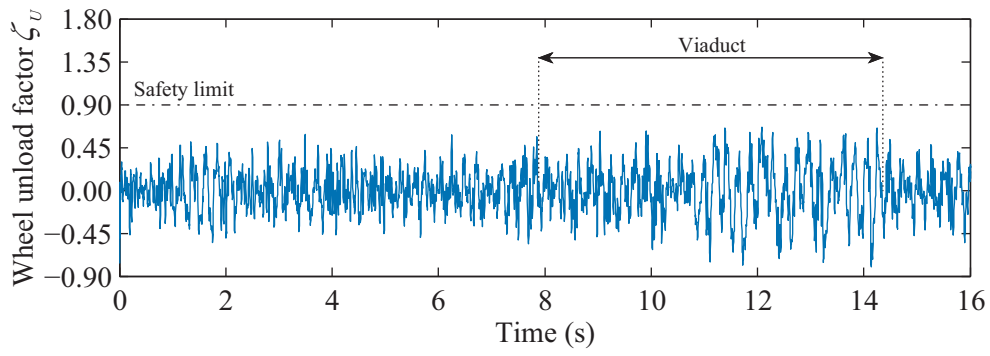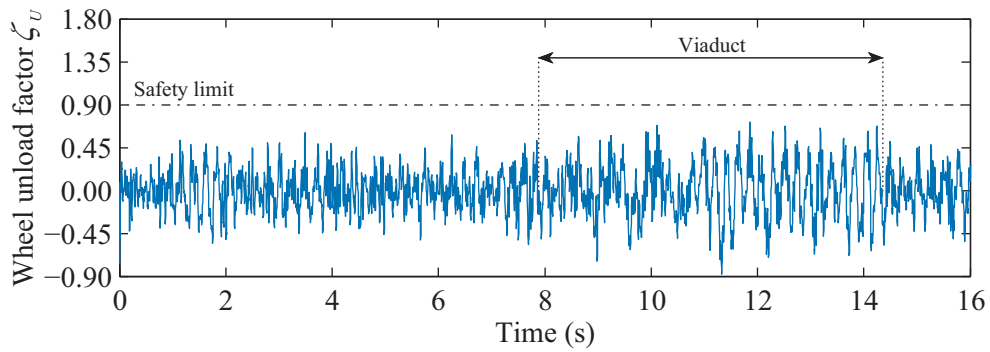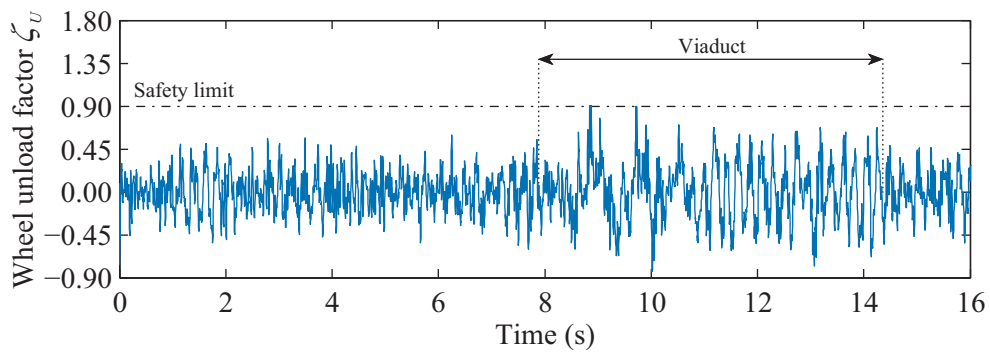(d) $T = 310$ years

Figure 6.50 - Unloading factor relative to the left wheel of the 2nd wheelset for the scenario $i = 2$ (equation (6.1)), $V = 350$ km/h and track quality corresponding to the regular operation limit.

6.8.3 Influence of the train running speed

The maximum values of the running safety criteria obtained for speeds ranging from 200 km/h to 350 km/h in a scenario with a track quality corresponding to the alert limit and an earthquake action with a return period of 150 years are shown in Table 6.7. The values presented in this table correspond to an envelope of results regarding all the five scenarios described in Section 6.3.2 and all the wheels of the vehicle. As a first observation, it is clear that the vehicle speed has an important influence in both the vertical and the lateral dynamics, since the maximum values of all the criteria significantly increase with the increase in speed.

The results show that for speeds above 250 km/h, which is the lower limit value for the railway traffic to be considered as high-speed, all the criteria indicate a significant risk of derailment. Special attention should be given, therefore, in the design of high-speed railway bridges located in regions prone to earthquakes. Furthermore, the quality of the track is also an important factor that may jeopardize the train's safety in high-speed railways, since the values of the safety criteria for the present scenario significantly increase when compared to those presented in Table 6.6 (see the values in Table 6.6 corresponding to the seismic action with $T = 150$ years). The influence of this factor is discussed with more detail in Section 6.8.4.

Table 6.7 - Maximum values of the safety criteria for different running speeds.

Vehicle speed (km/h)	Modified Nadal	Prud'homme	Rail roll	Wheel unloading
200	0.75	0.90	0.46	0.88
250	0.82	0.99	0.52	0.89
300	0.95	0.97	1.04	0.90
350	2.64	1.68	1.15	1.00

As an example to illustrate the influence of the running speed on the train's safety, the time-histories of the safety criteria obtained for the circumstances mentioned above and for speeds between 200 km/h and 350 km/h are plotted in Figures 6.51 to 6.54. All the results correspond to the scenario $i = 3$ according to equation (6.1). The Nadal and wheel unloading criteria refer to the right wheel of the second wheelset, while the Prud'homme and rail roll criteria are related to the second wheelset and to the right side of the first bogie, respectively. It is clear that, contrary to what is observed in Section 6.8.2, both the lateral and the vertical dynamics are affected by the speed of the vehicle. This is due to the fact that the track irregularities in poor quality tracks (alert limit level) come to play a predominant role in the vehicle's vertical and lateral dynamics.
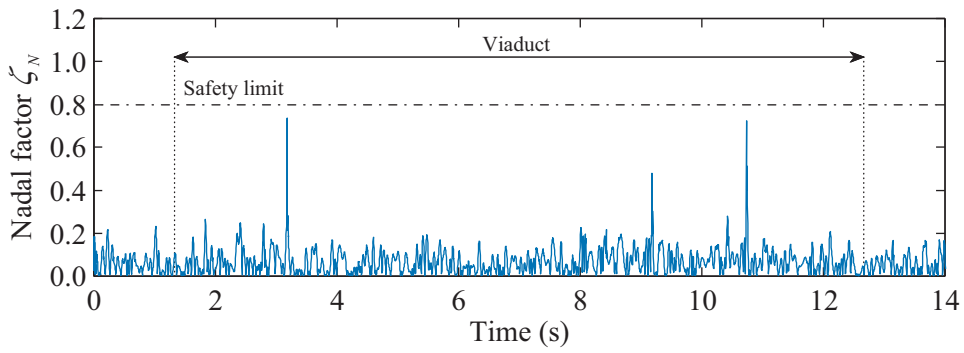
(a) *V* = 200 km/h
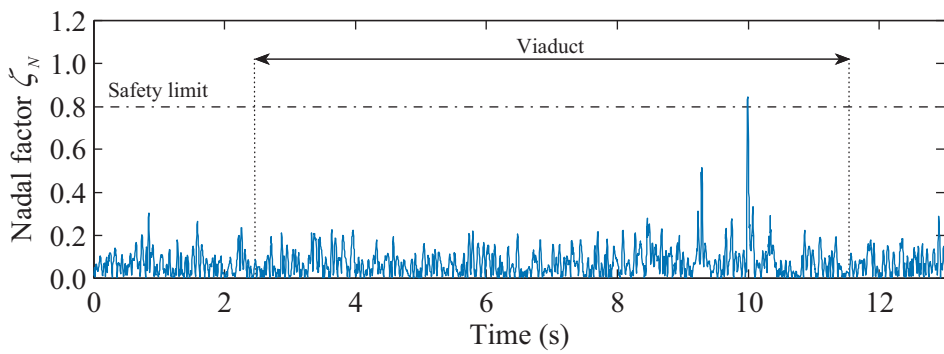
(b) *V* = 250 km/h
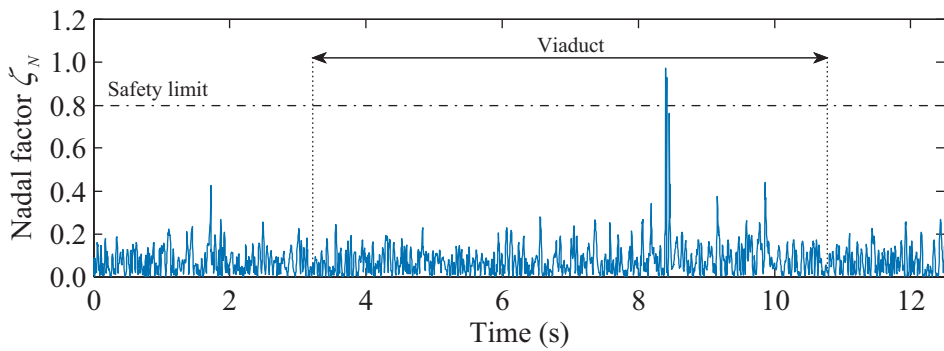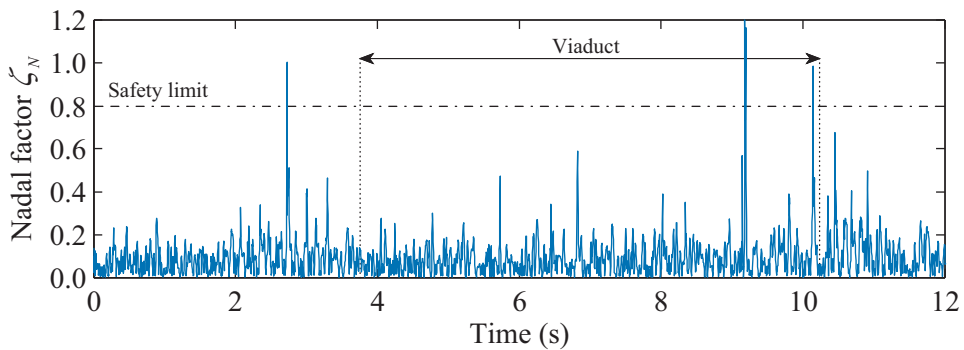
(c) *V* = 300 km/h

(d) *V* = 350 km/h

Figure 6.51 - Nadal factor relative to the right wheel of the 2nd wheelset for the scenario *i* = 3 (equation (6.1)), seismic action with *T* = 150 years and track quality corresponding to the alert limit.
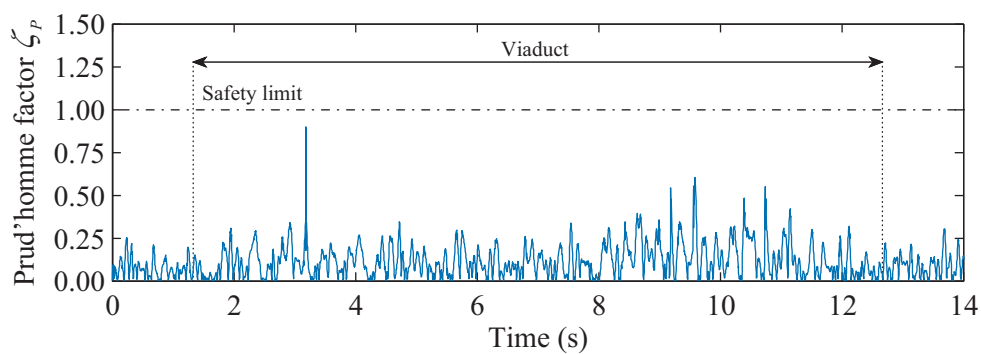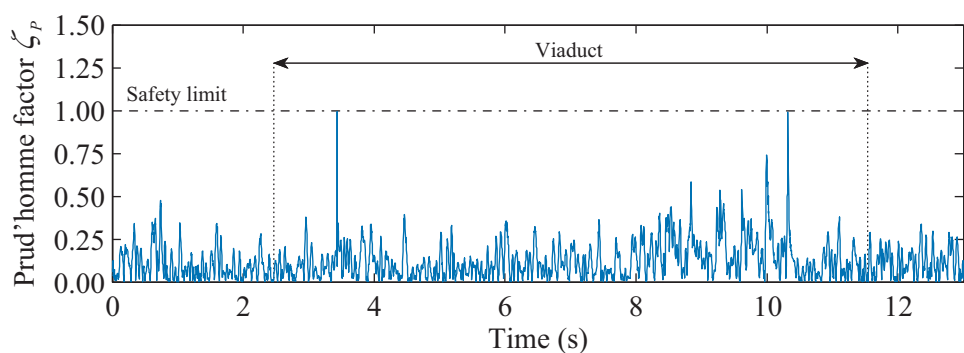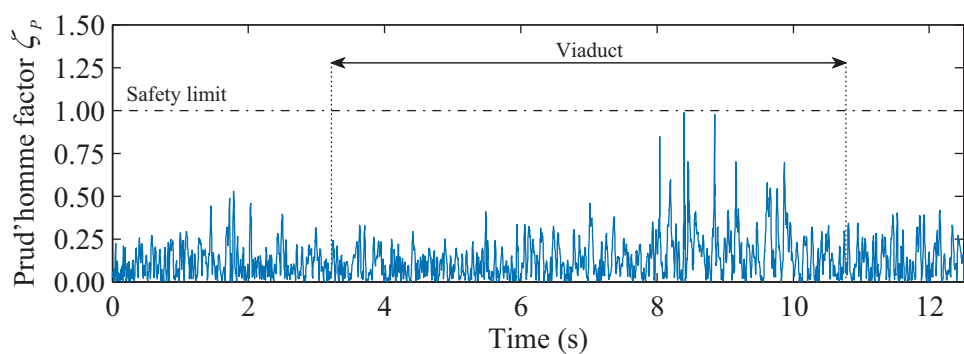
(a) $V = 200$ km/h
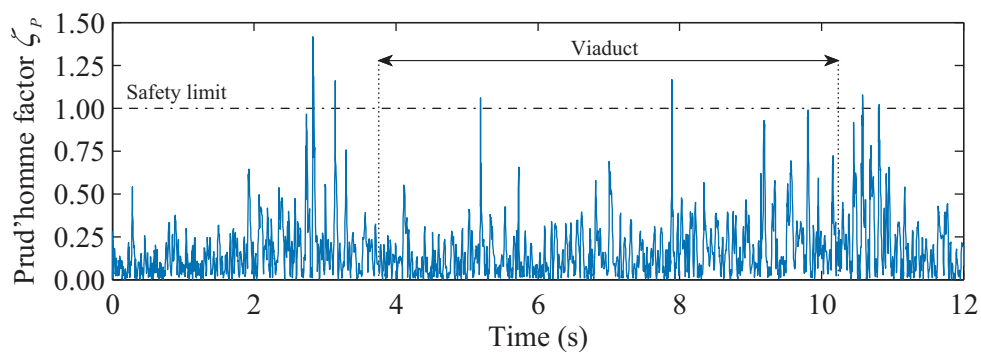
(b) $V = 250$ km/h

(c) $V = 300$ km/h

(d) $V = 350$ km/h

Figure 6.52 - Prud'homme factor relative to the 2nd wheelset for the scenario $i = 3$ (equation (6.1)), seismic action with $T = 150$ years and track quality corresponding to the alert limit.
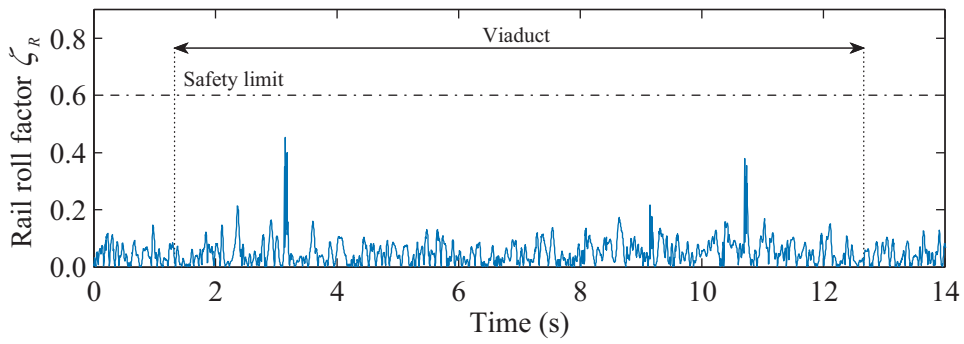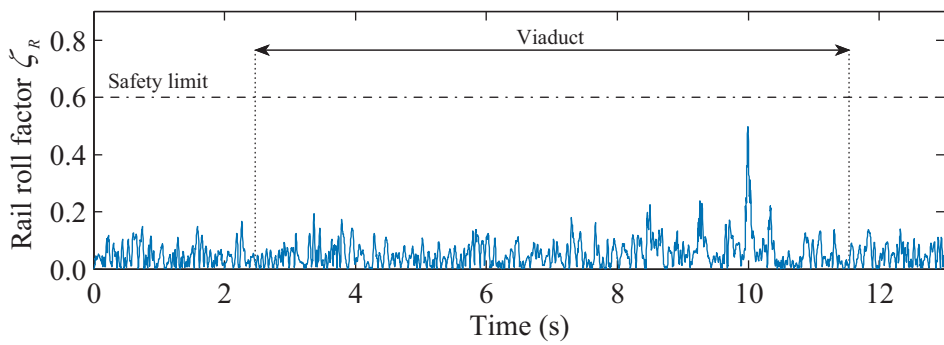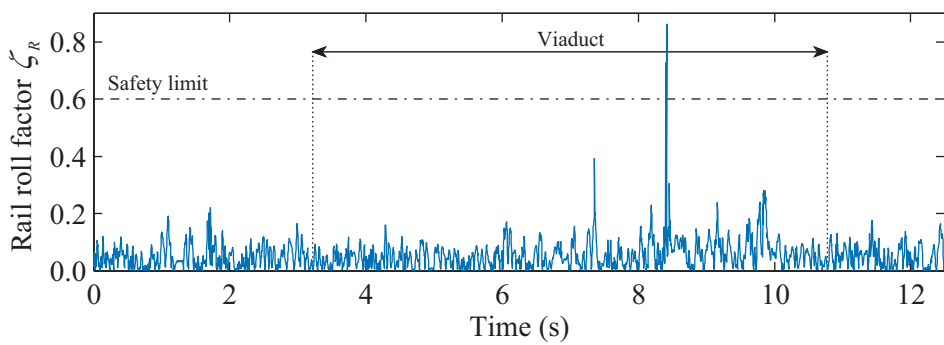
(a) $V = 200$ km/h
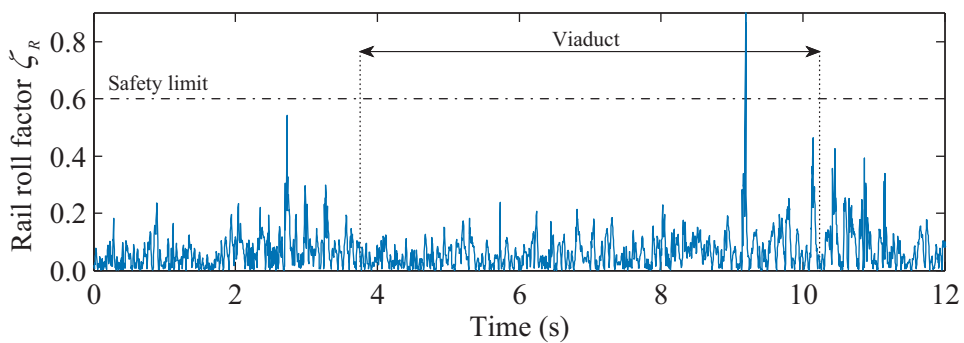
(b) $V = 250$ km/h

(c) $V = 300$ km/h

(d) $V = 350$ km/h

Figure 6.53 - Rail roll factor relative to the right side of the 1st bogie for the scenario $i = 3$ (equation (6.1)), seismic action with $T = 150$ years and track quality corresponding to the alert limit.
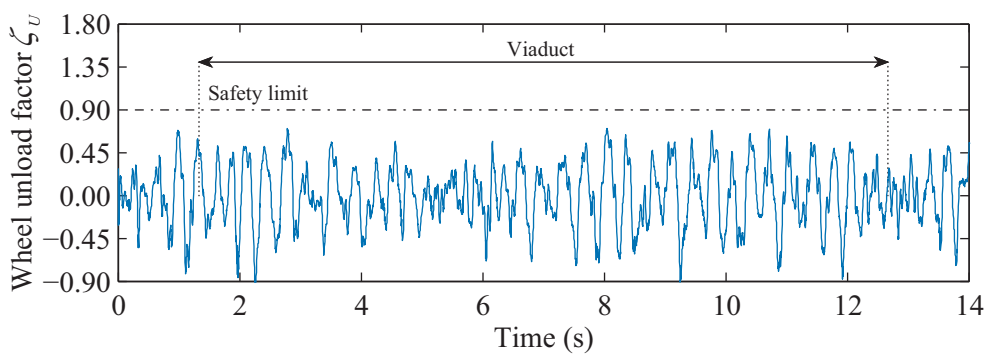
(a) $V = 200$ km/h
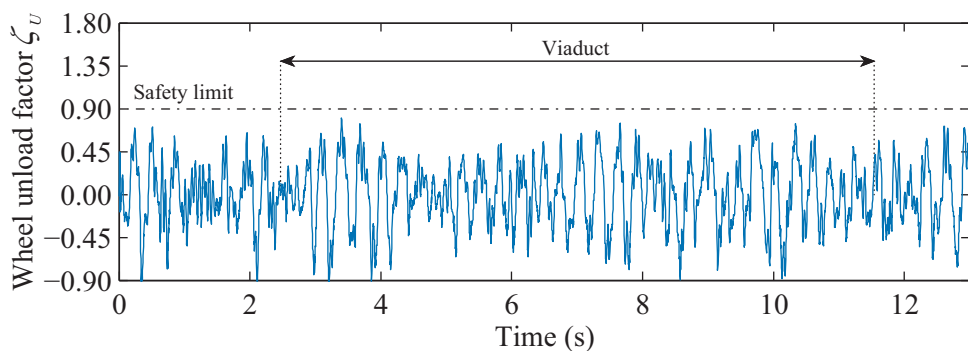
(b) $V = 250$ km/h
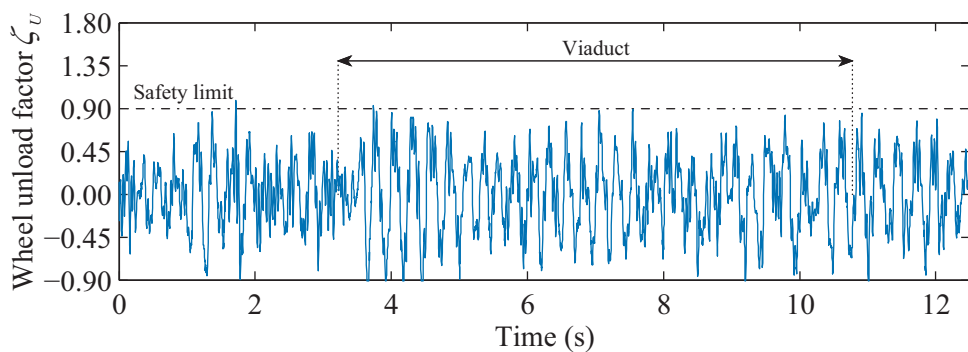
(c) $V = 300$ km/h
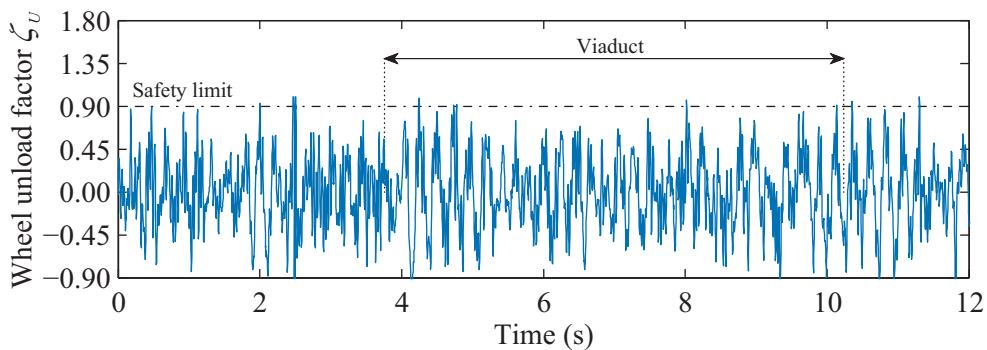
(d) $V = 350$ km/h

Figure 6.54 - Unloading factor relative to the right wheel of the 2nd wheelset for the scenario $i = 3$ (equation (6.1)), seismic action with $T = 150$ years and track quality corresponding to the alert limit.

6.8.4 Influence of the track quality

The maximum values of the safety criteria obtained for the two levels of irregularity considered in this work in a scenario in which the vehicle crosses the viaduct at 350 km/h without earthquake are presented in Table 6.8. The values shown in this table correspond to an envelope of results regarding all the five scenarios described in Section 6.3.2 and all the wheels of the vehicle. It can be seen that the irregularities may significantly influence the safety, since even without earthquake, all the limit values are exceeded for the track with worse quality. On the other hand, for the regular operation limit of irregularities, the risk of derailment is null and the values of the running safety criteria are far below the limit. This result was expected, since the train is supposed to remain safe during ordinary operation for this level of track quality if no other actions are considered.

It is common to associate the track quality with the comfort of the passengers rather than with the vehicle stability. In fact, if the design requirements for the track are met, the track irregularities do not pose a significant problem to the running safety of the vehicle. However, the present results show that, in extreme situations when the track quality is very poor, the stability of the train may be put at risk, particularly at high speeds.

Table 6.8 - Maximum values of the safety criteria for different levels of track quality.

Track quality	Modified Nadal	Prud'homme	Rail roll	Wheel unloading
Regular operation	0.26	0.37	0.16	0.72
Alert limit	1.45	1.68	0.70	0.90

The comparison between the safety criteria obtained for the regular operation limit level of irregularities and for the alert limit level, when the vehicle crosses the viaduct at 350 km/h with no earthquake, is shown in Figures 6.55 to 6.58. The Nadal and wheel unloading criteria correspond to the left wheel of the first wheelset, while the Prud'homme and rail roll criteria are related to the first wheelset and to the left side of the first bogie, respectively. As seen earlier in Section 6.8.3, several peaks can be observed in the Nadal, Prud'homme and rail roll criteria factors when the vehicle runs on the track with worse quality. These peaks are mostly related with lateral impacts between the wheel flange and the rail (see Figures 6.40 and 6.41).
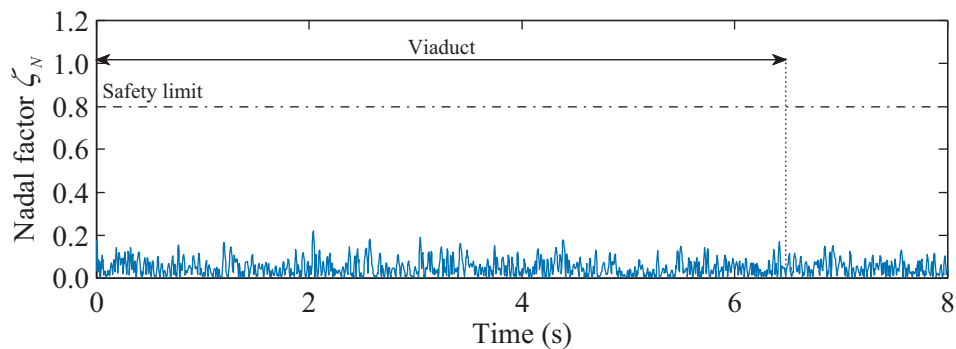
(a) Regular operation limit
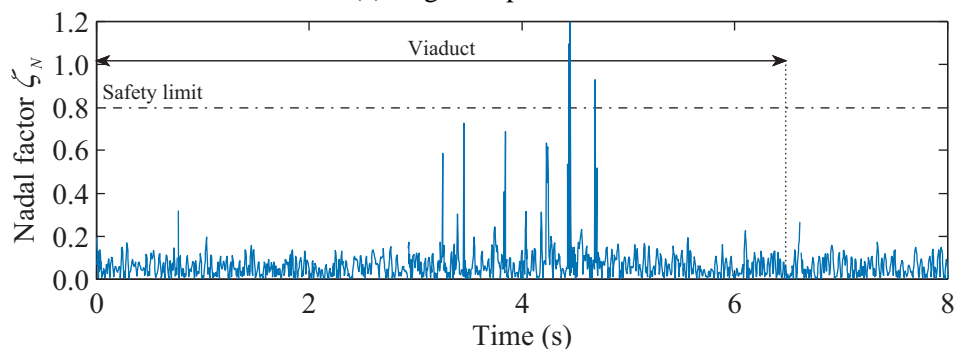
(b) Alert limit

Figure 6.55 - Nadal factor relative to the left wheel of the 1st wheelset for a scenario without earthquake and train speed of V = 350 km/h.
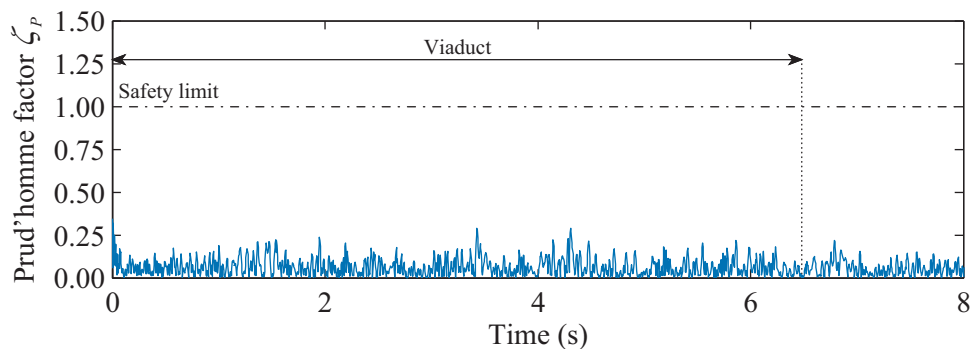
(a) Regular operation limit
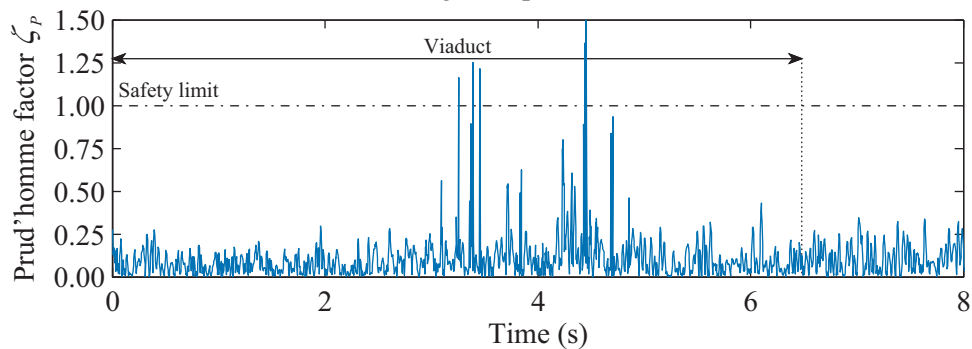
(b) Alert limit

Figure 6.56 - Prud'homme factor relative to the 1st wheelset for a scenario without earthquake and train speed of V = 350 km/h.
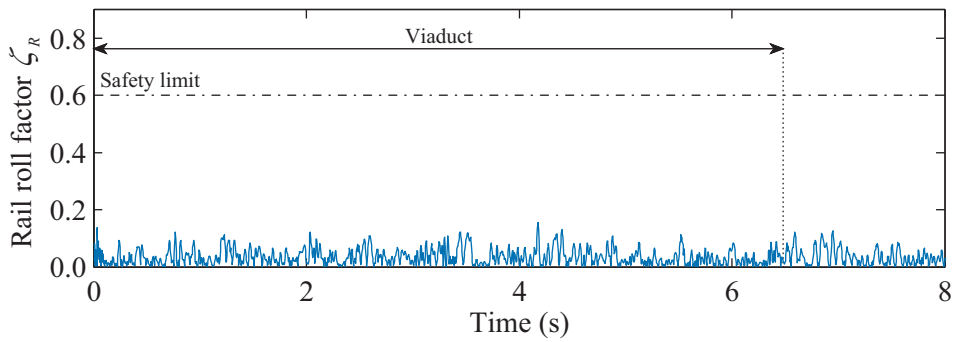
(a) Regular operation limit
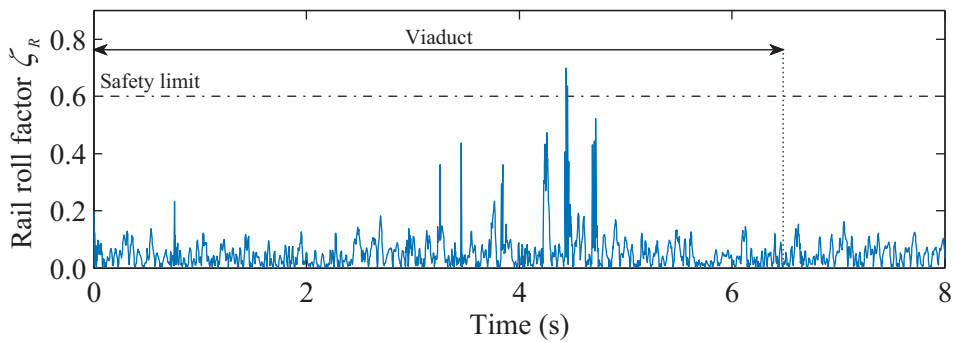
(b) Alert limit

Figure 6.57 - Rail roll factor relative to the left side of the 1st bogie for a scenario without earthquake and train speed of V = 350 km/h.
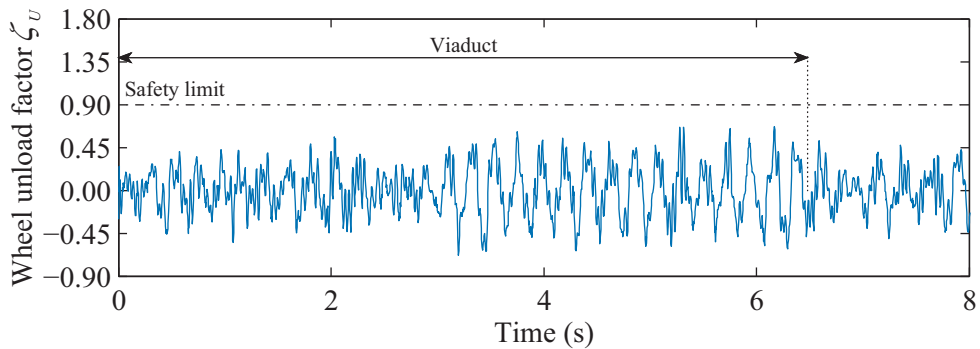
(a) Regular operation limit
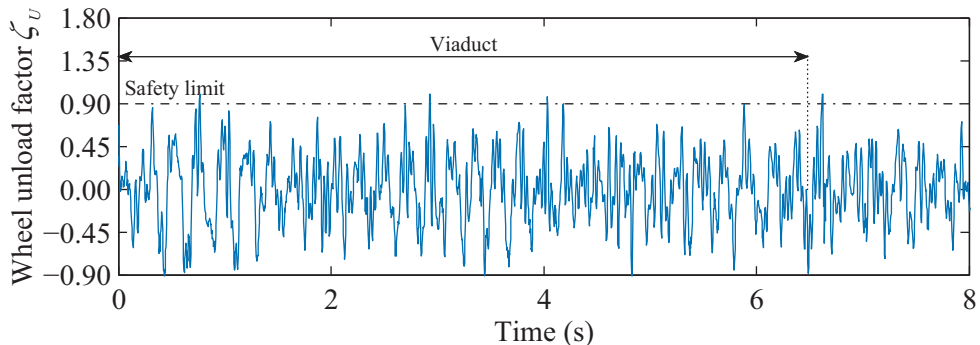
(b) Alert limit

Figure 6.58 - Unloading factor relative to the left wheel of the 1st for a scenario without earthquake and train speed of V = 350 km/h.

6.8.5 Running safety charts

The global envelopes of each of the analyzed safety criterion, as function of the vehicle's speed and seismic intensity, calculated for the two track quality levels considered in the present work, are plotted in Figure 6.59. Each point corresponds to the maximum seismic intensity that guarantees the safety of the vehicle for each running speed, considering the envelope of the five scenarios to account for the time offset between the beginning of the earthquake and the entry of the vehicle in the viaduct and the envelope of the results obtained in all the wheels, wheelsets and bogie sides of the vehicle. Therefore, if a given criterion is violated at least in one wheel, the circulation is considered to be unsafe. The gray area, called *safety zone*, correspond to the combinations of seismic intensity and running speed that do not put the safety of the vehicle at risk.

(a)

(b)
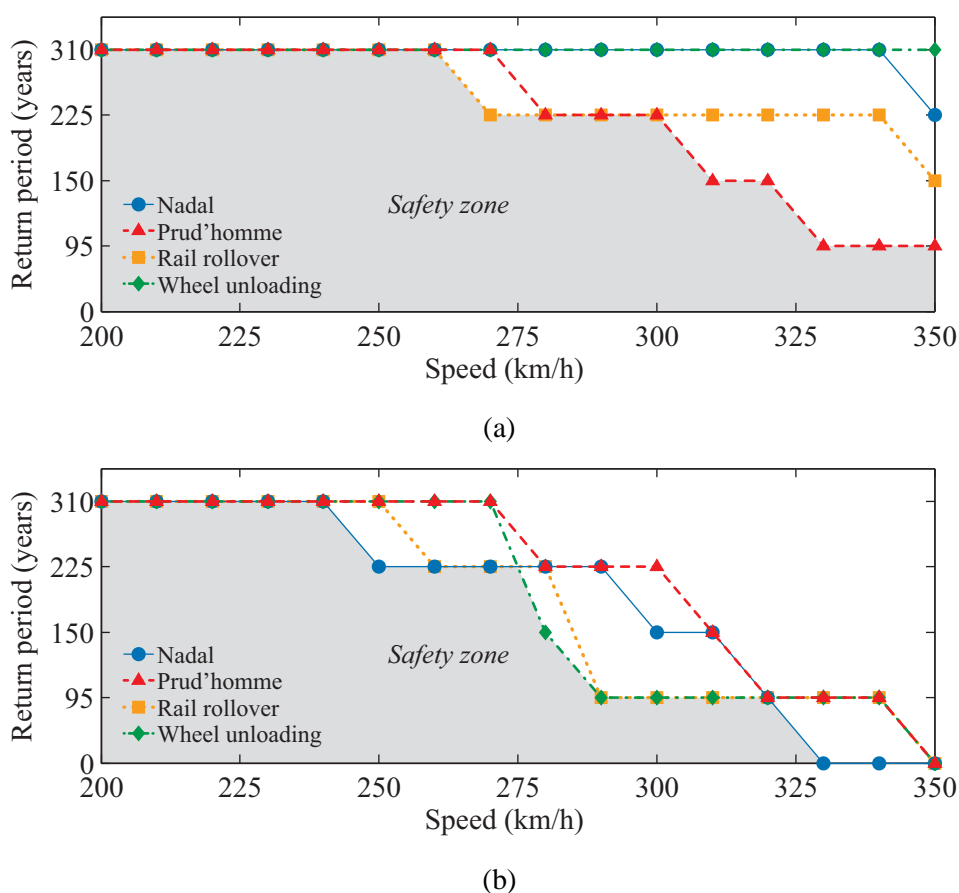
Figure 6.59 - Running safety charts obtained for levels of irregularities corresponding to the (a) regular operation limit and to the (b) alert limit.

As expected, the trend observed in all the criteria is similar, indicating that the risk of derailment increases with the increasing of the running speed and seismic intensity. It may be observed that the risk of derailment due to the wheel unloading is null when the train runs over

a track whose quality corresponds to the regular operation limit. For this level of irregularities, the Prud'homme criterion proved to be the most conservative, since it controls the derailment risk for almost all the speeds. However, this tendency changes for poorer quality tracks, in which the Nadal, rail roll and wheel unloading criteria define the safety zone, as may be seen in Figure 6.59b. Hence, for the track with better quality, the vehicle remains safe at every speed if no earthquake occurs, while for the track with poorer quality, the derailment risk predicted with the majority of the criteria significantly increases for speeds above 270 km/h.

6.8.6 Critical analysis of the running safety criteria

As a final remark, it is important to confront the results obtained with the safety criteria with the actual behavior of the vehicle. Past studies proved that some of the commonly used safety criteria are too conservative, leading to the detection of possible derailments in situations in which the vehicle is yet far from derail. Therefore, the present section aims to evaluate the actual behavior of the vehicle when the limits of the safety criteria are exceed.

6.8.6.1 Nadal criterion evaluation

As mentioned before in Section 3.5 of Chapter 3, the studies carried out by Ishida and Matsuo (1999) shown that, when the Nadal criterion limit is reached, the wheel rises less than 1 mm. These results proved that the Nadal criterion is conservative, since the actual derailment occurs when the wheel lifts 30 mm relative to the rail (flange height), thus tending to run out of the track.

In order to evaluate the actual derailment risk in the most critical scenario, i.e., when the vehicle crosses the viaduct at 350 km/h over a track whose quality corresponds to the alert limit during the occurrence of the earthquake with $T = 310$ years, the time-history of the Nadal criterion factor of the left wheel of the second wheelset, along with the wheel-rail configuration in an instant in which the Nadal limit is exceeded, is illustrated in Figure 6.60. As it can be observed, although the Nadal limit is exceeded, the wheel does not rise sufficiently to cause derailment, proving the high degree of conservativeness of this criterion.

(a)   (b)
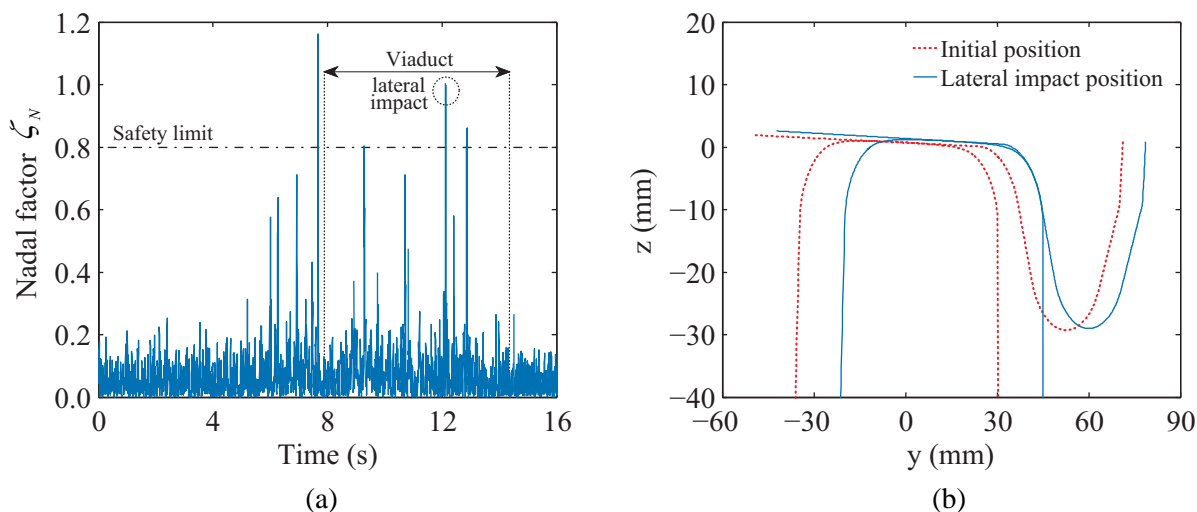
Figure 6.60 - Evaluation of the Nadal criterion: (a) time-history of the Nadal criterion factor and
(b) wheel-rail configuration during a lateral impact.

Figure 6.61 shows the lateral and vertical relative displacements between the wheel and rail for the same scenario described above. As expected, the lateral relative displacement between wheel and rail barely exceeds 6 mm in one of the directions due to the constraint imposed by the flange when it impacts with the rail, which means that the wheel is not climbing the rail. The same conclusion can be drawn from the small relative vertical displacements between the wheel and rail plotted in Figure 6.61b.

(a)   (b)
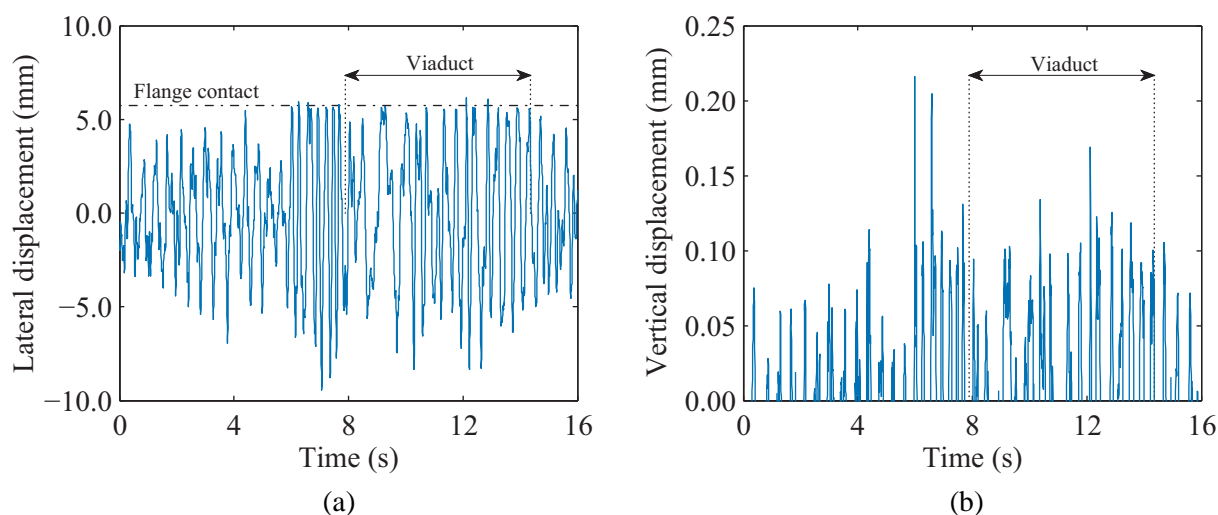
Figure 6.61 - Relative displacements between the wheel and rail: (a) lateral and (b) vertical direction.

Nevertheless, since the Nadal criterion is used as a code provision to avoid train derailment, the conservative predictions provided by this criterion may be considered acceptable. However, a more exhaustive study about the derailment phenomena could contribute for the development of more sophisticated running safety criteria.

6.8.6.2 Wheel unloading criterion evaluation

The wheel unloading criterion aims to evaluate the risk of derailment in scenarios in which one of the wheels loses contact with the rail. However, the detachment of one wheel does not necessarily mean that the train will derail, i.e., the wheel may lose contact with the rail for a short period of time without compromising the train running safety.

In order to evaluate the degree of conservativeness of this criterion, the time-history of the wheel unloading criterion factor for the left wheel of the second wheelset obtained in the scenario described in the previous section, together with the wheel-rail configuration in an instant in which the wheel detaches from the rail, is plotted in Figure 6.62. Although the separation between the wheel and rail is notorious, it is not enough to provoke derailment, since the wheel flange is still far from rising above the rail.

(a)

(b)

(c)
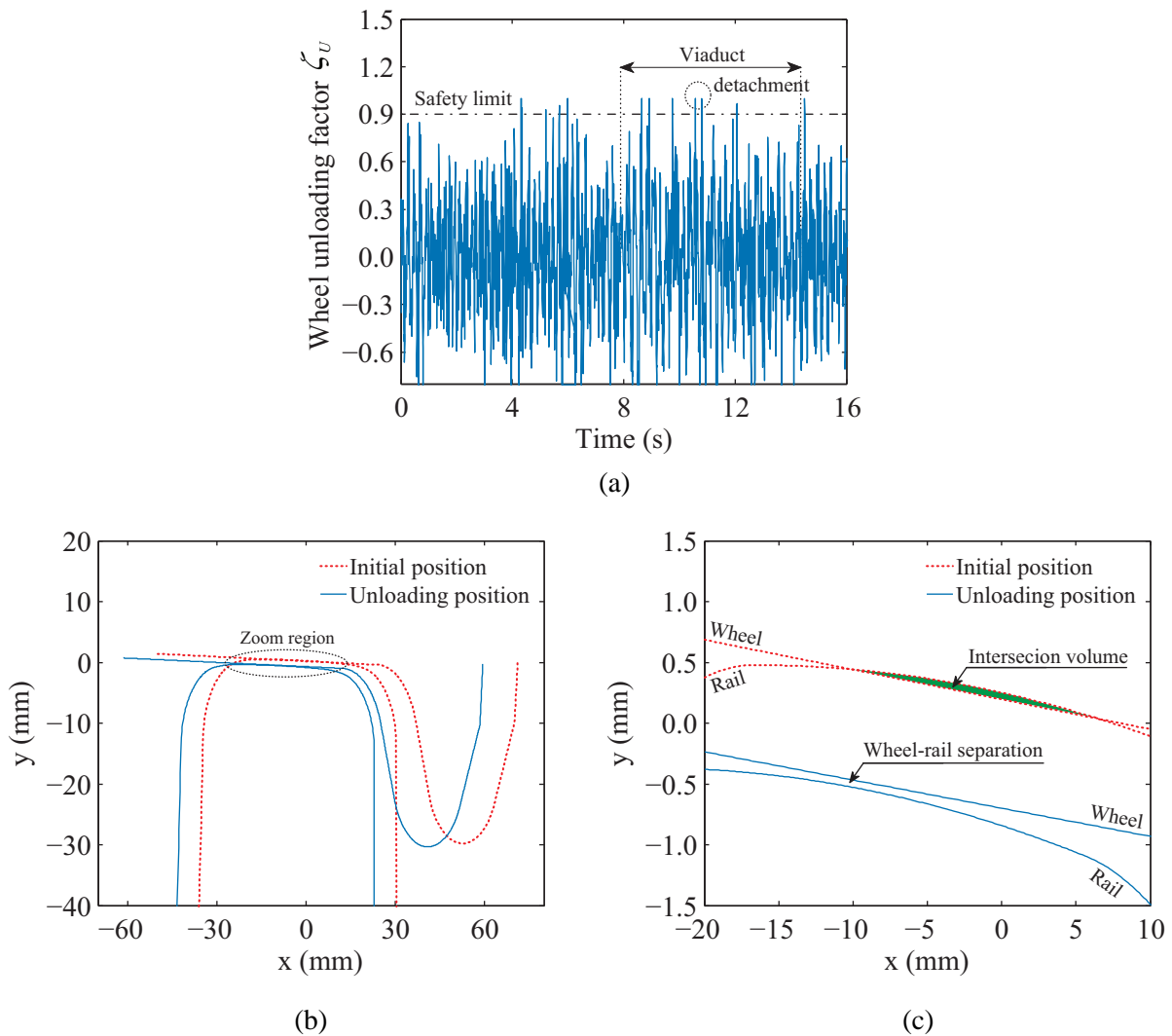
Figure 6.62 - Evaluation of the wheel unloading criterion: (a) time-history of the wheel unloading criterion factor, (b) wheel-rail configuration during detachment and (c) zoom on the tread region.

6.8.6.3 Evaluation of the remaining criteria

Regarding the remaining criteria, both of them may also be open to criticism. The Prud'homme criterion is based on the lateral resistance of a standard track, which may be far different from the actual track that is being studied. Furthermore, the lateral resistance of the track may be easily changed by improving the ballast quality or the rail fasteners, leading to an even more conservative limit value given by the Prud'homme criterion. Similar conclusions may be drawn regarding the rail roll criterion, since the rotation of the rails is strongly influenced by the stiffness provided by the rail fasteners. Therefore, the adoption of these two criteria to evaluate the running stability of a railway vehicle without taking into account the characteristics of the existing track should be made with some precautions.

6.9 CONCLUDING REMARKS

A study regarding the assessment of the running safety of trains on bridges subjected to earthquakes is presented. The vehicle-structure interaction method presented in Chapter 4, which takes into account the geometry of the wheel and rail surfaces and the behavior of the contact interface in the normal and tangential directions, is adopted to solve the dynamic problem.

The study focuses on the dynamic analysis of a high-speed train running over an idealized viaduct based on an existing flyover type structure of the Portuguese railway network situated in the city of Alverca. This viaduct has been extensively studied by Malveiro et al. (2013), both numerically and experimentally, thus providing essential data for developing the numerical model. However, for simplicity of the model, a constant span length of 21 m, based on the most typical span of the actual structure, and a constant pier height of 10 m are adopted.

The two main sources of excitation of the train-structure system considered in the present study are the track irregularities and the earthquake action. The irregularities are defined as a stochastic Gaussian ergodic process and artificially generated based on analytical PSD functions. Regarding the earthquake action, it is represented in terms of artificial accelerograms generated from the elastic spectra described in EN 1998-1 (2004), with PGA corresponding to moderate seismic events with relatively high probability of occurrence and return periods ranging from 95 to 310 years. This type of seismic actions is of the utmost importance, since the running safety of the trains might be jeopardized due to the excessive vibrations caused to the track, even if the structure does not experience significant damage. Therefore, all the

dynamic train-structure interaction analyses are performed in the elastic domain, being the reduction in the stiffness of the piers due to concrete cracking evaluated by a methodology specially developed for this purpose. The methodology consists of calibrating the effective stiffness of the piers in order to obtain, with a linear dynamic analysis, levels of displacement on the piers similar to those obtained with the nonlinear dynamic analysis. In the present study, a good agreement is observed between the two responses, proving the efficiency of the methodology for dealing with moderate earthquakes.

The dynamic responses of both the viaduct and vehicle are analyzed. Since only the lateral component of the earthquake is considered in the present work, the vertical response of the deck is not affected by the seismic action. On the other hand, in the lateral direction, the deck response is mainly dominated by the earthquake, being the influence of the vehicle almost negligible.

The influence of the effective stiffness of the piers on the lateral response of the viaduct is also assessed. Two scenarios of seismicity are analyzed with reference return periods of 95 years and 310 years. As would be expected, although the spectral acceleration decreases due to the increase in the period of the structure, the amplitude of the response increases due to the fact that the piers become less stiff and therefore may experience larger displacements during the earthquake.

Regarding the vehicle and its vertical response, the efficiency of the suspensions on filtering the high frequencies arising from the contact between wheel and rail is perfectly clear when comparing the accelerations on the wheelset and carbody, especially at high-speeds. The maximum vertical acceleration at the wheelset increases from 5.4 m/s^2 to 17.5 m/s^2 for speeds of 200 km/h and 350 km/h, respectively, while the acceleration at the carbody remains approximately constant (3.46 m/s^2 and 3.65 m/s^2 for the minimum and maximum speed mentioned earlier). It is important to notice that the increase in speed also influences the vertical contact forces between wheel and rail, since the maximum values obtained for speeds of 200 km/h and 350 km/h are, respectively, 85 kN and 110 kN, which represents an increase of about 54 % and 100 % over the static load value of 55 kN of each wheel.

Unlike in the vertical direction, the lateral response of the vehicle is significantly affected by the earthquake. Under seismic conditions (seismic action with $T = 310$ years), the maximum lateral displacement of the carbody, relative to the lateral displacement of the track centerline, is approximately six times higher than the maximum displacement of the wheelset, while

without earthquake this difference is almost negligible. In order to avoid excessive lateral displacement of the carbody during the occurrence of an earthquake, most of the high-speed trains have stoppers installed in the secondary transversal suspensions. However, for the levels of seismicity considered in the present work, these devices do not have an important impact in the lateral response of the vehicle, since the maximum displacements of the carbody with and without the presence of stoppers do not show considerable differences.

In the last part of the chapter, the influence of the seismic intensity level, running speed and track quality on the running safety of the railway vehicle moving over the viaduct is discussed. Unlike the majority of studies in this field, in which the earthquake is assumed to start at the instant the train enters the bridge, the time offset between the beginning of the earthquake and the entry of the vehicle in the viaduct is taken into account by considering five scenarios corresponding to different instants in which the earthquake starts to excite the viaduct. The consideration of these scenarios is of the utmost importance, since the random nature of the seismic action, together with the vast number of possible combinations regarding the time offset between the start of the earthquake and the entry of the vehicle in the viaduct, makes it almost impossible to find a unique scenario that could be representative of all possible situations. Thus, as expected, the sensibility analysis carried out in the present chapter proved that the most critical scenario is not always the same for the different scenarios considered in this work. Nevertheless, a stochastic approach of the problem would be necessary to obtain a more representative range of results.

Regarding the running safety analysis, the results show that, even for the moderate seismic intensities considered in the present study, the train safety is put at risk in a considerable number of scenarios, thus proving the importance of taking low intensity earthquakes into account in the design of railway bridges, even if they do not represent a major threat to the structural integrity. The train running speed is also an important factor to take into account during the design of railway bridges, especially in regions prone to earthquakes, since all the safety criteria show that, in the presence of a seismic excitation, the risk of derailment significantly increases for speeds above 250 km/h. Moreover, the vibrations caused by the presence of irregularities in poorly maintained tracks may considerably increase the risk of derailment, even without the presence of earthquakes.

All the information obtained in the dynamic analyses is condensed in the running safety charts, which consist of the global envelope of each analyzed safety criterion as function of the

running speed of the vehicle and of the seismic intensity level. These charts allow a quick interpretation of the results, providing a useful tool for analyzing which scenarios may pose a significant threat to the stability of the vehicle and, consequently, to the safety of the passengers. As would be expected, the trend observed in all the criteria is similar, indicating that the risk of derailment increases with the increasing of the running speed and seismic intensity. It may be observed that the risk of derailment due to the wheel unloading is null when the train runs over a track whose quality corresponds to the regular operation limit. For this level of irregularities, the Prud'homme criterion proved to be the most conservative, since it controls the derailment risk for almost all the speeds. However, this tendency changes for poorer quality tracks, in which the Nadal, rail roll and wheel unloading criteria define the safety zone. Hence, for the track with better quality, the vehicle remains safe at every speed if no earthquake occurs, while for the track with poorer quality, the derailment risk predicted with the majority of the criteria significantly increases for speeds above 270 km/h.

Finally, the critical analysis regarding the safety criteria adopted in the present work show that the Nadal criterion is very conservative, even considering that it is only violated if the ratio between lateral and vertical contact forces exceeds the maximum value for more than 0.015 s, as proposed by the Japanese standards. Such conclusion becomes clear when looking at the lateral relative displacement between wheel and rail. These displacements barely exceed 6 mm in one of the directions due to the constraint imposed by the flange when it impacts with the rail, which means that the wheel is not climbing the rail. Furthermore, the wheel unloading criterion proved to be conservative as well, since even when the wheel detaches from the rail, the wheel flange is still far from rising above the rail.

Chapter 7

CONCLUSIONS AND FUTURE DEVELOPMENTS

7.1   CONCLUSIONS

The present thesis is focused on the assessment of the running safety of trains on bridges, with special emphasis given to the running safety against earthquake. The methodology proposed to achieve this goal includes the development, implementation, validation and application of a numerical tool to analyze the dynamic coupling between the train and the structure.

In Chapter 2, an overview of the recent studies carried out in the field of rail traffic stability over bridges, with special focus on the running safety against earthquakes, was presented. In this chapter, a review of the different existing methods for analyzing the dynamic response of the vehicle-structure system was also made, emphasizing the main advantages and disadvantages of each one in terms of accuracy and computational cost. Since the majority of the running safety criteria are related with the control of the wheel-rail contact forces, the wheel-rail contact model used in the vehicle-structure interaction tool is of the utmost importance to obtain accurate results. Therefore, the most common wheel-rail contact models existing in the literature were revisited, together with the recommendations and norms regarding the stability and safety of trains defined in the standards from different regions of the world.

As mentioned earlier, the main objective of the present thesis consisted on developing a methodology for evaluating the running safety of trains moving on bridges. The proposed methodology was, therefore, described in Chapter 3, in which the risk of derailment is evaluated using safety criteria based on the wheel-rail contact forces computed in the train-structure interaction dynamic analysis. The seismic motion applied to the system was represented in terms of ground acceleration time-histories using artificial accelerograms that were generated from the elastic spectra described in EN 1998-1 (2004), with PGA corresponding to moderate events with relatively high probability of occurrence and low return periods. Since no significant nonlinearity is expected to be exhibited in the bridge piers for these levels of seismicity, all the analysis were performed in the elastic domain with a reduction in the stiffness of the piers to account for concrete cracking. This reduced stiffness, referred to as effective stiffness, was calculated based on a simplified methodology that proved to be efficient for dealing with moderate earthquakes.

Another important source of excitation that was also included in the methodology consisted in the track irregularities. These deviations of the rail from the ideal geometry were artificially generated, based on a stationary stochastic process described by PSD functions.

According to the proposed methodology, for each analyzed scenario, the circulation is considered to be safe as long as none of the adopted safety criteria used to assess the train running safety is violated during the whole time that the vehicle is crossing the bridge.

The train-structure interaction method developed in the present thesis was formulated in Chapter 4 and validated in Chapter 5. The tool was implemented in MATLAB, being the structural models of both the vehicle and bridge developed in the finite element software ANSYS. The structural matrices are imported by MATLAB from ANSYS using an efficient interconnection tool between both softwares. The main feature of the method consists in a wheel-rail contact model that takes into account the geometry of the wheel and rail surfaces in order to accurately evaluate the lateral interaction. This contact model is divided in three main parts, namely the geometric problem, the normal problem and the tangential problem.

The geometric problem, which consists of detecting the position of the contact points between wheel and rail, is solved online. Although this procedure is computationally more expensive than an offline contact approach, in which the location of the contact points is precalculated as a function of the relative displacements between wheel and rail, its higher accuracy outweighs this drawback. The proposed method is able to look for potential contact

points in any types of geometrical surfaces (convex or concave) at both the tread and the flange of the wheel. Thus, the formulation is suitable to investigate not only scenarios related to ordinary railway operation, but also derailment situations, in which the flange contact plays an important role.

Regarding the normal contact problem, the nonlinear Hertz theory was used to compute the normal contact forces between wheel and rail. Although this theory rests on a series of assumptions that may limit its range of application, it offered a good compromise between computational efficiency and accuracy for dealing with the dynamic analysis of railway vehicles.

For simulating the behavior at the contact interface in the tangential direction, three different approaches were adopted. Since the exact theory of rolling contact proposed by Kalker is impracticable to be used in dynamic analysis of railway vehicles due to its excessive computational cost, the Polach method, the Kalker's book of tables and the Kalker's linear theory were implemented and integrated in the proposed formulation. The first two methods combine accuracy with computational efficiency, while the latter is limited to scenarios with small creepages.

The coupling between the vehicle and the structure was accomplished by the direct method, which complements the governing equilibrium equations of the vehicle and structure with additional constraint equations that relate the displacements of the contact nodes of the vehicle with the corresponding nodal displacements of the structure. These equations form a single system, with displacements and contact forces as unknowns, that is solved directly using an optimized block factorization algorithm.

The train-structure interaction method mentioned above was validated with three numerical applications and one experimental test described in Chapter 5. The first application consisted of validating the creep models implemented and integrated in the numerical tool. Four test cases based on examples presented in Kalker (1990), in which the longitudinal and lateral creep forces are computed for distinct ranges of creepages and semi-axes ratios of the contact ellipse, were reproduced. All the three creep models proved to be adequate to deal with scenarios with small creepages. However, the Kalker's linear model could not predict reasonable values of the creep forces when the creepages increase and the tangential stresses approach the saturation limit. For higher values of translational creepages and low values of spin, both the Polach method and the Kalker's book of tables provided adequate results, but only the latter was

sufficiently accurate for situations where the spin creepages were also higher. For these reasons, the implemented book of tables was used in the majority of the dynamic simulations presented in this thesis.

In the second application, the Manchester Benchmark was revisited. The benchmark comprised a series of tests that consisted of prescribing, both statically and dynamically, lateral displacements and yaw rotations to a single wheelset in order to analyze its behavior. Several contact characteristics were analyzed, namely the contact point positions on both wheels of the wheelset, the rolling radius difference between wheels, the contact angles and the creepages. The results obtained with the proposed method for all the analyzed quantities showed an excellent agreement with those obtained with widely used softwares in railway vehicle dynamics, such as GENSYS, NUCARS and VAMPIRE.

The third numerical example consisted of evaluating the lateral stability of a single wheelset running at several speeds. The dynamic response of the wheelset calculated with the proposed method was compared with that obtained using a semi-analytical model with two degrees of freedom available in the literature. The model follows a number of simplifying assumptions whereby the dynamics of the wheelset could be described by simple linear differential equations. A good agreement between the responses obtained with the proposed method and those obtained by the integration of the equations of motion of the semi-analytical model was observed. As expected, for speeds below the critical limit, both the lateral displacement and the yaw rotation of the wheelset tended to damp out after being driven away by a lateral disturbance. This was due to the energy dissipation provided by the creep forces and to the stability provided by the suspensions. However, when the speed exceeded the critical value, the behavior of the wheelset became unstable, leading to a hunting motion that grew indefinitely.

In the last application, an experimental test conducted in the rolling stock test plant of the RTRI in Japan, in which a full scale railway vehicle ran over a track that was subjected to vertical and lateral deviations, was reproduced numerically. The lateral accelerations inside the carbody measured during the test were compared with those obtained with the proposed method and with the train-structure interaction software DIASTARS. The results showed a good agreement, even during extreme situations, such as flange-rail impacts due to excessive lateral vibrations cased by the rail deviations. Some discrepancies, however, were observed between the numerical and experimental results. These may be caused by the fact that vehicle was modeled using rigid bars and thus important deformations were not considered.

Furthermore, the incapacity of the actuators to reproduce with precision the track rotations could also contribute for the differences between the experimental and numerical results.

In summary, the results obtained in the four validation applications showed that the implemented tool is sufficiently accurate to deal with a vast range of scenarios regarding the running safety of trains moving on bridges.

Finally, in Chapter 6, a study regarding the assessment of the running safety of a train moving on a viaduct subjected to earthquakes was carried out. The dynamic analyses were performed with the vehicle-structure interaction method presented in Chapter 4 and validated in Chapter 5.

The study focused on the dynamic analysis of a high-speed train running over an idealized viaduct based on an existing flyover type structure of the Portuguese railway network. This viaduct has been extensively studied in the past, both numerically and experimentally, thus providing essential data for developing the numerical model.

The two main sources of excitation of the train-structure system considered in the study were the track irregularities and the earthquake load, which were described in Chapter 3. Since the seismic excitation was not expected to cause significant damage to the structure, all the dynamic train-structure interaction analyses were performed in the elastic domain, being the reduction in the stiffness of the piers due to concrete cracking evaluated using the methodology exposed in Chapter 3. As mentioned before, the methodology consisted of calibrating the effective stiffness of the piers in order to obtain, with a linear dynamic analysis, levels of displacement on the piers similar to those obtained with the nonlinear dynamic analysis. In the present study, a good agreement was observed between the two responses, proving the efficiency of the methodology.

Before starting the running safety analysis, a preliminary study for evaluating the dynamic behavior of the train-structure system was carried out. As a first conclusion, the vertical response of both the structure and the vehicle was barely affected by the seismic action, since only the lateral component of the earthquake was considered in the present work. On the other hand, in the lateral direction, the deck response was mainly dominated by the earthquake, being the influence of the vehicle load almost negligible.

The influence of the effective stiffness of the piers on the lateral response of the viaduct was also assessed. Two scenarios of seismicity were analyzed with reference return periods of

95 years and 310 years. Although the spectral acceleration decreased due to the increase in the period of the structure, the amplitude of the response increased due to the fact that the piers became less stiff and therefore could experience larger displacements during the earthquake.

Regarding the vehicle, when the viaduct was subjected to the strongest earthquake considered in this study, the maximum lateral displacement of the carbody, relative to the lateral displacement of the track centerline, was approximately six times higher than the maximum displacement of the wheelset, while without earthquake this difference was almost negligible. In order to avoid excessive lateral vibrations, the high-speed trains are equipped with stoppers installed in the secondary lateral suspensions. However, it was concluded that for the levels of seismicity considered in the present work, these devices do not have an important impact in the lateral response of the vehicle.

Finally, the influence of the seismic intensity level, running speed and track quality on the running safety of the railway vehicle was discussed. Unlike the majority of studies, in which the earthquake is assumed to start at the instant the train enters the bridge, a time offset between the beginning of the earthquake and the entry of the vehicle in the viaduct was taken into account by considering five scenarios corresponding to different instants in which the earthquake starts to excite the viaduct. The adoption of these scenarios proved to be of the utmost importance, since the results obtained in the sensibility analysis carried out in this chapter showed that the most critical scenario for the train's running safety was not always the same for the different situations considered in the study. This conclusion was expected, since it is very difficult to find a unique scenario that could be representative of all possible cases.

The running safety analysis showed that even for the moderate seismic intensities considered in the present study, the train safety was put at risk in a considerable number of scenarios, thus proving the importance of taking low intensity earthquakes into account in the design of railway bridges, even if they do not represent a major threat to the structural integrity. The train running speed is also an important factor to take into account during the design of railway bridges, especially in regions prone to earthquakes, since all the safety criteria showed that, in the presence of a seismic excitation, the risk of derailment significantly increased for speeds above 250 km/h. Moreover, the vibrations caused by the presence of irregularities in poorly maintained tracks may considerably increase the risk of derailment, even without the presence of earthquakes.

All the information obtained in the dynamic analyses was condensed in the running safety charts, which consist in the global envelope of each analyzed safety criterion as function of the running speed of the vehicle and seismic intensity level. These charts allow a quick interpretation of the results, providing a useful tool for analyzing which scenarios may pose a significant threat to the stability of the vehicle and, consequently, to the safety of the passengers. The trend observed in all the criteria was similar, indicating that the risk of derailment increases with the increasing of the running speed and seismic intensity. It could be observed that the risk of derailment due to the wheel unloading was null when the train ran over a track whose quality corresponded to the regular operation limit. For this level of irregularities, the Prud'homme criterion proved to be the most conservative, since it controls the derailment risk for almost all the speeds. However, this tendency changed for poorer quality tracks, in which the Nadal, rail roll and wheel unloading criteria defined the safety zone. Hence, for the track with better quality, the vehicle remained safe at every speed when no earthquake was considered, while for the track with poorer quality, the derailment risk predicted with the majority of the criteria significantly increased for speeds above 270 km/h.

Finally, the critical analysis regarding the safety criteria adopted in the present work shown that the Nadal criterion is very conservative, even considering that it is only violated if the ratio between lateral and vertical contact forces exceeds the limit value for more than 0.015 s, as proposed by the Japanese standards. The results showed that in the instants in which the limit value of the criterion was exceeded, the relative lateral displacement between the wheel and the rail barely exceeded 6 mm due to the constraint imposed by the wheel flange, showing that the wheel was not climbing the rail as the criterion intended to prove.

7.2 FUTURE DEVELOPMENTS

The work presented in this thesis focuses on developing a methodology for the assessment of the train running safety on bridges, including a train-structure interaction tool fully developed by the author. However, the course of this research raised several questions that were not addressed. In this context, some topics requiring further analysis are referred in the following paragraphs:

a) The train-structure interaction tool developed in this thesis still requires further work, especially regarding the computational efficiency. The use of direct integration to solve the dynamic equations of motion of the train-structure system represents a significant

fraction of the total time needed to solve the whole dynamic problem. The implementation of the modal superposition method could be an important step towards a better computational efficiency in linear problems. Moreover, it would be interesting to exploit the potential of the parallel computation provided by the *Graphic Processing Unit* (GPU) toolbox of MATLAB. Although there are still no functions in this toolbox to solve system of equations defined by sparse matrices, this could be an important improvement in the near future;

b) Still regarding the interaction tool, further work is needed in the wheel-rail contact model developed in this thesis. A better computational efficiency is necessary in the geometric contact problem, especially on the algorithm used to locate the contact points in concave regions. This is an important drawback in analysis with worn profiles, where the concave region that exists in the transition between the tread and flange plays an important role. Moreover, the time needed to locate the contact points in each wheel is still an important limitation in the analysis of long trains with a large number of cars;

c) The implementation of more realistic models to deal with the normal contact problem may also be an important development in the future. Although the Hertz theory offers a good compromise between computational efficiency and accuracy in the dynamic analysis of railway vehicles, a more realistic model would be needed to deal with local problems such as wear;

d) It is intended to extend the formulation to deal with curve tracks. Although the high-speed railway recommendations impose restrictions on the curve radii, the curve negotiation is a topic of the utmost importance in railway engineering, since it is one of the major causes of derailments. To accomplish this goal, the wheel-rail contact model requires some improvements, since, in the two-point contact scenario, the contact point search is no longer restricted to only one plane;

e) In the present work, only moderate earthquakes that do not represent a major threat to the structural integrity were studied. However, the evaluation of the running safety of trains under stronger seismic conditions is a topic to be addressed in the future. To achieve that, the structure model has to account for the effects of both the material inelasticity and the geometric nonlinearity due to the large displacements caused by the earthquake;

f) The analysis of the influence of the vertical ground motion on the running safety of trains moving on bridges is also an important topic to be addressed in the future. Although the majority of the authors reported that the vehicle running safety against earthquake has a stronger relation to the lateral ground motions than to the vertical excitations, the inclusion of the vertical ground motion might contribute to a better understanding of some of the derailment mechanisms presented in this thesis;

g) The case study presented in this thesis focuses on the running safety analysis of a railway vehicle running over a simply supported multi-span viaduct based on an existent viaduct belonging to the Portuguese railway network. However, a wider parametric study, comprehending different types of viaducts and bridges (different support conditions, pier heights and structural solutions), different types of trains and more types of earthquake (different soil conditions and seismic zones), might contribute to a more representative conclusion;

h) It is intended to evaluate in the future the running safety of trains moving over bridges under other types of actions, such as crosswinds. Although the methodology proposed in the present thesis allows this type of analysis, only the running safety against earthquakes is addressed in the case study;

i) It may be necessary in the future a stochastic approach to deal with the type of problems discussed in this work, since there is a vast number of uncertainties presented. For example, the random nature of the seismic action, together with the vast number of possible combinations regarding the time offset between the start of the earthquake and the entry of the vehicle in the viaduct, makes it difficult to obtain representative results exclusively with a deterministic approach.

j) The running safety criteria adopted in the present work are, in most cases, very conservative. In fact, some experimental tests referred in Chapter 2 reported that a train might be far from derail if the criteria limits are exceeded only for a short period of time. Moreover, the critical analysis performed at the end of Chapter 6 led to similar conclusions. Therefore, a better understanding of the physical meaning of the derailment phenomena may contribute for the development of more sophisticated running safety criteria.

k) It would be interesting to integrate the numerical tool proposed in the present thesis in a railway monitoring system used to evaluate the necessity of maintenance. With such

kind of monitoring system, it would be possible to avoid the huge periodic maintenance operations, contributing to a more optimized maintenance program.

Appendix A

IMPLEMENTATION OF A CONTACT LOOKUP TABLE

A.1 INTRODUCTION

For computing the contact lookup table, the track and wheelset are assumed to be rigid. The relative motion between them occurs in a plane perpendicular to the track, being the wheelset allowed to rotate about the track longitudinal axis (roll rotation). Furthermore, the contact between the wheel and rail occurs at only one point and no separation is allowed. Under these assumptions, the surface parameters s_r and s_w (see Section 4.3.1 of Chapter 4) can be computed as a function of the relative lateral displacement y_w between the wheelset and track.

A.2 COORDINATE SYSTEMS

For the computation of the contact lookup tables and assuming that the wheelset is rigid, two new coordinate systems have to be introduced, namely the track centerline and the wheelset coordinate systems (see Figure A.1).

The track centerline coordinate system (x_{tc}, y_{tc}, z_{tc}) has its origin at a point equidistant from the two rails that is located at the same height as the point where the wheel contacts the rail when the wheelset is centered with the track. The x_{tc} axis is orientated tangent to the track centerline, while the y_{tc} and z_{tc} are contained in the rail cross-section plane orientated,

respectively, parallel and perpendicular to the rail-bed horizontal plane. Since the track rotations are not considered in the contact table computation, the axes that form the track centerline coordinate system are parallel to those which form the target element and the rail profile coordinate systems.

The wheelset coordinate system (x_{ws}, y_{ws}, z_{ws}) is fixed with the wheelset and has its origin at the center of mass of the wheelset. The y_{ws} and z_{ws} are contained in the wheelset cross-section plane, being the former orientated along the wheelset axis. The transformation matrix from the track centerline coordinate system to the wheelset coordinate system is analogous to the matrix $\mathbf{T}^{tw}$ defined in equation (4.8), since the wheelset behaves as a rigid body and the track rotations are not considered.
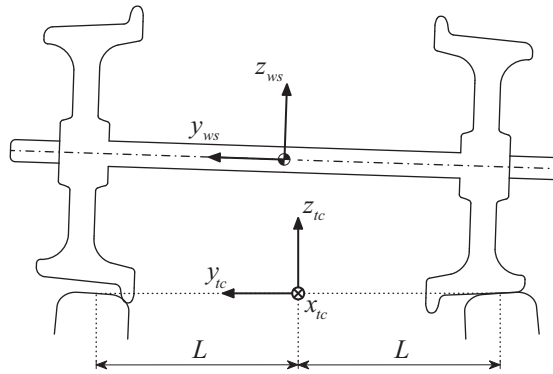
Figure A.1 - Track centerline and wheelset coordinate systems.

A.3 PARAMETERIZATION OF THE RAIL AND WHEEL PROFILES

A.3.1 Parameterization of the rail profile

The two-dimensional surface geometry of the rail is parameterized with respect to the centerline coordinate system and described in terms of the surface parameter s_r, as depicted in Figure A.2.
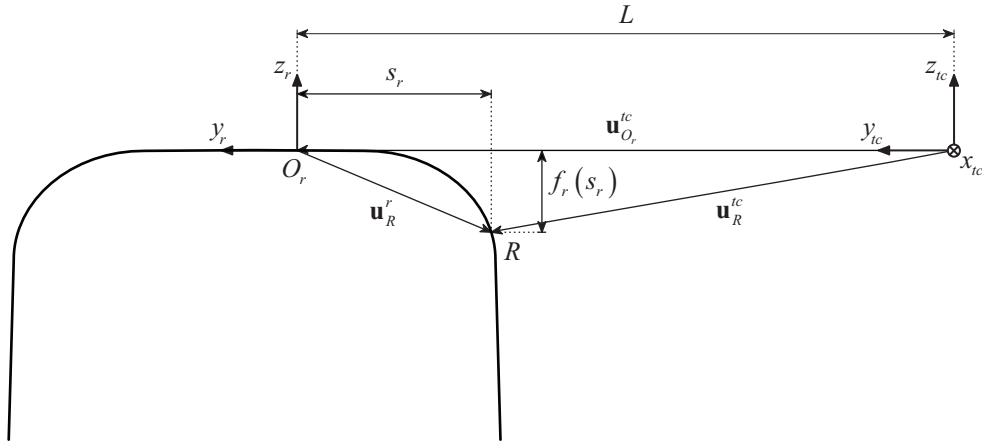
Figure A.2 - Parameterization of the rail profile with respect to the track centerline coordinate system.

The position vector $\mathbf{u}_R^{tc}$ of an arbitrary point R of the rail surface, defined with respect to the track centerline coordinate system, is given by

$$\mathbf{u}_R^{tc} = \mathbf{u}_{O_r}^{tc} + \mathbf{u}_R^{r} \tag{A.1}$$

where $\mathbf{u}_R^{r}$ is defined in equation (4.10) and $\mathbf{u}_{O_r}^{tc}$ is the position vector of the origin of the rail profile coordinate system, defined with respect to the track centerline coordinate system, written as

$$\mathbf{u}_{O_r}^{tc} = \begin{bmatrix} 0 & \pm L & 0 \end{bmatrix}^{\mathrm{T}} \tag{A.2}$$

where L is the distance along the y_{tc} axis between the origins of the track centerline and rail profile coordinate systems (the sign depends whether the left or right wheel is being analyzed).

A.3.2 Parameterization of the wheel profile

Assuming that the wheel belongs to a rigid wheelset, its profile is parameterized with respect to the centerline coordinate system and described in terms of the surface parameter s_w, as shown in Figure A.3.
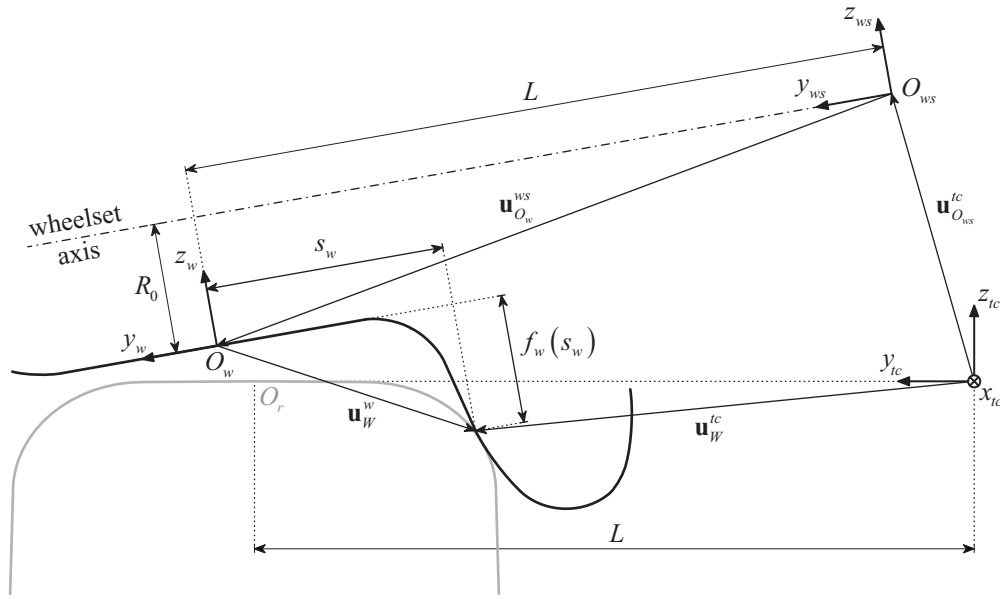
Figure A.3 - Parameterization of the wheel profile belonging to a rigid wheelset with respect to the track centerline coordinate system.

The position vector $\mathbf{u}_W^{tc}$ of an arbitrary point W of the wheel surface, defined with respect to the track centerline coordinate system, is given by

$$\mathbf{u}_W^{tc} = \mathbf{u}_{O_{ws}}^{tc} + \mathbf{T}^{twT}\left(\mathbf{u}_{O_w}^{ws} + \mathbf{u}_W^{w}\right) \tag{A.3}$$

where $\mathbf{u}_W^w$ is defined in equation (4.16) of Chapter 4, $\mathbf{u}_{O_{ws}}^{tc}$ is the position vector of the origin of the wheelset coordinate system, defined with respect to track centerline coordinate system, expressed as

$$\mathbf{u}_{O_{ws}}^{tc} = \begin{bmatrix} 0 & y_w^{tc} & \left(R_0 + z_w^{tc}\right) \end{bmatrix}^{\mathrm{T}} \tag{A.4}$$

where y_w^{tc} and z_w^{tc} are, respectively, the lateral and vertical displacements of the center of mass of the wheelset, defined with respect to the track centerline coordinate system, and R_0 the initial rolling radius of the wheel. The position vector of the origin of the wheel profile coordinate system $\mathbf{u}_{O_w}^{ws}$, defined with respect to the wheelset coordinate system, is given by

$$\mathbf{u}_{O_w}^{ws} = \begin{bmatrix} 0 & \pm L & -R_0 \end{bmatrix}^{\mathrm{T}} \tag{A.5}$$

A.4 CONTACT POINT SEARCH AND TABLE STORAGE

Since the accuracy of the contact table depends on the degree of discretization used, the wheel and rail surfaces are discretized by a set of points that reliably represent the profile geometry. Hence, for a given lateral displacement of the wheelset, the vertical distances between each point of the wheel and rail surfaces are evaluated, as shown in Figure A.4. Using this set of vertical distances, the points with maximum absolute value, which belong to the intersection between the wheel and rail surfaces, are considered to be potential contact points. Since the wheelset is rigid, the potential contact points are in contact only if the following condition is met:

$$\left| \Delta z_{\max}^{lft} - \Delta z_{\max}^{rht} \right| < \varepsilon \qquad (A.6)$$

where $\Delta z_{\max}$ is the maximum vertical distance between the wheel and rail in the region where the surfaces intersect each other, and ε is a specified tolerance. The superscripts *lft* and *rht* indicate left and right side of the wheelset, respectively. For each side, the distance $\Delta z_{\max}$ is given by

$$\Delta z_{\max} = \max\left\{ \left(\overline{\mathbf{u}}_{w,i}^{tc} - \mathbf{u}_{w,i}^{tc} \right) \cdot \mathbf{e}_{z_{tc}} \right\}, \quad i = 1, 2, \ldots, n_w \qquad (A.7)$$

where n_w is the number of points that discretize the wheel surface, $\mathbf{e}_{z_{tc}}$ is a unit base vector of the track centerline coordinate system, $\mathbf{u}_{w,i}^{tc}$ is defined by equation (A.3) and $\overline{\mathbf{u}}_{w,i}^{tc}$ is the position vector of the vertical projection of the *i*th wheel point into the rail surface, defined with respect to the track centerline coordinate system, as depicted in Figure A.4. Note that the calculation of the vertical distances Δz_i could also be performed, in an analogous way, using the points of the rail surface.
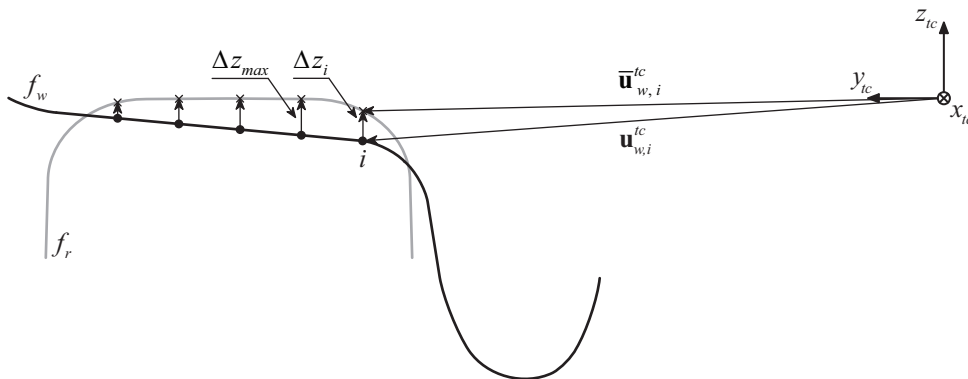
Figure A.4 - Vertical distances between wheel and rail (intersection scale exaggerated).

If the condition (A.6) is not fulfilled, the wheelset roll rotation ϕ_w^{tc}, defined with respect to the track centerline coordinate system, has to be iteratively adjusted. According to Li (2002), the number of iterations can be substantially reduced if the roll rotation of the wheelset is adjusted by an angle $\Delta\phi_w^{tc}$ given by

$$\Delta\phi_w^{tc} = \frac{\Delta z_{\max}^{lft} - \Delta z_{\max}^{rht}}{\left(\mathbf{u}_{w,\max}^{tc,lft} - \mathbf{u}_{w,\max}^{tc,rht}\right) \cdot \mathbf{e}_{y_{tc}}} \tag{A.8}$$

where $\mathbf{u}_{w,\max}^{tc}$ is the position vector of the point of the wheel with maximum vertical distance to the rail in the region where the surfaces intersect each other, with respect to the track centerline coordinate system, and $\mathbf{e}_{y_{tc}}$ is a unit base vector of the track centerline coordinate system. The contact search is repeated until the tolerance specified in the condition (A.6) is satisfied, being the surface parameters that define the contact point position in each wheel of the wheelset stored in the contact table.

The vertical displacements of the center of mass of the wheelset z_w^{tc} and the wheelset roll rotation ϕ_w^{tc}, the contact angles on both wheels γ and the surface parameters s_r and s_w, defined as a function of the lateral displacement of the center of mass of the wheelset y_w^{tc}, are plotted in Figures A.5 to A.7. These results refer to the S1002 wheel and UIC60 rail.

(a)　　　　　　　　　　　　　　　　　　(b)
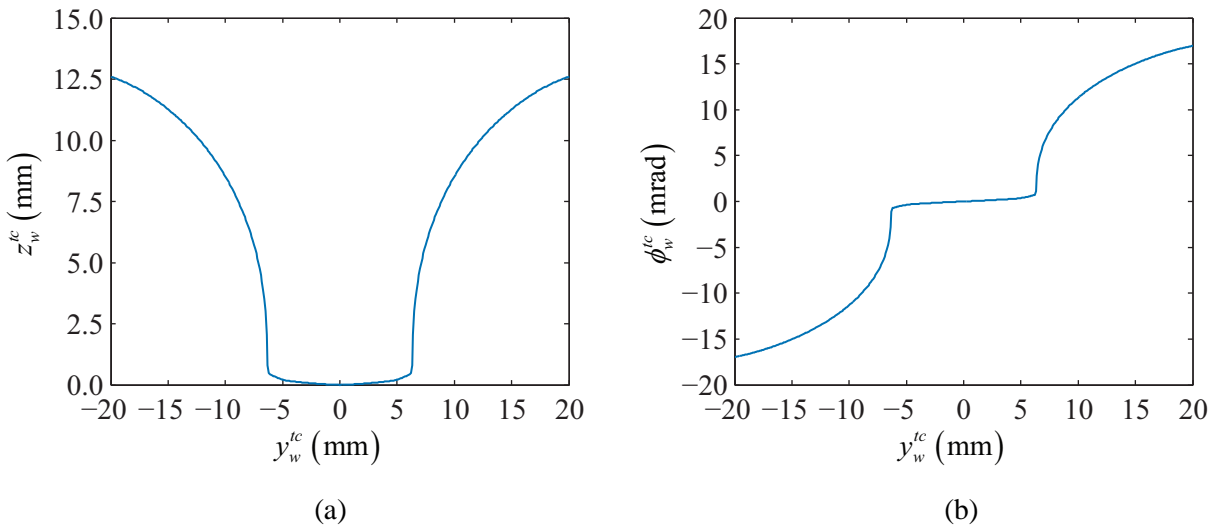
Figure A.5 - Wheelset movement as a function of the relative lateral displacement between wheelset and rail: (a) vertical displacements and (b) roll rotations.
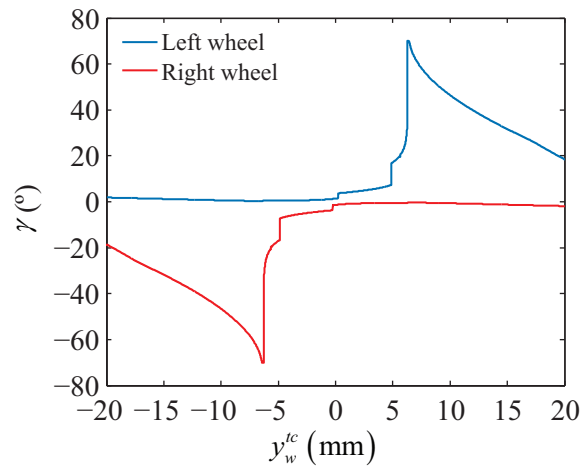
Figure A.6 - Contact angles as a function of the relative lateral displacement between wheelset and rail.

(a)   (b)
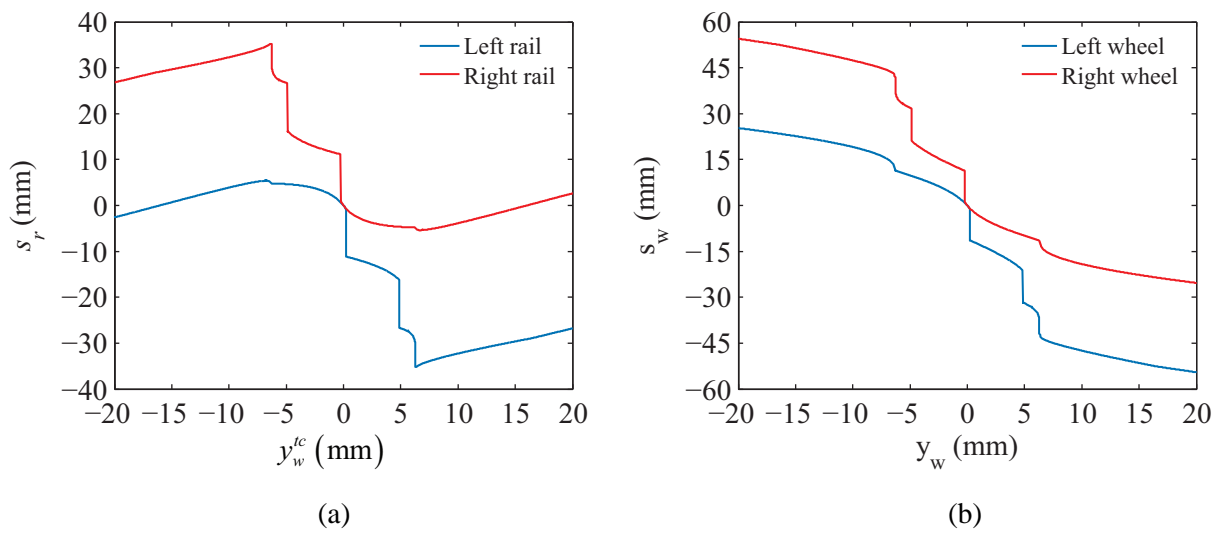
Figure A.7 - Surface parameters as a function of the relative lateral displacement between wheelset and rail: (a) rail parameter and (b) wheel parameter.

Appendix B

COEFFICIENTS FOR THE NORMAL AND TANGENTIAL CONTACT PROBLEMS

B.1 INTRODUCTION

This appendix aims to summarize the coefficients needed for solving the normal and tangential contact problems described in Sections 4.4 and 4.5, respectively, of Chapter 4. These are:

a) Hertz coefficients m and n for computing the semi-axes of the contact ellipse;

b) Hertz constant C_h for computing the generalized stiffness coefficient;

c) Kalker's creepage coefficients c_{ij}.

B.2 HERTZ COEFFICIENTS FOR COMPUTING THE SEMI-AXES OF THE CONTACT ELLIPSE

The Hertz coefficients m and n used to compute the semi-axes of the contact ellipse (see equation (4.37)) are given as a function of the angular parameter θ defined in equation (4.38). These coefficients are summarized in Table B.1 for values of θ ranging from 0 to 180 degrees.

Table B.1 - Hertz coefficients *m* and *n* (Hertz, 1882; Andersson et al., 1999; Shabana et al., 2008).

θ (degrees)	*m*	*n*	θ (degrees)	*m*	*n*
0	∞	0	100	0.8930	1.128
1	36.890	0.1314	110	0.8020	1.284
2	22.260	0.1691	120	0.7170	1.486
3	16.500	0.1964	130	0.6410	1.754
6	9.790	0.2552	140	0.5670	2.136
10	6.604	0.3112	150	0.4930	2.731
20	3.813	0.4125	160	0.4125	3.813
30	2.731	0.4930	170	0.3112	6.604
40	2.136	0.5670	172	0.2850	7.860
50	1.754	0.6410	174	0.2552	9.790
60	1.486	0.7170	177	0.1964	16.500
70	1.284	0.8020	178	0.1691	22.260
80	1.128	0.8930	179	0.1314	36.890
90	1.000	1.000	180	0	∞

B.3 HERTZ CONSTANT FOR COMPUTING THE GENERALIZED STIFFNESS

The Hertz constant C_h used to compute the generalized stiffness coefficient expressed in equation (4.40) is presented in Table B.2 as a function of the ratio *A/B* (see equation 4.32).

Table B.2 - Hertz constant C_h (Goldsmith, 1960; Shabana et al., 2008).

A/B	C_h
∞	0
1.0	0.3180
0.7041	0.3215
0.4903	0.3322
0.3333	0.3505
0.2174	0.3819
0.1325	0.4300
0.0718	0.5132
0.0311	0.6662
0.00765	1.1450
0	∞

B.4 KALKER'S CREEPAGE COEFFICIENTS

The Kalker's creepage coefficients c_{ij} depend on the semi-axes ratio a/b (see equation (4.37)) and on the Poisson's ratio of the wheel and rail materials v. Table B.3 summarizes these coefficients, including closed-form expressions to compute their values for high and low semi-axes ratios.

Table B.3a - Kalker's creepage coefficients c_{ij} for $b > a$ (Garg and Dukkipati, 1984; Kalker, 1990).

a/b	c_{11}			c_{22}			$c_{23=}$ -c_{32}			c_{33}		
	$v = 0$	0.25	0.5	$v = 0$	0.25	0.5	$v = 0$	0.25	0.5	$v = 0$	0.25	0.5
0	Equation (B.1)			Equation (B.2)			Equation (B.3)			Equation (B.4)		
0.1	2.51	3.31	4.85	2.51	2.52	2.53	0.33	0.47	0.73	6.42	8.28	11.7
0.2	2.59	3.37	4.81	2.59	2.63	2.66	0.48	0.60	0.81	3.46	4.27	5.66
0.3	2.68	3.44	4.80	2.68	2.75	2.81	0.61	0.72	0.89	2.49	2.96	3.72
0.4	2.78	3.53	4.82	2.78	2.88	2.98	0.72	0.82	0.98	2.02	2.32	2.77
0.5	2.88	3.62	4.83	2.88	3.01	3.14	0.83	0.93	1.07	1.74	1.93	2.22
0.6	2.98	3.72	4.91	2.98	3.14	3.31	0.93	1.03	1.18	1.56	1.68	1.86
0.7	3.09	3.81	4.97	3.09	3.28	3.48	1.03	1.14	1.29	1.43	1.50	1.60
0.8	3.19	3.91	5.05	3.19	3.41	3.65	1.13	1.15	1.40	1.34	1.37	1.42
0.9	3.29	4.01	5.12	3.29	3.54	3.82	1.23	1.36	1.51	1.27	1.27	1.27

Table B.3b - Kalker's creepage coefficients c_{ij} for $a > b$ (Garg and Dukkipati, 1984; Kalker, 1990).

b/a	c_{11}			c_{22}			$c_{23=}$ -c_{32}			c_{33}		
	$v = 0$	0.25	0.5	$v = 0$	0.25	0.5	$v = 0$	0.25	0.5	$v = 0$	0.25	0.5
1.0	3.40	4.12	5.20	3.40	3.67	3.98	1.33	1.47	1.63	1.21	1.19	1.63
0.9	3.51	4.22	5.30	3.51	3.81	4.16	1.44	1.59	1.77	1.16	1.11	1.06
0.8	3.65	4.36	5.42	3.65	3.99	4.39	1.58	1.75	1.94	1.10	1.04	0.95
0.7	3.82	4.54	5.58	3.82	4.21	4.67	1.76	1.95	2.18	1.05	0.97	0.85
0.6	4.06	4.78	5.80	4.06	4.50	5.04	2.01	2.23	2.50	1.01	0.89	0.75
0.5	4.37	5.10	6.11	4.37	4.90	5.56	2.35	2.62	2.96	0.96	0.82	0.65
0.4	4.84	5.57	6.57	4.84	5.48	6.31	2.88	3.24	3.70	0.91	0.75	0.55
0.3	5.57	6.34	7.34	5.57	6.40	7.51	3.79	4.32	5.01	0.87	0.67	0.45
0.2	6.96	7.78	8.82	6.96	8.14	9.79	5.72	6.63	7.89	0.83	0.60	0.34
0.1	10.7	11.7	12.9	10.7	12.8	16.0	12.2	14.6	18.0	0.80	0.53	0.23
0	Equation (B.6)			Equation (B.7)			Equation (B.8)			Equation (B.9)		

The c_{ij} coefficients for low values of the *a/b* ratio (see Table B.3a) are given by

$$c_{11} = \frac{\pi^2}{4\,(1-v)} \tag{B.1}$$

$$c_{22} = \frac{\pi^2}{4} \tag{B.2}$$

$$c_{23} = \frac{\pi\,\sqrt{a/b}}{3\,(1-v)}\left[1+v\left(\frac{1}{2}\Lambda_\downarrow + \ln 4 - 5\right)\right] \tag{B.3}$$

$$c_{33} = \frac{\pi^2}{16\,(1-v)\,(a/b)} \tag{B.4}$$

where $\Lambda_\downarrow$ is given by

$$\Lambda_\downarrow = \ln\left[\frac{16}{(a/b)^2}\right] \tag{B.5}$$

The c_{ij} coefficients for high values of the *a/b* ratio (see Table B.3b) are given by

$$c_{11} = \frac{2\pi}{(\Lambda_\uparrow - 2v)\,(b/a)}\left[1 + \frac{3-\ln 4}{\Lambda_\uparrow - 2v}\right] \tag{B.6}$$

$$c_{22} = \frac{2\pi}{\left[(1-v)\Lambda_\uparrow + 2v\right]\,(b/a)}\left[1 + \frac{(1-v)(3-\ln 4)}{(1-v)\,\Lambda_\uparrow + 2v}\right] \tag{B.7}$$

$$c_{23} = \frac{2\pi}{3\,(b/a)\,\sqrt{b/a}}\frac{1}{(1-v)\,\Lambda_\uparrow - 2 + 4v} \tag{B.8}$$

$$c_{33} = \frac{\pi}{4}\left[1 - \frac{(\Lambda_\uparrow - 2)v}{(1-v)\Lambda_\uparrow - 2 + 4v}\right] \tag{B.9}$$

where $\Lambda_\uparrow$ is given by

$$\Lambda_\uparrow = \ln\left[\frac{16}{(b/a)^2}\right] \tag{B.10}$$

Appendix C

BLOCK FACTORIZATION SOLVER

C.1 INTRODUCTION

The present block factorization algorithm is based on that developed by Neves et al. (2012) and later extended by Montenegro et al. (2015b) to deal with the three-dimensional contact. This algorithm aims to solve the system of equations (4.102) efficiently by taking into account the specific properties of each block, namely symmetry, positive definiteness and bandwidth.

C.2 SOLVER FORMULATION

Since the submatrix $\overline{\mathbf{K}}_{YY}$ presented in equation (4.102) may be indefinite and therefore may not have a stable factorization without pivoting, the lines and columns of the system matrix corresponding to the incremental displacements $\Delta \mathbf{a}_Y$ and contact forces $\Delta \mathbf{X}$ have to be grouped together. Hence the block factorization of the system of equations (3.101) is presented below using the following notation.

$$\begin{bmatrix} \mathbf{A}_{11} & \mathbf{A}_{21}^T & \mathbf{A}_{31}^T \\ \mathbf{A}_{21} & \mathbf{A}_{22} & \mathbf{A}_{32}^T \\ \mathbf{A}_{31} & \mathbf{A}_{32} & \mathbf{A}_{33} \end{bmatrix} \begin{bmatrix} \mathbf{x}_1 \\ \mathbf{x}_2 \\ \mathbf{x}_3 \end{bmatrix} = \begin{bmatrix} \mathbf{b}_1 \\ \mathbf{b}_2 \\ \mathbf{b}_3 \end{bmatrix} \tag{C.1}$$

where $\mathbf{x}_1$ and $\mathbf{x}_2$ correspond to $\Delta \mathbf{a}_I$ and $\Delta \mathbf{a}_R$, respectively, and $\mathbf{x}_3$ corresponds to the group

formed by $\Delta\mathbf{a}_Y$ and $\Delta\mathbf{X}$. The coefficient matrix presented in equation (C.1) admits the following factorization

$$\begin{bmatrix} \mathbf{A}_{11} & \mathbf{A}_{21}^T & \mathbf{A}_{31}^T \\ \mathbf{A}_{21} & \mathbf{A}_{22} & \mathbf{A}_{32}^T \\ \mathbf{A}_{31} & \mathbf{A}_{32} & \mathbf{A}_{33} \end{bmatrix} = \begin{bmatrix} \mathbf{L}_{11} & \mathbf{0} & \mathbf{0} \\ \mathbf{L}_{21} & \mathbf{L}_{22} & \mathbf{0} \\ \mathbf{L}_{31} & \mathbf{L}_{32} & \mathbf{L}_{33} \end{bmatrix} \times \begin{bmatrix} \mathbf{L}_{11}^T & \mathbf{L}_{21}^T & \mathbf{L}_{31}^T \\ \mathbf{0} & \mathbf{L}_{22}^T & \mathbf{L}_{32}^T \\ \mathbf{0} & \mathbf{0} & \mathbf{U}_{33} \end{bmatrix} \qquad \text{(C.2)}$$

where $\mathbf{L}$ and $\mathbf{U}$ are lower and upper triangular matrices, respectively. For simplicity, the permutation matrices associated with the factorization of $\mathbf{A}_{33}$ are not represented. The block factorization solver is divided into three stages, which are described below.

By equating part of the corresponding blocks in equation (C.2) the following relations are obtained

$$\mathbf{A}_{11} = \mathbf{L}_{11}\mathbf{L}_{11}^T \qquad \text{(C.3)}$$

$$\mathbf{A}_{21}^T = \mathbf{L}_{11}\mathbf{L}_{21}^T \qquad \text{(C.4)}$$

The first stage consists of factorizing $\mathbf{A}_{11}$, which is assumed to be symmetric positive definite and therefore admits a Cholesky factorization (Burden and Faires, 1997), and calculating $\mathbf{L}_{21}$ by forward substitution as follows. Since $\mathbf{A}_{11}$ and $\mathbf{A}_{21}^T$ are time-independent, the operations associated with equations (C.3) and (C.4) have to be performed only once at the beginning of the analysis.

By equating the remaining blocks in equation (C.2) the following relations are obtained

$$\mathbf{A}_{31}^T = \mathbf{L}_{11}\mathbf{L}_{31}^T \qquad \text{(C.5)}$$

$$\overline{\mathbf{A}}_{22} = \mathbf{L}_{22}\mathbf{L}_{22}^T \qquad \text{(C.6)}$$

$$\mathbf{A}_{32}^T = \mathbf{L}_{21}\mathbf{L}_{31}^T + \mathbf{L}_{22}\mathbf{L}_{32}^T \qquad \text{(C.7)}$$

$$\overline{\mathbf{A}}_{33} = \mathbf{L}_{33}\mathbf{U}_{33} \qquad \text{(C.8)}$$

where

$$\overline{\mathbf{A}}_{22} = \mathbf{A}_{22} - \mathbf{L}_{21}\mathbf{L}_{21}^T \qquad \text{(C.9)}$$

$$\overline{\mathbf{A}}_{33} = \mathbf{A}_{33} - \mathbf{L}_{31}\mathbf{L}_{31}^T - \mathbf{L}_{32}\mathbf{L}_{32}^T \qquad \text{(C.10)}$$

The second stage consists of obtaining the remaining matrices of the right hand side of equation (C.2) in an analogous way. It is assumed that the matrix $\overline{\mathbf{A}}_{22}$ admits a Cholesky

factorization, whereas the submatrices $\mathbf{L}_{33}$ and $\mathbf{U}_{33}$ are obtained using an *LU* factorization with pivoting. Since the matrices involved in equations (C.5) to (C.8) depend on the time and contact conditions, the operations belonging to the second stage have to be performed in each Newton iteration.

Finally, the third stage of the block factorization algorithm consists of obtaining the solution of the system of equations through the following two steps.

$$
\begin{bmatrix} \mathbf{L}_{11} & \mathbf{0} & \mathbf{0} \\ \mathbf{L}_{21} & \mathbf{L}_{22} & \mathbf{0} \\ \mathbf{L}_{31} & \mathbf{L}_{32} & \mathbf{L}_{33} \end{bmatrix} \begin{bmatrix} \mathbf{y}_1 \\ \mathbf{y}_2 \\ \mathbf{y}_3 \end{bmatrix} = \begin{bmatrix} \mathbf{b}_1 \\ \mathbf{b}_2 \\ \mathbf{b}_3 \end{bmatrix} \tag{C.11}
$$

$$
\begin{bmatrix} \mathbf{L}_{11}^T & \mathbf{L}_{21}^T & \mathbf{L}_{31}^T \\ \mathbf{0} & \mathbf{L}_{22}^T & \mathbf{L}_{32}^T \\ \mathbf{0} & \mathbf{0} & \mathbf{U}_{33} \end{bmatrix} \begin{bmatrix} \mathbf{x}_1 \\ \mathbf{x}_2 \\ \mathbf{x}_3 \end{bmatrix} = \begin{bmatrix} \mathbf{y}_1 \\ \mathbf{y}_2 \\ \mathbf{y}_3 \end{bmatrix} \tag{C.12}
$$

The vectors $\mathbf{y}_1$ to $\mathbf{y}_3$ are obtained by forward substitution as following

$$
\mathbf{L}_{11}\mathbf{y}_1 = \mathbf{b}_1 \tag{C.13}
$$

$$
\mathbf{L}_{22}\mathbf{y}_2 = \mathbf{b}_2 - \mathbf{L}_{21}\mathbf{y}_1 \tag{C.14}
$$

$$
\mathbf{L}_{33}\mathbf{y}_3 = \mathbf{b}_3 - \mathbf{L}_{31}\mathbf{y}_1 - \mathbf{L}_{32}\mathbf{y}_2 \tag{C.15}
$$

being the solution of the system of equations (C.1) obtained by back substitution

$$
\mathbf{U}_{33}\mathbf{x}_3 = \mathbf{y}_3 \tag{C.16}
$$

$$
\mathbf{L}_{22}^T\mathbf{x}_2 = \mathbf{y}_2 - \mathbf{L}_{32}^T\mathbf{x}_3 \tag{C.17}
$$

$$
\mathbf{L}_{11}^T\mathbf{x}_1 = \mathbf{y}_1 - \mathbf{L}_{21}^T\mathbf{x}_2 - \mathbf{L}_{31}^T\mathbf{x}_3 \tag{C.18}
$$

REFERENCES

A

AAR. *M1001: Manual of standards and recommended practices: Section C, Part II - Design, Fabrication, and Construction of Freight Cars*, Association of American Railroads, Washington, DC, USA, 2011.

ABAQUS. Release 6.10, Dassault Systèmes S.A., Paris, France, 2010.

Alexander, N.A. *Multi-support excitation of single span bridges, using real seismic ground motion recorded at the SMART-1 array*, Computers & Structures, 2008, **86** (1-2), pp. 88-103. DOI:10.1016/j.compstruc.2007.05.035.

Allemang, R.J. *The Modal Assurance Criterion (MAC): Twenty tears of use and abuse* Sound and Vibration, 2003, **37** (8), pp. 14-21.

Andersson, E., Berg, M., Stichel, S. *Rail vehicle dynamics: Fundamentals and guidelines*, Royal Institute of Technology, Stockholm, Sweden, 1999.

ANSYS. Academic Research, Release 13.0, ANSYS Inc., Canonsburg, PA, USA, 2010.

Antolín, P. *Efectos dinámicos laterales en vehículos y puentes ferroviarios sometidos a la acción de vientos transversales*, PhD Thesis, Universidad Politécnica de Madrid, Madrid, Spain, 2013 [in Spanish].

Antolín, P., Goicolea, J.M., Oliva, J., Astiz, M.A. *Nonlinear train-bridge lateral interaction using a simplified wheel-rail contact method within a finite element framework*, Journal of Computational and Nonlinear Dynamics, 2012, **7** (4), pp. 041014(1) - 041014(9). DOI:10.1115/1.4006736.

Ashford, S.A., Kawamata, Y. *Performance of transportation systems during the 2004 Niigata Ken Chuetsu, Japan, Earthquake*, Earthquake Spectra, 2006, **22** (1), pp. 111-132. DOI:10.1193/1.2172282.

Ayasse, J.B., Chollet, H. *Determination of the wheel rail contact patch in semi-Hertzian conditions*, Vehicle System Dynamics, 2005, **43** (3), pp. 161-172. DOI:10.1080/00423110412331327193.

Ayasse, J.B., Chollet, H., Maupu, J.L. *Paramètres caractéristiques du contact roue-rail (Rapport INRETS 225)*, INRETS, Paris, France, 2000.

B

Baker, C., Cheli, F., Orellano, A., Paradot, N., Proppe, C., Rocchi, D. *Cross-wind effects on road and rail vehicles*, Vehicle System Dynamics, 2009, **47** (8), pp. 983-1022. DOI:10.1080/00423110903078794.

Barron de Angoiti, I. *High speed rail: Development around the world*, In R. Calçada, R. Delgado, A. Carvalho & G. Degrande (Ed), Workshop Noise and Vibration on High-Speed Railways, Porto, Portugal, 2008.

Bathe, K.J. *Finite element procedures*, Prentice-Hall, Upper Saddle River, NJ, USA, 1996.

Bozzone, E., Pennestrì, P., Salvini, P. *Dynamic analysis of a bogie for hunting detection through a simplified wheel–rail contact model*, Multibody System Dynamics, 2011, **25** (4), pp. 429-460. DOI:10.1007/s11044-010-9233-8.

Brehm, M., Zabel, V., Bucher, C. *An automatic mode pairing strategy using an enhanced modal assurance criterion based on modal strain energies*, Journal of Sound and Vibration, 2010, **329** (25), pp. 5375–5392. DOI:10.1016/j.jsv.2010.07.006.

Burden, R.L., Faires, J.D. *Numerical analysis*, 6th ed., Vol. ITP, Pacific Grove, CA, USA, 1997.

C

Carter, F.W. *On the action of a locomotive driving wheel*, Proceedings of the Royal Society of London A, 1926, **112**, pp. 151-157. DOI:10.1098/rspa.1926.0100.

Chen, G., Zhai, W. *A new wheel/rail spatially dynamic coupling model and its verification*, Vehicle System Dynamics, 2004, **41** (4), pp. 301-322. DOI:10.1080/00423110412331315178.

Chopra, A.K. *Dynamics of structures. Theory and Applications to Earthquake Engineering*, Prentice Hall, Englewood Cliffs, NJ, USA, 1995.

Claus, H., Schiehlen, W. *Modeling and simulation of railway bogie structural vibrations*, Vehicle System Dynamics, 1998, **29** (1), pp. 538-552. DOI:10.1080/00423119808969585.

Clough, R.W., Penzien, J. *Dynamics of structures*, Third Edition, McGraw-Hill, Inc., New York City, NY, USA, 2003.

CONTACT. Release 11.1, VORtech Computing, Delft, the Netherlands, 2011.

CorbisImages. *Corbis Images from the 1995 Kobe Earthquake* Retrieved from: http://www.corbisimages.com/stock-photo/rights-managed/42-15858537/train-derailed-following-the-kobe-earthquake-in (accessed in October 2014).

D

Dai, G., Hu, N., Liu, W. *The recent improvement of high-speed railway bridges in China*, In IABSE Reports (Ed), 34th IABSE Symposium for Bridge and Structural Engineering: Large Structures and Infrastructures for Environmentally Constrained and Urbanised Areas, Venice, Italy, 2010.

Delgado, R., Santos, S.M. *Modelling of railway bridge-vehicle interaction on high speed tracks*, Computers & Structures, 1997, **63** (3), pp. 511-523. DOI:10.1016/S0045-7949(96)00360-4.

Du, X.T., Xu, Y.L., Xia, H. *Dynamic interaction of bridge–train system under non-uniform seismic ground motion*, Earthquake Engineering and Structural Dynamics, 2012, **41** (1), pp. 139–157. DOI:10.1002/eqe.1122.

Dukkipati, R.V. *Vehicle Dynamics*, Alpha Science International Limited, Pangourne, UK, 2000.

E

Elkins, J.A., Carter, A. *Testing and analysis techniques for safety assessment of rail vehicles: the state-of-the-art*, Vehicle System Dynamics, 1993, **22** (3-4), pp. 185-208. DOI:10.1080/00423119308969026.

Elnashai, A.S., Sarno, L.D. *Fundamentals of Earthquake Engineering*, John Wiley & Sons Ltd, Chichester, UK, 2008.

EN 1990-Annex A2. *Eurocode 0: Basis of structural design - Annex 2: Application for bridges (normative)*, European Committee for Standarization (CEN), Brussels, 2001.

EN 1991-1-4. *Eurocode 1: Actions on structures - Part 1-4: General actions - Wind actions*, European Committee for Standarization (CEN), Brussels, 2005.

EN 1991-1-7. *Eurocode 1: Actions on structures - Part 1-7: General actions - Accidental actions*, European Committee for Standarization (CEN), Brussels, 2006.

EN 1991-2. *Eurocode 1: Actions on structures - Part 2: Traffic loads on bridges*, European Committee for Standarization (CEN), Brussels, 2003.

EN 1992-1-1. *Eurocode 2: Design of concrete structures - Part 1-1: General rules and rules for buildings*, European Committee for Standarization (CEN), Brussels, 2004.

EN 1998-1-NA. *Eurocode 8: Design of structures for earthquake resistance - Part 1: General rules, seismic actions and rules for buildings - Portuguese National Annex*, European Committee for Standarization (CEN), Brussels, 2009.

EN 1998-1. *Eurocode 8: Design of structures for earthquake resistance - Part 1: General rules, seismic actions and rules for buildings*, European Committee for Standarization (CEN), Brussels, 2004.

EN 1998-2. *Eurocode 8: Design of structures for earthquake resistance - Part 2: Bridges*, European Committee for Standarization (CEN), Brussels, 2005.

EN 13848-5. *Railway applications - Track - Track geometry quality - Part 5: Geometric quality assessment*, European Committee for Standarization (CEN), Brussels, 2005.

EN 14067-6. *Railway applications - Aerodynamics - Part 6: Requirements and test procedures for cross wind assessment*, European Committee for Standarization (CEN), Brussels, 2010.

ERRI D 202/RP 11. *Improved knowledge of forces in CWR track (including switches): Parametric study and sensivity analysis of CWERRI*, European Rail Research Institute, Utrecht, 1999.

ERRI D 214/RP 5. *Rail bridges for speeds > 200 km/h: Numerical investigation of the effect of track irregularities at bridge resonance*, European Rail Research Institute, Utrecht, 1999.

F

Falomi, S., Malvezzi, M., Meli, E. *Multibody modeling of railway vehicles: Innovative algorithms for the detection of wheel-rail contact points*, Wear, 2010, **271** (1-2), pp. 453-461. DOI:10.1016/j.wear.2010.10.039.

Fernandes, M. *Comportamento dinâmico de pontes com tabuleiro pré-fabricado em vias de alta velocidade*, MSc Thesis, Universidade do Porto, Faculdade de Engenharia, Porto, Portugal, 2010 [in Portuguese].

Filippou, F.C., Popov, E.P., Bertero, V.V. *Effects of bond deterioration on hysteretic behaviour of reinforced concrete joints*, In (Ed), Report EERC 83-19, Earthquake Engineering Research Center, University of California, Berkeley, CA, 1983.

Fragiadakis, M., Pinho, R., Antoniou, S. *Modelling inelastic buckling of reinforcing bars under earthquake loading*, In M. Papadrakakis, D. C. Charmpis, N. D. Lagaros & Y. Tsompanakis (Ed), COMPDYN 2007 - 1st ECCOMAS Thematic Conference on Computational Methods in Structural Dynamics and Earthquake Engineering, Rithymno, Crete, Greece, 2007.

Frýba, L. *Dynamics of railway bridges*, Thomas Telford Ltd., Prague, Czech Republic, 1996.

Frýba, L., Yau, J.D. *Suspended bridges subjected to moving loads and support motions due to earthquake*, Journal of Sound and Vibration, 2009, **319** (1-2), pp. 218-227. DOI:10.1016/j.jsv.2008.05.012.

G

Garg, V.K., Dukkipati, R.V. *Dynamics of railway vehicle systems*, Academic Press Inc., Orlando, FL, USA, 1984.

Gasparini, D.A., Vanmarcke, E.H. *Simulated earthquake motions compatible with prescribed response spectra*, Massachusetts Institute of Technology, Cambridge, MA, USA, 1976.

Goicolea, J.M., Antolín, P. *Dynamic effects of railway traffic due to lateral motion in long viaducts with high piers*, In M. Papadrakakis, M. Fragiadakis & V. Plevris (Ed), COMPDYN 2011 - 3rd ECCOMAS Thematic Conference on Computational Methods in Structural Dynamics and Earthquake Engineering, Corfu, Greece, 2011.

Goicolea, J.M., Gabaldón, F. *Dynamics of high-speed railway bridges: Methods and design issues*, In H. Xia, G. D. Roeck & J. M. Goicolea (Ed), Bridge Vibration and Controls: New Research (pp. 89-111), Nova Science Publishers, Inc., Hauppauge, NY, USA, 2012.

Goldsmith, W. *Impact: The theory and physical behaviour of colliding solids*, Edward Arnold Ltd., London, UK, 1960.

Guo, W., Xia, H., Xu, Y. *Running safety analysis of a train on the Tsing Ma Bridge under turbulent winds*, Earthquake Engineering and Engineering Vibration, 2010, **9** (3), pp. 307-318. DOI:10.1007/s11803-010-0015-3.

H

Hertz, H. *Ueber die Berührung fester elastischer Körper [On the contact of elastic solids]*, Journal für die reine und angewandte Mathematik, 1882, **92**, pp. 156-171.

Hu, B., Schiehlen, W. *On the simulation of stochastic processes by spectral representation*, Probabilistic Engineering Mechanics, 1997, **12** (2), pp. 105-113. DOI:10.1016/S0266-8920(96)00039-2.

Hughes, T.J.R. *The finite element method: Linear static and dynamic finite element analysis*, Dover Publications, New York City, NY, USA, 2000.

Hwang, E., Nowak, A. *Simulation of dynamic load for bridges*, Journal of Structural Engineering, 1991, **117** (5), pp. 1413–1434. DOI:10.1061/(ASCE)0733-9445(1991)117:5(1413).

I

Ishibashi, T. *Shinkansen structures in Japan*, In R. Calcada, R. Delgado & A. Campos e Matos (Ed), Workshop on Bridges for High-Speed Railways, Porto, Portugal, 2004.

Ishida, H., Matsuo, M. *Safety criteria for evaluation of railway vehicle derailment*, Quarterly Report of Railway Technical Research Institute, 1999, **40** (1), pp. 18-25. DOI:10.2219/rtriqr.40.18.

J

JFE Steel Corporation. *JFE Steel Corporation, Rail Catalogue No. D1E-001-00*, Retrieved from: http://www.jfe-steel.co.jp/en/products/list.html (accessed in July 2014).

Johnson, K.L. *The effect of a tangential contact force upon the rolling motion of an elastic sphere on a plane*, Journal of Applied Mechanics, 1958, **25**, pp. 339-346.

Johnson, K.L. *Contact mechanics*, Cambridge University Press, Cambridge, UK, 1985.

Jun, X., Qingyuan, Z. *A study on mechanical mechanism of train derailment and preventive measures for derailment*, Vehicle System Dynamics, 2005, **43** (2), pp. 121-147. DOI:10.1080/0042311041233132201.

K

Kalker, J.J. *On the rolling contact of two elastic bodies in the presence of dry friction*, PhD thesis, Delft University of Technology, Delft, The Netherlands, 1967.

Kalker, J.J. *The computation of three-dimensional rolling contact with dry friction*, International Journal for Numerical Methods in Engineering, 1979, **14** (9), pp. 1293-1307. DOI:10.1002/nme.1620140904.

Kalker, J.J. *A fast algorithm for the simplified theory of rolling contact*, Vehicle System Dynamics, 1982a, **11** (1), pp. 1-13. DOI:10.1080/00423118208968684.

Kalker, J.J. *Introduction to the Fortran IV programs DUVOROL and CONTACT for the solution of 3D elastostatic half-space contact problems with and without friction*, Technical Report of the Department of Mathematics and Informatics no. 82-29, Delft Technical University, Delft, The Netherlands, 1982b.

Kalker, J.J. *Three-Dimensional Elastic Bodies in Rolling Contact*, Kluwer Academic Publishers, Dordrecht, The Netherlands, 1990.

Kalker, J.J. *Wheel-rail rolling contact theory*, Wear, 1991, **144** (1-2), pp. 243-261. DOI:10.1016/0043-1648(91)90018-P.

Kalker, J.J. *Book of tables for the Hertzian creep-force law*, In I. Zobory (Ed), 2nd Mini Conference on Contact Mechanics and Wear of Wheel/Rail Systems, Budapest, Hungary, 1996.

Kao, T.C., Lin, C.K. *Taiwan high speed rail & its impact to regional development*, In K. C. Chang (Ed), 4th CECAR - Civil Engineering Conference in the Asian Region, Taipei, Taiwan, 2007.

Kim, C.W., Kawatani, M. *Effect of train dynamics on seismic response of steel monorail bridges under moderate ground motion*, Earthquake Engineering and Structural Dynamics, 2006, **35** (10), pp. 1225–1245. DOI:10.1002/eqe.580.

Klingel, W. *Über den Lauf der Eisenbahnwagen auf gerader Bahn*, Organ für die Fortschritte des Eisenbahnwesens, 1883, **20**, pp. 113-123.

Knothe, K., Böhm, F. *History of stability of railway and road vehicles*, 1999, **31** (5-6), pp. 283-323. DOI:10.1076/vesd.31.5.283.8362.

Kreyszig, E. *Differential geometry*, Dover Publications Inc., New York City, NY, USA, 1991.

L

Lee, Y.S., Kimb, S.H. *Structural analysis of 3D high-speed train–bridge interactions for simple train load models*, Vehicle System Dynamics, 2010, **48** (2), pp. 263-281. DOI:10.1080/00423110902751912.

Lei, X., Noda, N.A. *Analyses of dynamic response of vehicle and track coupling system with random irregularity of track vertical profile*, Journal of Sound and Vibration, 2002, **258** (1), pp. 147-165. DOI:10.1006/jsvi.2002.5107.

Li, Y., Qiang, S., Liao, H., Xu, Y.L. *Dynamics of wind–rail vehicle–bridge systems*, Journal of Wind Engineering and Industrial Aerodynamics, 2005, **93** (6), pp. 483–507. DOI:10.1016/j.jweia.2005.04.001.

Li, Z. *Wheel-rail rolling contact and its application to wear simulation*, PhD thesis, Delft University of Technology, Delft, The Netherlands, 2002.

Luo, X. *Study on methodology for running safety assessment of trains in seismic design of railway structures*, Soil Dynamics and Earthquake Engineering, 2005, **25** (2), pp. 79-91. DOI:10.1016/j.soildyn.2004.10.005.

Luo, X., Miyamoto, T. *Method for running safety assessment of railway vehicles against structural vibration displacement during earthquakes*, Quarterly Report of Railway Technical Research Institute, 2007, **48** (3), pp. 129-135. DOI:10.2219/rtriqr.48.129.

M

Malveiro, J., Ribeiro, D., Calçada, R., Delgado, R. *Updating and validation of the dynamic model of a railway viaduct with precast deck*, Structure and Infrastructure Engineering: Maintenance, Management, Life-Cycle Design and Performance, 2013, pp. [Article in press]. DOI:10.1080/15732479.2013.833950.

Mander, J.B., Priestley, M.J.N., Park, R. *Theoretical stress-strain model for confined concrete*, Journal of Structural Engineering, 1988, **114** (8), pp. 1804-1826. DOI:10.1061/(ASCE)0733-9445(1988)114:8(1804).

Martínez-Rueda, J.E., Elnashai, A.S. *Confined concrete model under cyclic load*, Materials and Structures, 1997, **30** (3), pp. 139-147. DOI:10.1007/BF02486385.

MATLAB. Release R2011b, The MathWorks Inc., Natick, MA, USA, 2011.

Matsumoto, N., Tanabe, M., Sogabe, M., Wakui, H. *Running safety analysis of vehicles on structures subjected to earthquake motion*, Quarterly Report of Railway Technical Research Institute, 2004, **45** (3), pp. 116-122. DOI:10.2219/rtriqr.45.116.

Matsumoto, Y. *Japanese Railway Technology Today*, East Japan Railway Culture Foundation, Tokyo, Japan, 2001.

Menegotto, M., Pinto, P.E. *Method of analysis for cyclically loaded R.C. plane frames including changes in geometry and non-elastic behaviour of elements under combined normal force and bending*, In (Ed), IABSE Symposium on the Resistance and Ultimate Deformability of Structures Acted on by Well Defined Repeated Loads, Lisbon, Portugal, 1973.

Miura, S. *Deformation of track and the safety of train in earthquake*, Quarterly Report of Railway Technical Research Institute, 1996, **37** (3), pp. 139-146.

Miyamoto, T., Ishida, H., Matsuo, M. *Running safety of railway vehicle as earthquake occurs*, Quarterly Report of Railway Technical Research Institute, 1997, **38** (3), pp. 117-122.

Miyamoto, T., Matsumoto, N., Sogabe, M., Shimomura, T., Nishiyama, Y., Matsuo, M. *Railway vehicle dynamic behavior against large-amplitude track vibration - A full-scale experiment and numerical simulation*, Quarterly Report of Railway Technical Research Institute, 2004, **45** (3), pp. 111-115. DOI:10.2219/rtriqr.45.111.

Montenegro, P.A., Calçada, R., Vila Pouca, N., Tanabe, M. *Running safety assessment of trains moving over bridges subjected to earthquakes*, Earthquake Engineering and Structural Dynamics, 2015a, (submitted).

Montenegro, P.A., Neves, S.G.M., Calçada, R., Tanabe, M., Sogabe, M. *Wheel-rail contact formulation for analyzing the lateral train-structure dynamic interaction*, Computers & Structures, 2015b, **152**, pp. 200-214. DOI:10.1016/j.compstruc.2015.01.004.

N

Nadal, J. *Locomotives à vapeur*, Collection Encyclopédie Scientifique, Bibliotèque de Mecanique Appliquée et Genie, Vol.186, Doin Éditeurs, Paris, France, 1908.

Nazmy, A.S., Abdel-Ghaffar, A.M. *Effects of ground motion spatial variability on the response of cable-stayed bridges*, Earthquake Engineering and Structural Dynamics, 1992, **21** (1), pp. 1–20. DOI:10.1002/eqe.4290210101.

Neves, S.G.M., Azevedo, A.F.M., Calçada, R. *A direct method for analyzing the vertical vehicle-structure interaction*, Engineering Structures, 2012, **34**, pp. 414-420. DOI:10.1016/j.engstruct.2011.10.010.

Neves, S.G.M., Montenegro, P.A., Azevedo, A.F.M., Calçada, R. *A direct method for analyzing the nonlinear vehicle–structure interaction*, Engineering Structures, 2014, **69**, pp. 83-89. DOI:10.1016/j.engstruct.2014.02.027.

Nguyen, D.V., Kim, K.D., Warnitchai, P. *Dynamic analysis of three-dimensional bridge-high-speed train interactions using a wheel-rail contact model*, Engineering Structures, 2009a, **31** (12), pp. 3090-3106 DOI:10.1016/j.engstruct.2009.08.015.

Nguyen, D.V., Kim, K.D., Warnitchai, P. *Simulation procedure for vehicle–substructure dynamic interactions and wheel movements using linearized wheel–rail interfaces*, Finite Elements in Analysis and Design, 2009b, **45** (5), pp. 341-356. DOI:10.1016/j.finel.2008.11.001.

Nishimura, K., Terumichi, Y., Morimura, T., Sogabe, K. *Development of vehicle dynamics simulation for safety analyses of rail vehicles on excited tracks*, Journal of Computational and Nonlinear Dynamics, 2008, **4** (1), pp. 011001(1) - 011001(9). DOI:10.1115/1.3007901.

O

Owen, D.R.J., Hinton, E. *Finite Elements in Plasticity: Theory and Practice*, Pineridge Press Limited, Swansea, UK, 1980.

P

Pascal, J.P. *About multi-Hertzian-contact hypothesis and equivalent conicity in the dase of S1002 and UIC60 analytical wheel/rail profiles*, Vehicle System Dynamics, 1993, **22** (2), pp. 57-78. DOI:10.1080/00423119308969021.

Piotrowski, J. *A theory of wheelset forces for two point contact between wheel and rail*, Vehicle System Dynamics, 1982, **11** (2), pp. 69-87. DOI:10.1080/00423118208968690.

Piotrowski, J., Chollet, H. *Wheel–rail contact models for vehicle system dynamics including multi-point contact*, Vehicle System Dynamics, 2005, **43** (6-7), pp. 455-483. DOI:10.1080/00423110500141144.

Piotrowski, J., Kik, W. *A simplified model of wheel/rail contact mechanics for non-Hertzian problems and its application in rail vehicle dynamic simulations*, Vehicle System Dynamics, 2008, **46** (1-2), pp. 27-48. DOI:10.1080/00423110701586444.

Polach, O. *A fast wheel-rail forces calculation computer code*, Vehicle System Dynamics, 1999, **33**, pp. 728-739.

Pombo, J. *A multibody methodology for railway dynamics application*, PhD Thesis, Universidade Técnica de Lisboa, Instituto Superior Técnico, Lisbon, Portugal, 2004.

Pombo, J., Ambrosio, J., Silva, M. *A new wheel-rail contact model for railway dynamics*, Vehicle System Dynamics, 2007, **45** (2), pp. 165-189. DOI:10.1080/00423110600996017.

Prud'homme, A. *La résistance de la voie aux efforts transversaux éxercés par le material roulant*, Revue Generale des Chemins de Fer, January 1967.

Q

Quost, X., Sebes, M., Eddhahak, A., Ayasse, J.B., Chollet, H., Gautier, P.E., Thouverez, F. *Assessment of a semi-Hertzian method for determination of wheel–rail contact patch*, Vehicle System Dynamics, 2006, **44** (10), pp. 789–814. DOI:10.1080/00423110600677948.

R

RTRI. *Outline of design standards for railway structures and commentary (seismic design)*, Railway Technical Research Institute (Ed.), Maruzen Co., Ltd., Tokyo, 1999.

RTRI. *Outline of design standards for railway structures and commentary (displacement limits)*, Railway Technical Research Institute (Ed.), Maruzen Co., Ltd., Tokyo, 2006.

RTRI. *Railway Technical Research Institute - Testing facilities*, Retrieved from: http://www.rtri.or.jp/eng/rd/rd_test.html (accessed in December 2013).

S

Sánchez Doblado, M. *El desarrollo de una red ferroviaria moderna*, In Fundación Caminos de Hierro (Ed), Jornadas Técnicas: Ingeniería para Alta Velocidad. Veinte años de experiencia en España, Córdoba, Spain, 2007 [in Spanish].

Santamaria, J., Vadillo, E.G., Gomez, J. *A comprehensive method for the elastic calculation of the two-point wheel-rail contact*, Vehicle System Dynamics, 2006, **44** (1), pp. 240-250. DOI:10.1080/00423110600870337.

SeismoArtif. Version 2.1, SeismoSoft, Pavia, Italy, 2013.

SeismoStruct. Version 6.5, SeismoSoft, Pavia, Italy, 2013.

Shabana, A., Berzeri, M., Sany, J.R. *Numerical procedure for the simulation of wheel/rail contact dynamics*, Journal of Dynamic Systems, Measurement and Control, Transactions of the ASME, 2001, **123** (2), pp. 168-178. DOI:10.1115/1.1369109.

Shabana, A., Tobaa, M., Sugiyama, H., Zaazaa, K.E. *On the computer formulations of the wheel/rail contact problem*, Nonlinear Dynamics, 2005, **40** (2), pp. 169-193. DOI:10.1007/s11071-005-5200-y.

Shabana, A., Zaazaa, K.E., Escalona, J.L., Sany, J.R. *Development of elastic force model for wheel/rail contact problems*, Journal of Sound and Vibration, 2004, **269** (1-2), pp. 295-325. DOI:10.1016/S0022-460X(03)00074-9.

Shabana, A., Zaazaa, K.E., Sugiyama, H. *Railroad vehicle dynamics: A computational approach*, CRC Press - Taylor & Francis Group, Boca Raton, FL, USA, 2008.

Shackleton, P., Iwnicki, S. *Wheel-rail contact benchmark*, In (Ed), Manchester Metropolitan University, Manchester, UK, 2006.

Shackleton, P., Iwnicki, S. *Comparison of wheel–rail contact codes for railway vehicle simulation: an introduction to the Manchester Contact Benchmark and initial results*, Vehicle System Dynamics, 2008, **46** (1-2), pp. 129-149. DOI:10.1080/00423110701790749.

Shen, Z.Y., Hedrick, J.K., Elkins, J.A. *A comparison of alternative creep force models for rail vehicle dynamic analysis*, Vehicle System Dynamics, 1983, **12** (1-3), pp. 79-83. DOI:10.1080/00423118308968725.

Sogabe, M., Furukawa, A., Shimomura, T., Iida, T. *Displacement limits of structures for high-speed train operation*, Railway Technical Research Institute Report, 2006, **20** (12), pp. 13-18 [in Japanese].

Sogabe, M., Furukawa, A., Shimomura, T., Iida, T., Matsumoto, N., Wakui, H. *Deflection limits of structures for train speed-up*, Quarterly Report of Railway Technical Research Institute, 2005, **46** (2), pp. 130-136. DOI:10.2219/rtriqr.46.130.

Sogabe, M., Ikeda, M., Yanagisawa, Y. *Train-running quality during earthquakes and its improvement for railway long span bridges*, Quarterly Report of Railway Technical Research Institute, 2007, **48** (3), pp. 183-189. DOI:10.2219/rtriqr.48.183.

Sonneville, R., Bentot, A. *Elastic and lateral strength of the permanent way*, Bulletin of the International Railway Congress Assn., 1955, **32** (3), pp. 184-208.

Sugiyama, H., Araki, K., Suda, Y. *On-line and off-line wheel/rail contact algorithm in the analysis of multibody railroad vehicle systems*, Journal of Mechanical Science and Technology, 2009, **23** (4), pp. 991-996. DOI:10.1007/s12206-009-0327-2.

Sugiyama, H., Suda, Y. *On the contact search algorithms for wheel/rail contact problems* Journal of Computational and Nonlinear Dynamics, 2009, **4** (4), pp. 041001(1) - 041001(7). DOI:10.1115/1.3187211.

T

Tanabe, M., Matsumoto, N., Wakui, H., Sogabe, M. *Simulation of a Shinkansen train on the railway structure during an earthquake*, Japan Journal of Industrial and Applied Mathematics, 2011a, **28** (1), pp. 223-236. DOI:10.1007/s13160-011-0022-4.

Tanabe, M., Matsumoto, N., Wakui, H., Sogabe, M., Okuda, H., Tanabe, Y. *A simple and efficient numerical method for dynamic interaction analysis of a high-speed train and railway structure during an earthquake*, Journal of Computational and Nonlinear Dynamics, 2008, **3** (4), pp. 041002(1) - 041002(8). DOI:10.1115/1.2960482.

Tanabe, M., Wakui, H., Matsumoto, N. *The finite element analysis of dynamic interaction of high-speed Shinkansen, the rail, and bridge*, In F. Kinoglu, A.Bennett, A. Busnaina, K. Ishii, M. Khoswrowjerdi, G. Kinzel, H. Tzou & G. Yip (Ed), Computers in Engineering: Book No. G0813A (pp. 17-22), ASME, New York City, NY, USA, 1993.

Tanabe, M., Wakui, H., Matsumoto, N., Okuda, H., Sogabe, M., Komiya, S. *Computational model of a Shinkansen train running on the railway structure and the industrial applications*, Journal of Materials Processing Technology, 2003, **140** (1-3), pp. 705-710. DOI:10.1016/S0924-0136(03)00777-5.

Tanabe, M., Wakui, H., Sogabe, M., Matsumoto, N., Gotou, K., Tanabe, Y. *Computational model for a high speed train running on the railway structure including derailment during an earthquake*, Advanced Materials Research, 2012, **579**, pp. 473-482. DOI:10.4028/www.scientific.net/AMR.579.473.

Tanabe, M., Wakui, H., Sogabe, M., Matsumoto, N., Tanabe, Y. *An efficient numerical model for dynamic interaction of high speed train and railway structure including post-derailment during an earthquake*, In G. D. Roeck, G. Degrande, G. Lombaert & G. Müller (Ed), EURODYN 2011 - Proceedings of the 8th International Conference on Structural Dynamics, Leuven, Belgium, 2011b.

Tanabe, M., Yamada, Y., Wakui, H. *Modal method for interaction of train and bridge*, Computers & Structures, 1987, **27** (1), pp. 119–127. DOI:10.1016/0045-7949(87)90187-8.

TSI. *Technical specification for interoperability relating to the infrastructure subsystem of the trans-European high-speed rail system*, Official Journal of the European Union, Brussels, 2002.

U

UIC 774-3-R. *Track/bridge interaction - Recommendations for calculation*, 2nd Edition, International Union of Railways (UIC), Paris, 2001.

V

Valtorta, D., Zaazaa, K.E., Shabana, A.A., Sany, J.R. *A study of the lateral stability of railroad vehicles using nonlinear constrained multibody formulation*, In (Ed), Proceedings of the ASME 2001 International Mechanical Engineering Congress and Exposition, New York, NY, USA, 2001.

Vermeulen, P.J., Johnson, K.L. *Contact of nonspherical elastic bodies transmitting tangential forces*, Journal of Applied Mechanics, 1964, **31** (2), pp. 338-340. DOI:10.1115/1.3629610.

W

Weinstock, H. *Wheel climb derailment criteria for evaluation of rail vehicle safety*, In (Ed), Proceedings of ASME Winter Annual Meeting, 84-WA/RT-1, New Orleans, LA, USA, 1984.

Wickens, A.H. *Fundamentals of rail vehicle dynamics: guidance and stability*, Swets & Zeitlinger B.V., Lisse, the Netherlands, 2003.

Wikipedia/Shinkansen. *Shinkansen High-Speed Train*, Retrieved from: http://en.wikipedia.org/wiki/Shinkansen (accessed in September 2014).

Wriggers, P. *Computational Contact Mechanics*, John Wiley & Sons Ltd, Chichester, UK, 2002.

Wu, H., Wilson, N. *Railway Vehicle Derailment and Prevention*, In S. Iwnicki (Ed), Handbook of Railway Vehicle Dynamics (pp. 209-238), CRC Press - Taylor & Francis Group, Boca Raton, FL, USA, 2006.

Wu, Y.S., Yang, Y.B. *Steady-state response and riding comfort of trains moving over a series of simply supported bridges*, Engineering Structures, 2003, **25** (2), pp. 251-265. DOI:10.1016/S0141-0296(02)00147-5.

Wu, Y.S., Yang, Y.B., Yau, J.D. *Three-dimensional analysis of train-rail-bridge interaction problems*, Vehicle System Dynamics, 2001, **36** (1), pp. 1-35. DOI:10.1076/vesd.36.1.1.3567.

X

Xia, H., Guo, W., Wu, X., Pi, Y.L., Bradford, M.A. *Lateral dynamic interaction analysis of a train–girder–pier system*, Journal of Sound and Vibration, 2008, **318** (4-5), pp. 927-942. DOI:10.1016/j.jsv.2008.05.002.

Xia, H., Han, Y., Zhang, N., Guo, W. *Dynamic analysis of train-bridge system subjected to non-uniform seismic excitations*, Earthquake Engineering and Structural Dynamics, 2006, **35** (12), pp. 1563–1579. DOI:10.1002/eqe.594.

Xu, Y.L., Zhang, N., Xia, H. *Vibration of coupled train and cable-stayed bridge systems in cross winds*, Engineering Structures, 2004, **26** (10), pp. 1389–1406. DOI:10.1016/j.engstruct.2004.05.005.

Y

Yang, F., Fonder, G. *An iterative solution method for dynamic response of bridge-vehicles systems*, Earthquake Engineering and Structural Dynamics, 1996, **25** (2), pp. 195-215. DOI:10.1002/(SICI)1096-9845(199602)25:2<195::AID-EQE547>3.0.CO;2-R.

Yang, Y.B., Chang, C.H., Yau, J.D. *An element for analysing vehicle-bridge systems considering vehicle's pitching effect*, International Journal for Numerical Methods in Engineering, 1999, **46** (7), pp. 1031-1047. DOI:10.1002/(SICI)1097-0207(19991110)46:7<1031::AID-NME738>3.0.CO;2-V.

Yang, Y.B., Wu, Y.S. *A versatile element for analyzing vehicle-bridge interaction response*, Engineering Structures, 2001, **23** (5), pp. 452-469. DOI:10.1016/S0141-0296(00)00065-1.

Yang, Y.B., Wu, Y.S. *Dynamic stability of trains moving over bridges shaken by earthquakes*, Journal of Sound and Vibration, 2002, **258** (1), pp. 65-94. DOI:10.1006/jsvi.2002.5089.

Yang, Y.B., Yau, J.D. *Vehicle-bridge interaction element for dynamic analysis*, Journal of Structural Engineering, 1997, **123** (11), pp. 1512-1518. DOI:10.1061/(ASCE)0733-9445(1997)123:11(1512).

Yang, Y.B., Yau, J.D., Wu, Y.S. *Vehicle-Bridge Interaction Dynamics, with Application to High-Speed Railways*, World Scientific, Singapore, 2004.

Yau, J.D. *Dynamic response analysis of suspended beams subjected to moving vehicles and multiple support excitations*, Journal of Sound and Vibration, 2009, **325** (4-5), pp. 907–922. DOI:10.1016/j.jsv.2009.04.013.

Yau, J.D., Frýba, L. *Response of suspended beams due to moving loads and vertical seismic ground excitations*, Engineering Structures, 2007, **29** (12), pp. 3255–3262. DOI:10.1016/j.engstruct.2007.10.001.

Z

Zaazaa, K.E., Schwab, A.L. *Dynamic effects of railway traffic due to lateral motion in long viaducts with high piers*, In K. Anderson & G. Flowers (Ed), IDETC/CIE 2009 - Proceedings of the ASME 2009 International Design Engineering Technical Conference & Computers and Information in Engineering Conference, San Diego, CA, USA, 2009.

Zhai, W., Wang, K., Cai, C. *Fundamentals of vehicle-track coupled dynamics*, Vehicle System Dynamics, 2009, **47** (11), pp. 1349-1376. DOI:10.1080/00423110802621561.

Zhang, N., Xia, H., Guo, W. *Vehicle-bridge interaction analysis under high-speed trains*, Journal of Sound and Vibration, 2008, **309** (3-5), pp. 407-425. DOI:10.1016/j.jsv.2007.07.064.